Building Blocks and Structural Patterns in Silicon Clusters:

Global and local optimizations employing empirical potentials, density functionals, and ab-initio calculations

PhD thesis

Submitted for the degree of “Doktor rerum naturae”
to the Faculty of Mathematics and Science
Christian-Albrechts University of Kiel

Adem Tekin
Kiel 2004

This PhD work was carried out at the Institute of Theoretical Chemistry at Stuttgart University from October 2001 until March 2002 and continued at the Institute of Physical Chemistry at Christian-Albrechts University of Kiel from April 2002 until November 2004. I certify that this thesis does not incorporate, without acknowledgement, any material previously submitted for a degree in any university, and that, to the best of my knowledge, it does not contain any material previously published or written by another person. The work in this thesis is my own, except for the contributions made by others as described in the Acknowledgements.

Adem Tekin

Referent/in: ....

Korreferent/in: ....

Tag der mündlichen Prüfung: ....

Zum Druck genehmigt: Kiel, ...

Der Dekan

Summary

Building Blocks and Structural Patterns in Silicon Clusters:
Global and local optimizations employing empirical potentials, density functionals,
and ab-initio calculations

Silicon is one of the most important semiconductors used in the microelectronics industry. If the current miniaturization trends continue, atomic clusters at various sizes might be used to design new devices. For this reason, silicon clusters have been the subject of a large number of theoretical and experimental studies in recent years. There is a general consensus on structures up to Si_n (n = 10), from ab-initio and DFT calculations. In addition, for small Si_n (n <8) clusters, global minimum structures are also established by several experiments. For the larger clusters, finding the global minimum structures becomes a challenge because of the exponential increase in the number of local minima. In addition, with increasing cluster size, performing an ab-initio or DFT calculation with a reasonable basis set turns out to be expensive.

In spite of these facts, in this thesis, Si_n clusters in the size range n=4-35 have been investigated, using a combination of global structure optimization methods with DFT and ab-initio calculations. One of the central aims is to provide explanations for the structural transition from prolate to spherical outer shapes at about n=25, as observed in ion mobility measurements. First, several existing empirical potentials for silicon and a newly generated variant of one of them were better adapted to small silicon clusters, by global optimization of their parameters. The best resulting empirical potentials were then employed in global cluster structure optimizations. The most promising structures from this stage were relaxed further at the DFT level with a hybrid B3LYP functional. For the resulting structures, single point energies have been calculated at the LMP2 level with a reasonable medium-sized basis set, cc-pVTZ. These DFT and LMP2 calculations were also carried out for the best structures proposed in the literature including the most recent ones, to obtain the currently best and most complete overall picture of the structural preferences of silicon clusters.

Results obtained at the DFT level strongly support the shape transition form prolate to spherical structures beginning with Si_{26}. Up to n=25, the best structures have prolate outer shapes. In their inner structures, a small set of characteristic building blocks is found repeatedly. For $n \geq 25$, spherical isomers begin to dominate. They exhibit different characteristics in shape, but all contain cages with inner atoms.

In stark contrast, at the LMP2 level, the dominance of spherical structures after the transition region could not be confirmed. Instead, just as before the transition region, prolate isomers are obtained as the lowest-energy structures for $n \leq 29$.

This discrepancy in theoretical results can only be settled by higher-level calculations (e.g. CCSD(T)/cc-pVQZ). Unfortunately, such calculations still are too expensive to be performed for many cluster isomers in this size range.

Simultaneously, comparisons between experimental and simulated mobilities indicate that mobility data alone are not sufficient to decide between several different cluster isomers. Therefore, while the present study is an important intermediate stage, the final elucidation of the first shape transition of silicon clusters has to await further theoretical and experimental progress.

Zusammenfassung

Bausteine und Strukturelle Muster in Siliciumclustern:
Globale und lokale Optimierung unter Anwendung von empirischen Potentialen,
Dichtefunktionaltheorie sowie ab-initio-Berechnungen

Silicium ist einer der wichtigsten Halbleiter, der in der mikroelektronischen Industrie verwendet wird. Falls der aktuelle Trend zur Miniaturisierung von Bauteilen anhält, könnten atomare Cluster verschiedener Größen verwendet werden, um neue Baugruppen zu entwickeln. Aus diesem Grund sind Siliciumcluster im Laufe der letzten Jahre in einer großen Anzahl experimenteller und theoretischer Studien näher untersucht worden. Dichtefunktional- und Ab-Initio-Rechnungen stimmen bei den gefundenen Strukturen bis zu einer Clustergröße von Si_{10} überein. Zusätzlich wurden für kleinere Clustergrößen (Si_n mit $n<8$) verschiedene Strukturen aus globalen Optimierungsverfahren experimentell verifiziert. Für größere Clusterstrukturen ist es eine Herausforderung, global optimierte Strukturen zu finden, da die Anzahl lokaler Minima exponentiell mit der Anzahl an Atomen im Cluster ansteigt. Gleichzeitig werden ab-initio- oder DFT-Rechnungen mit einem angemessenen Basissatz für diese Systeme zu teuer.

Trotz dieser Umstände wurden Siliciumcluster Si_n (mit n=4-35) in dieser Arbeit untersucht. Dazu wurde eine Kombination aus globalen Geometrieoptimierungsverfahren, DFT- und ab-initio-Berechnungen verwendet. Eines der zentralen Ziele war es, Erklärungen für den strukturellen Übergang bei Siliciumclustern bei n=25 zwischen länglichen und sphärischen äußeren Formen zu liefern, der in Ionen-Mobilitätsexperimenten beobachtet wurde. Dazu wurden zunächst bestehende empirische Potentiale, sowie eine neu entwickelte Variante eines dieser Potentiale, mittels globaler Optimierung der Potentialparameter besser an kleine Siliciumcluster angepaßt. Das beste Potential wurde anschließend für die globale Geometrieoptimierung der Clusterstrukturen verwendet. Die vielversprechendsten Strukturen wurden daraufhin auf DFT-Niveau mit einem B3LYP-Hybridfunktional weiter relaxiert. Die dabei gefundenen Strukturen wurden einer Einzelpunkt-Energieberechnung auf LMP2-Niveau mit einem mittleren Basissatz (cc-pVTZ) unterzogen. Diese DFT- und LMP2-Berechnungen wurden auch für die in der Literatur vorgeschlagenen Strukturen durchgeführt - inklusive der allerneuesten - um einen aktuellen und auch kompletten Überblick über den Aufbau von Siliciumclustern zu bekommen.

Die Ergebnisse aus den DFT-Berechnungen stützen stark den Strukturübergang von länglich nach sphärisch, beginnend bei Si_{26}. Bis hin zu n=25 weisen die energetisch günstigen Strukturen eine längliche äußere Form auf. Für den inneren Bereich dieser Clusterstrukturen wurde eine Anzahl sich wiederholender charakteristischer Baugruppen gefunden. Für $n \geq 25$ fangen die sphärischen äußeren Formen an zu dominieren. Sie weisen unterschiedliche Merkmale auf, bestehen aber alle aus einem Käfig mit inneren Atomen.

In starkem Kontrast dazu stehen die Berechnungen auf LMP2-Niveau. Die Dominanz der spärischen Strukturen nach dem Strukturübergang konnte nicht verifiziert werden. Stattdessen wurden längliche Strukturen für $n \leq 29$ als am energetisch günstigsten gefunden.

Diese Diskrepanz in den theoretischen Ergbnissen kann nur durch noch bessere Berechnungen (z.B. CCSD(T)/cc-pVQZ) behoben werden. Unglücklicherweise sind Berechnungen dieser Art noch immer viel zu teuer. Gleichzeitig zeigen Vergleiche zwischen experimentellen Daten und simulierten Mobilitätsexperimenten, dass Daten aus Mobilitätsversuchen alleine nicht ausreichen, um zwischen verschiedenen Clusterisomeren unterscheiden zu können. Deshalb stellt diese Arbeit einen wichtigen Zwischenschritt zu einer endültigen Erläuterung dieses ersten Strukturübergangs von Siliciumclustern dar, die erst durch weitere theoretische Berechnungen auf höherem Niveau gefunden werden kann.

Acknowledgments

I especially acknowledge Prof. Dr. Bernd Hartke for admission in his research group, the assignment to this interesting research project and for a personal and friendly supervision of this work, giving me a lot of motivation and important contribution during the writing of the manuscript but also for the interesting stimulating discussions.

Furthermore, I would like to thank all my colleagues for valuable discussions:

Franziska Schulz,

Rungtiva Palangsuntikul,

Bernhard Bandow,

Frank von Horsten,

Andre Janz

I also acknowledge Prof. Martin Jarrold (Indiana University, USA), Prof. Koblar Jackson (Michigan University, USA), Prof. X. C. Zeng (University of Nebraska, USA), and Dr. Alexander Sieck and Prof. Dr. Thomas Frauenheim (University of Paderborn, Germany) for sending us detailed information on their silicon cluster findings.

Table of Contents

List of Figures

List of Tables

List of Abbreviations

AIP	Adiabatic Ionization Potential
AO	Atomic Orbital
BA	Bolding and Anderson
B&B	Branch and Bound
BFGS	Broyden-Fletcher-Goldfarb-Shanno
BH	Biswas and Hamann
BO	Born-Oppenheimer
CAM	Cutting Angle Method
CID	Collision Induced Dissociation
CCSD	Coupled Cluster Singles and Doubles
CCSD(T)	CCSD including Triple excitations perturbatively
CFF	Classical Force Field
CPMD	Car-Parinello MD
CSA	Conformational Space Annealing
CSFs	Configuration State Functions
DFP	Davidon-Fletcher-Powell
DFPMIN	Davidon-Fletcher-Powell Minimization
DFT	Density Functional Theory
DFTB	Density Functional Tight Binding
EAM	Embedded-Atom Method
ECP	Effective Core Potential
EHSS	Exact Hard Sphere Scattering
ERIs	Electron Repulsion Integrals
FMM	Fast Multipole Method
FRPRMN	Fletcher-Reeves-Polak-Ribiere Minimization
FT-ICR	Fourier Transform Ion Cyclotron Resonance
GA	Genetic Algorithm
HF	Hartree-Fock
IMM	Ion Mobility Measurements
IR	Infrared
KDS	Khor and Das Sarma
L-BFGS-B	Limited memory BFGS method
LDA	Local Density Approximation
LJ	Lennard-Jones
LJM	Li, Johnston, and Murrell
LMP2	Local 2nd order Møller-Plesset perturbation theory
MARI-*J*	Multipole Accelerated Resolution of the Identity for *J*
MC	Monte Carlo
MCM	Monte Carlo with Minimization
MD	Molecular Dynamics
MO	Molecular Orbital
MP2	2nd order Møller-Plesset theory
NP	Non-deterministic Polynomial

PA	Projection Approximation
PES	Potential Energy Surface
PTHT	Pearson, Takai, Halicioglu, and Tiller
RI	Resolution of the Identity
SA	Simulated Annealing
SA-MD	Simulated Annealing Molecular Dynamics
SCF	Self-Consistent Field
SW	Stillinger-Weber
SWG	Stillinger-Weber-Gong
TB	Tight Binding
TTP	Tetra-capped Trigonal Prism
TM	Trajectory Method
TS	Tabu Search

1 Introduction and Motivation

1.1 Importance and properties of silicon

Silicon (Si), one of the base elements of the earth's crust by making up 25.7% in weight, is the foundation of the modern information society. Modern electronics would be unthinkable without the development of silicon transistors; such transistors are made possible only by the outstanding characteristics and stability of silicon and its oxides. Silicon is a semiconductor with an indirect band gap of 1.1 eV and its conductivity can be widely varied by doping. The most common acceptor type is Boron and the most common donator types are Phosphorus and Arsenic. Silicon can be grown in single crystals more than 1 meter long and 30 cm across, weighing approximately 200 kg. Silicon is found largely as silicon oxides such as sand (silica), quartz, and etc. Silicates, the anionic forms (SiO_3^{2-}, SiO_4^{4-}), exist in a variety of polymeric structures both in naturally occurring and also in artificially produced zeolites. Also, it is a main ingredient of ceramics and glass. Zeolites are used as molecular sieves in separation technology and in catalytic processes and as ion-exchangers in water purification.

There is normally no need to make silicon in the laboratory as it is readily available commercially. Silicon is readily available through the treatment of silica, SiO_2, with pure graphite (as coke) in an electric furnace.

$$SiO_2 + 2C \longrightarrow Si + 2CO$$

Very pure silicon can be made by the reaction of $SiCl_4$ with hydrogen.

$$SiCl_4 + 2H_2 \longrightarrow Si + 4HCl$$

Si, thus prepared is usually impure and is purified by what is known as zone melting or zone refining. In zone melting, Si rods to be purified are heated to very close to melting point by a heater coil that can be moved slowly from bottom to top. Impure silicon melts at a lower temperature than pure silicon. When such an impure melt is cooled very slowly, the pure compound crystallizes out first leaving the impurity in the molten part.

Semiconductor devices are made primarily of silicon. Pure silicon forms rigid crystals because of its four valence electrons. In particular, one Si atom bonds to four other Si atoms forming a very regularly shaped tetrahedral diamond pattern. Pure silicon is not a conductor because there are no free electrons; all the electrons are tightly bound to neighboring atoms. To make silicon conducting, producers combine or "dope" pure silicon with very small amounts of other elements like boron or phosphorus. Phosphorus has five outer valence electrons. When three silicon atoms and one phosphorus atom bind together in the basic silicon crystal cell of four atoms, there is an extra electron and a net negative charge. Figure 1.1 (a) shows the crystal structure of phosphorus doped silicon. This type of material is called n-type silicon. The extra electron in the crystal cell is not strongly attached and can be released by normal thermal energy to carry current; the conductivity depends on the amount of phosphorus added to the silicon. Boron has only three valance electrons. When three silicon atoms and one boron atom bind with each other there is a "hole" where another electron would be if the boron atom were silicon; see Fig.1.1 (b). This gives the crystal cell a positive net charge (referred to as p-type silicon), and the ability to pick up an electron easily from a neighboring cell.

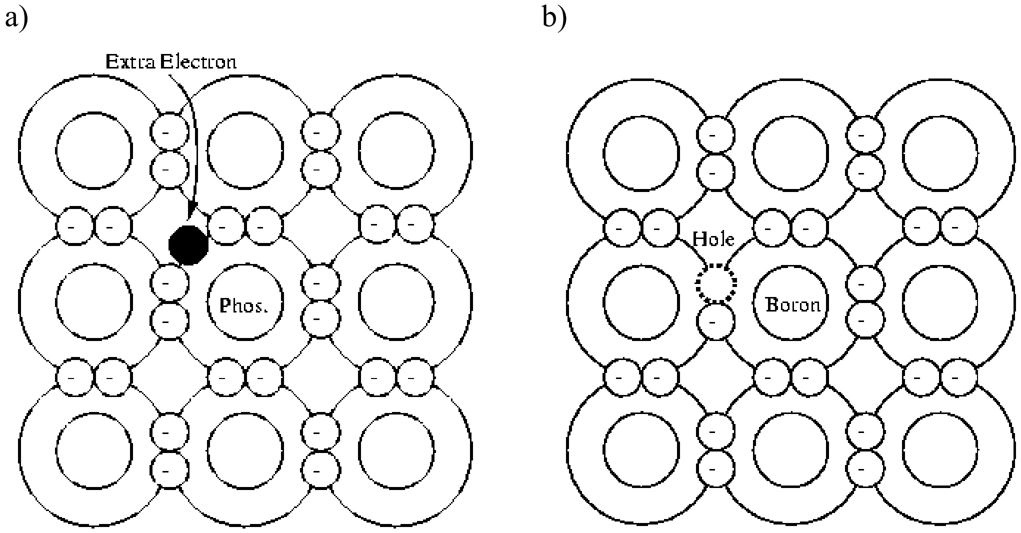

Figure 1.1: a) Silicon Doped with Phosphorus and b) Silicon Doped with Boron

After 1947, with the invention of the semiconductor transistor, miniaturization became the hallmark of the semiconductor industry and the basis for Moore's Law. Moore predicted in 1965 that for each new generation of memory chip and microprocessor unit on the market, the device size would reduce by 33%, the chip size would increase by 50%, and the number of components of a chip would quadruple every three years. So far this trend has shown no sign of stopping. The critical device size is predicted to decrease from 200 nm in 1988 to 50 nm in 2012. If the typical Si-Si bond distance (0.235 nm) is considered, the roughly estimated number of silicon atoms in such structures with an edge length of 200 nm and 50 nm become 850 and 210 respectively. This miniaturization trend approaches the cluster size so that it becomes necessary to investigate the structural properties of the silicon clusters. It is known that the most stable solid state structure of silicon is the diamond structure in which every silicon atom is tetrahedrally bonded to four nearest neighbors. However, this bonding characteristic is not observed for the smallest silicon clusters. The transition from non-diamond structural pattern to the diamond structure is also not known at this moment. This might be clarified by the investigation of nanostructures with decreasing size or of the growth pattern of smaller silicon clusters. Unfortunately, these two options do not seem to be fulfilled easily, in spite of numerous efforts being exerted for silicon clusters, both experimentally and theoretically. Until recently, only the structures of the smallest silicon clusters with up to seven atoms could be determined by experiment and also confirmed by theory. Briefly, an isosceles triangle for Si_3, a planar rhombus for Si_4, and a trigonal and a pentagonal bipyramid for Si_5 and Si_7, respectively, are deduced from experiments and found theoretically as global minima. Amongst these small silicon clusters, Si_6 turns out to be an exceptionally difficult case. Experimental Raman spectra match best with the octahedral structure. However, in addition to the octahedron other candidate structures are predicted by high level theoretical studies and cannot be ruled out by experiment. As a result, there is no consensus about the global minimum structure of Si_6 to date. The picture starts to blur only slightly for Si_n clusters with n=8-10. And for $n > 11$, at higher levels of theory, the number of systematic theoretical studies begins to decrease by forcing the use of some lower-level approaches such as tight binding (TB) or DFT-LDA (local density approximation), often in combination with ad-hoc assumptions about likely structures. Not surprisingly, there are many discrepancies between the results. In order to change this picture one needs higher-level calculations, however, they start to become too expensive for exhaustive searching of configuration space which grows exponentially with increasing cluster size. On the experimental side, there are no direct structural measurements for silicon clusters, so that a combination of theoretical calculations and indirect experimental measurements must be used to definitively determine the structures of silicon clusters. For small silicon clusters, photoelectron, IR and Raman spectra are suited best. For larger clusters the small abundance of clusters makes it difficult to obtain reliable IR and Raman spectra. Today only photoelectron spectra, chemical reactivities, ionization potentials, and mobilities in a buffer gas have been measured for larger clusters. Amongst these experiments, the most valuable information about structural preferences of silicon cluster cations with n<56 and anions with n<82 has been obtained by ion mobility measurements (IMM) carried out by Jarrold and coworkers [1,2,3,4,5]. The most striking observation obtained from IMM is the break in measured mobilities starting approximately with Si_{24} and Si_{26} for cation and anions, respectively as shown in Fig. 1.2. Jarrold et al. [6] also modeled the dissociation of Si_n neutrals and cations in the $n \leq 26$ range, finding Si_6 and Si_{10} as the most stable fragmentation products. After combining the results of IMM and dissociation calculations, Jarrold proposed that the break in mobilities might be due to a structural transition from prolate to more

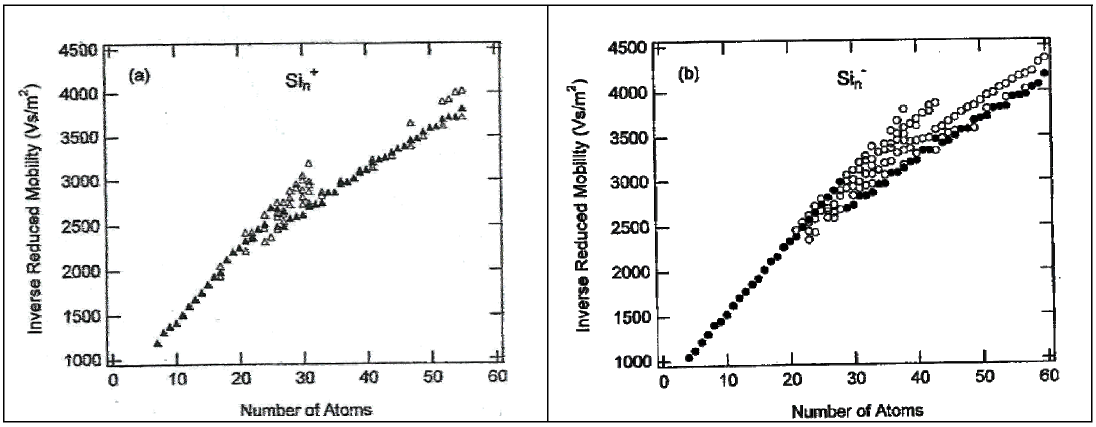

Figure 1.2: Plot of inverse reduced mobilities versus number of atoms for Si_n^+ and Si_n^-. The filled points correspond to the most abundant peak observed for each cluster size while additional isomers are shown as open points. (These figures are taken from reference [4])

spherical structures. In the ion mobility technique, structural information can be extracted by comparing the calculated mobilities of the candidate structures to the experimentally obtained ones. Actually, IMM can only give structural information about the outer shape of the cluster, not about its inner structure. Based on a restricted global search at the DFT level, Jarrold and coworkers [7] could also find several new optimal silicon cluster structures in the size range n=10-20 that fitted their mobility data. In these clusters, the tetra-capped trigonal prism (TTP) structure, the generally accepted global minimum structure for Si_{10}, featured as a subunit several times, leading to a proposal of a continuation of this TTP-based structural trend also for larger clusters. However, their lowest-energy structures for n=19 and 20 were spherical, and calculated mobilities of these structures did not match with the measured ones.

Additionally, binding energy measurements of Schäfer et al. [8] and ionization potential measurements of Fuke et al. [9] yielded the same structural transition in medium-sized silicon clusters. However, at the latter experiments, the transition to spherical structures was predicted to be between n=20 and 22. In the study of Schäfer et al. [8] the binding energies per atom of neutral Si_n cluster with $65 \leq n \leq 890$ were determined calorimetrically. They combined the results of collision induced dissociation (CID) experiments [10] performed for Si_n cluster with $5 \leq n \leq 70$ and Knudsen mass spectrometric measurements [11,12,13] performed for Si_n cluster with $2 \leq n \leq 7$, with the results of their calorimetric measurements and obtained a consistent picture of a large size region. This picture, as binding energies of Si_n cluster versus $n^{-1/3}$ (inverse of cluster radius) is shown as Fig. 1.3.

In the Fig. 1.3, three different regions can be identified clearly. Starting with the silicon dimer, the binding energies rapidly increase as linearly depending on the inverse of cluster radius until a cluster size of $n \approx$ 7-10 is reached. For clusters containing from $n \approx 10$ to $n \approx 25$ atoms the binding energies are nearly constant, whereas in the third range of larger silicon clusters they become proportional to $n^{-1/3}$

again. The observed size dependence of the binding energies can be explained as a consequence of different growth patterns [8]. A linear dependence (with non-zero slope) of the binding energy on the inverse cluster radius can be interpreted as compatible with 3-dimensional growth. A constant binding energy, however, is compatible with growth only in one direction, as for example in a growing rod or tube. As a result, the data compiled by Schäfer et al. [8] also supports the shape transition from prolate to spherical structures starting approximately at *n*=25.

As will become clear during the remainder of this thesis, it is still an open question if this shape transition is due to first traces of diamond-like patterns appearing in the inner cluster structure. According to what has been observed in other systems, silicon clusters may well turn out to be more complicated than this. In that case, further structure and/or shape transitions can be expected at larger cluster sizes. But even then, this transition is the first one in need of being explained, since there is little doubt left for the region *n*=2-10. Also, reliable levels of ab-initio theory are now starting to become applicable to systems of such sizes. Therefore, the aim of this thesis is the theoretical study of the silicon shape transition at approximately *n*=25, as one of many stepping stones towards a solid theoretical foundation for silicon nanotechnology.

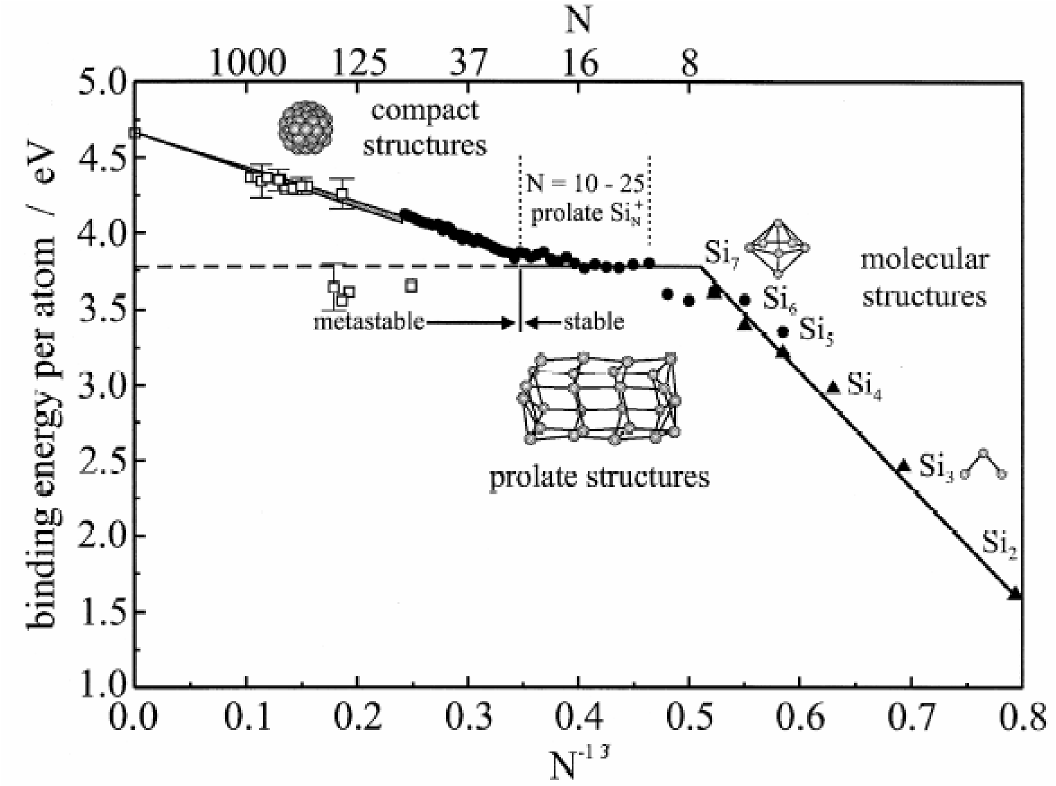

Figure 1.3: Size dependence of the binding energies of neutral silicon clusters. The open squares indicate binding energies of the two groups of cluster isomers found by calorimetric measurements. The black circles are data for neutral silicon clusters obtained from the CID experiments [10]. The black triangles belong to the Knudsen mass spectrometric measurements [11,12 ,13]. (These figures are taken from reference [8])

The methods of quantum chemistry, developed during the last decades, make it possible to accurately calculate the geometries and energies of small systems. While these methods in principle are applicable to systems of any size, for large systems, one has two major problems: i) expense of higher-level ab-initio calculations even on high performance parallel computers ii) exponentially increasing configuration space with increasing cluster size. This forces to use fast approximate methods like "*Genetic Algorithms*" (GA) or "*Simulated Annealing*" (SA) to determine the lowest-energy structures for a given cluster size. These two methods belong to the stochastic search algorithm class in which only selective search of configuration space is conducted. As an alternative to stochastic methods, the use of a deterministic method requiring the search of the whole configuration space turns out to be impractical for larger clusters.

In this thesis, Si_n clusters in the size range n=4-35 have been investigated, ultimately aiming at providing some more comprehensive explanations for the structural transition mainly observed in IMM. To do this, two strategies involving evolutionary algorithm, namely GAGA and PHENIX have been used. GAGA is a simple but effective scheme to allow for global geometry optimizations at expensive ab-initio levels. It combines global geometry optimizations on a model potential with global parameter optimizations of this model potential, using ab-initio single-point data. GAGA requires an empirical potential as guiding function. PHENIX, which is based on a Deaven-Ho-style genetic algorithm (GA) [14], is responsible for the actual global geometry optimizations of the silicon clusters. Some of the resulting structures obtained from global geometry optimization on the model potential were relaxed further at the DFT level with a hybrid B3LYP functional. For the resulting structures, single point energies have been calculated at the LMP2 level with a reasonable medium-sized basis set, cc-pVTZ. These DFT and LMP2 calculations were also carried out for the best structures proposed in the literature including the most recent ones to obtain an overall picture about the structural preferences of silicon clusters.

1.2 Outline

An understanding of the structure and physical properties of small clusters can help to explain phenomena such as crystal growth, catalysts, and surface reconstruction. For this reason, small silicon clusters have been extensively investigated by experimental techniques. The most important experimental studies carried out for silicon clusters, and additionally, the comparison of the theoretically obtained experimental data with the measurement is outlined in Chapter 2.

There have been a number of theoretical studies aiming to find the global minimum structures of silicon clusters. In Chapter 3, theoretical studies before this thesis and studies performed during this thesis are highlighted.

Since global optimization is not yet a standard tool in chemistry, in the fourth chapter, philosophies of stochastic and deterministic global optimization methods and the main differences between global and local optimization are explained. As will be explained, for good performance it is essential to combine ("hybridize") global and local search. Also, local optimizations have been performed as a refinement of the globally optimized parameter sets of the model potentials obtained via a genetic algorithm. Therefore, local optimization routines in this study are also detailed in Chapter 4.

Amongst the stochastic methods, GA currently seems to be the most promising one and it has already demonstrated its efficiency for silicon clusters. In this study, special versions of GAs are used in two major implementations, GAGA and PHENIX. These programs have been used for both global parameter optimization of the model potentials and global geometry optimization of silicon clusters at the model potential. In Chapter 5, basics of a GA are discussed and then fundamentals of the GAGA and PHENIX algorithms are introduced. Additionally, results obtained from other methods for silicon clusters are compared with those found with GA.

GAGA needs a model potential as guiding function, and PHENIX performs a global geometry optimization on the model potential. Several model potentials were reported in the literature for silicon. Mainly, there are two types of model potentials, Tersoff based potentials and Stillinger-Weber (SW) based potentials. The potentials most successful in reproducing the structures of small silicon clusters, including the important Si_{10}, were found to be the potentials based on the Stillinger-Weber formalism in which the total energy of the system is expanded into many-body terms. The most important potentials belonging to this class are the SW, SW-Gong (SWG), Mistriotis, and modified Mistriotis potentials. The latter potential, modified Mistriotis, was introduced in this study and successfully applied to silicon clusters. All these model potentials are described in detail on Chapter 6. Additionally, the tight-binding (TB) method is one of the most frequently used approximation for silicon clusters. It is more expensive than the empirical potentials but much less expensive than the ab-initio methods. For completeness, the basics of the TB scheme are also briefly summarized in Chapter 6.

In Chapter 7, details of theoretical computations (DFT, LMP2, and RI-DFT) performed in this thesis and general information about computer resources is given.

The remaining, major part of the thesis deals with the results produced in this study: For the global optimization of model potential parameters, Si_{10} is taken as a benchmark system, due to being a candidate building block for the medium-sized prolate clusters. The first task is to find globally optimized parameter sets of the model potentials such as the SWG, Mistriotis, and modified Mistriotis potentials. The quality of the resulting parameter set is ranked according to the reproduction of the accepted global minimum structure of Si_{10} as a tetra-capped trigonal prism (TTP) using the PHENIX algorithm for global geometry optimization. In this way, 4 different parameter sets have been obtained; only one of them gives TTP as global minimum. Then, these parameter sets have been used in PHENIX for global geometry optimization of silicon clusters in the size range $4 \leq n \leq 40$. The resulting globally optimized parameter sets and geometries are described in Chapter 8.

A good model potential does not necessarily have to reproduce the correct energy ordering of the cluster structures, but it should reliably lead to low-energy minima on the DFT or ab-initio level. Therefore, structures obtained from global geometry optimizations using Mistriotis and modified Mistriotis potentials were locally reoptimized at the DFT/B3LYP level with the standard 6-31G* basis set up to $n=15$, and a (3s3p1d) basis set with effective core potential approximation for $n \geq 16$. These DFT relaxations were followed by single point energy calculations at the LMP2 level with the standard cc-pVTZ basis set. These DFT and LMP2 calculations were also carried out for the best structures proposed in the literature including the most recent ones to obtain an overall picture about the structural preferences of silicon clusters. The structure and energy results for the Si_n clusters with $10 \leq n \leq 20$ are described in Chapter 9.

These DFT and LMP2 calculations were also carried out for the structural transition region $20 \leq n \leq 29$. A significant discrepancy between DFT and LMP2 calculations has been observed. DFT results support the structural transition from prolate to spherical structures, whereas LMP2 favors the prolate structures beyond the transition region. All the significant structures found and the important literature structures proposed for the structural transition region are examined in Chapter 10. Additionally, for the size range $30 \leq n \leq 35$, for the first time systematic results at a higher level, DFT/B3LYP, are shown in Chapter 10.

This thesis ends with summarizing the conclusions and making some suggestions for future work.

2 Experimental studies for silicon clusters

An understanding of the structure and physical properties of small clusters can help to explain phenomena such as crystal growth, catalysis, and surface reconstruction. For this reason, small silicon clusters have been extensively investigated by experimental techniques. However, since direct experimental observations of cluster structures are not possible, a combination of theoretical calculations and indirect experimental measurements must be used to definitively establish the cluster structures. Experimental studies with the help of theoretical predictions have only managed to elucidate the structures of small Si_n clusters with $n \leq 7$. However, other size regimes of clusters are also important: For example, in order to illuminate the structural transition from prolate to spherical for silicon clusters, one really needs to have structural information for the size interval $20 \leq n \leq 28$. The lack of direct experimental measurements for the determination of silicon cluster structures makes global geometry optimization methods virtually unavoidable. On the other hand, good theoretical predictions should encompass as many experimental findings as possible. To this end, all important experimental studies carried out for silicon clusters are discussed in Chapter 2. More specifically, infrared (IR), Raman, and photoelectron spectroscopy, dissociation and fragmentation studies, Knudsen mass spectrometry, polarizability measurements, ionization potential measurements, calorimetric measurements, chemical reactivity experiments, and ion mobility measurements (IMM) are detailed.

2.1 IR, Raman, and photoelectron studies

Early experimental studies employing anion photoelectron [15], Raman [16], and IR [17] spectroscopy techniques have confirmed the structures of the Si_n clusters with $n<8$.

Among these techniques, photoelectron spectroscopy is a very powerful tool for the structural characterization of free atomic clusters [18]. It reflects the electronic structure of neutrals at the anion geometry. Experimentally, the anion is photo-excited above the detachment threshold and the energy of released electrons is measured. Photoelectron spectra have been obtained for Si_n^- up to $n=12$ [15,19,20], but vibrational resolution could be achieved only for $n \leq 7$. Comparison of the measured frequencies with those computed for trial geometries has identified Si_3^- as a triangle, Si_4^- as a rhombus, and Si_5^- and Si_7^- as trigonal and pentagonal bipyramids, respectively. Matrix isolated neutrals have the same morphologies [16].

Chelikowsky et al. [21,22,23] have also used photoelectron spectroscopy. They have matched the observed electronic band profiles with those simulated for candidate isomers to assign cluster structures that have absent vibrational resolution. Using this approach, the geometries of Si_6^- and Si_{10}^- have been determined as bicapped tetrahedron and tetra-capped trigonal prism, respectively.

Recently, a theoretical attempt has been made in order to calculate the photoelectron spectra of Si_n cluster anions with $n \leq 20$ by Müller et al. [18]. In this study, vertical detachment energies (the energy needed to remove an electron from the HOMO without relaxing the rest of the system) have been calculated for the candidate structures taken from [24,25] and compared with the measured photoelectron spectra. The measured photoelectron spectra for $n \leq 7$ and $n=10$ were in agreement with the study of Chelikowsky et al. [21,22,23]. In general, for all $n \leq 19$, except $n=12$, the calculated photoelectron spectra were in agreement with the measured ones.

IR and Raman spectra of Si_n clusters have been determined theoretically by Jackson et al. [26]. They calculated the IR and Raman spectra of Si_n clusters, with $3 \leq n \leq 8$, and Si_{10} and Si_{13} (these cluster structures were taken from reference [27]) using the LDA approximation. They found good agreement with experimental data [17] for Si_n clusters, with $3 \leq n \leq 8$.

2.2 Dissociation and fragmentation studies

Dissociation and fragmentation studies have also been carried out with Si_n clusters to understand which cluster sizes are more stable upon dissociation. Bloomfield et al. [28] and Schaber et al. [29] have performed dissociation experiments. In these experiments, Si_6^+ and Si_{10}^+ were found to be the prominent clusters. In addition, these cluster sizes and Si_4^+ were found to have small photo-fragmentation cross-section, indicating that Si_4, Si_6, and Si_{10} are the magic numbers of silicon cluster ions. Smalley et.al. [30,31] have studied the dissociation of silicon clusters up to Si_{60}. They have found that clusters between Si_{12}-Si_{30} dissociate mainly by loss of Si_6, Si_7, or Si_{10}.

Additionally, Jarrold and Bower [32] have performed collision induced dissociation experiments. They have observed that silicon clusters with 12-18 atoms dissociate mainly by loss of 6 or 7 atom species and silicon clusters with 19-26 atoms fragment by ejecting Si_{10} units. The results obtained are very similar to that obtained in Smalley's [30,31] study.

2.3 Knudsen mass spectrometry studies

Si_n clusters, with $1 \leq n \leq 7$, have also been investigated using Knudsen cell mass spectrometric technique [11,12,13] which is one of the most useful experimental technique for studying the equilibrium between condensed and vapor phases. The Knudsen method [33] involves placing a condensed sample in a Knudsen cell that is uniformly heated until equilibrium is attained between the condensed and vapor phases. The vapor is continuously sampled by effusion through a small orifice in the cell. A molecular beam is formed from the effusing vapor and directed into a mass spectrometer for identification and pressure measurement of the species in the vapor phase. All classes of materials can be studied and all constituents of the vapor phase can be measured over a wide range of pressures ($\sim 10^{-4}$ to 10^{-11} bar) and temperatures (500-2800 K). In these experiments, atomization and formation enthalpies and binding energies of small silicon clusters have been measured.

2.4 Polarizability studies

Another item of interest in the experiments is to measure the polarizabilities of Si_n clusters. The polarizabilities of semiconductor clusters are related to the size of the HOMO-LUMO gap. Larger polarizabilities correlate with smaller gaps. An early attempt has been performed for Si_n clusters with $9 \leq n \leq 120$ by Schäfer et al. [34]. A striking result described in this study was a strong variation of the polarizability per atom as a function of cluster size. Generally, the polarizabilities were varying irregularly around the bulk limit (3.71 Å/atom). Only for a few sizes polarizabilities found were greater than the bulk limit such as Si_{10}, Si_{17}, Si_{23}, and Si_{29}, and $Si_{50,}$ as can be seen in Fig. 2.1. Surprisingly, the biggest polarizability value was found for Si_{10}. In these experiments, clusters are produced by a pulsed laser vaporization cluster source. The clusters leave the source through a nozzle with adjustable nozzle temperature and form a molecular beam. The beam is collimated and then deflected by an inhomogeneous electric field. The deflections are measured for each cluster size by means of a collimated ionization laser beam which scans the cluster beam. Thereby, size selective cluster beam profiles are obtained by detecting the ionized clusters with a time-of-flight mass spectrometer for each scanning position. The velocities of the clusters in the beam are measured size-selectively by means of a chopper. The beam profiles of clusters are slightly shifted by the applied field, as a consequence of an induced dipole moment. Here, a broadening of the profile and a decrease of the intensity on the beam axis can be observed. This effect is typical for particles with a permanent dipole moment and is usually used to calculate an effective dipole moment. From this value, one can furthermore estimate the clusters permanent dipole moment. In these experiments, the polarizabilities of silicon clusters have been calculated from the observed shift of the beam profiles by a given formula.

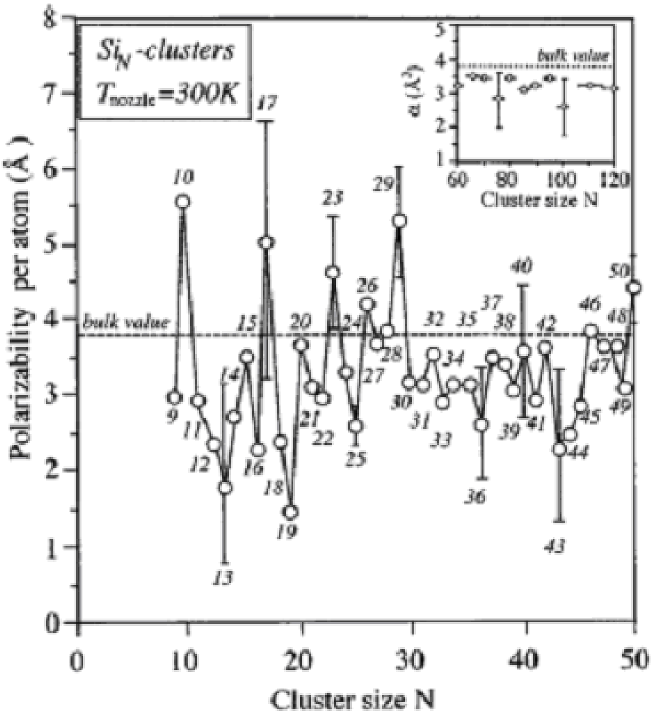

Figure 2.1: Polarizabilities of Si_n clusters with 9≤n≤120. this graph is taken from Schäfer et al. [34].

Polarizabilities of Si_n clusters, with 3≤n≤10, have also been calculated at the ab-initio level by Vasiliev et al. [35] for candidate structures that were determined by ab-initio MD simulations using the higher-order finite-difference-pseudopotential method to calculate the interatomic forces within the level of local density approximation (LDA). The computed polarizabilities per atom, all of them above the bulk limit, tend to decrease with increasing cluster size. This trend resembles the case of metallic clusters. Their candidate structures are isosceles triangle, flat rhombus, trigonal bipyramid, octahedron, pentagonal bipyramid, bicapped octahedron, capped bernal structure, and TTP, respectively, for 3≤n≤10. However, calculated polarizabilities were different for Si_9 and Si_{10} from the experimental study of Schäfer et al. [34]. Hence, experimental polarizabilities could not be reproduced in this study.

In addition to IR and Raman calculations, Jackson et al. [26] have also computed static polarizabilities for Si_n clusters, with n=1, 10, 13, 20, and 21, using again the LDA approximation. They have compared the computed polarizabilities with the experimental results of Schäfer et al. [34]. A weak agreement with the experimental values was observed in this comparison. More specifically, except for Si_1, for other silicon clusters calculated polarizabilities did not agree with the experiments. This discrepancy may be due to the use of candidate structures that were not the ones observed in the experiments. Actually, this may be true for larger clusters such as Si_{20} and Si_{21}. However, for Si_{10} a TTP structure (this structure has also been used by Vasiliev et al. [35]) has been used in this study, and this structure is known as the global minimum for Si_{10}. This strongly suggests using a higher level of theory to predict the polarizabilities.

Moreover, in a recent study, polarizabilities of small Si_n clusters up to $n \leq 13$ have also been calculated by Bazterra et al. [36] at the DFT level using the B3PW91 hybrid functional to find an explanation for the irregular polarizabilities found experimentally by Schäfer et al. [34]. Unfortunately, the tendency in the Schäfer et al. [34] study has not been observed in this study. Their calculated polarizabilities were slightly larger than the bulk silicon limit. Actually, Bazterra et al. [36] have obtained similar results to Jackson et al. [26]. However, this time, the level of theory has been updated form LDA to a hybrid functional. Nevertheless, the experimental findings could not be reproduced with both of these studies. To explain this discrepancy to the experiment, Bazterra and co-workers have suggested that the experimental values are likely to be incorrect.

As a summary, neither of the calculated polarizabilities from the studies of Vasiliev, Jackson, and Bazterra did reproduce the experimental data found by Schäfer. The interesting point in these studies is that the candidate structures for the computation of the polarizabilities are the known global minimum structures in the literature. For this reason, it is really surprising that the experimentally found polarizabilities could not be reproduced.

2.5 Ionization potential studies

Another experiment performed for Si_n clusters is ionization potential measurement. Ionization potentials (IPs) provide an important link to understand chemical reactivities and dissociation processes. In addition, the structural candidates found for the neutral species could possibly be distinguished using the IPs. This can be done by comparing the measured IPs with those obtained from the calculation. Experimentally, IPs of silicon clusters have been measured by the threshold photoionization method [37,38,39,40].

For example, Fuke et al. [39] have measured the IPs of Si_n clusters, with n=4-200. As can be seen in Fig. 2.2, the IPs showed major maxima at n=10 and 20 and a large gap between n=20 and 22. This gap seems to suggest the occurrence of a structural transition for neutral silicon clusters in this size range.

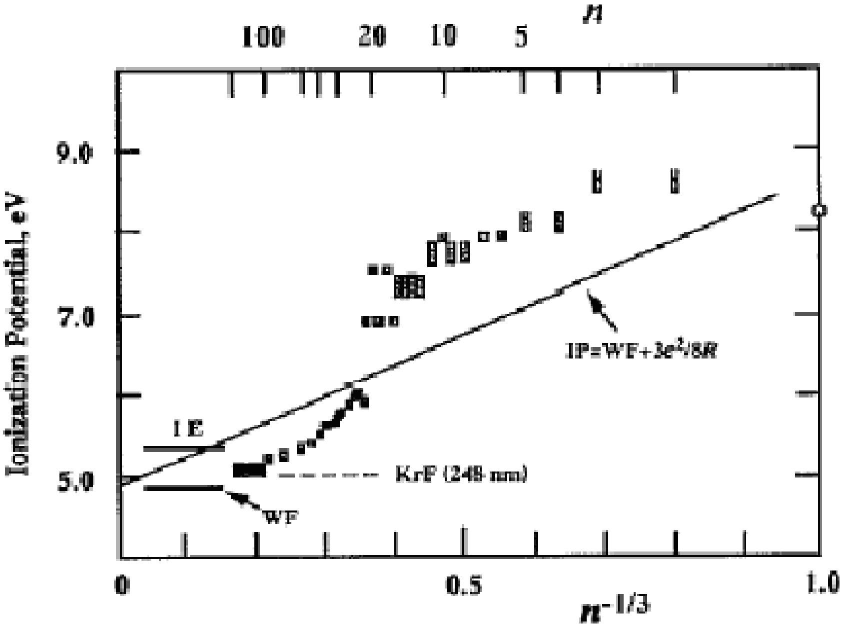

Figure 2.2: Ionization potentials of Si_n, n=2-200, plotted versus $n^{-1/3}$ (inverse of cluster radius). The solid line is the prediction of the conducting spherical droplet model. This model predicts a linear IP versus $n^{-1/3}$ relationship and often reproduces well the experimentally measured IPs for metal clusters such as Na_n, K_n, and Al_n.

Ideally, if the internal temperature of the neutral is close to absolute zero and the threshold is identified, the measurement would provide the adiabatic ionization potential (AIP). If the geometry changes significantly upon ionization, the true threshold would probably not be located, and the measured value would lie between the AIP and the vertical ionization potential (VIP) [41].

In the study of Jarrold et al. [41], AIPs and VIPs have been calculated for a number of candidate structures in the size range $n \leq 20$. Among these candidates, structures for $12 \leq n \leq 20$ were taken from the study of Ho et al. [7]. In this study [41], experimental features have been reproduced by these calculations at least qualitatively except for n=8, 11, 17, and 20.

2.6 Chemical reactivity studies

There were also chemical reactivity studies for Si_n clusters. Amongst them, Smalley and co workers have probed chemical reaction with ammonia [42], ethylene [42,43], and trimethylamine [44] with the Fourier transform ion cyclotron resonance (FT-ICR) mass spectrometer. On the other hand, Jarrold and co-workers have extensively studied chemical reaction with ethylene [45,46], O_2 [6,47], water [48], and ammonia [49,50] using the ion drift tube apparatus. There has been a serious controversy between results of these two groups. From FT-ICR reaction experiments with ammonia and ethylene performed by Smalley and co workers, Si_{21}, Si_{25}, Si_{33}, Si_{39}, and Si_{45} were demonstrated to be unreactive. (Clusters containing more than 47 atoms were highly reactive and they did not display strong oscillations in reactivities as a function of cluster size. Similar results were obtained with methanol, ethylene, and water. On the other hand, nitric oxide (NO) and oxygen were found to react readily with all clusters in this size range). However, ion drift tube experiments showed no specialty in these cluster sizes. Jarrold et al. [2] has also observed that for Si_{29}^+, the fast moving component (spherical isomer) has all reacted with ethylene leaving behind the less reactive slower moving component (prolate isomer). As a result, the prolate isomer can be said to be unreactive to ethylene. Similar results were found for Si_{24}^+ and Si_{28}^+. For Si_{26}^+, they have separated 3 isomers such as a reactive spherical, an unreactive spherical, and an unreactive prolate isomer. For Si_{25}^+, they have identified at least four isomers. They found that Si_{13}^+ is unreactive towards C_2H_4, O_2, and H_2O. With ethylene, the spherical isomers are generally more reactive than the prolate isomers for clusters with n=24-30. When a broader range of cluster sizes (n>30) is examined it appears that there is not a systematic change in reactivity associated with the prolate-spherical structural change.

Recently, Maruyama et al. [51] studied the chemical reaction of small Si_n^+ with $11 \leq n \leq 20$ with ethylene with a FT-ICR mass spectrometer. The reaction rate of chemisorption of first ethylene molecule was generally in good agreement with the ion drift tube experiments. $Si_n(C_2H_4)_m^+$ with $n+m=19$ were observed to be remarkably stable.

2.7 Calorimetric measurement studies

Another valuable experiment has been performed by Schäfer et al. [8]. He has calorimetrically determined the binding energies per atom of neutral Si_n cluster with $65 \leq n \leq 890$. The measurements of the binding energies were performed within a molecular beam experiment, in which the released heat during the deposition of Si_n clusters on a Si surface was measured with a pyroelectric thin film calorimeter. Schäfer et al. [8] combined the results of collision induced dissociation (CID) experiments [10] performed for Si_n cluster with $5 \leq n \leq 70$ and Knudsen mass spectrometric measurements [11,12,13] performed for Si_n cluster with $2 \leq n \leq 7$, with the results of his calorimetric measurements. Then, the binding energies of Si_n cluster versus $n^{-1/3}$ (inverse of cluster radius) were plotted as already shown in Fig. 1.3.

In the Fig. 1.3, as explained before, three different regions can be identified clearly. Starting with the silicon dimer, the binding energies rapidly increase as linearly depending on the inverse of cluster radius until a cluster size of $n \approx 7$-10 is reached. For clusters containing from $n \approx 10$ to $n \approx 25$ atoms the binding energies are nearly constant, whereas in the third range of larger silicon clusters they become proportional to $n^{-1/3}$ again. The observed size dependence of the binding energies can be explained as a consequence of different growth patterns [8]. A linear dependence (with non-zero slope) of the binding energy on the inverse cluster radius can be interpreted as compatible with 3-dimensional growth. A constant binding energy, however, is compatible with growth only in one direction, as for example in a growing rod or tube. As a result, the data compiled by Schäfer et al. [8] also supports the shape transition from prolate to spherical structures starting approximately at n=25.

2.8 Ion mobility studies

Another experiment that gives indirect information about the cluster structure is ion mobility measurements (IMM). The mobility of an ion is a measure of how rapidly it moves through a buffer gas under the influence of an electric field. In the low field limit, the mobility of a cation or anion depends on its orientationally-averaged collision integral with the buffer gas, which in turn depends on the ion's geometry [1]. Ions with open geometries undergo more collisions with the buffer gas and hence travel more slowly than compact ions. Thus, ion mobility provides a way to characterize an ion's physical structure. However, the structural information can only be about the outer shape of the ion, not about its inner structure. This is simply because inner atoms are not responsible for the collisions with the buffer gas atoms.

Mobility measurements are usually performed in a drift tube. The drift tube contains the buffer gas and provides a uniform electric field for the ions. There are two basic experimental configurations; i) the injected ion drift tube (which usually has a buffer gas pressure < 10 Torr) and ii) the high resolution configuration (with a buffer gas pressure of hundreds of Torr).

In the injected ion drift tube approach, cluster ions are generated by pulsed laser vaporization and then mass selected by a quadrupole mass spectrometer. This is followed by the injections of ions into a drift tube through a small aperture. After traveling across the drift tube, some of the ions exit through another aperture. They are then mass analyzed and detected. Mobilities are measured by injecting a short packet of ions and recording how long it takes for them to reach the detector.

The high resolution configuration [52], simply illustrated in Fig. 2.3, consists of four

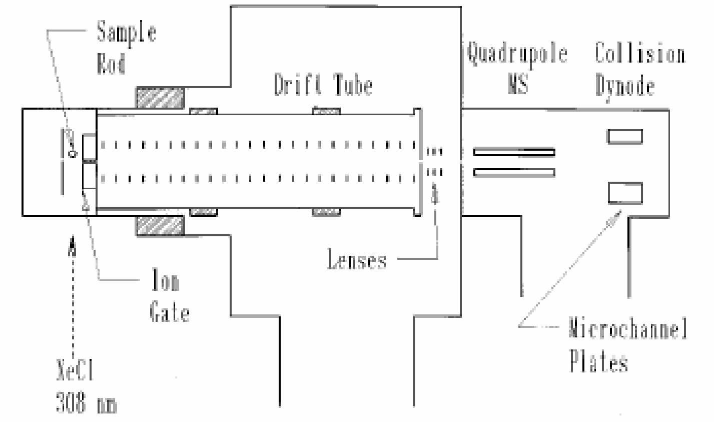

Figure 2.3: Schematic diagram of the high resolution ion mobility apparatus.

main regions: i) the source, where the clusters are produced; ii) the ion gate, which connects the source to the drift tube and prevents neutral species from entering the drift tube; iii) the drift tube; and iv) the mass spectrometer and the ion detector.

The source is a novel laser vaporization/desorption source with a near static buffer gas. The buffer gas pressure in the source is around 500 Torr. Clusters are produced by laser vaporization of a target rod of the material to be studied. Then, cluster ions are guided from the target rod toward the entrance of the ion gate by an electric field. By adjusting the voltage on the rod, one can adjust the residence time of the clusters in the source and vary the cluster size distribution. Only ionic species are extracted form the source.

The function of the ion gate is to allow ions to pass from the source into the drift tube while preventing neutral species from entering the drift tube. This is accomplished by a uniform electric field to carry the ions through the ion gate and a counterflow of buffer gas to prevent neutral species from passing through. The ion gate is a 2.4 cm long cylindrical channel with an inside diameter of 0.5cm.

The drift tube has a length of 63 cm. A uniform electric field is generated along the axis of the drift tube. At the end of the drift tube the ions are carried by the buffer gas through a hole into the vacuum chamber.

After exiting the drift tube, the ions are accelerated and focused by a set of electrostatic lenses. The ions are directed through an aperture into a differentially pumped chamber that houses a quadrupole mass spectrometer and an ion detector. At the end of the quadrupole, ions are detected by an off-axis collision dynode and dual microchannel plates. Signals from the microchannel plates are processed with a fast preamplifier and a fast amplifier/discriminator. The signals are then recorded with a computer. Drift tube distributions are recorded by measuring the arrival time distribution at the detector using a multichannel scaler board, with a start pulse provided by the vaporization laser.

Structural assignments for unknown species observed in mobility measurements become possible by comparison of the measured mobilities with mobilities computed for reasonable candidate geometries [1].

Mobilities (or collision integrals) of candidate geometries can be computed in three ways:

1. The projection approximation (PA). In this method, the ion is modeled by a collection of overlapping hard spheres with radii equal to hard sphere collision distances. The orientationally-averaged geometric cross section is determined by averaging the geometric cross section over all possible collision geometries. The PA method neglects all longe-range attractive interactions between the ion and buffer gas atoms. It also ignores the details of the scattering process. For a body made entirely of convex surfaces the effects of scattering are not important and the

collision integral evaluated from the scattering angles is equal to that obtained from the PA method. However, when atoms are scattered on bodies with concave surface some of the trajectories experience multiple collisions. The collision integral calculated from the scattering angles then exceeds that obtained form the PA method.

2. The exact hard sphere scattering (EHSS) method. The ion is modeled by a collection of overlapping hard spheres with radii equal to hard sphere collision distances (as above). The orientationally-averaged momentum transfer cross section is calculated by determining the scattering angles between the incoming buffer gas atom trajectory and the departing buffer gas atom trajectory. While this model is a significant improvement over the PA method, it still ignores all long-range interactions between the ion and buffer gas atoms.

3. The trajectory method (TM). The long-range interactions are incorporated by propagating classical trajectories between buffer gas atoms and the target ion in a realistic intermolecular potential. The potential between the ion and buffer gas atom is assumed to consist of two parts: van der Waals and charge-induced dipole interactions. The first term is modeled as a sum of pair-wise Lennard-Jones (LJ) (6-12) interactions between the buffer gas atoms and each atom in the ion. The charge-induced dipole term was initially evaluated assuming that the charge was uniformly delocalized over all atoms. A charge distribution obtained from first-principle calculations is now usually employed. The effective potential is obtained by summing over the individual atomic contributions and then trajectories are run in this potential to obtain the scattering angle (the angle between the incoming and departing buffer gas atom trajectory). The orientationally-averaged collision integral is determined by averaging over all possible collision geometries.

In the three methods described above, the clusters are represented through the position of atomic nuclei. In reality, the buffer gas atoms interact with ions via their electronic wave functions, thus the mobility actually characterizes not the nuclear geometry of an ion, but the electron density distribution. The TM method should give the most reliable estimate. The PA method generally gives numbers that are smaller than TM while EHSS generally gives values that are greater than those obtained by TM. The deviations increase with increasing size of the ion. This is because the PA ignores multiple scattering (where the ion and buffer gas have more than one encounter) and EHSS tends to overestimate the effects of multiple scattering.

IMM has also been applied to C [53], Pb [54], Ge [1], Sn [1] as well as silicon [1,2,3,4,5] clusters. In the IMM of Si_n anions and cations as shown in Fig 1.2, there is a break in mobilities starting approximately with Si_{24} and Si_{26}, respectively. Additionally, Jarrold et al. [6] modeled the dissociation of Si_n neutrals and cations in the $n \leq 26$ range. In this study, the dissociation energy of a Si_n neutral along the channel leading to Si_m and Si_{n-m} is;

$$D_{(n,m)} = nE_n - mE_m - (n-m)E_{n-m} \tag{5.1}$$

where E_n is the cohesive energy per atom of the Si_n cluster. Jarrold et al. [6] predicted the dissociation energy for any fragmentation pathway of a Si_n neutral, using the values of E_n calculated for the candidate structures. The calculated dissociation energies of small Si_n neutrals with $n \leq 8$ were in agreement with experiment [11,12 ,13]. As the larger neutral clusters could not be size selected, their dissociation energies and pathways are not directly measurable. In addition, the calculated fragmentation patterns for Si_n cations with $n<27$ were also quite similar to experimental results of collision induced dissociation [32] and photoionization [28,31,37,38].

Jarrold has combined the results of IMM and dissociation studies by proposing that this break in mobilities might be due to the structural transition from prolate to more spherical structures.

2.9 Summary

As a summary, Si_n clusters have been the subject of a tremendous experimental effort. Only for small Si_n clusters, structural information has been obtained from these experiments. For medium sized Si_n clusters, structural assignments have remained insufficient.

The biggest drawback of these experiments is that they can only provide indirect information about the structures of Si_n clusters. To eliminate this drawback, one also needs theoretical calculations for the properties of Si_n clusters. Unfortunately, for the theoretical calculations, starting candidate structures for Si_n clusters have to be the global minimum ones in order to get agreement with experiment. This is an extremely hard task to achieve. Even if one has the global minimum structures for theoretical calculations, this does not mean that one can find comparable results to experiment. This is because of either the accepted global minimum structures are not the true global minima or the structures processed in experiments are not true global minima. Unfortunately, this happened for the calculation of polarizabilities of Si_n clusters. In that case, the global minimum structures accepted in the literature did not produce the experimental data.

Another striking result of these experiments, which is the main motivation of this current research, is the observation of the structural transition form prolate to spherical beginning approximately with Si_{25}. This shape transition has been proposed by ion mobility measurements, and supported by ionization potential and binding energy measurements.

3 Theoretical studies for silicon clusters

There have been a number of theoretical studies aiming to find the global minimum structures of silicon clusters. Clusters with up to 10 atoms have been extensively studied by Raghavachari et al. [55,56,57]. Their calculations are based on all-electron ab-initio molecular-orbital techniques. Mainly, Hartree-Fock (HF) theory and Møller-Plesset perturbation theory up to fourth-order were carried out in their calculations. They have been quite successful to locate the global minimum structures confirmed by experiment up to Si_{10}. More specifically, for the biggest cluster size considered in their calculations, Si_{10}, they have found the global minimum structure to be tetra-capped trigonal prism (TTP) at the level of QCISD(T) [57]. Small silicon clusters are also the benchmark systems for application of many empirical potentials such as Mistriotis [58] and Bolding & Anderson [59] potentials to test their ability to reproduce the known global minimum structures.

As the cluster size increases there are not only more electrons to be included in the electronic structure calculations, but there is also an increase in the number of possible geometric structures that need to be considered. For clusters with up to 6 atoms it is feasible to perform a detailed search of the potential energy surface to identify the lowest energy structures. For larger clusters this type of detailed search is simply too time consuming and impractical. Nevertheless, several theoretical attempts before this thesis have been performed. But, none of these studies could deal with the structural transition region in a systematic way. However, special larger clusters such as Si_{33} and Si_{45} have also been investigated with first-principle techniques [60,61,62]. But, the structures considered in these studies were not obtained via an optimization strategy; instead they were created by chemical intuition. There were also structures for silicon clusters in the literature obtained using an optimization strategy. However, in these studies, the biggest cluster sizes considered only reached approximately 23 atoms. In particular, Sieck et al. [63] studied silicon clusters with 9 to 14 atoms using a nonorthogonal tight-binding (TB) method based on density functional theory (DFT). Then, the study of Ho et al. [7] made an extensive contribution to the literature of medium-sized silicon clusters. They especially examined the cluster sizes between 12 and 20 with a GA, finding new structures. Two years later, another valuable contribution was made by Rata et al. [25]. In this contribution, silicon clusters in the size range of 13-23 were optimized using a single parent GA.

Several studies have been published during my work for this thesis. The most important studies are as follows: Sieck et al. [64] investigated selected cluster sizes such as Si_{25}, Si_{29}, and Si_{35} with simulated annealing molecular dynamics (SA-MD). For Si_{25}, both prolate and spherical structures were located. For clusters containing 29 or 35 atoms, their lowest-energy isomers exhibit a spherical shape. Another study was performed by Zeng et al. [65] using basin-hopping optimization to locate the lowest-energy structures of Si_{21} and Si_{25} clusters. In this study, structures obtained for these cluster sizes were spherical in shape. To find a spherical lowest-energy structure for Si_{21} seems to be in contradiction to the experimentally observed shape transition. After finding the lowest-energy structures, they calculated B3LYP and CCSD energies using the 6-31G* basis set. They also compared the energies of their structures to that of the literature (such as structures obtained from references [7,25]). In their calculations, their structures seem lower in energy than the literature ones. In addition to geometry optimization study, Zeng carried out ab-initio all-electron molecular-orbital calculations (using MP2 and CCSD(T)) to study the structure and relative stability of small silicon clusters, Si_n, with n=7-11 [66] and medium-sized silicon clusters, Si_n, with n=12-20 [67]. In these calculations, almost all of the important structures in the literature including the structures proposed in references [7,25] were considered. Most recently, another contribution was made by Jackson et al. [68] a few weeks before the generation of similar results in this thesis. They especially dealt with the experimentally observed shape transition region, Si_n, with n=20-27. In this study, they used a brute-force method (in which, spherical and prolate cluster structures are randomly generated, arbitrarily compressed to enhance exploration, and then locally optimized using a hierarchy of DFTB and DFT methods) and apparently invested lots of computer time. Using this method, they found very low-energy structures in the region of interest and also an apparent shape transition. They even claimed that their findings explain the shape transition. However, this seems not completely true for the following reasons: i) their DFT results seem to be in conflict with LMP2 results obtained in this thesis, ii) their DFT results for the Si_{28} case do not support their claim (probably, for this reason, Si_{28} was not included in their publication [68]), and iii) they could not provide an actual explanation for the shape transition, they merely generated some DFT results that happen to reproduce it.

All of the results of these studies mentioned above as well as other literature results are extensively compared to the results obtained in this work in the following chapters.

4 Optimization

Optimization is simply the process of finding an entity which is judged by a certain criterion to be "best". Mathematically, a "criterion" is simply a function which maps a set of entities into a set of "values" which has the property that it is possible to say when one value is greater than another.

The optimization task can be local (the highest or lowest function value in a finite neighborhood) or global (the highest or lowest function value of all). Even if some algorithms may fail to find the local minimum, local optimization problems are in principle solvable. It is rather obvious that global optimization is a much more difficult task than local optimization. Global optimization is conducted in the presence of a large number of local minima, aiming to find the best local minimum amongst them. This may suggest that global optimization problems are in principle solvable if enough time is given. For this reason, in order to obtain a solution to any global optimization problems within a reasonable time, the effort exerted to solve the problem must be scaled with problem size. To have a better understanding about local and global minima, I show a small portion of the

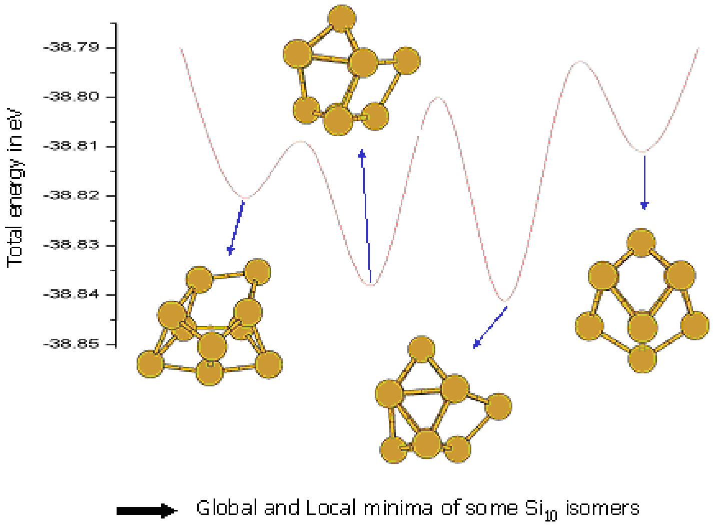

Figure 4.1: A small portion of PES of Si_{10} at the DFT/B3/LYP level, representing some local minima and the global minimum structure of Si_{10}.

potential energy surface (PES) of Si_{10} at the DFT/B3LYP level in Fig. 4.1. There are three local minima and a global minimum. The major challenge to find the global minimum among the local minima can be realized if one looks at the general structure of the PES. In contrast to local minimization going “down hill”, global minimization also has to be able to “go uphill”, in order not to get trapped in a local minimum. This immediately raises the problems of how to decide when to go up, how far to go up, and in which direction(s) – none of these problems are of any importance in local optimization. Even if the algorithm is not trapped in a local minimum, the next problem immediately arises, namely when global optimization should be stopped. Any global optimization algorithm should be equipped with tools that solve these problems. This increases the sophistication of any global optimization algorithm compared to local optimization ones.

4.1 Local and global optimization

Local optimization algorithms are able to handle large scale non linear optimization problems. In certain problem classes, local optimality implies global optimality. This is for example the case for convex problems. For these problems, nonlinear local optimization algorithms can provide good approximations to global optima. Most nonlinear optimization problems are defined by the minimization of an objective function on a feasible region defined algebraically by equality and/or inequality constraints.

Most local optimization methods for nonlinear optimization are iterative and each iteration is based on some form of direction along which some displacement is performed. The step direction calculation is a fundamental tool and influences most of the features of the method, including its computational cost. Newton-based methods, quasi-Newton or secant methods, gradient and reduced gradient methods, conjugate gradient methods, are some of the most popular and well-known schemes to compute step directions [69].

In the global optimization, an easy strategy would be to make several trials using different starting positions. The starting positions could be determined for instance by random in the region of interest. It is also easy imagining that several trials might result in finding the same minimum or the trials might progressively give better and better minima. However, at the end, one cannot in general be sure about whether the global minimum is located or not (except in the rare cases where deterministic global optimization methods are applicable to real-world problems, see below).

There are many differences between local and global search. These are mainly;

- Local search typically proceeds with parabolic steps, as illustrated in the left hand-side of Fig. 4.2. First, an initial starting point is chosen. At this point, the function is expanded in a Taylor series up to second order. Then, the point is moved to the minimum of the resulting parabola. There, the true function value is calculated. Repeating these steps, one can find the local minimum. In this search the direction is downhill. Therefore, one can never escape from this local minimum by climbing upwards. This parabolic movement strategy is applied to all considered problems, with the rationale that a Taylor series is a good local approximation to most functions occurring in practice.

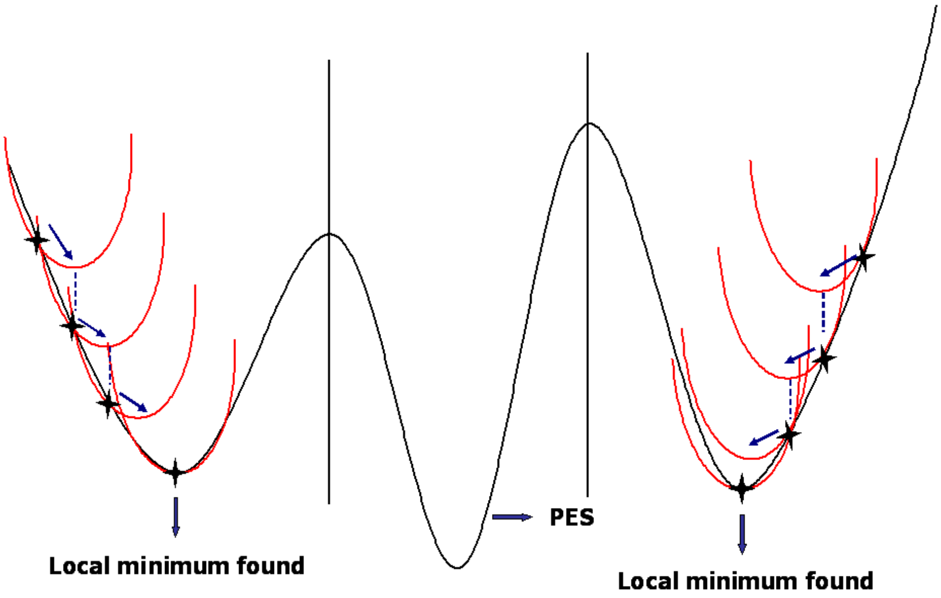

Figure 4.2: Progress of a local optimization algorithm. The right and left minima are local, but the minimum in the middle represents a global minimum for this PES.

○ Such a movement is not applicable for global search. Moreover, the search strategy can change from one problem to another. There is no standard way of doing a global search.

● During the search, information about first and second derivatives about the function to be optimized can be helpful for a local search.

○ The local character of the derivative information makes it useless for global optimization.

● Local optimization is confined to the basin of attraction (it is shown in Fig. 2.2 as vertical lines) in which the starting point happened to be. If one starts the local search from the right hand-side of Fig. 4.2, by proceeding with the same parabolic steps one will reach another local minimum. As a result, local search is completely dependent on the starting point.

○ In contrast, global search is independent of the starting point.

● In local optimization, there is a safe termination criterion which is easy to test. There is no possibility to go further downhill after reaching a local minimum.

○ There is no safe termination criterion in global optimization.

- Local optimization scales only polynomially with problem size.
- Exact/deterministic global optimization scales exponentially. Hence, global optimization can be placed in the non-deterministic polynomial [70] (NP)–hard problem class. Problems in this class are known as the toughest ones in the computational sciences. The exponential scaling renders useless even the fast development in computing power. Therefore, currently the only hope is clever approximative solution strategies.

In spite of the difficulties global optimization faces, it is an indispensable and necessary approach for real-life problems. In this current study, I try to find the optimal structures of silicon clusters of non-trivial sizes. Such a problem can be solved only by an application of a global optimization algorithm, since the number of local minima is already very far beyond practical tractability at these cluster sizes. This does not mean that local optimization algorithms have become obsolete. On the contrary, they are an important part of most global optimization tools. In particular, the following three types of such combinations are used for different purposes:

- A local technique is used to obtain a local minimum. Then a global technique is applied to escape from this local minimum and to find a new point which can be used as an initial guess for a new round of local search.
- Points obtained by a global technique are used as initial points for a local search.
- To solve auxiliary optimization problems such as relaxations of the original problem for generating improved bounds or bound constraint approximations. A relaxation is a modification of the original problem whose solution is tractable and gives some information about the possible location of the global minimum.

4.2 Local optimization methods

Many successful local search algorithms have been proposed. The objective function to be optimized contains generally a number of variables, this leads to an N-dimensional optimization problem. In one-dimensional optimization, it is possible to bracket a minimum, so that the success of a subsequent isolation is guaranteed (unless the objective function has one or more singularities in the bracket). However, there is no analogous procedure in N-dimensional optimization. For N-dimensional optimization, feeding the algorithm with starting guess points is necessary. Then, the algorithm searches through the very complex N-dimensional topography, until it encounters a minimum. Unless the topography of the objective function is very simple, the starting guess determines which of several possible minima is found.

In this current study, the parameters of the empirical potentials are locally optimized. Besides, local optimizations are performed inside PHENIX algorithm in several places such as after mutation, crossover, and the generation of the first population. To accomplish these tasks, implementations of several local optimization routines such as powell, frprmn, dfpmin, and l-bfgs-b have been used. In addition, simplex algorithm has been implemented. In the following, a few characteristics of these algorithms are listed (such as whether they need derivative information or not), to illustrate which of these algorithms was chosen for which purpose.

4.2.1 Simplex

A simplex is a geometrical figure consisting, in *N* dimensions, of *N+1* points and all their interconnecting line segments, polygonal faces, etc. In two dimensions, a simplex is a triangle. In three dimensions, it is a tetrahedron, not necessarily the regular tetrahedron.

The simplex method [69] requires only function evaluations, not the derivatives of the function. It is not very efficient in terms of the number of function evaluations that it requires. For this reason, if the evaluation of the objective function is very fast and the calculation of derivatives of the objective function is very expensive or impossible, this method is very promising.

This method must be started with *N+1* points, defining an initial simplex. If one of these points (it does not matter which) is choosen as the initial starting point P_0, then one can take the other *N* points to be

$$P_i = P_0 + \lambda e_i \tag{4.1}$$

where the e_i's are *N* unit vectors, and where λ is a constant which is a guess length scale. It is also possible that one can have different λ_i's for each vector direction.

The simplex takes a series of steps, most steps just moving the point of the simplex where the function is largest through the opposite face of the simplex to a lower point. These steps are summarized in Fig. 4.3. In this figure:

- a) Reflection: The largest function value is moved through the opposite face of the simplex. The new point is kept if the function value is reduced.
- b) Reflection and expansion: If the function at the new point is the smallest point among all points, then the simplex expands.
- c) Reflection and contraction: If the function value is increased, a smaller step is tried in that direction.

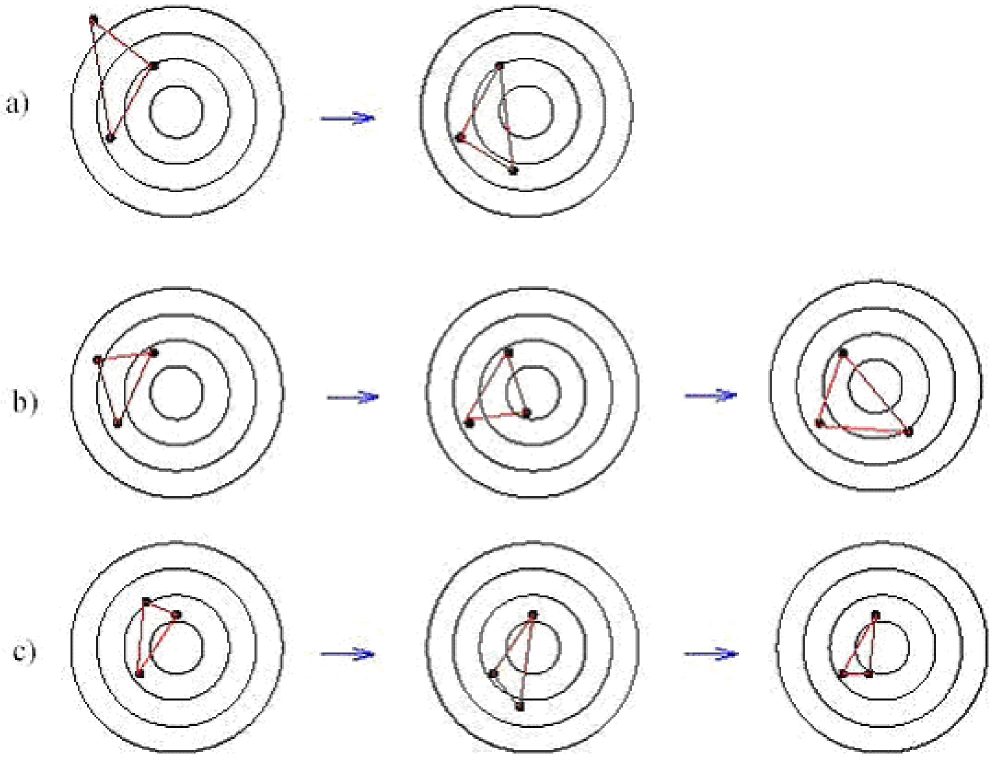

Figure 4.3: Representation of steps in the Simplex method.

The simplex moves in a quite flexible fashion: When it reaches a valley floor, the simplex contracts itself and tries to pass through the valley. If there is a situation where the simplex is trying to pass through the eye of a needle, it contracts itself in all directions. If the distance moved by the simplex is smaller than a given tolerance value, the method terminates, normally having located a local minimum.

4.2.2 Direction-Set based methods

If one starts at a point *P* in *N*-dimensional space, and proceeds from there in some vector direction *n*, then any function of *N* variables *f (P)* can be minimized along the line *n* by one-dimensional line minimization methods. *N*-dimensional minimization can be thought of as sequences of such line minimizations. The process in line minimizations is an iterative scheme such that it makes a movement along the first initial direction to its minimum, then from there along the second direction to its minimum, and so on, until the function stops decreasing.

Generally, in methods containing line minimizations, a set of directions is updated as the method proceeds. One important idea when choosing the next direction is to use "non-interfering" directions in which line minimization along one direction is not destroyed by subsequent line minimizations along the other directions. These non-interfering directions are called *conjugate directions*. The condition that enables two directions to be conjugate is that for a given direction, the gradient of the function must be perpendicular to this direction at the line minimum. Conjugate directions can be found as long as the function is quadratic about the minimum. Otherwise, the directions will be only approximately conjugate, but the method improves the rate of convergence in any case.

4.2.3 Powell's method

Powell [69] first discovered a method that contains direction sets which produce *N* mutually conjugate directions. One of the features of Powell's method is that it does not need gradient information to obtain the conjugate directions. In Fig. 4.4, steps applied in Powell's method are sketched. These steps try to find the minimum of the objective function in an iterative manner:

- Powell's method starts with an initial set of directions (which need not be conjugate). An *N*-dimensional space will have *N* search directions.
- After searching in these *N* directions, a conjugate direction is created from the vector that results from the movement from the initial point to the final point.
- In the next step, this conjugate direction is used to create a new conjugate direction.

This iteration is continued until if finds the minimum point.

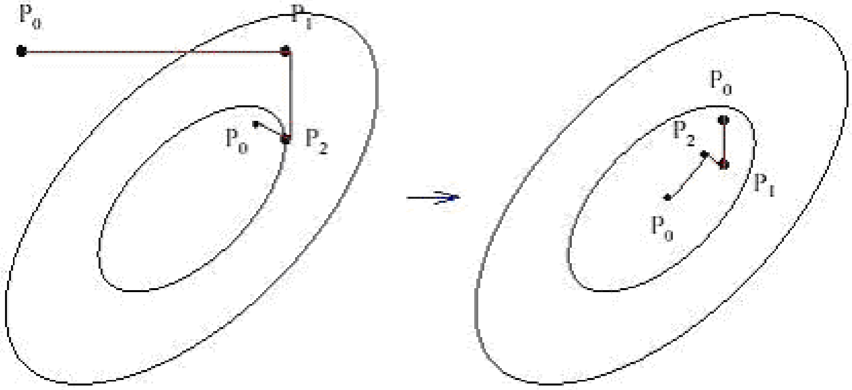

Figure 4.4: Schematic representation of Powell's method.

For a quadratic function, after *n* iterations, all the directions will be conjugate, and thus the minimum will be found after *n* one-dimensional minimizations. However, Powell's method has a problem in replacing directions: This can lead to a set of directions that are linearly dependent. As a result, not the whole search space can be explored. One way that prevents this handicap is to replace the direction that resulted in the largest decrease in the function instead of replacing the current direction.

4.2.4 Gradient based methods

If the gradient of the objective function can be evaluated easily, the speed of convergence for locating the minimum can be improved using both the information of the function itself and its gradient.

Steepest descent is one of the famous gradient methods that iterate the following steps:

- Minimizations done along the direction given by the gradient at that point.
- Move to this new minimum
- This cycle is iterated, until it finds the minimum of the function.

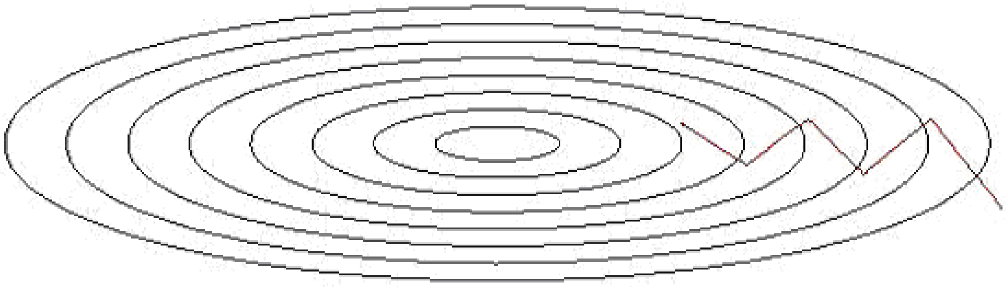

Figure 4.5: Orthogonal dependence of directions in steepest descent method.

As shown in Fig. 4.5, even for a quadratic function this method can lead to many small steps being taken, because each direction must be orthogonal to the previous one. This is in contrast to the methods involving conjugate directions, see above: There, the step directions are not orthogonal to each other but conjugate to each other. For this reason, they can locate the minimum of an *N*-dimensional quadratic function in *N* steps.

4.2.4.1 FRPRMN from the numerical recipes

FRPRMN (Fletcher-Reeves-Polak-Ribiere Minimization) [69] local minimization belongs to the gradient methods class. In this method, directions are conjugate to each other. This is achieved by the use of derivative information. In this way, conjugate directions can be found much more elegantly than with Powell's method. The frprmn method can be summarized as follows:

- Start from an initial point (x_0).
- Minimize along the steepest descent direction at x_0, giving a new point x_1.
- The next direction *d* needs to be conjugate to the previous direction of movement, x_1-x_0. In general, two directions, for example, *u* and *v* (supposing that function is minimized along the direction *u*) are conjugate directions if the gradient vector (∇f) along the direction *u* remains zero when moving

along direction *v*. The next direction *d* can be found using a combination of the two gradient vectors at points x_0 and x_1.

- These steps are iterated until the method reaches the minimum solution.

4.2.5 Variable metric methods

The goal of variable metric methods, which are sometimes called *quasi-Newton* methods, is not different from the goal of conjugate gradient methods. These methods also need gradient information of the objective function. The variable metric methods differ from the conjugate gradient methods in building up, iteratively, a good approximation to the inverse Hessian matrix in the quadratically approximated function. This method seems very similar to Newton's method for finding roots of a function, hence the name *quasi-Newton* methods. The "quasi" in quasi-Newton method is because the actual Hessian matrix of the function is not used, but instead an approximation of it.

Variable metric methods can be divided into two categories; one is the Davidon-Fletcher-Powell (DFP) algorithm, and the other is the Broyden-Fletcher-Goldfarb-Shanno (BFGS) algorithm. The DFP and BFGS algorithms differ only in details such as the convergence tolerance that is employed and how the Hessian is updated. However, it has been generally recognized that the BFGS algorithm is superior in these details.

In this thesis, implementations of variable metric methods such as DFPMIN [69] and L-BFGS-B [71] have also been used.

4.3 Global optimization methods

The field of global optimization has been expanding in all directions at an astonishing rate during the last few decades. New algorithmic and theoretical techniques have been developed. At the same time one of the most striking trends in global optimization is the constantly increasing interdisciplinary nature of the field. Many deterministic and stochastic approaches have been developed to solve global optimization problems.

4.3.1 Global optimization problems

Many famous hard optimization problems, such as the traveling salesman problem or the protein folding problem, are global optimization problems. There are no general algorithms that solve a given global optimization problem in a time that is polynomial in the problem description length.

Typical and most popular global optimization problems are [72]:

- Many problems in graph theory are global optimization problems. For example the maximum clique problem asks for the maximum number of mutually adjacent vertices in a given graph.

- Packing problems: The problem is to place a number of 3-dimensional objects of known shape within a number of larger regions of known shape in such a way that there is no overlap and a measure of waste is minimized. The simplest packing problem is the knapsack problem where a maximal number of objects of given weights is to be placed into a container with given maximum weight capacity.
- Scheduling problems: The problem is to match tasks (or people) and slots (time intervals, machines, rooms, airplanes, etc.) such that every task is handled in exactly one slot and additional constraints are satisfied. If there are several feasible matchings, one which minimizes some cost or dissatisfaction measure is wanted.
- Nonlinear least square problems: In many applications, one needs to fit data to functional expressions. This leads to optimization problems with an objective function.
- Protein folding: The protein folding problem consists in finding the equilibrium configuration of the N atoms in a protein molecule with given amino acid sequence, assuming the forces between the atoms are known. These forces are given by the gradient of the $3N$-dimensional potential energy function. Because short-range repulsive forces act like packing constraints, there are numerous local minima.
- Chemical equilibrium problems: The task here is to find the number and composition of the phases of a mixture of chemical substances allowed to relax to equilibrium.

In addition to the above problems, there is also a huge number of problems in very different fields [73]. Some of them are: mechanical design, launch vehicle design and costing, hydrodynamic modeling, robotics equipment design, chemical reactor network synthesis, conformational problems in clusters of atoms and molecules, enzyme reaction analysis, composite manufacturing, thin film design, dynamic optimization problems in parameter estimation, database optimization, data classification and pattern recognition, adaptive learning via neural nets, brain activity, bio-mechanical design, therapy (dosage and schedule) optimization, bio-informatics, environmental resource management, combination of negotiated expert opinions (forecasts, votes, assessments, etc.), etc.

4.3.2 Types of global optimization

There are several logical ways to classify global optimization strategies. One of them is to divide the global optimization into deterministic and stochastic methods. Deterministic methods provide a rigorous guarantee for finding the global minimum. However, the associated computational burden easily can become excessive, for larger dimensional problems, and /or for more complicated model functions.

For this reason, in higher dimensions and without special model structures, there is perhaps more practical hope in stochastic algorithms and heuristic methods which have a stochastic global search component. Stochastic methods do not have strict convergence guarantees; however, in many cases, they have a proven record, and may offer practical tools to handle models that are out of the reach of deterministic methods.

4.3.2.1 Deterministic global optimization and techniques

In the deterministic approach it is tacitly assumed that all essential problem characteristics are known with certainty. This assumption represents only an approximation of real-life situations, in which uncertainties and statistical variations of system behavior frequently play an important role. The main features of deterministic global optimization are;

- Finding the global optimum is guaranteed.
- Directly or indirectly, the whole configuration space has to be searched to find the global minimum, by looking at all of the local minima in the search space.
- The methods are hard to implement.

By definition, a deterministic approach finds the global minimum, however the considered system size must be very small. For this reason, in many real-life problems, these approaches are far away from applicability. Additionally, good heuristics also play a role in deterministic methods, mainly to provide cheaply a good local minimum that benefits the systematic search. There are many deterministic approaches proposed for optimization problems. A few of them are mentioned in the following and in the next section. More information can be found in references [72,73,74].

The simplest deterministic method for constrained problems is *grid search*, where all points on finer grids are tested, and the best point on each grid is used as a starting point for a local optimization. Since the number of points on a grid grows exponentially with the number of dimensions of a problem, grid search is efficient only in one and two dimensions.

Branch and bound (B&B) is an approach to search for an optimal solution by searching only a part of the search space, while the derived bounds on the objective function guarantee that no optimal solution exists on the excluded parts of the search space. B&B guarantees to find a global minimum with a desired accuracy after a predictable number of steps. The basic idea is that the set of feasible solutions is branched or partitioned into many simpler (smaller) subsets and an effort is made to search the best feasible solution or compute a lower bound of the objective function on the subsets. Each subset will be the set of feasible solutions of a subproblem. The treatment of each subproblem ends in one of the following ways:

- The best feasible solution in that subset is found.
- It is discovered that the subset is empty.

- Based on the bounds, it is proved that no optimal solution in that subset exists.

If none of the above targets can be achieved for a given subset, that subset may again be partitioned into smaller subsets and the same process is repeated on them. The B&B approach computes and uses both lower and upper bounds for the objective value. A lower bound can be obtained by relaxing the problem. Computing a good lower bound is an essential component of B&B method. Otherwise, the B&B approach may degenerate into searching the whole space and become impractical. An upper bound of the optimal value is the current best solution value found in a subset. If the lower bound in a subproblem is worse than an upper bound already obtained in another subproblem, then the first subproblem will never contain a better solution than the current solution. Therefore, it needs not to be explored further.

Global optimization methods that use interval techniques provide rigorous guarantees that a global minimum is found. Interval techniques are used to compute global information about functions over large regions (box-shaped). Most global optimization methods using interval techniques employ a branch and bound strategy. These algorithms decompose the search domain into a collection of boxes for which the lower bound on the objective function is calculated by an interval technique.

Interval methods require that the objective function be formulated by an analytic expression that is provided to the algorithm; this expression is used by an interval technique to compute the bounds. The basic design for interval methods does not require the calculation of the derivative information, though the efficiency of these algorithms can be improved if the derivative or Hessians are available. The application of interval methods to high dimensional problems remains an open problem.

Enumerative methods are based upon a complete enumeration of all possible solutions. These methods are applicable to combinatorial optimization problems.

In relaxation (outer approximation) strategies, the global optimization problem is replaced by a sequence of relaxed sub-problems that are easier to solve. Successive refinement of sub-problems to approximate the initial problem is applied.

Tunneling methods [75,76] are deterministic methods in the sense that they find a sequence of local minima with monotonically decreasing objective function. This is accomplished by a two-phase process of local minimization to find x^*, followed by a tunneling step to find a point x^{tun} in another valley, with lower or equal value of the optimal objective function $f(x^{tun}) \leq f(x^*)$, that will serve as the initial point for the next local minimization.

Tunneling methods also have a stochastic element functioning when starting the search for points in another valley (in the tunneling phase) in random directions. This stochastic element can be exploited to perform a smart exploration of the feasible space in parallel processors, to improve the performance and the speed of the method.

In the cutting angle method (CAM) [77,78], the original optimization problem is replaced by a sequence of simpler (relaxed) optimization problems, each with a global minimum that is relatively easy to find and verify. These relaxed problems are constructed so that they converge to the original optimization problem and the sequence of their solutions converges to the global minimum of the original optimization problem. This method can be used for both differentiable and non-differentiable functions. The one-dimensional Piyavskii–Shubert algorithm, illustrated in Fig. 4.6, is a special case of the cutting angle method.

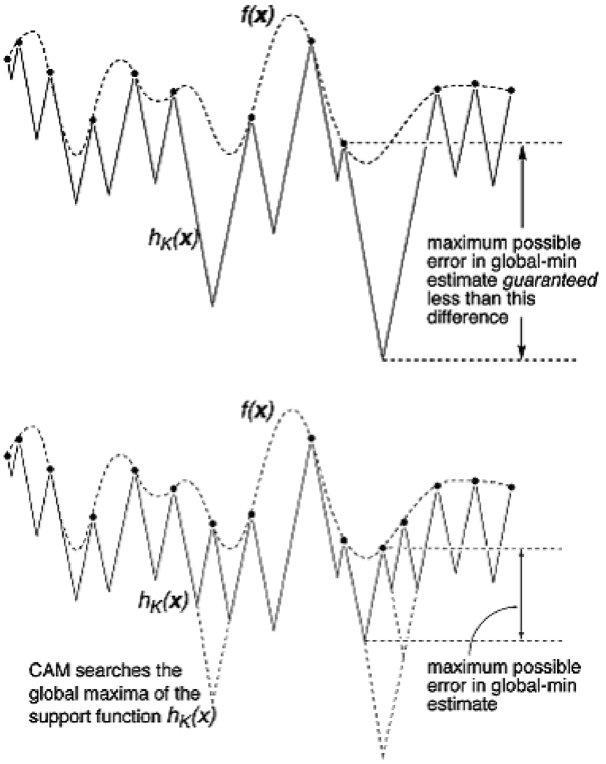

Figure 4.6: Generalized cutting plane method of Lipschitz optimization (Pijavski-Schubert method). All local minima of the saw-tooth cover can be explicitly enumerated. As the number of function evaluations increases, the teeth become smaller and the supporting functions $h_K(x)$ converges to the global minimum of $f(x)$.

In this figure, a function f has been evaluated at several points: x_1, x_2, x_3,. . .,x_K. From each evaluated point on the function f, it is possible to construct a hypercone, with slope L, and with its apex touching the function f. The maximum of these hypercones, $h_K(x)$, gives a lower approximation to the function f, also called the saw-tooth cover because of its shape. As more points $f(x)$ are evaluated (lower panel of Fig. 4.6), the sequence of lower approximations, $h_K(x)$, K=1,2,. . ., converges to f, and the sequence of global minima of $h_K(x)$ converges to the global minimum of f under very mild conditions. The conceptual global optimization algorithm consists of the following steps:

- Using K known function values and L, build the saw-tooth cover $h_K(x)$.
- Find the global minimum, x^*, of $h_K(x)$.
- Evaluate f at x^*.

- Set $x^{K+1} = x^*$, increment K and return to first step.

The algorithm continues until the error (the difference between the smallest computed value of f and the global minimum $h_K(x^*)$) is smaller than a given tolerance.

4.3.2.2 Stochastic global optimization and techniques

When the size of the problem to be solved increases, it is out of the question to look for a deterministic algorithm, unless in very special cases. Hence, when dealing with large scale and computationally expensive global optimization problems, employment of a stochastic procedure is necessary. The main features of stochastic global optimization are:

- There is no guarantee for finding the global minimum.
- Only a restricted search of configuration space is carried out. This is compensated for by some search heuristic that tries to guess promising regions in advance and/or exclude others.
- The methods are relatively easy to implement.
- The methods require no mathematical structure of the problem and are therefore more generally applicable.

Like deterministic ones, many stochastic procedures have been proposed to solve the global optimization problems. The simplest stochastic method is multiple random start (multistart), consisting of picking random starting points and performing local optimizations from these points, in the hope that one of them is in the basin of attraction of the global minimum. Most stochastic methods can be regarded as techniques devised to speed up this basic method, by picking the points more carefully and by doing the local optimizations only selectively.

Smoothing (continuation) methods, illustrated in Fig. 4.7, are based on the intuition that, in nature, macroscopic features are usually an average effect of microscopic details; averaging smoothes out the details in such a way as to reveal the global picture. A huge valley seen from far away has a well-defined and simple shape; only by looking more closely, the many local minima are visible, more and more at smaller and smaller scales. The hope is that by smoothing a rugged objective function surface, most or all local minima disappear, and the remaining major features of the surface only show a single local minimum. By adding more and more details, the approximations made by the smoothing are undone, and finally one ends up at the global minimum of the original surface.

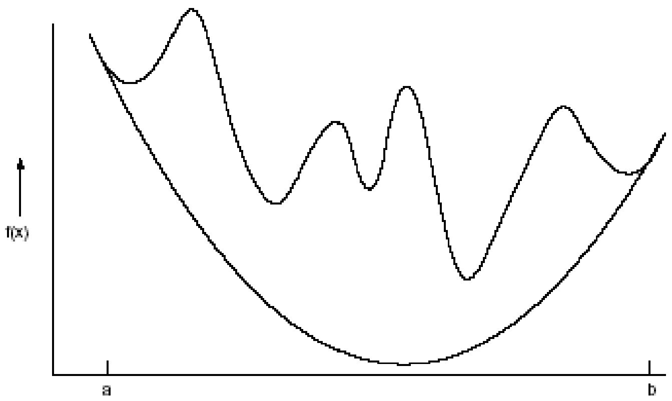

Figure 4.7: Schematic representation of the continuation approach using smoothing.

Tabu search (TS) forbids search moves to points already visited in the search space, at least within the next few steps. Tabu search methodology has been primarily used to solve combinatorial optimization problems.

Statistical global optimization algorithms employ a statistical model of the objective function to bias the selection of new sample points. These methods are justified with Bayesian arguments that suppose that the particular objective function that is being optimized comes from a class of functions that is modeled by a particular stochastic function. Information from previous samples of the objective function can be used to estimate parameters of the stochastic function, and this refined model can subsequently be used to bias the selection of points in the search domain.

Statistical methods generally assume that the objective function is sufficiently expensive so that it is reasonable for the optimization method to perform some nontrivial analysis of the points that have been previously sampled. Many statistical methods rely on dividing the search region into partitions. In practice, this limits these methods to problems with a moderate number of dimensions.

Clustering global optimization methods can be viewed as a modified form of the standard multistart procedure, which performs a local search from several points distributed over the entire search domain. A drawback of multistart is that when many starting points are used the same local minimum may be identified several times, hence leading to an inefficient global search. Clustering methods attempt to avoid this inefficiency by carefully selecting points at which the local search is initiated. The three main steps of clustering methods are performed until some stopping condition is fulfilled:

- The points are concentrated to some local minima by either leaving out points like in the “Mode-Seeking” algorithm or by performing some steps of a local minimization algorithm.
- The clusters are identified by using some cluster analysis technique.
- Retain every best point in each cluster and go to step 1.

Finally the global minimum can be determined by starting a local minimization algorithm from the best point in each cluster. These methods assume that the objective function is relatively inexpensive since many points might be sampled to identify the clusters. Clustering methods are most effective for low dimensional problems.

Simulated annealing (SA) takes its intuition from the fact that the heating and slow cooling (annealing) of a metal brings it into a more uniformly crystalline state that is believed to be the state where the free energy of bulk matter takes its global minimum. The role of temperature is to allow the configurations to reach higher energy states, so that they can overcome energy barriers that would otherwise force them into local minima.

For a given function to optimize and some initial values for the variables, SA starts at a high, artificial temperature. While reducing the temperature slowly, it repeatedly chooses a subset of the variables and changes them randomly in a certain neighborhood of the current point. If the objective function has a lower function value at the new iterate, the new values are chosen to be the initial values for the next iteration. If the function value is higher, the new values are chosen to be the initial values for the next iteration with a certain probability, depending on the change in the value of the objective function and the temperature. The higher the temperature and the lower the change, the more probable the new values are chosen to be the initial variables for the next iteration. Throughout this process, the temperature is decreased gradually, until eventually the values do not change anymore [79]. Geman and Geman proved that if the temperature is reduced slowly enough SA is guaranteed to find the global minimum [80]. Unfortunately, such a slow pace makes the method inapplicable to search for the lowest-energy structures of clusters or molecules with even a small number of atoms.

A strategy similar to SA is the basin-hopping method, firstly introduced for protein folding [81] and then adapted to global cluster geometry optimization [87]. This algorithm does a series of MC steps followed by local minimizations. This corresponds to an MC treatment on a modified PES, which is transformed by the local optimizations to a series of plateaus and steps with fewer and lower barriers in-between. Due to the large number of local minimizations, computational expense is rather high for this method. Furthermore, its size scaling is approximately n^5, which limits its applicability to larger clusters.

Conformational space annealing (CSA) [82], which is a powerful stochastic global optimization method, incorporates essential ingredients of three optimization methods, Monte Carlo with minimization (MCM), Genetic Algorithms (GA), and SA. First, as in MCM, only local minima are considered. Second, as in GA, many configurations (called a bank in CSA) are considered, and a subset of bank configurations (seeds) are perturbed by using other bank configurations. This procedure is similar to mating in GA. However, in contrast to the typical mating procedure in GA, small portions of a seed are often replaced with the corresponding parts of bank configurations in order to search the neighborhood of the seed configuration. Finally, as in SA, a parameter is introduced, D_{cut}, which plays the role of the temperature in SA. The diversity of sampling is directly controlled in CSA by introducing a distance measure between two configurations and comparing it with D_{cut}. The value of D_{cut} is slowly reduced just as in SA.

Genetic algorithms: In this study, this method has been successfully applied to silicon clusters to find their global minimum structures. Therefore, this method is described in more detail in Chapter 5.

4.4 Application of deterministic and stochastic global optimization techniques to the cluster problem

One of the challenging optimization problems is to locate the global minimum structures for clusters. The challenge is mainly due to the number of local minima increasing exponentially with cluster size. In order to solve this problem, several deterministic and almost all of the stochastic methods have been applied. As will be explained below, stochastic methods currently are the methods of choice, since deterministic methods are limited to cluster sizes that are normally too small to be of interest.

Generally, Lennard-Jones (LJ) clusters have been used as a benchmark system. The LJ potential is a simplified model for noble gas clusters and it can be constructed by pairwise van-der-Waals type interactions;

$$E = 4\varepsilon \sum_{i,j} \left[\left(\frac{\sigma}{r_{ij}} \right)^{12} - \left(\frac{\sigma}{r_{ij}} \right)^{6} \right] \tag{4.2}$$

The PES of LJ clusters is dominated by one geometry species, the *Mackay icosahedra*, for most cluster sizes. However, at certain sizes, other structures are slightly lower in energy, such as for n=38 a face centered cubic type and for n=75,76,77 and n=102,103,104 a decahedral type, while most of configuration space is still dominated by icosahedra. This situation makes it extremely difficult for all global optimization methods to treat these particular cluster sizes.

4.4.1 Application of deterministic methods

Adjiman et al. [83] applied the B&B method to find the global minimum structure of clusters containing flexible molecules.

Firstly, B&B was applied for n-butane which has two conformers. The conformer search is started from a minimized structure of butane. At this structure, values of all the equilibrium bond lengths, bond angles and torsional angles are determined. The values of the bond lengths and angles are not expected to vary significantly from this equilibrium value, and, hence, tight bounds can be assigned to them.

Secondly, B&B was applied for *n*-butane/ethylamine pair. Both ethylamine and *n*-butane have two conformers. Furthermore, this small system has multiple minima depending on how two molecules are oriented with respect to each other. For the optimization, the individual molecules are almost fixed at their global minimum conformer but are allowed slight variations to their bond lengths, angles and torsions due to the interactions with the other molecule.

In these case studies, they published only the potential energies of global minimum structures found for n-butane and n-butane/ethylamine pair. They did not attempt to make a further comparison for their global minimum structures and those proposed in the literature. This suggests that their structures and methodology might not be as successful as claimed.

Beliakov et al. [77] applied the CAM for several molecular conformation problems such as propanal, 1,2,3-trichloro-1-fluoropropane, single amino acids, and unsolvated met-enkephalin. Amongst these problems, the last one is a challenging case since its PES involves in the order of 10^{11} local minima [84]. In all these problem cases, all the bond lengths and bond angles have been held fixed. Hence, the conformations of the various molecules considered in this study depend only on the torsional or dihedral angles. As a result, the potential energy depends only on the torsional potential energy terms and those corresponding to interactions between non-bonded atoms. For all the molecules considered in this study, CAM was able to locate the global minimum proposed in the literature for the same PES.

An early attempt for LJ clusters has been reported by Maranas and Floudas [85]. They have performed deterministic global optimization for finding the global minimum structures of LJ clusters using the DC transformation technique. First, the original nonconvex total potential energy function is transformed to the difference of two convex functions (DC transformation) via a procedure performed for each pair potential that constitutes the total potential energy function. Then, a decomposition strategy [86] is designed to provide tight bounds on the global minimum through the solutions of a sequence of relaxed dual subproblems. In this study, global minima have been located as an equilateral triangle, a tetrahedron, a trigonal bipyramid, an octahedron, and a pentagonal bipyramid structures for LJ clusters containing 3-7 atoms, respectively.

For larger LJ clusters, the complexity of the problem limits the use of the general global optimization procedure. As a result, a “relaxation” of the global optimization procedure was presented [85] for larger clusters containing 8-24 atoms, which yields tight lower and upper bounds on the total potential energy as well as excellent initial points for a possible local optimization approach. In this relaxation procedure, a number of structures whose coordinates are very close to the coordinates of the structures involving the global minimum were found.

Recently, Gomez et al. [76] also applied a parallel version of the tunneling method to larger LJ clusters containing 38 and 40 atoms. This size was selected since the first non-icosahedral structure found for LJ clusters was the 38-atom cluster. They reproduced the global minimum structures proposed in the literature for these sizes. Especially for LJ clusters containing 38 their parallel version using 3-processors found the global minimum 258 times faster than the serial version of the tunneling method.

Amongst these studies, the considered problem sizes are very small. Additionally, for the global optimization LJ clusters only Maranas and Floudas [85] performed a systematic effort. However, in this study for $n>7$, they could not keep up their fully deterministic scheme, and hence they could not guarantee finding the global minima for $n>7$.

4.4.2 Application of stochastic methods

One of the first systematic attempts were performed by Wales et al. [87] for the determination of the global minimum structures of LJ clusters. They have made global optimizations using the basin-hopping method up to $n\leq110$. Almost all the known global minima were reproduced, and those for $n=69$, 78, 107 were updated. Slightly after that, Hartke [88] also reproduced all the known global minima up to $n\leq150$ with the Phenix (see Chapter 5) algorithm.

Locatelli and Schoen [89] considered the continuation approach for the global optimization of the LJ clusters. They first minimized a modified convex potential function, which is related to the LJ potential. The local minimum of this modified potential was then used as a starting point for a local optimization of the LJ potential function. Some difficult cluster structures have been rediscovered with different parameter settings. However, two pitfalls limit the practical use of their approaches. The first is the lack of a general rule to choose a set of parameters that is sufficiently good for a large range of clusters. The other is that they use a random generation mechanism in their implementation. Therefore, some 10000 random trials might be needed to rediscover one cluster structure. They have reproduced the global minimum structures accepted in the literature for LJ clusters containing up to 80 atoms.

Then, more recently, Locatelli and Schoen [90] have proposed a stochastic global optimization method which incorporates the basin hopping method with a two-phase local search procedure which is capable of significantly enlarging the basin of attraction of the global minimum. This strategy has been applied to most challenging LJ clusters containing 75, 98, and 102 atoms. All the known global minimum structures for these considered sizes have also been reproduced with this new approach.

Shao et al. [91] have also considered the LJ cluster problem using a smoothing approach. They have firstly proposed a new and simple algebraic way of smoothing the LJ model potential. Then, the algorithm was applied to 9-atom, 30-atom, and 34-

atom LJ clusters. For the 9-atom case, all the local minima have been found, however, for other cases only a tiny portion of the local minima has been determined.

In the recent study of Lee et al. [82], the CSA method has been successfully applied to LJ clusters containing 201 atoms. They have reproduced all the known global minima up to this size. Additionally, the stochastic methods have now reached a LJ cluster size containing 309 atoms [82].

A stochastic approach has also been recently applied to heteronuclear LJ clusters by G. Bilalbegovic [92]. They examined heteronuclear clusters consisting of one alkali-metal ion and of up to 79 neutral rare gas atoms using the basin-hopping Monte Carlo minimization method. Rare gas atoms interact with the LJ potential, whereas the interaction between a neutral atom and an ion impurity is given by the Mason-Schamp potential. It was observed that starting with eight rare gas atoms the alkali-metal ion is always placed inside the cage composed of rare gas atoms.

Apart from these studies in the literature, SA [93,94,95], basin-hopping [96] and GA [7,25] strategies have been extensively applied to silicon clusters.(Results of these studies are extensively discussed throughout this theses). It is not surprising that all these methods are stochastic since the complexity of the problem cannot be handled by deterministic methods as in the case of Maranas and Floudas' study [85] where for LJ clusters containing more than 7 atoms, the global minimum structures were not located.

It is obviously clear that stochastic global optimization methods can reach very complex regions beyond the scope of the deterministic optimization methods. Silicon clusters are a much harder problem compared to LJ clusters. Additionally, it is necessary to search the peculiar transition region in silicon clusters, and this region is totally out of the consideration of the deterministic tools. Hence, using a stochastic approach seems necessary to find the global minimum structures of silicon clusters. Moreover, stochastic approaches should inevitably be used for other optimization problems in which there are a huge number of local minima.

5 Genetic algorithm

Genetic algorithms (GAs), pioneered by John Holland [97], are search algorithms based on the mechanics of natural selection and natural genetics to evolve solutions to global optimization problems. They belong to the class of stochastic search methods. The principle idea is the survival of the best individual in a population. In this chapter GA will be described starting with the general considerations. Then, its application to global cluster geometry optimization will be discussed. This will be followed by explaining the details of the algorithms (GAGA and PHENIX) that have been used for this current study.

5.1 Introduction to standard GA

In GA, solutions are expressed as sequences of values. Each sequence is called a "chromosome" or a "string", and each parameter within the chromosome is defined as a "gene". The entire set of genes constitutes the "genotype", and the solution to which this genotype corresponds is known as the "phenotype" [98].

Each string represents a solution to the problem under consideration. It is generally in coded form, and the GA makes a search through this coded search space. The aim of coding is to create a representation which allows easy and flexible modification of the string. It may represent a calculated infra red (IR) spectrum, a sequence of temperatures, the molecular constants which define the geometry of a molecule, or as it is in this current study, the cartesian coordinates of atomic silicon clusters which defines the geometry of a cluster. GA strings are generally one-dimensional, but two-dimensional and higher-order strings have also been used where such a representation permits more efficient calculation.

In early GAs, the strings were almost always in binary form, containing only 0's and 1's. However, for some types of problem, it may be more convenient to use real-valued strings, in which each real number represents part of the solution in uncoded form. There is a debate on which representation is more promising. Some claim that using a binary representation is an advantage because one needs more digits to represent a given number and this suggests more flexibility to search strategies such as crossover. However, others claim that it does not really matter which representation scheme is selected, because in principle it should be possible to implement the same operators in binary or real-valued representations. Thus, while this debate continues, a practical intermediate conclusion is that one should choose a representation that allows for an easy construction of a wide range of promising operators.

In Fig.5.1, the standard GA is schematized, in which there is only selection, crossover, and mutation genetic operators. In this figure, the GA starts with the initialization of a population of random strings. If there is specific information available about the problem considered, it may be used to initialize the first population.

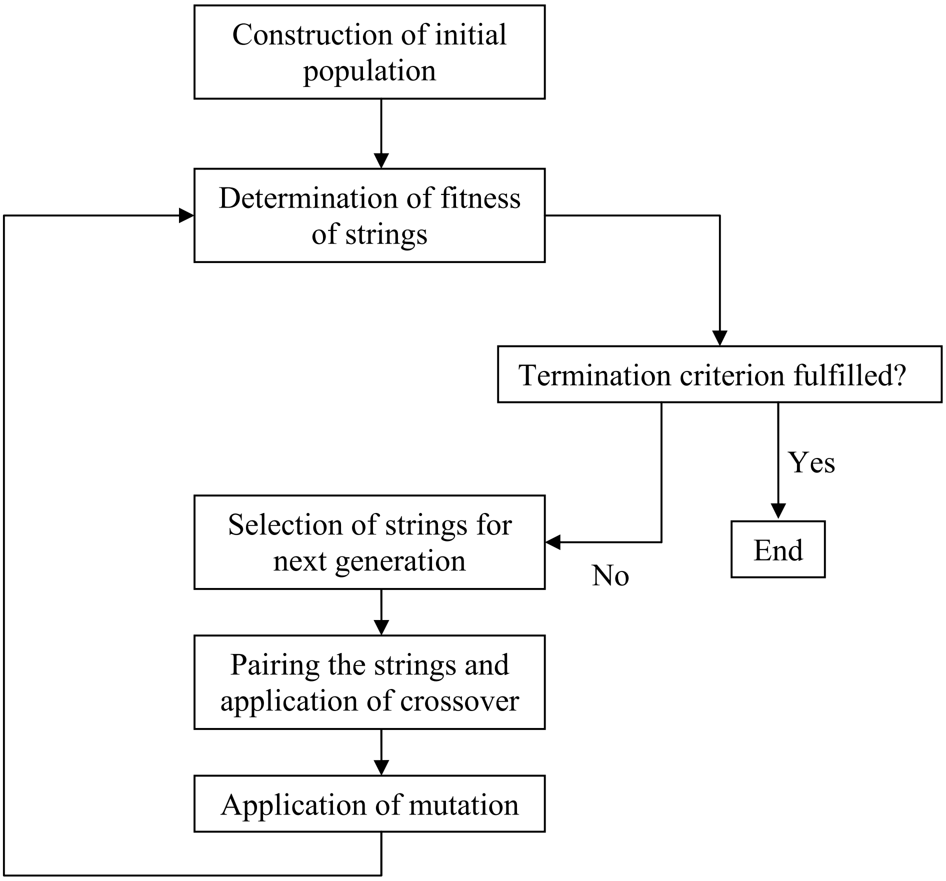

Figure 5.1: Schematic representation of simple GA.

After the initialization of the first population, the fitness of each string is calculated after the genotype has been decoded into the corresponding phenotype. The fitness is a measure that shows to which extent the solution satisfies the requirements of the problem.

Once the fitness of each string has been found, selection is applied. During selection, the most satisfying strings determined according to their fitness value are selected. Selection for the next population can be done in several ways such as deterministic (the better of two possible solutions is always retained, while the other is invariably discarded), stochastic (the best of two or more solutions is chosen with a probability related to the fitness of the solutions), or a combination of these. A variety of methods have been proposed for the selection step. One of the earliest is the roulette wheel, in which the probability of a string being chosen is proportional to the fraction of the total fitness of the population. On the roulette wheel, each string is allocated a segment whose size is proportional to the string's fitness as seen in Fig. 5.2. The wheel is spun, and the string which is in the position indicated by the roulette wheel after its spin is selected into the new population. The process is repeated until the new population is equal in size to the starting population. This procedure has the advantage of simplicity, but since it is stochastic there is no certainty that the best string in the parent population will be selected into the new population. Additionally, if there are big differences between the fitness values, low-fitness strings may disappear completely if the population is not large enough.

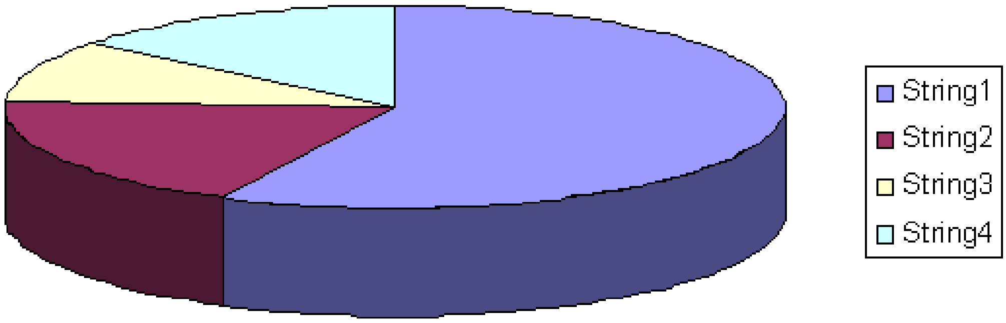

Figure 5.2: Roulette wheel selection.

The other popular selection method is rank selection. In the selection, the population is first ranked and then every string receives fitness value determined by this ranking. The worst will have the fitness 1, the second worst 2 etc. and the best will have fitness *N* (number of strings in population). It can be seen in Fig. 5.3, how the situation changes after changing fitness to the numbers determined by the ranking. With the help of this selection procedure, all the strings have a chance to be selected. However this method can lead to slower convergence, because the best strings do not differ much from other ones.

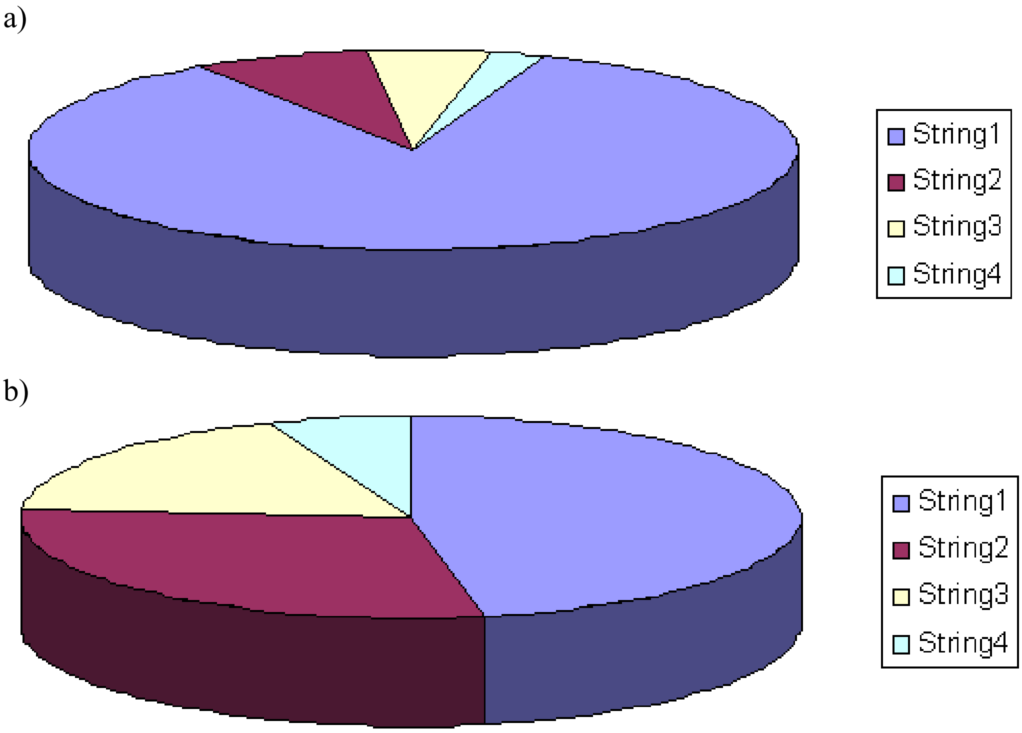

Figure 5.3: Rank Selection, a) Situation before ranking (graph of fitnesses), b) Situation after ranking (graph of order numbers).

There are also other procedures for selection such as tournament selection (pairs of parent strings are chosen at random and the string of higher fitness is copied into the next population), steady-state selection (in every generation a few good (with higher fitness) strings are selected for creating new offspring. Then some bad (with lower fitness) strings are removed and replaced by the new offspring. The rest of population survives to the new generation), elitism (the best or a few best strings are directly copied to the new population, and the rest of the population is constructed using any of the selection procedures. Elitism can rapidly increase the performance of GA, because it prevents loss of the best found solution.), and truncation selection (the candidate solutions are ordered by fitness, and some proportion, *p*, (e.g. *p*=1/2, 1/3, etc.), of the fittest individuals are selected and reproduced 1/*p* times. Truncation selection is less sophisticated than other selection methods, and is not often used in practice.

After the selection of the new population, individual strings are paired to provide exchange of genetic information. The genetic information exchange can be done in a variety of ways. The simplest way is one-point crossover in which pairs of strings are cut at randomly selected positions. The segments between these cuts are swapped. Then two new offspring are produced. One-point crossover is illustrated in Fig. 5.4.

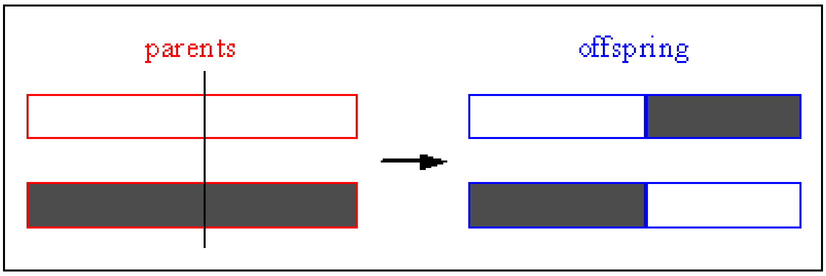

Figure 5.4: One-point crossover.

Crossover can also be done by a two-point crossover operator. In that case, two crossover positions are selected along each string and the segments between these positions are swapped. Moreover, these one-point and two-point crossover operators can be seen as a special case of a multi-point crossover operator in which *m* crossover positions are selected as illustrated in Fig. 5.5 and the segments between those crossover positions are swapped.

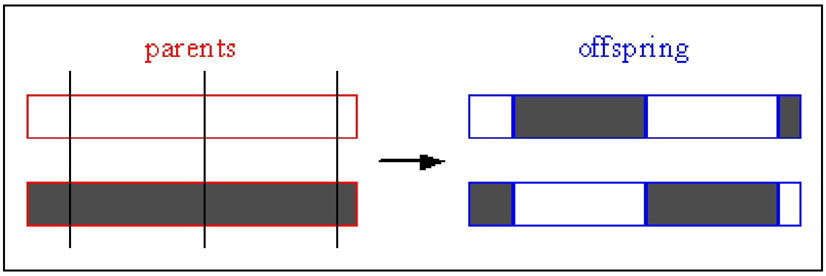

Figure 5.5: Multi-point crossover.

When crossover is complete, a small fraction of strings are mutated to introduce new genetic material. A mutation may consist of the replacement of a randomly selected gene by a random value, the swapping of the values of two randomly chosen genes within a single string, a modification to the value of a gene in a randomly selected direction, or some other processes. Mutation rates are usually low because while mutations introduce new information, they also destroy potentially valuable information which has evolved during the search.

After these operations, the algorithm either terminates with giving the optimal solution or continues for a new cycle. Many termination criteria may be used to finalize the algorithm. A simple criterion is to stop after some predetermined number of generations. Other criteria might be: when a solution reaches a prespecified level of fitness, or when the variation of individuals from one generation to the next reaches a prespecified level of stability. Obviously, none of these criteria imply a guarantee that the global optimum has been found. With that, one would be back at the deterministic methods, together with their disastrous size scaling that makes them impractical.

Further inspiration from nature leads to other advanced genetic operators such as “dominance”, “diploidity”, “inversion”, “segregation”, “translocation”, “duplication”, “deletion”, and “niche”. Within the simple GA, a single-stranded string contains all the information relevant to the problem. However, in nature, genetic processes are controlled with “diploid” or “double-stranded strings”. In the diploid form, there are two single-stranded strings containing information for the same function. However, a conflict arises in this representation because of the occurrence of alleles. To eliminate this conflict, a dominance operator can be used. This operator decides which allele is dominant. After establishing the dominant allele, this allele takes precedence over the alternate allele. Under the effect of the inversion operator two positions are chosen along the string, similar to two-point crossover, then the string is cut at these positions, and the end points of the segments are swapped. In nature, many organisms carry more than two strings (chromosomes). To borrow this phenomenon into the GA, it is necessary that the information relevant to the problem is carried with those strings. A segregation operator controls random selection of one string among those strings. A translocation operator works as an inter-string crossover operator. An intra-chromosomal duplication operator acts by duplicating a particular part of the string and placing it on the string. A deletion operator removes a duplicated part of the string from the string. Finally, a niche can be defined as a class of strings that have common characteristics [99].

GAs containing some or all of these ingredients have been applied successfully to several problems in a variety of fields as diverse as engineering, mathematics, medicine, economics, and political sciences. Details of applications can be found in Goldberg’s book [99].

GAs are different from normal global optimization and search procedures for the following reasons:

- Standard GAs work with a coding of the parameter set, not with the parameters themselves. The coding of parameters can be achieved by using finite-length string representations.
- GAs search from a population of points (solutions), not from a single point. In many optimization methods, algorithms proceed from the current point to the next point by some transition rules. This point-to-point method can be dangerous since the algorithm can get stuck in a local solution in a multidimensional search space. GAs use many points simultaneously. Thus, the probability of finding a false local minimum is reduced.
- GAs use objective function information, not derivatives or other auxiliary knowledge.
- GAs use probabilistic transition rules, not deterministic rules [99].

To implement a GA for a given problem, the following main features are required [100]:

- an objective function (cost function) to optimize
- a chromosomal representation of solutions to the problem
- a way to create an initial population of solutions
- a fitness function for selection
- genetic operators (such as selection, crossover and mutation)
- values for the parameters that the GA uses (population size, probabilities of applying genetic operators, etc.)

5.2 Global cluster geometry optimization problem

The aim of global cluster geometry optimization is to find the lowest-energy (global minimum) cluster structure among a large number of local minima of the corresponding potential energy surface (PES). However, this search becomes a challenge since even small clusters are too large for an ab-initio calculation including electron correlation. Actually, global search becomes prohibitively expensive at some cluster size for all methods, not because of the expense of the method but because of the vastness of the search space. This is also true for a search that is performed on an empirical potential.

Global cluster geometry optimization is in the class of NP-hard problems like exact electronic structure determination (full configuration interaction (CI) scales exponentially, but approximate ab-initio methods scale only polynomially) or protein folding. This means that the search space and the number of local minima increase exponentially with increasing system size. This problem can be overcome by an equally massive restriction of search space, using suitable external information, higher level descriptions, or intelligent adaptive growth strategies.

There are also other methods different from GA to deal with global cluster geometry optimization. One of these methods is molecular dynamics (MD). The aim of molecular dynamics is to model the detailed microscopic dynamical behavior of many different types of systems. The nuclear motion of the particles is modeled using the laws of classical mechanics. There is a link between MD and statistical mechanics. This is basically a connection of the microscopic details of a system to the physical observables such as equilibrium thermodynamic properties, transport coefficients, and spectra. Statistical mechanics is based on Gibbs' ensemble concept. That is, many individual microscopic configurations of a very large system lead to the same macroscopic properties, implying that it is not necessary to know the precise detailed motion of every particle in a system in order to predict its properties. It is sufficient to simply average over a large number of identical systems, each in a different configuration; i.e. the macroscopic observables of a system are formulated in terms of ensemble averages. Statistical ensembles are usually characterized by fixed values of thermodynamic variables such as energy, E; temperature, T; pressure, *P*; volume, *V*; particle number, *N*; or chemical potential μ. One fundamental ensemble is called the micro-canonical ensemble and is characterized by constant particle number, *N*; constant volume, *V*; and constant total energy, *E*, and is denoted the NVE ensemble. Other examples include the canonical or NVT ensemble, the isothermal–isobaric or NPT ensemble, and the grand canonical or μVT ensemble. The thermodynamic variables that characterize an ensemble can be regarded as experimental control parameters that specify the conditions under which an experiment is performed. In MD, detailed time evolution of systems can be helpful to study chemical reactions, absorption, desorption, and structural phase transitions.

The concept of traditional MD is widely extended by a family of techniques called ab-initio MD. In one of techniques, ab-initio MD simulations consider the motion of the nuclei on a Born-Oppenheimer (BO) surface and are thus called BOMD. Because at each timestep an electronic structure calculation has to be performed such an approach is computationally demanding for high-level quantum chemical methods. Car-Parinello MD (CPMD) is a successful variant of ab-initio MD, which performs the dynamical study at the DFT level. In this method, the particles follow classical trajectories and the forces between them are calculated with DFT methods. However, its computational expense, similar to that of BOMD, is extremely high due to the use of DFT methods to calculate the interatomic interactions.

Traditional MD uses empirical potentials or force fields to calculate the interatomic interactions, whereas in ab-initio MD this is done at the ab-initio level and then particles move classically. In ab-initio MD, mostly DFT is used to obtain the total energy of the interacting system of electrons with classical nuclei fixed. Traditional MD compared to ab-initio MD is much faster. This means that large problems can be attacked only by traditional MD.

Traditional MD and all ab-initio MD methods give direct access to thermodynamic quantities and structural information at experimentally relevant temperatures. They also offer direct insight into dynamical processes. This can be even for very large biochemical systems in the case of employing traditional MD. But, there are also some disadvantages. Path integrals give (quantum) statistical mean values, no true quantum dynamics of the nuclei. For large systems, one cannot even approximate quantum dynamics with traditional dynamics. For these reasons, the explicit insight into dynamics is actually limited to more or less representative single trajectories. Furthermore, for sufficiently good statistics and systems of non-trivial size, the computational expense is very large, even for traditional MD on empirical potentials.

For determination of lowest-energy structures, the expense of global optimization methods (SA, GA, etc.) is smaller than for MD calculations since there is no need to generate statistically relevant trajectories. In comparison to typical MD and Monte Carlo (MC) calculations, this allows a faster and more direct deduction of dependencies between terms in the potential energy function and structural preferences; this obviously simplifies the construction and improvement of empirical potentials for clusters. MD can be combined with tight-binding (TB) approach or SA. However, this combination also increases the computational effort.

As opposed to MD and MC calculations, global optimizations are purely static, in the sense of producing only the global minima of potential energy surface. With appropriate vibrational analyses of the sets of local minima, one can extend the results up to full thermodynamic data and with sufficiently large data sets on minima and transition state geometries even to an approximative relexation dynamics.

Even today there are still cluster structure studies being done without any global optimization tools. It was pointed out several years ago that such approaches can lead to qualitatively wrong results even for very small clusters [101]. In one case of an empirical silicon potential, spurious low-energy planar minima for n=6,8 escaped the attention of researchers using traditional local optimization methods; they were detected only with global optimization techniques [102]. Thus, cluster studies using exclusively local optimization can be taken seriously only if a huge number of minima are generated.

The exponentially increasing configuration search space of clusters and the resulting difficulties are also recognized in other areas of theoretical research, for example, in MD and MC studies. For example, several groups noticed that the notorious case of LJ_{38} is not treated adequately even by some of the standard techniques, and thus more advanced sampling techniques had to be established to overcome these problems [103,104,105]. In spite of this, repeated quenches from standard MD trajectories are sometimes still being employed to find low-energy minimum structures of clusters [106].

Traditional standard SA is also still being used in some cluster studies [107,108]. There seems to be a consensus in the global cluster geometry optimization community that standard SA is not as efficient as GA or basin-hopping [101]. Recently, SA variants incorporating some of the improved sampling techniques have been applied to clusters [109], and there have been many improvements to the basic recipe of SA. So far, however, it is still unclear if any of this improves SA to the point of being competitive with GA, for the cluster optimization problem.

A variant of basin-hopping method applied to the standard LJ cluster benchmark by Wales and Doye [87]. They could find all the global minima accepted without prior information, up to n=110, including the difficult cases n=38,75-77,103-105 (but missing the tetrahedral case n=98). Solving these difficult cases took at least 1 order of magnitude more computer time than solving the neighboring easier cases. Two years later, this result could be roughly matched by Hartke [88] using a GA implementation. In this study, all accepted global minima up to n=150 were located. Comparing these two algorithms, the GA was slower for smaller clusters but had a better size scaling (n^3 versus approximately n^5).

5.3 Historical developments of GA

GAs have been applied to the global cluster geometry optimization problem in the early 1990's [101]. The first application to atomic clusters (Si_4) [110] was closely followed by the first application to molecular clusters (benzene dimer, trimer, and tetramer) [111]. In those first applications, coordinates of the particles were encoded as binary strings. Zeiri [112] was the first to try a real-valued string representation containing the cartesian coordinates of the cluster; he also introduced various genetic operators for this representation. Even more important developments were done by Deaven and Ho [14] by introducing several ideas to increase the efficiency of the GA. They have reduced the number of individuals, m, in the population to very low sizes. In the standard algorithm, *m* individuals are chosen for reproduction, partially weighted by fitness and partially at random. From these *m*/2 pairs, crossover and mutation generates *m* new individuals that constitute the next generation. In the new Deaven-Ho scheme, all possible unique combinations of parent individuals to pairs were realized, and thus $m\times(m-1)$ children were generated. From this intermediate pool, *m* individuals were chosen for the next generation in a sequential fashion, starting with the individual with the lowest energy but then discarding individuals with energies too close to the energies of already selected individuals. Thus, this implementation contained an indirect control over population diversity via energies.

Deaven and Ho also introduced variants of crossover and mutation operators that operated directly on the clusters in coordinate space. Their mating operation is done in this way: Two parent geometries *G* and *G`* producing a child *G``* are selected. A random plane passing through the center of mass of each parent cluster is chosen. The parent clusters are cut in this plane. Child *G``* is assembled from the atoms of *G* which lie above the plane and the atoms of *G`* which lie below the plane. If the child generated in this manner does not contain the correct number of atoms, the parent clusters are translated an equal distance in opposing directions normal to the cut plane to produce a child *G``* which contains the correct number of atoms.

This idea has two advantages:

- It makes it much easier to design new and efficient genetic operators, and to control their effects and usage, since they operate not on abstract strings but directly in the space were the cluster particles live.
- It gets rid of the representation problem by eliminating the need for a representation.

Additionally, Deaven and Ho have used local optimizations (conjugate-gradient or molecular dynamics quenching) to improve each new cluster structure after its formation by the genetic operators. A method having such a mixture of local and global optimizations is called a hybrid method in the GA literature. With this new efficient algorithm, Deaven and Ho optimized carbon clusters up to *n*=60 in a tight-binding (TB) model, and managed to find the fullerene structure without introducing external information.

In 1996, Gregurick et al. [113], also incorporated local optimizations by using a conjugate-gradient method into their implementation, but still worked with a binary string representation. Shortly afterwards, Niesse and Mayne [114] published a "space-fixed" version of a similar implementation integrating the real coding of Zeiri and the hybrid algorithm of Gregurick, which was then applied to Si_n, $n \leq 10$, on an empirical model potential [115] presented by Bolding and Anderson. Niesse and Mayne also concluded that their "space-fixed" algorithm is more than ten times faster in CPU time than the hybrid method of Gregurick. It is unclear if this enhanced efficiency is due to the representation type (binary or real-valued) employed in these two studies. Then, Tomasulo and Ramakrishna [116] applied a GA for the first time at the DFT level.

Subsequent to these efforts, Judson [117] compared the GA with traditional simulated annealing (SA) based on the MC method concluding that the former method is more powerful than the latter. Michaelian [118] proposed a "symbiotic" GA in an application to LJ clusters at selected sizes. In this variant, the optimization of larger clusters is broken down to the optimization of smaller pieces. This is a promising idea to deal with the size-scaling problem. However, this variant has not been successful for some competing structures and structural transition regions. In the same year, Zacharias et al. [119] combined Deaven and Ho style GA with SA for the case of Si_n, n=6, 10, 20, using a TB model. Niesse and Mayne [120] compared binary-coded GA with local optimization and basin-hopping, arriving at the conclusion that traditional binary GA without local optimization is not competitive, while the other two are comparable.

GAs have also found an application area in silicon clusters because of their technological importance. An early attempt was made by Hartke [110,121] to predict the ground state structures of Si_4 and Si_{10} by means of a binary string representation and by a novel GA-optimized growth strategy, respectively. Niesse and Mayne, as mentioned earlier, searched small silicon clusters at the region n=3-10 [115]. Then, Hartke [122] with a real-valued string representation of the cartesian coordinates optimized the silicon clusters with sizes n=4, 6, 7, 10 finding the lowest minimum structures that are accepted in the literature. Iwamatsu [123] simplified the space-fixed GA of Niesse and Mayne and calculated the lowest energy structure of silicon clusters for the region $3 \leq n \leq 15$ by using empirical potentials of Stillinger and Weber (SW) and Gong. In this GA, during the mating process one of the genetic operators is randomly selected among inversion (one child from one parent), arithmetic mean (one child from parents), geometrical mean (one child form parents), and m-points crossover (two children from two parents). In this study, optimizations did not reproduce the ab-initio or DFT results. However, the lowest minimum structures of SW and Gong potentials were found. Hobday et al. [124] used GA to determine the minimum energy structures of silicon clusters in the range n=4-14 by using the Tersoff empirical potential. In addition to silicon clusters, GA was applied to carbon, hydrocarbons, and LJ clusters in this study. However, the structures obtained were different from the literature ones, and generally square based structures were found, for instance for Si_{11} a tri-capped cube structure. Ho et al. [7] used GA successfully to optimize silicon clusters in the region *n*=12-20. In this study, especially for *n*=15, 17, and 18, it is found that clusters are built by a structural motif containing a sequence of stacked Si_9 (tri-capped trigonal prism). However, for *n*≥19, it is found that near spherical cage structures become more stable.

Another successful application of GA to silicon clusters was made by Rata et al. [25]. Contrary to standard GA, in this algorithm there is only a single parent. Additionally two new genetic operators are proposed namely "piece reflection" and "piece rotation". In both of these operators, a cluster is cut by two randomly oriented parallel planes. These divide the cluster into three parts, such that the outer two pieces contain the same number of atoms. In reflection, one of the outer pieces is replaced by reflecting the other through a third parallel plane including the cluster center of mass. In rotation, one of the outer pieces is simply rotated by a random angle about an axis normal to the cutting planes and passing through the cluster center of mass. After each of these transformations, a conjugate-gradient relaxation is performed to take the newly formed cluster to the nearest local minimum, which is then defined as the offspring cluster. A lower energy offspring always replaces the parent cluster, while those with a higher energy replace the parent with a Boltzmann probability based on the energy difference between the parent and offspring. Additionally, in this algorithm, a mutation operator is used in such a way that an offspring is accepted regardless of its energy. This algorithm was tested for LJ clusters and found all known global minima up to 105 atoms. In the case of silicon clusters, the 13≤n≤23 region was studied. In this study, it was found that the Si_9 (tri-capped trigonal prism) structural motif is less favorable. Instead, stable six- and eight-atom subunits appeared as a new structural motif. More specifically, the six-atom ring resembles the six-atom chair in the diamond structure of bulk silicon. Therefore, they claimed that the first structural elements of bulk silicon appear at *n*≤20.

As explained in the above paragraphs, GA studies so far have only attempted to determine cluster structures up to Si_{23}, mostly by suggesting some structural growth patterns. As explained in section 1.1, a very interesting and important size region is just above this limit, around *n*=25, since experiments point to a shape transition region there.

There are also other studies in which different geometry optimization methods have been employed, such as basin-hopping [96], SA [93,94,95], SA-MD [125],steepest descent [59], tight-binding density functional MD [126], MD-quenching [127], and CPMD [128]. These methods also have not been applied to the whole transition region, instead they have mainly been used to study small silicon clusters or a few selected medium-sized ones. For example, in the study with SA-MD [125], some bigger-sized silicon clusters such as Si_{25}, Si_{29}, and Si_{35} have been investigated.

Comparing results obtained from these methods to that obtained from GA studies [7,25], it can be clearly seen that GA results are better. Thus, application of a GA to the problem of global cluster geometry optimization in the important transition region around *n*=25 is imperative.

Therefore, in this study, a GA based algorithm containing two ingredients GAGA and PHENIX has been employed to search the Si_n $4 \leq n \leq 40$ region including the transition region.

5.4 Detailed description of the algorithm used in this study

The whole algorithm used in this study contains two major ingredients namely GAGA and PHENIX. GAGA is a simple but effective scheme to allow for global geometry optimizations at expensive ab-initio levels. It combines global geometry optimizations on a model potential with global parameter optimizations of this model potential, using ab-initio single-point data. The actual global geometry optimization is done by PHENIX, which is based on a Deaven-Ho-style GA [14] but contains not only the genetic operators mentioned in section 1 but also a few new and more powerful ones.

5.4.1 GAGA

In GAGA, global cluster geometry optimization is done on a model potential, in parallel with global optimization of the parameters of this model potential. The latter is done by minimization of the differences between model and ab-initio or DFT energies at the minimum structures found during the global geometry optimization. In this fashion, the expensive global geometry optimization work is transferred to the cheap model potential, leaving only a few local optimizations at the ab-initio level. As the algorithm proceeds, the model potential is fitted progressively better to ab-initio data [122].

This strategy mainly depends on how well the model potential approaches the ab-initio potential. However, a perfect fit between model potential and ab-initio potential is not necessary. It is not even necessary that there is a one-to-one relation between minima on the model potential and minima on the ab-initio potential. Additionally, a correct energy ordering of the minima on the model potential is not required. It is sufficient that at the place where there is the global minimum on the ab-initio potential, there is also an important minimum on the model potential.

If the model potential matches the ab-initio potential perfectly, no parameter optimization is needed and the task of global optimization on the ab-initio potential reduces to a global optimization on the model potential. In this case, however, the computational expense of verifying such a perfect fit between model and ab-initio potentials might be as large as performing a global optimization on the ab-initio potential. If one uses a complex model potential with many parameters, it may become difficult to find reasonable intervals within which parameters can be varied without destroying the suitability of the model potential. Therefore, in practice, the model potentials used in GAGA so far have been standard model potential functional forms of limited complexity. Their appropriateness and performance should be checked, which fortunately can be done rather easily by monitoring the deviation between model energies and ab-initio energies during the GAGA runs.

The GAGA scheme can be summarized in five steps as follows:

- Initialization: calculation of model energies $E_{mod,i}$ and ab-initio energies $E_{true,i}$ for i=1,…,n random geometries.
- Use a GA to optimize the model potential parameters globally, by minimizing the quadratic deviation measure

$$\sum_{i=1}^{n}\left(E_{\mathrm{mod},i}-E_{true,i}\right)^2 \tag{5.1}$$

  for all n geometries.
- Perform a global geometry optimization on the model potential (with the parameters found in Step 2). This leads to a new geometry.
- Calculate $E_{mod,i}$ and $E_{true,i}$ for this new geometry.
- Go to step 2, until the model potential parameters are converged or until no new type of cluster geometry appears.

In GAGA, a GA is used two times, one is for geometry optimization of the cluster and the other one for the parameter optimization of the model potential. This two-times usage of GA is the reason for the name GAGA.

All cluster geometries generated in this fashion can then be refined by local geometry minimizations on the ab-initio level. The hypothesis is that the resulting final structures will correspond to energetically low-lying minima on the ab-initio potential energy surface and will also include the global minimum with a high probability. This was verified in several applications [122,129].

5.4.2 PHENIX

PHENIX is a GA-based global geometry optimization tool that can be run as a stand-alone program or as part of the GAGA strategy. The backbone of the PHENIX algorithm is a Deaven-Ho-style GA as shown in Fig. 5.6. The main fitness criterion in this algorithm is the potential energy of each cluster, generated from the position coordinates of its constituent atoms via a given potential energy function. The main objective is to find the global minimum of this potential energy hypersurface. Local minimizations of the clusters turn out to be essential for an effective operation of the whole algorithm. Therefore, local minimizations are performed in several places by conjugate-gradient or quasi-Newton routines in the production of generation zero, after crossover and mutation, and after each post-processing operation in each generation.

Generation zero is produced by setting all coordinates of all cluster constituents to random numbers or feeding in some already known geometries, followed by a local optimization of each cluster. Random setting of the cartesian coordinates is done within certain upper and lower limit values for particle pair distances. Upper limits are needed to prevent dissociation of the cluster, and lower limits are employed to avoid numerical difficulties in the local optimization process.

From this zeroeth generation, all unique pairs are formed. To each pair, a crossover operator is applied. The crossover operator is the generalization of the simple one-point string crossover operator to the 3-dimensional physical space. In crossover, each cluster in a pair is cut in two parts by a plane, and two children are made by reassembling these parts in a crossover fashion. The cutting plane does not need to pass through the center of mass of the cluster to generate cluster halves. Instead, partitioning of the cluster can deviate from a 50:50 partitioning with a Gaussian distribution around the exact halves, such that a 90:10 partitioning occurs with a non-negligible frequency. Orientation of the cutting plane can be selected in two ways:

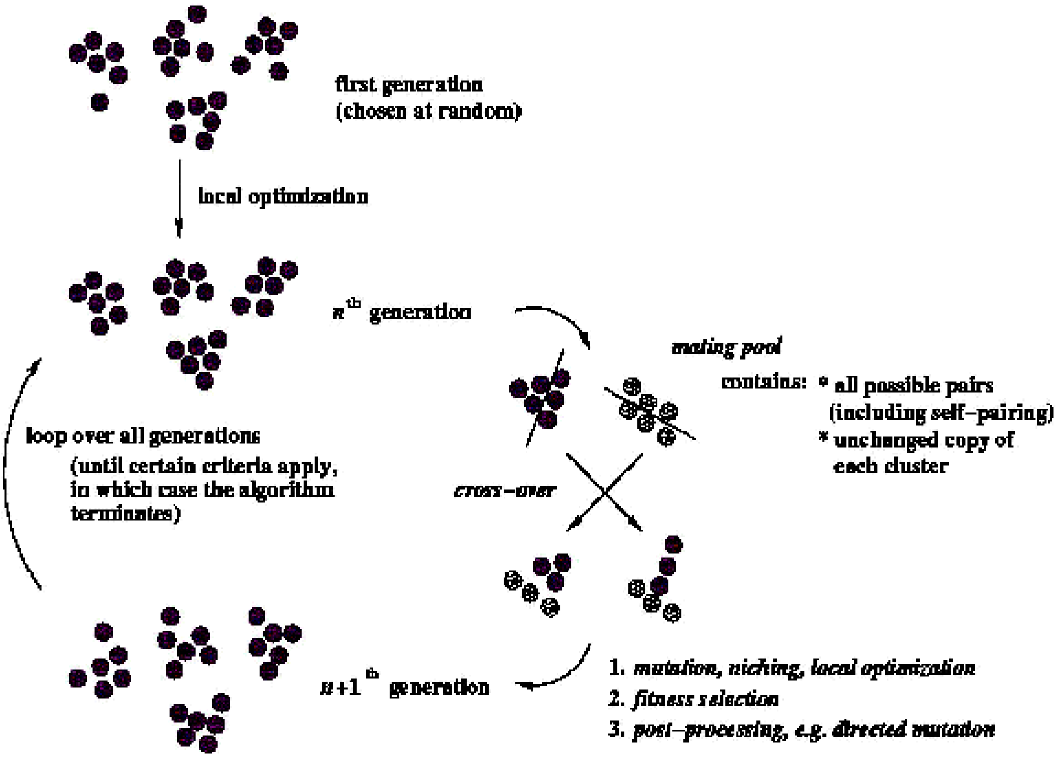

Figure 5.6: Schematic representation of PHENIX.

- the cutting plane is chosen at random for each cluster.
- the cutting plane is oriented deterministically in such a way that it separates the best part of the cluster from the worst part. (Best and worst parts of the

> clusters can be easily determined by summing the pair potential terms of each constituents in these parts.) Then the worst half of one geometry replaces the best half of the other. From the resulting geometries, one has usually a lower energy than both parents, while the other one has a higher energy. (However, with random orientation of the cutting plane, the energies of the children are usually in the range of the energies of the parents.)

It is found that if the cutting plane is oriented deterministically in about 50% of the cases, the overall algorithm performance is improved by 10-20 %. After reassembly of the parts, the distance between them and their relative rotational orientation is optimized, before a full local minimization is applied to the two new child clusters.

After crossover, a mutation operator is applied with given probability to a small number of randomly chosen constituents of the cluster. Each of these is moved by a random distance in a random direction, subjected to the limitations that a move must not place the moved constituent far away from the cluster or too close to another constituent. Each geometry is then locally optimized.

With the help of crossover and mutation operations an intermediate pool containing the newly produced children is formed. All parent geometries are also added to the intermediate pool to ensure that good solutions already found do not get lost again. The selection of the next generation from this intermediate pool is done with three criteria; the usual fitness measure based on the potential energy of each cluster, minimum energy distance, and geometric diversity using niches.

To distribute different types of clusters into niches, a measure is needed that is varying according to the geometric characteristics of the cluster. Niching is very important because it prevents a single geometry type from dominating the whole population [88].

For this study, a new niching criterion is implemented to distinguish directly prolate and spherical geometries. This is based on an analysis of the principal moments of inertia for a given cluster calculated by diagonalization of the moments of inertia tensor. This calculation gives the three principal moments of inertia (*pm* values), namely *pm1*, *pm2*, and *pm3*.

These pm values are evaluated for many geometries including prolate and spherical ones to understand how these values are changing from a spherical to a typical prolate geometry. To arrive at a size-independent criterion, only the ratios *pm2*/*pm1*, *pm3*/*pm1*, and *pm3*/*pm2* are considered. For spherical geometries, it is observed that these ratios give 1, this means that all the three *pm* values are the same, as expected. For typical prolate geometries, ratios of *pm2*/*pm1* and *pm3*/*pm1* give 2 and the ratio of *pm3*/*pm2* gives 1, suggesting that *pm2* and *pm3* are almost the same and different from *pm1*. This different behavior of *pm* values offers us an identification strategy for a given cluster, especially considering the change in ratios of *pm2*/*pm1* or

$pm3/pm1$. The ratio of $pm3/pm2$ is not suitable since it gives almost the same value for both prolate and spherical geometries.

In this current implementation, to identify prolate and spherical geometries, only the $pm2/pm1$ ratio is considered. The value range (the lower limit of the range is 1 and the upper limit is undefined) of this ratio is divided into 10 intervals as shown in Fig 5.7. Limiting the number of individuals with $pm2/pm1$ ratios falling into each of these intervals avoids the dominance of only one species (prolate or spherical) in a generation. This also helps for an unbiased search by having both prolate and spherical structures in a generation. In this implementation, the values for intervals are determined statically and cannot change form one generation to the next.

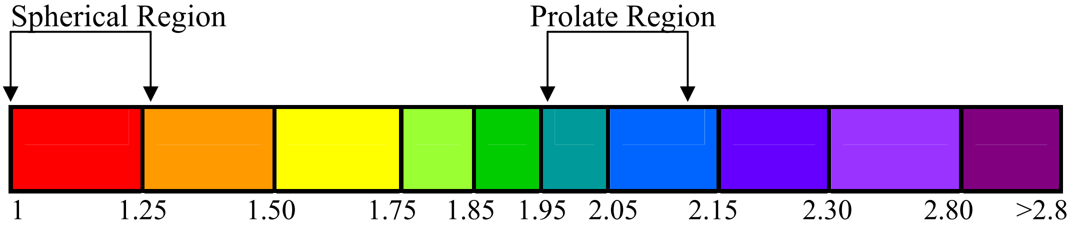

Figure 5.7: Schematic representation of portioning of pm values.

Before the selection process, the whole intermediate pool is sorted by potential energy and additionally each cluster is assigned niching numbers classifying its geometry. Starting from the clusters with the lowest potential energy, each cluster of the intermediate pool is inspected and compared to the clusters already selected into the next generation. If its geometry classification number deviates more than a given difference from the corresponding classification number of the already selected clusters, it is also selected, irrespective of its potential energy, and constitutes a new geometrical niche of its own. If its geometry classification number is closer than a given difference to one of an already selected cluster, it is selected only if the number of clusters in this niche does not exceed a given limit and its potential energy differs from the other clusters in this niche by more than a given amount. There is also a special niche for mutants, which is filled with clusters that were operated on by the mutation operator. There are no other criteria for this niche, but a minimum energy difference criterion also applies. This selection process continues until a desired number of clusters have been selected.

After each new generation is established, it is subjected to a set of post-processing operators, applied in random selection to each cluster to further refine the selected clusters. One post-processing operator is a simple repetition of local minimization but this time with a much tighter threshold.

Another post-processing operator is directed mutation. Often the algorithm quickly converges to the vicinity of the correct global minimum solution but then takes a long time to move a very small number of misplaced constituents into their optimal places. And sometimes, there might be no change in energy in any member of the population from one generation to the next. These situations can be fixed by the application of the directed mutation operator. A very small number of the worst constituents is removed from the cluster and re-introduced into the most promising positions. The worst constituent and the best vacancy in the cluster are located by using the distribution of the total potential energy into individual contributions of constituents.

The production of new generations is cycled until the termination criterion is satisfied. If the best energy does not change significantly over several generations, then the algorithm stops, giving the desired number of geometries and their corresponding energies.

6 Interatomic interactions

Interatomic interactions within a given system can be calculated in a number of ways, such as using an empirical potential, a tight-binding (TB) approach or any ab-initio method. Empirical potentials are mathematical expressions containing parameters that are fit to experimental data. In TB and ab-initio methods, interactions arising from the existence of electrons are evaluated by fist-principle calculations (by solving the Schrödinger equation). The main difference between the TB approach and ab-initio methods is that in the TB approach, the exact many-body Hamilton operator is represented with a parametrized Hamiltonian matrix, where the matrix elements are fitted to the electronic structure of a suitable reference system. In this way, the TB approach allows to perform fast calculations compared to ab-initio methods. However, using an empirical potential instead of a TB approach will reduce the computational cost again, by several orders of magnitude. Due to these main characteristics, both empirical potentials and TB approaches are successfully derived for and applied to silicon clusters. In Chapter 6, interatomic interactions are discussed in detail. Especially, the most important empirical potentials (Stillinger-Weber based and Tersoff based potentials) are described.

6.1 Empirical potentials

Empirical potentials (sometimes referred to as analytic or classical potentials) are simplified mathematical expressions that attempt to model interatomic interactions for a given system. Calculating the potential energy by evaluating the analytic expression of an empirical potential is several orders of magnitude less expensive than by performing an ab-initio quantum chemistry calculation. Especially, empirical potentials can be used in the areas of MC and MD simulations to examine the structural and dynamical behavior of very large systems such as crystal growth and surface reconstruction, or, as in this work, to reliably find global minimum structures of clusters of non-trivial size. However, standard empirical potentials typically involve a significant loss of accuracy compared to quantum-mechanical methods. Another drawback of commonly used empirical potentials is that they have difficulties to reproduce some quantum-mechanical effects such as Jahn-Teller distortions especially emerging for small clusters. This might be overcome if one allows considerably higher complexity of the empirical function. As a result, the requirement for one-to-one correspondence between the local minima on the empirical potential energy surface and the local minima on the quantum-mechanical potential energy surface is difficult to fulfill.

The construction of an empirical potential is not an easy task because such a potential must have as wide a range of fitting data as possible, should be able to accurately reproduce the fitting data and to describe some structures not included in the fitting data. Last but not least, it must be computationally effective.

Simple empirical potentials such as LJ or Morse potentials can be successfully applied to rare gas atoms, simple metals, and highly ionic systems. However, in the case of semiconductors such as silicon, these traditional potentials cannot describe the directional aspects of covalent bonding. For this reason, many more elaborate empirical potential have been proposed in the literature.

Many of these potentials can be divided into three main categories, namely Stillinger & Weber (SW)-type, Tersoff-type (based on the second-moment approximation), and potentials derived directly from ab-initio data. Also, many other potential are proposed for silicon that do not fit into these categories.

6.1.1 SW-type empirical potentials

The SW [130], Gong [131], Mistriotis [58,132], and Modified Mistirotis potentials belong to this potential class. In these potentials, the total potential energy is expanded into many-body terms. Based on the Keating model [133], any potential energy function Φ describing interactions among N identical particles can be exactly expanded into one-body, two-body, three-body, etc. contributions as follows:

$$\Phi(1,...,N) = \sum_{i} \upsilon_1(i) + \sum_{\substack{i,j \\ i<j}} \upsilon_2(i,j) + \sum_{\substack{i,j,k \\ i<j<k}} \upsilon_3(i,j,k) + ... + \upsilon_N(1,...,N) \tag{6.1}$$

In the above expression, υ_1 describes the external potential and generally it is called the one-body term. υ_2 (two-body) and υ_3 (three-body) describe the interactions between atoms *i-j* and *i-j-k*, respectively, and so on. There are at least two motivations to use this expansion: One is the hope that the first few terms of it are sufficient. This is actually supported a priori by ab-initio calculations on many different systems, indicating that all terms beyond the five-body term usually are negligibly small and that in many cases even the four- and five-body terms may be omitted. A second motivation is the hope that functional forms for these individual terms may be easier to construct and to fit than for the full potential.

6.1.1.1 SW potential

Stillinger & Weber [130] approximated the potential energy function *Φ* as a combination of two- and three-body terms in order to reproduce the strong and directional bonds in the silicon crystal. In reduced units, these two- and three-body terms are of the form;

$$\upsilon_2\left(r_{ij}\right)=\varepsilon\ f_2\ \left(r_{ij}/\sigma\right)$$
$$\upsilon_3\left(r_i,r_j,r_k\right)=\varepsilon\ \ f_3\ \left(\ r_i/\sigma,r_j/\sigma,r_k/\sigma\ \right) \tag{6.2}$$

where ε is chosen to give f_2 depth -1 and σ is chosen to make $f_2\left(2^{1/6}\right)$ vanish.
A two-body functional form containing five-parameters was selected as follows;

$$f_2(r)=\begin{cases}\mathrm{A}\left(\mathrm{B}r^{-p}-r^{-q}\right)\exp\left[(r-a)^{-1}\right], & r<a\\ 0, \ r\geq a\end{cases} \tag{6.3}$$

where A, B, p, and q are positive. This pair potential is cut off at $r=a$.

Then, a repulsive three-body functional form is chosen;

$$f_3\left(r_i,r_j,r_k\right)=h\left(r_{ij},r_{ik},\theta_{jik}\right)+h\left(r_{ji},r_{jk},\theta_{ijk}\right)+h\left(r_{ki},r_{kj},\theta_{ikj}\right) \tag{6.4}$$

where θ_{jik} is the angle between the vectors r_{ij} and r_{ik}. The function h containing two parameters ($\lambda,\gamma>0$) and the same cutoff a can be written as follows;

$$h\left(r_{ij},r_{ik},\theta_{jik}\right)=\lambda\exp\left[\gamma\left(r_{ij}-a\right)^{-1}+\gamma\left(r_{jk}-a\right)^{-1}\right]\left(\cos\theta_{jik}+1/3\right)^2 \tag{6.5}$$

If θ_{jik} is the ideal tetrahedral angle (θ_T), then the three-body contribution will be zero (see Fig. 6.1). Otherwise it always increases the total energy. In the three-body term, the parameter λ controls the amplitude of the three-body term.

Bulk properties, such as the cohesive energy for the diamond lattice (ground-state structure of bulk silicon), the melting temperature of diamond, and the nearest neighbor distance determined by this potential are in good agreement with experimental data. Since the potential is derived only from bulk silicon, it gives a poorer description for under- and over-coordinated silicon. For this reason, it failed to reproduce small silicon structures where under- and over-coordination occurs frequently.

6.1.1.2 Gong potential

Gong [131] has compared the bond-angle distributions of silicon clusters obtained from the SW potential and from Density Functional Theory (DFT) calculations in the Local Density Approximation (LDA). In this comparison, in the results of the LDA, there is a large peak at 60° and a smaller peak at about 100°-110°, but in the results of the SW potential, there is only one broad peak at about 100°-110°. He has also noticed that in the bond-angle distributions of liquid and amorphous silicon, there is also a big peak at 60°. From this comparison, it became clear that the SW potential could be improved by enforcing a lower energy for angles at ~ 60°. Unfortunately, this could not be described by the three-body term of the SW potential (see equation 6.5), since it has a large value at an angle of ~ 60°. Therefore, to lower the energy at an angle of ~ 60°, the three-body term of the SW potential has been modified by replacing the angular part by a more complicated trigonometric function as follows,

$$\lambda_1(\cos\theta + 1/3)^2\left[(\cos\theta + c_0)^2 + c_1\right] \tag{6.6}$$

where c_0 and c_1 are new parameters that are determined by fitting to the phase diagram of bulk silicon. In Fig. 6.1, the behavior of the angular part of the three-body terms of the SW and Gong potentials is displayed. It is clear from Fig. 6.1 that Gong's potential gives a lower energy for an angle of ~ 60° and ~ 100°-110°.

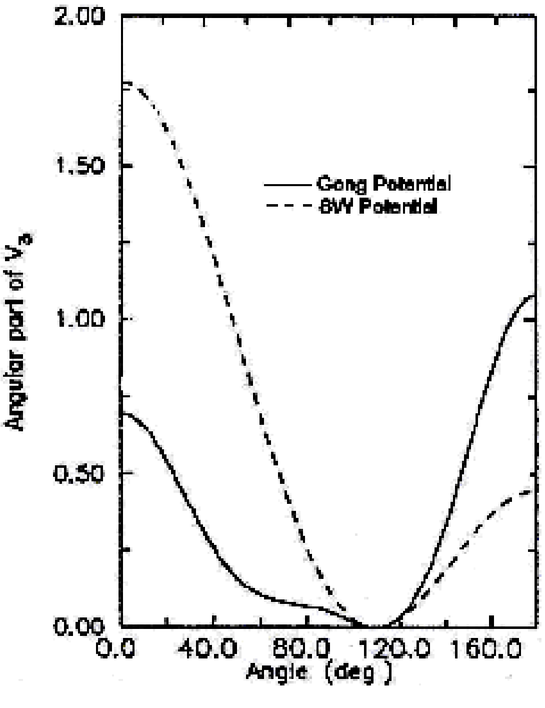

Figure 6.1: The change of the angular part of the SW and Gong' potential with angle. The solid line represents Gong's potential and the dashed line represents the SW potential. Upon changing the three-body angular form of the SW potential, at an angle of ~ 60° and ~ 110° the Gong potential has lower energy values.

With this new potential, the diamond structure has been found to have the lowest energy. In addition, the total energies of other phases (sc, bcc, β-tin, simple hexagonal, fcc) are reasonably close to that of diamond. Calculated bulk properties such as lattice constant and bulk modulus are also very similar to results of the SW potential and they are in good agreement with the experimental data.

To study the structural properties of small silicon clusters, Simulated Annealing Molecular Dynamics (SA-MD) has been performed [131]. In the results, there is a better agreement to literature data than for the SW potential. More specifically, for

Si_4, a tetrahedron and a flat rhombus are found at almost the same energy, while a square is found with the SW potential. Additionally, for Si_5 and Si_6, a trigonal bipyramid and a one-capped distorted trigonal bipyramid are the lowest energy structures for the new potential, respectively. However, the SW potential found a pentagon for Si_5 and a trigonal prism for Si_6. The most fascinating result is for Si_{10} for which the tetracapped trigonal prism (TTP), known as the lowest energy structure in the literature, and also a bicapped tetragonal antiprism having almost the same energy are found. Additionally, the Gong potential predicts a distorted tri-capped trigonal prism for Si_9.

6.1.1.3 Mistriotis potential

In the Mistirotis potential [58,132], the same two-body term is used as in the SW potential. Additionally, the functional form of the three-body term of the SW potential is changed and a four-body term is added. Mistriotis claimed that this potential models small silicon clusters in the size range of 7-100 atoms, where π-bonding is not significant because of a large degree of coordination, without losing some important properties of bulk silicon.

In the Mistirotis potential, the three-body term has been constructed in a similar fashion as the Sorbie-Murrell function using ab-initio data of Si_3. Then, Mistriotis obtained the structures and energies for larger clusters using this new three-body function. However, a disagreement was found and this is attributed to the predominance of π bonding in small silicon clusters (containing 2-4 atoms). It is believed that for clusters with more than six atoms, the bonds are better described with sp^3 orbitals. For this reason, Mistriotis has obtained unsatisfactory results with the new three-body function. Upon this failure, Mistriotis decided to produce a potential which is valid for clusters with more than four atoms, surfaces, and bulk silicon. For this purpose, Mistriotis modified the Stillinger-Weber potential. In particularly, Mistriotis used a different angular dependence in the three-body term. This angular dependent function has the form of

$$\lambda\left\{1-\exp\left[-Q(\cos\theta+1/3)^2\right]\right\} \tag{4.7}$$

where the parameter Q only controls the amplitude of the angular part of the three-body term, while λ determines the amplitude of the whole three-body term. In the functional form of the SW potential (equation 6.5) only one parameter (λ) is used for these purposes. With this new angular form of the three-body term, the energies of the ground states of the clusters approach those found from ab-initio calculations.

Mistriotis noticed that the contribution of the repulsive three-body term to the energy of the clusters increases slower than what is expected from the ab-initio results, as the average coordination number per atom is increasing. To compensate this discrepancy Mistirotis formulated a four-body term containing only first neighbors since the number of four-body terms increases with cluster size faster than that of the three-body terms.

After these modifications, the three-body term is of the form;

$$h\left(r_{ij}, r_{ik}, \theta_{jik}\right) = \lambda_3 \exp\left[\gamma\left(r_{ij} - R\right)^{-1} + \gamma\left(r_{jk} - R\right)^{-1}\right] \left\{1 - \exp\left[-Q\left(\cos\theta_{jik} + 1/3\right)^2\right]\right\} \tag{6.8}$$

And the four-body term is as follows;

$$\upsilon_4\left(r_i, r_j, r_k, r_l\right) = g_{ijkl} + g_{jikl} + g_{kijl} + glijk \tag{6.9}$$

where

$$g_{ijkl} = \lambda_4 \exp\left\{\gamma \left[\left(r_{ij} - R\right)^{-1} + \left(r_{ik} - R\right)^{-1} + \left(r_{il} - R\right)^{-1}\right]\right\} \times \\ \left(1 - \exp\left\{-Q\left[\left(\cos\theta_{jik} + 1/3\right)^2 + \left(\cos\theta_{jil} + 1/3\right)^2 + \left(\cos\theta_{kil} + 1/3\right)^2\right]\right\}\right) \tag{6.10}$$

With this new interatomic potential, Mistriotis determined the ground state structures of small silicon clusters using the SA method. Unfortunately, some of the proposed structures differed from the accepted structures in the literature, especially for Si_9 and Si_{10} as distorted tricapped octahedron and distorted tricapped trigonal prism with an additional cap atom, respectively. Furthermore, this potential could not give the correct ground state energies of bulk silicon modifications except for the diamond structure.

Then, Mistriotis added the second-neighbor interactions to the four-body term to describe surface properties and other bonding characteristics of silicon more precisely. For example, the diamond structure is more stable than the wurtzite structure for silicon. The energy difference between these two structures can only be explained by the inclusion of second-neighbor interactions. After this addition, the resulting four-body term becomes

$$\upsilon_{4n} = gn_{ijkl} + gn_{jikl} + gn_{kijl} + gn_{lijk} \tag{6.11}$$

where

$$gn_{ijkl} = \lambda_{4n} \exp\left\{\gamma \left[\left(r_{ij} - R\right)^{-1} + \left(r_{jk} - R\right)^{-1} + \left(r_{kl} - R\right)^{-1}\right]\right\} \times \\ \left(1 - \exp\left\{-Q\left[\left(\cos\theta_{ijk} + 1/3\right)^2 + \left(\cos\theta_{ijkl} - 1/3\right)^2\left(\cos\theta_{ijkl} + 1\right)^2 + \left(\cos\theta_{jkl} + 1/3\right)^2\right]\right\}\right) \tag{6.12}$$

where θ_{ijkl} is the angle between the vectors r_{ji} and r_{kl}. This new four-body term depends on the dihedral angle between two next-nearest-neighboring bonds. Therefore it models a longer-range interaction.

6.1.1.4 Modified Mistriotis

In this current study, after failing to get satisfactory results with the Gong and the Mistriotis potentials, the Mistriotis potential (including the second-neighbor interactions) has been modified by following Gong's modification of the SW potential.The functional form of the three-body term of the Gong potential (equation 6.6) was added to the three-body term of the Mistirotis potential (equation 6.8), increasing the complexity of the three-body term. The other two- and four-body terms of the Mistirotis potential are kept the same. In the resulting potential, the number of parameters is increased from 11 to 13 with addition of c_0 and c_1.

The modified three-body term is of the form;

$$\begin{gathered} h\left(r_{ij}, r_{ik}, \theta_{jik}\right) = \lambda_3 \exp\left[\gamma\left(r_{ij} - R\right)^{-1} + \gamma\left(r_{jk} - R\right)^{-1}\right] \times \\ \left\{1 - \exp\left[-Q\left(\cos\theta_{jik} + 1/3\right)^2 \left[\left(\cos\theta_{jik} + c_0\right)^2 + c_1\right]\right]\right\} \end{gathered} \tag{6.13}$$

The resulting potential has given all the accepted ground state structures in the size range of n=5-10 as described in the study of Tekin and Hartke [134].

6.1.2 Tersoff-type potentials

The main feature of these potentials is that the bonding is explained via a bond-order concept that depends on the local environment of the atom. The potentials of Tersoff [135,136,137], Dow & Baskes [138,139], Cai [140], Bolding & Anderson [59], and Conrad & Scheerschmidt [141] can be put in this group.

The second-moment approximation can lead to the bond-order concept. According to the moments theorem, the second moment is related to the number of nearest neighbors. Furthermore, the bond energy for each atom arising from the molecular orbitals is approximately proportional to the square root of the number of neighbors. This is called the second-moment approximation. To develop an empirical potential from the second-moment approximation, a definition of neighboring atoms is needed. To do this, Finnis and Sinclair assumed that the coordination could be replaced with a sum of functions that decay exponentially with distance. Tersoff-type potentials basically are a modification of these functions [142].

6.1.2.1 Tersoff potential

The Tersoff potential [135,136,137] depends on the local environment of the atom. The total energy E of the system can be written as;

$$\mathrm{E} = \sum_i \mathrm{E}_i = \frac{1}{2} \sum_{i, j \neq i} \upsilon_{ij} \tag{6.14}$$

where E_i is the site energy for site i, υ_{ij} is the interaction energy between atoms *i* and *j*. υ_{ij} can be written as a Morse-like functional form as follows;

$$\upsilon_{ij} = f_c(r_{ij}) \left[\mathrm{A} \exp(-\lambda_1 r_{ij}) - \mathrm{B}_{ij} \exp(-\lambda_2 r_{ij}) \right] \tag{6.15}$$

where r_{ij} is the distance between atoms *i* and *j*. *A*, *B*, λ_1, and λ_2 are all positive parameters, with $\lambda_1 > \lambda_2$, and f_c is the cutoff function. In this equation, the first term represents the repulsive interaction while the second term describes the bonding behavior. B_{ij} defines the bond order, which is a monotonically decreasing function of the coordination number, depending on the local environment. Inclusion of B_{ij} into the second term was firstly proposed by Abell [143]. Although this potential seems to have only two-body interactions, many-body interactions are effectively included in the second term.

There are 13-parameters in the Tersoff potential and these are fitted to bulk silicon (diamond) and other important ground state structures of the bulk. Unfortunately, this parameter-set described the elastic properties of silicon worse than the experimental results. As a result, Tersoff made a new fitting for the parameter set that can accurately reproduce the elastic properties of silicon. Also, this new parametrization improved the description of the structure of the liquid and amorphous states. However, the energies of some surface geometries are less accurate than for the first parametrization.

6.1.2.2 Dow & Bakes potential

Dow and Baskes [138,139] developed the Embedded-Atom method (EAM) to describe the interactions in metals. This method is a semi-empirical method based on the local electron density theory. Baskes [144] extended the EAM to describe the covalent bonding by adding the gradient and higher-order terms to the local electron density. With this modified EAM, diamond is found as the ground state structure of bulk silicon and other properties of the bulk phase are reproduced well.

6.1.2.3 Cai potential

Inspired by the EAM, Cai [140] proposed a new potential. In the EAM, the total energy of a system can be written as a sum of pair interactions of atoms *i* and *j* and the embedded-atom energy arising from the local electron density of atom *i*. For a system with two atoms, *i* and *j*, there is only one contribution of the electron density to atom *i* from atom *j* or vice versa. If the third atom *k* is added to the system the contribution of electron density from atom *j* will be effectively screened by atom *k*. The role of the atom *k* upon atoms *i* and *j* can be represented by the screening function. The resulting potential also reproduced some of the important properties of silicon.

6.2 Bolding & Anderson potential

Bolding and Anderson (BA) [59] proposed a potential that is a generalization of the Tersoff potential. The bond-order term B_{ij} in the second term of the Tersoff potential (see equation 6.15) is now expressed as a sum of π - and σ - bonding terms which are independently influenced by the local environment. The parameters in this potential are fitted to both small silicon clusters and bulk silicon. To compare the structural properties of small silicon clusters for various potentials, these authors performed geometry optimizations with the steepest-descent method including the SW, Tersoff, and Biswas & Hamann (BH) [145,146] potentials. In their results, the BA, Tersoff and the SW-BH potentials seem to behave very similarly, probably due to the fact that these pair potentials have very similar forms. Unfortunately, except for Si_3, Si_4, and Si_7, the BA potential could not reproduce the structures accepted in the literature. However, an improvement over the SW and BH potentials could be achieved. More specifically, for example in the case of Si_9, a tri-capped trigonal prism is found as the ground state structure, which is very close in energy to a one-atom capped sandwich of two rhombi, while a one-capped distorted cube is found for the SW potential and a one-capped distorted square antiprism for the BH potential. The situation is similar for the cases of Si_6, Si_8, and Si_{10}. Bulk silicon properties such as the cohesive energy, elastic constants and lattice constant agree with the experimental data. Although there is no fitting to any phonon-dispersion data, the BA potential found phonon frequencies similar to those found with the SW potential. Additionally, this potential correctly predicts the phase transition from the diamond to β-tin structure of bulk silicon at high pressure.

6.2.1.1 Conrad & Scheerschmidt potential

Similar to Tersoff's bond-order potential, Conrad and Scheerschmidt [141] developed a potential in which the bond-order term B_{ij} (see equation 6.15) of the Tersoff potential is described by the tight-binding second-moment approximation. The second-moment is related to the number of nearest neighbors according to the moments theorem in such a way that the local electronic bond energy for each atom is approximately proportional to the square root of the number of neighbors. Actually, in this respect, the potentials by Baskes, Cai, Bolding & Anderson, and Tersoff can be regarded as approximations of the second-moment approximation.

6.2.2 Potentials derived form ab-initio data

Another trend in the development of empirical potentials is to rely less on assumed functional forms for various terms of the potential, combined with fitting to experimental data, and to replace all this by a more extensive use of ab-initio results.

For this trend, the potentials by Bazant & Kaxiras [147] and Rasammy, Valiev, and Fernando [148] can be seen as pioneering steps.

6.2.2.1 Bazant & Kaxiras potential

Bazant and Kaxiras [147] used inverted ab-initio energy data, which can be as little as the cohesive energy curve of one phase of bulk silicon, to obtain so-called “parameter-free” many-body potentials. To construct this potential, there is no need to make a fitting to any defect structures, energies of other phases of the bulk silicon, and any surface reconstructions, contrary to the cases of the SW and Tersoff potentials. Transferability of such a potential can then be checked by repeating the procedure for other bulk phases.

6.2.2.2 Rasammy, Valiev, and Fernando potential

Another approach is made by Rasammy, Valiev, and Fernando [148] to generate an interatomic potential from first-principle calculations via the effective-action formalism. In the RVF potential, the system is described by an ion-pair density leading to an effective two-body potential. This approach is quite analogous with density functional theory (DFT) where the description of the system is based on the electron density. This potential contains the effects of three- and higher-body terms and reproduces the exact pair density of the fully interacting system. The generation of the potential starts with a guess of the potential. Several configurations are generated with this guessed potential in Monte Carlo (MC) or Molecular Dynamics (MD). Energies of each configuration are calculated at the ab-initio level. Then, the difference between the energies obtained from the ab-inito calculations and those obtained from the guessed potential is minimized.

6.2.3 Other important potentials

Tremendous interest has been devoted to develop empirical potentials describing the covalent bonding in silicon, and many of them do not fit into the above categories. The most important ones are Pearson, Takai, Halicioglu, and Tiller [149], Li, Johnston, and Murrell [150], Biswas and Hamann [145,146], Khor and Das Sarma [151], and Chelikowsky, Philips, Kamal and Strauss [152,153].

Pearson, Takai, Halicioglu, and Tiller (PTHT) [149] proposed a potential with a long-range two-body term and a nonseparable three-body term to describe accurately the properties of non-tetrahedral forms of silicon. However, the PTHT potential found incorrect cohesive energies for the bulk silicon structures. But it succeeded to simulate the phase transition from the diamond to the β-tin structure of bulk silicon at high pressure, like the BA potential.

Another interatomic potential is proposed by Li, Johnston, and Murrell (LJM) [150] containing only two- and three-body terms. There are 14-parameters in the LJM potential. They are fitted to phonon frequencies and elastic constants of the diamond structure and a number of properties of the other stable structures of bulk silicon. The LJM potential has been tested if it correctly reproduces the structures of small silicon clusters. It seems that the LJM potential tends to give open geometries in the size range of n=4-8. Specifically, a square, a square prism, a one-capped square prism, a two-capped square prism and a cube structure is found for Si_4, Si_5, Si_6, Si_7, and Si_8, respectively. Unfortunately, neither of these structures is the lowest-energy structure accepted in the literature.

Biswas and Hamann [145,146] developed an empirical potential containing two- and three-body terms (BH). All the parameters are fitted to the LDA results of several ground state structures of bulk silicon by a least-squares method. They have calculated energies of structural isomers of bulk silicon with their potential and with the LDA, the SW, and PTHT potentials [149]. Compared to the results of SW and PTHT potentials, the BH potential produces better agreement with the LDA results. They have also compared the energy of a four-layer Si(111) construction calculated with these methods. They have found that the BH potential is in good agreement with the LDA results whereas the SW and PTHT potentials deviate from the LDA results, giving higher and lower energies, respectively. The three body term of the BH potential has a very weak dependence on the angle for $90^\circ \leq \theta \leq 180^\circ$, with a minimum at $\theta \sim 110°-115°$. There is a very strong repulsion between bonds for $\theta \leq 70°$. The minimum of the two-body potential, ~2.77 A°, is quite small compared to the minimum of SW potential, ~3.77 A°. It seems that their two-body fitting to Si_2 did not yield satisfactory results. With a modification of the three-body term, the BH potential [146] agreed much better with the LDA results for the Si(111) construction. However, the bulk structures are much less accurately fit than with their previous potential. Biswas and Hamann performed structural optimizations of small silicon clusters with a combination of steepest-descent and simulated annealing method. However, results obtained by both versions of their potential do not seem in agreement with the literature results. For example, they have found a square and a pyramid for Si_4 and a pentagon for Si_5. The tetra-capped octahedron structure for Si_{10} that does not seem to be the ground state structure in their calculations (their ground state structure is a two-capped twisted cube (decahedron) is known as a very important low-energy minimum structure for $Si_{10.}$

Khor and Das Sarma (KDS) [151] constructed a potential following Abel [143] to deal with large bond-angle distortions of the tetrahedral geometry. The KDS potential uses a slightly different functional form and parameter set for modeling the surface and bulk crystal behavior. The functional form of the KDS potential is not only designed for Si but also for C and Ge and it gives the correct cohesive energies and equilibrium distances for a range of structures of bulk silicon such as diamond, graphite, β-tin.

Chelikowsky, Philips, Kamal and Strauss [152,153] proposed a seven-parameter potential which they call classical force field (CFF). With the addition of four backbonding parameters, designed to reduce surface forces, the structures obtained for small silicon clusters reasonably agree with the literature ones. Nevertheless, a tetrahedron and an octahedron are found for Si_4 and Si_6, respectively, contrary to the literature. Moreover, this potential predicts an icosahedral growth pattern for the medium-sized silicon clusters, with $10<n<20$. This prediction is also not in agreement with the literature.

In summary, much effort has been made to construct empirical potentials for silicon. Some of them describe bulk properties such as cohesive energies, lattice and elastic constants of the ground state bulk structures in very good agreement with the experimental data. Other models simulate the melting behavior accurately. And again others produce reasonable agreement with the best cluster structures proposed in the literature. Nevertheless, none of the empirical potentials proposed in the literature is able to describe all the properties of small silicon clusters and bulk silicon in consistently good agreement with ab-initio data and/or experimental values. Therefore, unfortunately, it has to be expected that all of them will have difficulties in reproducing the structural transitions expected to occur between small clusters and the bulk. For this reason, we exercised considerable care in using some of these potentials: First, we made sure that the structures of the smallest silicon clusters (up to at least n=10) were reproduced sufficiently well, after global refitting of the parameters. This should ensure that the functional form of the potential is flexible enough at least in this size range. For larger clusters, we then refitted the parameters once again, in a size-dependent fashion, to ensure good performance even for changing structural preferences.

More specifically, in this study, the SW, Gong, and Mistriotis potentials are used because these potentials seem fairly successful to reproduce the structures of small silicon clusters. And we expected them to be able to favor the tetra-capped trigonal prism structure (TTP) for Si_{10} as the ground state structure. This cluster size is selected as a test case for those empirical potentials because the accepted ground structure seems a challenge for an empirical potential and there are some low-lying isomers that are very close in energy to the TTP structure. Additionally, their easy implementation is another attractive point.

However, none of these potentials reproduced the TTP structure for Si_{10}. At this point, a promising modification to the Mistriotis potential has been done. With this modified potential, we have found the TTP structure as the ground state structure of $Si_{10.}$ Besides, other silicon clusters up to the size n=10 are fairly well reproduced (see Chapter 7).

6.3 Tight-binding approach

In the tight-binding (TB) scheme, electronic structure is modeled in a simplified parameterized way. Nevertheless, it incorporates quantum effects going beyond classical empirical potentials. For this reason, TB can be considered as a link between classical concepts and full-scale modeling of the quantum nature of chemical bonding. Because of its working principle, TB is very similar to semiempirical methods.

The standard TB method expands the eigenstates of a system in terms of an orthogonalized basis of atomic-like orbitals, representing the exact many-body Hamilton operator with a parametrized Hamiltonian matrix, where the matrix elements are fitted to the electronic structure of a suitable reference system. Then, the resulting Schrödinger equation is solved. A small number of basis functions are usually used, those roughly corresponding to the atomic orbitals in the energy range of interest. For example, when modeling graphite or diamond, the *1s* orbitals are neglected, and only *2s* and *2p* orbitals are considered [154].

The TB approach has been demonstrated to work very well for covalently bonded systems (C, Si, Ga, Ge, In, etc.) and transitional d-band metals. The TB method can be employed for calculating characteristics of both periodic and amorphous solids, as well as atomic clusters. The main advantage of this method is that it is computationally efficient.

At first, TB was intended for investigations of the electronic band structure of periodic solids. Later, TB ideas have been generalized to an atomistic total energy method. To make this transition, in the TB scheme, the total energy as a function of all atomic coordinates can be written as;

$$E_{tot} = E_{bs} + E_{rep} \tag{4.16}$$

where E_{bs} (band-structure energy) is the sum over the occupied electronic eigenstates of the TB Hamiltonian and E_{rep} stands for a short-range repulsive two-particle interaction, including the ionic repulsion and corrections due to approximations made in E_{bs}. The repulsive interactions versus distance may be determined in a parametrized functional form for reproducing cohesive energies and elastic constants (bulk-moduli) for crystalline systems.

Hence, such a TB calculation and its results clearly depend on the parametrization scheme used, and the transferability to different systems and problems is rather limited. In order to reduce the difficult parametrization within a multiconfigurational space and to achieve general chemical transferability at a high accuracy, more sophisticated, yet efficient, TB schemes have been developed.

Additional to the derivation of the TB model from HF theory, it can also be derived from DFT. For example, the Hamiltonian and overlap matrices from a DFT-LDA-derived local orbital basis and some integral approximations can be used to avoid using any empirical parametrization. This method includes first-principle concepts in relating the Kohn-Sham orbitals of the atomic configuration to a minimal basis of the localized atomic-like valence orbitals of all atoms. Each valence orbital is represented by a set of twelve Slater-type functions.

TB schemes can be either orthogonal or non-orthogonal. Orthogonal TB schemes assume that the orbitals of each atom remain orthogonal at all times, while nonorthogonal schemes treat their overlap explicitly, by introducing additional matrix elements that are used to construct an overlap matrix.

The TB method is a very popular approach for the simulation of materials. It has advantages over both empirical potentials and more accurate first-principle calculations. By treating the electronic structure of the system in a very simplified way, TB incorporates many-body quantum effects better than empirical potentials. Additionally, its simplicity compared to the first-principle methods allows to study larger systems that are not accessible with first-principle calculations due to the much higher computational demands. However, the biggest drawback in TB approach seems its transferability. For example, a parametrization suitable for Si in the diamond structure is unlikely to be adequate for simulating liquid Si, unless information concerning the liquid phase is incorporated in the data used to construct the parametrization.

As mentioned earlier, silicon has also been modeled by tight-binding schemes. The study of Edwards et al. [155] can be given as an example. In this study, a tight-binding model including a minimal (*s* and *p*) basis and a repulsive pair potential is introduced for silicon. The parameters in this model are fitted to ab-initio force and energy data on clusters, liquid, and amorphous systems as well as experimental elastic constants, phonon frequencies, and Grüneisen parameter values. The resulting tight-binding potential reproduced fairly well the properties of bulk silicon compared with experimental data. This model also reproduced the ground state of silicon structures between n=2-5. For the crystalline phase, the diamond structure is found as the lowest energy structure. The transition from diamond to β-tin at low pressures is also seen, while the transition pressure is found to be too high. Additionally, this model does not accurately reproduce electronic levels.

7 Computation details

In this Chapter, details of theoretical computations performed in this thesis are given. First, in section 7.1, why DFT has been used, and with which functional of it has been used for the local reoptimization of structures obtained from the model potentials. DFT methods do not quite reach the level of agreement with experimental data that electron correlation methods can attain. Therefore, to investigate the effect of electron correlation, single point energy calculations at LMP2 level have been performed for optimized structures at DFT level. Details of LMP2 calculations are given in section 7.2. For fast DFT calculations for medium-sized silicon clusters, the RI-DFT method is used. Details of RI-DFT calculations are given in section 7.3. Finally, information about all quantum chemistry software and hardware used for all calculations performed in this thesis are given in section 7.4.

7.1 DFT

DFT has become one of the most popular quantum chemical methods in the last few years. For the investigation of electronic structures, DFT offers a less expensive alternative than the conventional correlation methods (MPn and Coupled Cluster). The accuracy of DFT with gradient-corrected and hybrid functionals is reaching that of MP2 for some cases. However, DFT is also known to have problems in certain areas, for example for reactions involving hydrogen atoms DFT fails to predict reaction barriers. DFT has also problems in the treatment of long-range interactions (e.g. van-der-Waals interactions). Considering these facts, one should handle DFT as a method that should be applied with care [156].

In the literature, many silicon cluster studies have used DFT approaches, mostly employing the LDA (local density approximation) [41,60,126,123] and GGA (generalized gradient approximation) [41,59,60,157]. Accumulated experience [158], however, recommends hybrid functional approaches; they yield more reliable energies and structures, with still modest requirements on the basis. Therefore, DFT calculations up to $n \leq 15$ were performed with the B3LYP functional, using a 6-31G* basis set, by treating all electrons. Beginning with $n \geq 16$, a (3s3p1d) basis set with an effective core potential (ECP) has been used instead. In the ECP approximation, the core electrons are replaced by an effective potential. This saves computational expense but may sacrifice some accuracy.

There are also performance tests for different DFT functional in the literature [159] supporting the use of a hybrid functional to obtain better results. As an example, in Table 7.1 and 7.2 [159], comparisons of the performance of DFT methods by mean absolute deviations are shown for the G2-1 data set (125 atomic and molecular properties have been used as reference) and the somewhat larger G2-2 data set, respectively. In the Gaussian-2 (G2), G2(MP2), and G2(MP2,SVP) models, calculations from different levels of theory are combined with the goal of producing energy differences accurate to about 1 kcal/mol, as compared to experimental results.

Table 7.1: Comparison of the performance of DFT methods by mean absolute deviations (kcal/mol).

Method	G2	LSDA	B88	BPW91	B3PW91
Atomization Energies	1.2	35.7	3.9	5.7	2.4
Ionization Potentials	1.4	6.3	11.2	4.1	3.8
Proton Affinities	1.0	5.6	2.4	1.5	1.2

Table 7.2: Comparison of the performance of DFT methods (kcal/mol).

Method	Mean absolute deviation	Maximum absolute deviation
G2	1.6	8.2
G2(MP2)	2.0	10.1
G2(MP2, SVP)	1.9	12.5
SVWN	90.9	228.7
BLYP	7.1	28.4
BPW91	7.9	32.2
B3LYP	3.1	20.1
B3PW91	3.5	21.8

The main difference in these methods is the way in which they try to extrapolate the correlation energy. Details of G2 methods can be found in reference [159].

In Tables 7.1 and 7.2, it is apparent that Local Spin Density Approximation (LSDA, also called SVWN) are the worst methods in producing energy differences. Gradient corrected methods give better energy differences than the LSDA method. The best approach to G2, G2(MP2), and G2(MP2, SVP) results is obtained by the B3LYP and B3PW91 hybrid functionals, with the former perhaps being slightly ahead. From these comparisons it is clear that hybrid functionals such as B3LYP are necessary to get DFT results that can reasonably be expected to come close to results produced by methods in which electron correlation is considered explicitly.

Comparing the high-level ab-initio results of Raghavachari et al. [55,56,57] with DFT results, and in particular also considering the multireference results by

Baumhauer [160], one may doubt if DFT calculations are sufficient for reliable results on silicon clusters. This question is actively pursued, but for the present purposes the answer is irrelevant: The purpose of this study is to show that a GAGA-optimized model potential will be able to reliably guide a search for the best structures on some ab-initio level. For this purpose, it will be enough to demonstrate this at the DFT level, since it is a reasonable assumption that the complexity of the search space at the DFT level will not be very different from the complexity of the lowest-energy solution at a high-level MCSCF/MRCI treatment: the latter will exhibit many real and avoided crossings, but the main effect of that will be a lowering of energy barriers between minima (which is not very relevant for an evolutionary algorithm search strategy) and not a marked increase in number and nature of the minima themselves. Also, at the DFT level, there is a possibility to compare our results to the literature and judge the performance of our methods, whereas higher-level ab-initio calculations on silicon clusters for $n \geq 11$ are rare to nonexistent, due to their computational expense.

For very similar reasons, a closed-shell restricted Kohn–Sham treatment is employed, implying a singlet total spin state for all clusters. Again, high-level treatments of very small clusters in the literature (including ref. [160]) indicate that e.g. triplet states may have a lower energy in certain cases. However, the differences in energies and structures typically are rather small and in any case hard to reproduce even qualitatively correctly with open-shell unrestricted DFT techniques, using the best available functionals. As shown below, the possible variations of structural preferences with cluster size provide much larger effects that need to be captured preferentially by a good guiding function.

7.2 LMP2

As shown in Tables 7.1 and 7.2, DFT methods, even with hybrid functionals like B3LYP, do not quite reach the level of agreement with experimental data that electron correlation methods can attain. This strongly suggests the necessity of the latter methods for quantitatively accurate results, for example to correctly reproduce small energy differences between various isomers, as in this study.

Until quite recently, the calculation of the dynamical correlation energy has been perceived as prohibitively expensive for larger molecular systems [161]. The least expensive method, second-order Møller-Plesset theory (MP2), has a formal $O(N^5)$ scaling, and more accurate methods scale formally as $O(N^6)$ (quadratic configuration interaction (QCISD)) or even $O(N^7)$ (MP4, QCISD(T), and CCSD(T)). Even a fifth-order scaling with the molecular size would indeed prohibit application of the method to large systems. This steep scaling is unphysical, and originates from using delocalized canonical orbitals, which distribute a few large local contributions to countless small ones. Electron correlation should asymptotically be less expensive than self-consistent field (SCF) for large systems since the interactions contributing to it are short ranged compared to SCF, which is dominated by long-range Coulomb interactions.

The computational cost of MP2 calculations is dominated by the integral transformation from the atomic orbital (AO) into the molecular orbital (MO) basis. If the sparsity of the AO integral list is exploited in the transformation, the formal $O(N^5)$ dependence of the dominant first transformation step can in practice be reduced to about $O(N^3)$. However, achieving this optimum scaling requires either keeping all transformed integrals in high-speed memory or on disk, leading again to an $O(N^4)$ dependence of the computational resources needed. The four-index integral transformation can be avoided by the resolution of the identity (RI-MP2) method. This strongly reduces the prefactor, but the actual scaling is then still $O(N^5)$.

The use of local orbital bases opens the way for two distinct approximations: First, for the correlation of each electron pair *ij* an individual subset (domain) of the virtual orbitals can be selected. The size of this domain is independent of the molecular size. This reduces the scaling of the number of configuration state functions (CSFs) and corresponding amplitudes from $O(N^4)$ to $O(N^2)$. Second, a hierarchical treatment of different electron pairs depending on the minimum distance R of the two correlated localized occupied MOs (LMOs) i and j can be devised. In the implementation of Schütz et al. [162], a subset of atoms is assigned to each LMO according to the procedure of Boughton and Pulay [163]. The pairs (*ij*) are then classified according to the minimum distance between any atoms in the two different subsets. Strong pairs ($R \leq 1$ bohr) are treated at the highest level. These involve pairs of local orbitals that share at least one atom and typically account for more than 90% of the correlation energy. Weak pairs ($1 < R \leq 8$ bohr) and distant pairs ($8 < R \leq 15$ bohr) are (optionally) treated by local MP2, while very distant pairs ($R > 15$ bohr) can be entirely neglected. For the distant pairs, the required integrals can be obtained using multipole approximations [164], leading to substantial savings. The neglect of very distant pairs leads to an overall linear dependence of the number of CSFs and of the corresponding transformed integrals. The multipole treatment of distant pairs further reduces the number of integrals which must be constructed via the four-index integral transformation. Combining all these ingredients, it is possible to devise an integral transformation algorithm for which all computational resources (CPU, memory, and disk) scale only linearly with system size.

Some tests have been performed to check the effect of electron correlation on silicon clusters, employing MP2 and LMP2 calculations. In particular, the reliability of energy orderings obtained from DFT/B3LYP is questioned. First, a medium-sized silicon cluster, Si_{21}, was taken as a benchmark system and calculations were performed for the most important structures proposed in the literature (these structures are considered in more detail in Chapter 10). These literature structures were relaxed at the DFT/B3LYP level with a (3s3p1d) basis set using the ECP approximation. At the relaxed geometries, single point energy calculations were then performed at the MP2 level with the cc-pVTZ basis set. The obtained results are shown in Table 7.3. (relative energy differences in kJ/mol and energy ordering of these isomers).

Table 7.3: Relative energies and energy orderings at both DFT/B3LYP and MP2 levels.

Structure	DFT Relative Energy	DFT Order	MP2 Relative Energy	MP2 Order
Jack-old-Si_{21}	0.0	1	0.0	1
Zeng-Si_{21}	6.29	2	138.19	3
Jar-Si_{21}	73.78	3	32.4	2

Note that there are differences between the test structures: Zeng-Si_{21} is a spherical isomer, whereas the remaining two structures are prolate. In the energy orderings shown in Table 7.3, there is no complete agreement. The lowest-energy structure is determined as the same in two methods, however the order of the other two low-energy isomers at the DFT level is swapped at the MP2 level. Surprisingly, at the MP2 level, the spherical structure is the least stable isomer, by a large margin. Obviously, electron correlation changes the picture obtained from DFT/B3LYP level, quantitatively and possibly even qualitatively.

As expressed above, the unfavorable scaling of MP2 with system size might be lowered with a local treatment (LMP2). Therefore, it is worthwhile to compare MP2 with LMP2 with regard to CPU time required for the calculation. For this purpose, the prolate Jar-Si_{21} isomer (relaxed structure at the DFT level) has been taken as a benchmark system. Single point energies have been calculated with MP2 and LMP2 with and without multipole approximation, as shown in Table 7.4.

Table 7.4: Comparison for required CPU time in MP2 and LMP2 single point energy calculations with both cc-pVDZ and cc-pVTZ basis sets for the Jar-Si_{21} isomer.

Method	Basis set	Energy (hartree)	CPU time (sec.)
MP2	cc-pVDZ	-6069.54860691	1739.58
MP2	cc-pVTZ	-6070.21939593	16168.49
LMP2	cc-pVDZ	-6069.53029207	2094.60
LMP2	cc-pVTZ	-6070.19803896	18412.75
LMP2*	cc-pVDZ	-6069.47628740	1788.07
LMP2*	cc-pVTZ	-6070.16679851	8822.01

* in these LMP2 calculations multipole approximation is used.

There are a few interesting points in Table 7.4: i) LMP2 without multipole approximation requires more CPU time than standard MP2. The time required for LMP2 using the cc-pVDZ and cc-pVTZ basis sets increases by approximately 20 % and 14 %, respectively. This is due to computational overheads in LMP2 calculations, compared to the simpler standard MP2 approach. ii) LMP2 with multipole approximation reduces CPU time considerably. However, in the case of a small basis set, cc-pVDZ, this reduction only compensates for the computational overhead mentioned above. But, for a larger basis set, cc-pVTZ, the multipole approximation has demonstrated its efficiency by lowering the required CPU time to half of that of LMP2 without multipole approximation or of standard MP2 calculations. This strongly suggests to use LMP2 with multipole approximation instead of the more demanding standard MP2 for the larger silicon clusters. Unfortunately, no analytical gradients have been implemented for LMP2 with multipole approximation. Therefore, at present, this approach can only be used for single-point calculations, not for geometry optimization. However, it can reasonably be expected that the DFT structures are fairly reliable, and that therefore MP2 single-point calculations for DFT structures are a reasonable first approximation to an explicit correlation treatment.

7.3 RI-DFT

The cost of density functional theory (DFT) calculations using Gaussian basis sets is dominated by the evaluation of a two-electron contribution to the total molecular energy consisting of a Coulomb (J) and an exchange-correlation (E_{xc}) term. In DFT methods, the two terms can be calculated separately which facilitates the development of efficient algorithms. The evaluation of the E_{xc} term can be performed very efficiently using numerical quadratures and has an almost linear scaling with molecular size. For hybrid functionals including Hartree–Fock exchange, several approaches have also been proposed to reduce the computational expense. The representation of the density matrix in MOs leads to a formal cost of evaluation for J that grows as the fourth power of the number of basis functions. The origin of this formal $O(N^4)$ scaling behavior is the calculation of the four-center two-electron repulsion integrals (ERI's). The time needed for the calculation of the Coulomb energy might be significantly reduced by employing hierarchical multipole methods such as the fast multipole method (FMM). These kinds of methods partition all interactions in a far-field (FF) and a near-field (NF) portion of the Coulomb problem. The NF interactions are evaluated analytically employing four-center ERI's. The FF part comprises the majority of interactions in a large molecule and is usually calculated in a tree algorithm using multipole expansions. For one- or diluted three-dimensional model systems such as *n*-alkanes or water clusters, and using small basis sets, these methods can achieve an almost linear scaling with system size. For most three-dimensional systems the scaling remains less favorable and the dominant cost is still associated with the calculation of the NF part due to a large number of remaining four-center ERI's. Recently, a method has been proposed by Sierka et al. [165] for reducing the computational cost of the Coulomb problem which is similar to the augmented plane-wave method [166]. The development of this method has been motivated by the observation that the calculation of the NF part requires an appreciable portion of the computational time in FMM treatments. In the "multipole accelerated resolution of identity for *J*" method (MARI-*J*) of Sierka et al. [165], the calculation of the NF contribution is based on the RI-*J* technique, which approximates the total electron density in terms of atom-centered auxiliary basis set. With the help of the RI-*J* technique the evaluation of the four-center integrals is reduced to a maximum of three centers. This leads to a more than tenfold decrease of computational effort for the evaluation of the Coulomb term, but the same $O(N^2)$ asymptotic behavior. Similar to the other multipole methods, the MARI-*J* approach partitions the Coulomb interaction of electron densities into NF and FF parts.

However, since the electron density is approximated by an expansion in an atom-centered auxiliary basis set, it is in-line with the already existing program structure to base the evaluation of the FF part on atom centered multipole expansions, without employing a tree algorithm. This is achieved by dividing the electron density into ‘‘atomic’’ and the auxiliary density into atom-centered distributions. The MARI-*J* approach leads to a formal $O(N^2)$ step, but it has the advantage that it reduces the number of terms in the multipole series needed for convergence. The FF part implemented this way is competitive with the hierarchical multipole methods for systems with up to 1000 atoms and up to 14 000 basis functions. The MARI-*J* method thus combines a low prefactor of the RI-*J* method employed for the NF part with a low-order scaling due to the multipole approximation for the FF contribution. Compared to other multipole-based methods, this approach allows for a significant reduction of the computational effort involved in the evaluation of the NF contribution.

7.4 Computer resources and software

In this current study, for all the ab-initio and DFT calculations and for geometry optimizations of larger clusters with model potentials, high-performance computers are required since all the calculations mentioned above, especially for larger clusters ($20 \leq n \leq 35$), become impossible to carry out on standard PC'-s and lower capacity clusters. For instance, a DFT/B3LYP geometry optimization for Si_{15} with 2 CPUs on Altix needs a CPU time between 10-16 hours. An LMP2 single point energy calculation with multipole approximation with 2 CPUs on HLRN needs almost 2 days of CPU time. Obviously, it is impossible to carry out the same calculations on standard PCs. Here is a list of computers used in this current study and their major features:

- NEC SX-5 (located at the computer center of the University of Kiel)
    - Theoretical peak performance per processor: 4 GFlop/s
    - Number of processors: 16
    - Total memory: 32 GBytes
- SGI Altix 3700 (located at computer center of University of Kiel)
    - Number of processors: 128
    - Theoretical peak performance per processor: 5.2 GFlop/s
    - Clock rate: 1.3 GHz
    - It allows parallel jobs on up to 64 CPU
    - Total memory: 512 GBytes
- HLRN (located on Berlin and Hannover)
    - The HLRN system consists of 32 (eserver) pSeries 690 servers. Each IBM pSeries 690 server contains 32 processors (1.3 GHz Power4),

    that share 64 GByte to 256 GByte of memory. This gives a total of 512 processors and 1.25 TByte memory per site (for Berlin and Hannover).
- BACH Cluster (located in the Physical Chemistry Institute)
    - 14 nodes, each node contains two CPUs, giving a total of 28 CPUs.
    - Clock rate: 1.5 to 2 GHz.
    - Total memory: 16.7 GB.

Several quantum chemistry software packages have been used for ab-initio and DFT calculations. These software packages and the usage purposes are listed below:

- Gaussian 98 [167] and Gaussian 03 [168]
    - For geometry optimization at the DFT level on NEC and ALTIX.
- Turbomole 5.6 [169]
    - For geometry optimization at the RI-DFT level on HLRN.
- Molpro 2002.8 [170]
    - For single point energy calculation at the LMP2 level on HLRN.

8 Global parameter and geometry optimization

In order to perform global geometry optimizations at the model potential level, one needs globally optimized parameters of the considered model potential. In this study, global parameter optimization of the model potentials have been carried out with the GAGA algorithm (see section 5.4.1). As a model potential, SWG, Mistriotis, and our modified Mistriotis potentials (see section 6.1.1.4) have been used. These model potentials are the most promising candidates for use as guiding function in GAGA studies. There are 8, 11, and 13 parameters to be optimized in the SWG, Mistirotis, and modified Mistirotis potentials, respectively.

Our first task was to find globally optimal parameter sets for these model potentials, judged by their ability to reproduce the optimal cluster geometries for small silicon clusters up to n =10, with greater weights on the larger structures. For this purpose, we employed a plain standard genetic algorithm operating on a binary string representation of the potential parameters. By a careful examination of the functional form of each contribution to the potentials, lower and upper limits for each parameter were determined. These were then used as constraints in the global optimization, in order to keep each contribution and the overall potential physically reasonable.

The best parameter set from this global optimization step was then subjected to an unconstrained local optimization, to allow efficient relaxation to the nearest minimum and to check for stability against drifts into unphysical regions of parameter space. The most efficient local optimization routines for this purpose were found to be implementations of the BFGS and DFPMIN algorithms. Other routines like FRPRMN, a plain Powell, and the simplex algorithm were found to be less efficient.

Several hundred candidate parameter sets were obtained in this way. These were then ranked according to their performance in correctly reproducing the structures of small silicon clusters, with Si_{10} as most important test. This was done by performing global cluster geometry optimizations, using the efficient evolutionary algorithm variant PHENIX.

In this Chapter, the results of the global parameter optimizations and the global geometry optimization in the size range 4≤n≤40 are reported.

8.1 Parameter optimization details

During the parameter optimization of the model potentials, several ingredients of the algorithm that affect the optimization have been systematically changed to obtain a better optimized parameter set. Mainly, the following conditions have been considered:

- Some parameters of the GAGA scheme:
  - Quadratic deviation measure (*rms*). *Rms* can contain only the energy differences, or it can also contain the differences of energy derivatives.
  - The total number of initial geometries.
  - The number of generations and individuals.
- Type of the model potential.
- Type of the local optimization algorithm.

8.1.1 Influence of the rms expression

As explained in section 5.4.1, in the GAGA scheme there is a standard GA that optimizes the model potential parameters globally, by minimizing the quadratic deviation measure. This measure simply indicates the deviation between ab-initio and model potential energies. An extended form of the rms has also been used:

$$rms = wa\sum_{i=1}^{n}\left(E_{\mathrm{mod},i} - E_{true,i}\right)^2 + wb\sum_{i=1}^{n}\left(\nabla E_{\mathrm{mod},i} - \nabla E_{true,i}\right)^2 \tag{8.1}$$

In this extended rms expression, the first term is the standard *rms* term. To this, a second term is added that captures deviations of the gradient. The absolute and relative weights of these two terms are controlled by the factors w_a and w_b.

In order to properly use the extended version of the rms definition, the effects of these weighting factors have to be tested by changing them systematically in several trials. For these test trials, only the Mistirotis potential and the DFPMIN local optimization routine have been used. Additionally, the same initial parameter ranges (lower and upper bounds) have been used for all these trials.

At first, w_a was kept constant, and only the effect of changing w_b was observed. It was surprisingly found that for w_b>100, local optimizations always failed, whereas for w_b<100 no promising parameter set could be obtained for further use in global geometry optimization. Then, w_b was kept constant, and w_a was changed. In this case, as long as w_a was smaller than 10000, several good parameter sets were obtained.

For w_a>10000, in every trial, a negative value was obtained for the second parameter (parameter *B*, see equation 6.3) of the Mistriotis potential. The second parameter is actually part of the two-body term of the Mistriotis potential and it gives the highest contribution to the total energy. If the parameter *B* becomes negative, the sign of the two-body term is reversed, resulting in unphysical energy values.

From these tests performed to locate the optimal values for weighting factors, the best promising parameter sets have been obtained for the value pairs (w_a=1000, w_b=1) and (w_a=500, w_b=1). Using these two pairs, several different initial parameter ranges have been tried to check if this changes the results. It was observed that changing the initial parameter ranges results in several good parameter sets. These obtained parameter sets were ranked using global geometry optimization performed with PHENIX for the Si_{10} benchmark case. The expected global minimum structure of Si_{10}, a tetra-capped trigonal prism (TTP), was found with several parameter sets. However, the TTP structure was not the global minimum, it was only a low-lying local minimum. The best two of these parameter sets are called Set3 and Set4 in the following. They were found with (w_a=1000, w_b=1) and (w_a=500, w_b=1), respectively. All parameter values in these two sets are listed in Table 8.1 and 8.2, as obtained after global optimization with a GA and a final local optimization.

Table 8.1: Optimized parameters of Set3, and lower and upper bounds of the initial parameter ranges. Global optimization is restricted to these parameter ranges, whereas local optimization is free to adopt any value, also outside of these ranges. This happened for α, γ, and q_3. This local optimization has ended after only 8 iterations. This is obviously a very fast convergence. The ratio $rms_{global} / rms_{local} \cong 9.5$ shows that rms is substantially lowered by local optimization.

Parameters	After Global Optimization	After Local Optimization	Lower bounds	Upper bounds
A/eV	12.70	12.67	0.0	30.0
B/Å	8.82	5.61	5.0	18.0
α/Å	2.79	0.78	1.0	3.0
R/Å	4.61	3.06	3.0	5.0
γ/Å	3.21	0.90	1.0	4.0
λ_3/eV	6.96	6.37	-10.0	15.0
q_3	5.90	6.10	4.0	6.0
λ_{41}/eV	2.35	3.69	-10.0	40.0
λ_{42}/eV	0.20	- 0.30	-10.0	40.0
q_{41}	5.50	5.55	4.0	6.0
q_{42}	5.76	5.75	4.0	6.0
rms	11356.27	1223.63		

Table 8.2: Optimized parameters of Set4 and lower and upper bounds of the initial parameter ranges. In the local optimization, A, B, α, R, γ, and q_{42} parameters have adopted values from the outside of the ranges. This local optimization has ended after only 7 iterations. The ratio $rms_{global} / rms_{local} \cong 3$ is not as good as for Set3.

Parameters	After Global Optimization	After Local Optimization	Lower bounds	Upper bounds
A/eV	16.55	17.04	16.0	16.6
B/Å	11.01	8.03	11.0	12.0
α/Å	1.99	1.05	1.75	2.25
R/Å	3.78	3.12	3.5	4.0
γ/Å	2.54	1.28	2.1	2.6
λ_3/eV	4.19	4.11	3.5	4.5
q_3	4.65	4.53	4.5	5.5
λ_{41}/eV	27.01	27.20	27.0	29.0
λ_{42}/eV	17.93	17.58	16.0	18.0
q_{41}	5.41	5.44	4.5	5.5
q_{42}	4.53	4.16	4.5	5.5
rms	2956.07	1079.15		

These results are an improvement since before the application of the extended rms criterion the TTP structure was never found, even as a low-lying local minimum.

8.1.2 Influence of the number of initial geometries

GAGA can run with either randomly selected initial geometries or from known geometries. To start from known geometries might be an advantage to get a fast and successful convergence. For this reason, known geometries were fed into GAGA instead of randomly selected geometries. For different numbers of initial geometries (14, 19, 40, and 86) and for several initial parameter ranges, a huge number of trials have been conducted. In these trials, the SWG, Mistriotis, and modified Mistriotis potentials have been used, together with the DFPMIN local optimization routine.

From these trials, it was observed that the increase in the number of initial geometries did not affect the quality of the resulting parameter sets. However, a strange and unexplained behavior in the rms values has appeared when trials were conducted with the standard *rms* definition. This behavior was actually observed while using smaller numbers of initial geometries compared to the above ones.

More specifically, for example with the Mistriotis potential, the variation of the number of initial geometries from 1 to 9 resulted in better parameter sets compared to the other trials where higher numbers of initial geometries have been fed into GAGA. In these trials, *rms* values obtained after the local optimization were extremely low, such as in the case of 9 initial geometries where an rms value of 10^{-23} has been obtained. However, when only one additional geometry was added to the 9 initial geometries, an *rms* value of 10^{-1} has been found. Moreover, the parameter sets obtained from the latter run after the local optimization were not satisfactory for global geometry optimization.

The same *rms* transition, from very low values at very low numbers of initial geometries to very high values at only slightly higher numbers of initial geometries, has also appeared in the case of the SWG potential. However, this time, it was observed with 3-5 initial geometries. In the case of the modified Mistriotis potential, the *rms* transition was almost the same as with the Mistriotis potential.

Promising parameter sets found with lower numbers of initial geometries have been used for global geometry optimization of Si_{10} using PHENIX. However, none of them has resulted in the TTP structure as a global minimum. Nevertheless, a few times TTP was obtained as a low-lying local minimum.

The same trials have been carried out with the modified rms definition. Contrary to the standard rms trials, in these trials no rms transition has been observed.

8.1.3 Influence of the number of generations and individuals

For the above trials, the numbers of generations and individuals were set to 10 and 10, respectively. 420-42 and 1000-100 generation-individual pairs have also been tested for the same input that applied in the case of the 10-10 pair. However, the obtained parameter sets were not better then for the 10-10 pair. Hence, the 10-10 pair has been used throughout the parameter optimization. In this way, the required computational time is significantly reduced.

In order to be sure about the above behavior of the generation-individual pairs, different pairs have also been tried such as 100-50, 200-50, and 700-70. Results similar to those with the 420-42 and 1000-100 pairs were obtained. Additionally, it was observed that the number of failed local optimizations in the parameter optimization process was increasing with the increase in the generation-individual pair.

8.1.4 Performance of the model potential

Different model potentials support extremely different global minimum structures. Our aim is to find the TTP structure as a global minimum for Si_{10} with changing the parameters of the GAGA scheme, the model potentials, and the local optimization methods. As a summary, none of the mentioned local optimizations and neither the SWG nor the Mistriotis model potentials were successful. Therefore, as described in section 6.1.1.4, the Mistriotis potential has been altered by adding an extra cosine function to the three-body term. The resulting new model potential is called modified Mistriotis. With this change, it was hoped that the desired global minimum structure of Si_{10} could be located.

At the trials with the modified Mistriotis potential, several promising parameter sets were obtained with the modified *rms* definition. Then, these sets have been used in

Table 8.3: Optimized parameters of Set1 and lower and upper bounds of the initial parameter ranges. In the local optimization, only the c_1 parameter has adopted a value from the outside of the ranges. This local optimization has ended after only 5 iterations. The ratio rms_{global} / rms_{local} ≅ 1.5.

Parameters	After Global Optimization	After Local Optimization	Lower bounds	Upper bounds
A/eV	20.39	20.42	5.0	30.0
B/Å	7.46	7.40	4.0	18.0
α/Å	1.49	1.51	1.2	2.8
R/Å	3.26	3.27	2.8	5.0
γ/Å	1.78	1.70	1.0	4.0
λ_3/eV	7.06	7.06	-10.0	15.0
q_3	7.39	7.38	2.0	8.0
λ_{41}/eV	10.98	10.98	-10.0	40.0
λ_{42}/eV	20.19	20.19	-10.0	40.0
q_{41}	6.96	6.96	2.0	8.0
q_{42}	3.51	3.45	2.0	8.0
c_0	0.47	0.36	-1.0	2.0
c_1	0.09	-0.02	0.0	0.1
rms	1496.53	1064.58		

Table 8.4: Optimized parameters of Set2 and lower and upper bounds of the initial parameter ranges. In the local optimization, the α and γ parameters have adopted a value from the outside of the ranges. This local optimization has ended after only 6 iterations. The ratio rms_{global} / rms_{local} ≅ 2.5, which is better than for Set1.

Parameters	After Global Optimization	After Local Optimization	Lower bounds	Upper bounds
A/eV	12.74	12.69	5.0	30.0
B/Å	8.56	7.55	4.0	18.0
α/Å	1.39	0.62	1.2	2.8
R/Å	3.52	2.97	2.8	5.0
γ/Å	1.90	0.86	1.0	4.0
λ3/eV	5.0	4.63	-10.0	15.0
q3	7.93	7.94	2.0	8.0
λ41/eV	26.86	26.94	-10.0	40.0
λ42/eV	3.33	3.11	-10.0	40.0
q41	7.55	7.55	2.0	8.0
q42	6.31	6.28	2.0	8.0
c_0	-0.79	- 0.9	-1.0	0.5
c_1	1.18	1.27	-2.0	2.0
rms	2383.00	1062.51		

PHENIX for the global geometry optimization of Si_{10}. TTP was found as the global minimum with only one parameter set called Set2. In addition to Set2, another parameter set called Set1 was also very successful in reproducing TTP as a low-lying local minimum. In tables 8.3 and 8.4, the parameters in Set1 and Set2 are shown.

8.1.5 Influence of the type of local optimization

As already mentioned in section 4.2, in this study several local optimization routines have been used, such as frprmn, dfpmin, simplex, powell, and bfgs. The task of local optimization in this context is further refinement of the parameter sets that were already globally optimized by a standard GA.

Among these routines, frprmn and powell turned out to be the worst ones. In general, they have failed without producing any result. In contrast, the simplex method was in most cases successful. However, global cluster structure optimizations with the resulting parameter sets were unsatisfactory. Finally, dfpmin routine has been successful in producing a parameter set that leads to the TTP structure as the global minimum for Si_{10}.

The BFGS routine is actually not considered in this parameter optimization process since dfpmin routine has already been successful to produce 4 different promising sets. It has been successfully implemented into the full-GAGA scheme (see section 5.4.1) and applied to only a few selected medium sized-silicon clusters such as Si_{20} and Si_{21}. Unexpectedly, full-GAGA results were found not better than the normal GAGA runs. For this reason, other cluster sizes were not tried.

In the above optimizations, GAGA was only used for the task of global optimization of model potential parameters.

8.1.6 Summary of global parameter optimization

GAGA has been successfully applied for the global optimization of the Mistriotis and modified Mistriotis model potentials. In Table 8.5, the most promising parameter sets from this optimization procedure are shown. Set1 and Set2 were obtained with the modified Mistriotis potential, and Set3 and Set4 with the Mistriotis potential. Only one parameter set, namely Set2 in Table 8.5, resulted in the TTP structure as the lowest-energy structure for Si_{10}. With Set1, TTP is higher in energy than the lowest minimum structure by 1.81 eV. The TTP structure also is a low-energy local minimum structure with the parameters Set3 and Set4, with even smaller energy differences to the global minimum: 0.58 eV and 0.03 eV, respectively. With the same approach, the SWG potential has never resulted in TTP as the lowest structure for Si_{10} in this study.

Table 8.5: Optimized parameter sets (Set1, Set2, Set3, and Set4) and the original parameter sets of the SWG and Mistriotis potentials.

Parameters	Gong (Original)	Mistriotis (Original)	Set1	Set2	Set3	Set4
A/eV	16.30	16.30	20.42	12.69	12.67	17.04
B/Å	11.58	11.58	7.40	7.55	5.61	8.03
α/Å	2.09	2.09	1.51	0.62	0.78	1.05
R/Å	3.77	3.77	3.27	2.97	3.06	3.12
γ/Å	2.40	2.40	1.70	0.86	0.90	1.28
λ_3/eV	4.00	4.00	7.06	4.63	6.37	4.11
q_3	n.a.	5	7.38	7.94	6.10	4.53
λ_{41}/eV	n.a.	28	10.98	26.94	3.69	27.20
λ_{42}/eV	n.a.	17	20.19	3.11	- 0.30	17.58
q_{41}	n.a.	5	6.96	7.55	5.55	5.44
q_{42}	n.a.	5	3.45	6.28	5.75	4.16
c_0	- 0.50	n.a.	0.36	- 0.9	n.a.	n.a.
c_1	0.15	n.a.	-0.02	1.27	n.a.	n.a.

In the obtained parameter sets, it is hard to find similarities between the individual parameters. Nevertheless, some of the parameters of Set1-Set4 and Set2-Set3 are similar to each other. Table 8.5 also suggests an explanation why the original parameter sets of the SWG and Mistriotis potentials did not produce the TTP structure for Si_{10}. Comparing the original Mistriotis potential parameter set with Set2 (which is the best parameter set found in this study), none of the parameters are similar in these two sets, with the possible exception of the parameter λ_{41}. Also, the unsatisfactory results obtained from the SWG and Mistriotis potentials clarify the necessity of this study.

These 4 different parameter sets (Set1, Set2, Set3, and Set4) have then been used in global geometry optimization of a broad size range of silicon clusters, Si_n, $4 \leq n \leq 40$. This part of the study was carried out with the PHENIX algorithm. There are some parameters that can be varied in PHENIX, such as the total number of generations, the number of geometries that have to be generated, parameters that controls the mutation, parameters for niching, etc. The effects of these parameters on the global geometry optimization have also been tested.

In the following section, the results of these global geometry optimizations will be discussed and compared with those obtained in the literature.

8.2 Global geometry optimizations with PHENIX

The best parameters found for the Mistriotis and the modified Mistriotis potentials have been used for global optimization of silicon clusters, Si_n, in the size range $4 \leq n \leq 40$. All cluster energies given in the following are negative total atomization energies. In the DFT calculations, the common B3-LYP hybrid functional with a 6-31G* basis set has been used.

8.2.1 Structures of Si_n clusters for $4 \leq n \leq 10$

Small silicon clusters in this size range have been extensively investigated in a number of both theoretical and experimental studies. Structures obtained from the present study are shown in Figs. 8.1 and 8.2. In the following, these structures are analyzed and compared to the literature results for each cluster size.

Si_4: Two different structures have been found, namely Si_4-1 (a flat rhombus) with Set3 and Si_4-2 (a tetrahedron) with both Set1 and Set2. At the DFT level, the former structure is much more favorable than the latter. The flat rhombus is also the experimentally predicted structure (see section 2.1).

The rhombus structure (Si_4-1) has also been found in several other studies. For instance, Ramakrishna et al. [126] found the rhombus structure using tight-binding molecular dynamics (TB-MD) followed by further relaxation using DFT/LDA. A DFT-based TB approach has been used in the study of Sieck et al. [63] resulting in the rhombus structure. In addition, they also reproduced the rhombus using a fully self-consistent-field (SCF)-LDA method. In another study, Lu et al. [171] have also found the rhombus with the Car-Parrinello (CP)–MD method. Bolding and Anderson [59] were successful in locating the rhombus using a steepest-descent method with their potential. Additionally, they have used the SW, Tersoff, and BH potentials to compare with their own BA potential. They found a square for the SW and BH potentials and a tetrahedron for the Tersoff potential. First-principle calculations have also been carried out for small Si_n clusters. Early and successful attempts were performed by Raghavachari et al. [55,56] using HF/STO-3G [55], HF/6-31G* [55], MP4/6-31G* [55], and MP4/6-31G* [56] levels of theory. In these calculations, the rhombus was found lower in energy than the other candidate structures. Hartke [122] also successfully applied GAGA in conjunction with DFT/B3-LYP and the Gong potential and found the rhombus structure.

In contrast, Luo et al. [172] found a distorted tetrahedron using a GA in which the energies of clusters have been calculated according to the fractional bond model. A tetrahedron was also found by Hobday et al. [173] using a GA with the Tersoff potential. Gong [131] found the rhombus and tetrahedron almost at the same energies using a MD study with Gong's potential. Iwamatsu [123] has also used the Gong potential with a GA and he found a tetrahedron. He also implemented the SW potential in a GA, and obtained a square.

Li et al. [150] has also identified a square using a numerical minimization routine (NAG (Numerical Algorithms Group) library routine E04JAF (which is a quasi-Newton algorithm)) and a Monte Carlo (MC)-based routine with their LJM potential. Wales et al. [174] used the same LJM potential with an MD-quenching method and also found the square structure.

As a summary, although Si_4 is a relatively easy case, some of the methods in conjunction with empirical potentials - such as Gong, SW, and LJM - have failed to find the rhombus as accepted global minimum structure. Silicon clusters significantly larger than Si_4 offers still more failings of various methods and potentials. Actually, for small silicon clusters failings can be speculated to be due to π-bonding contributions that are difficult to model with empirical potentials.

Si_5: A trigonal bipyramid structure is found as the global minimum with both Set1 and Set2. This structure can also be understood as a continuation of the Si_4 rhombus structure: Along a line through two opposite atoms, the rhombus is slightly "folded" out of plane, and the other two atoms are linked by a new atom. The same structure is also found in the literature [56,63,123,126,131,171,173,174]. In addition, the trigonal bipyramid is the experimentally predicted structure (see section 2.1).

Other low-energy isomers were also found for Si_5. For example, Iwamatsu [123] found the trigonal bipyramid with the Gong potential but a pentagon with the SW potential. Li et al. [150] could not locate an exact trigonal bipyramid, instead they found a compressed trigonal bipyramid. Surprisingly, in spite of the good quality they claim for their potential, Bolding and Anderson [59] also could not find the trigonal bipyramid. Their best structure using their potential was a capped flat rhombus. Additionally, they found a pentagon with the SW and BH potentials and a square prism with the Tersoff potential. Gong [131] successfully found the trigonal bipyramid using his potential but a pentagon with the SW potential, like Bolding and Andersen. Luo et al. [172] found a face-capped tetrahedron (a similar structure to trigonal bipyramid (with D_{3h} symmetry) but it has C_{2V} symmetry, differing from the above structures.

Si_6: This cluster size turns out to be an exceptionally difficult case. In this study, three isomers have been obtained: Si_6-1 (equatorially-capped trigonal bipyramid) was obtained with Set2, and Si_6-2 (edge-capped trigonal bipyramid) and Si_6-3 (tetragonal bipyramid or octahedron) were obtained with Set1. At the DFT level, capped trigonal bipyramids (Si_6-1 and Si_6-2) are energetically more favorable than the octahedron. More specifically, Si_6-1 is lower in energy than Si_6-2 and Si_6-3 by 0.91 eV and 2.26 eV, respectively. However, this situation is reversed for the model potential, where the octahedron is more favorable.

Observed agreement between experiment and theory for Si_4 and Si_5 is broken down for Si_6. In contrast to lowest-energy structure predicted from theoretical studies, experimental results support an octahedron (see section 2.1) for Si_6.

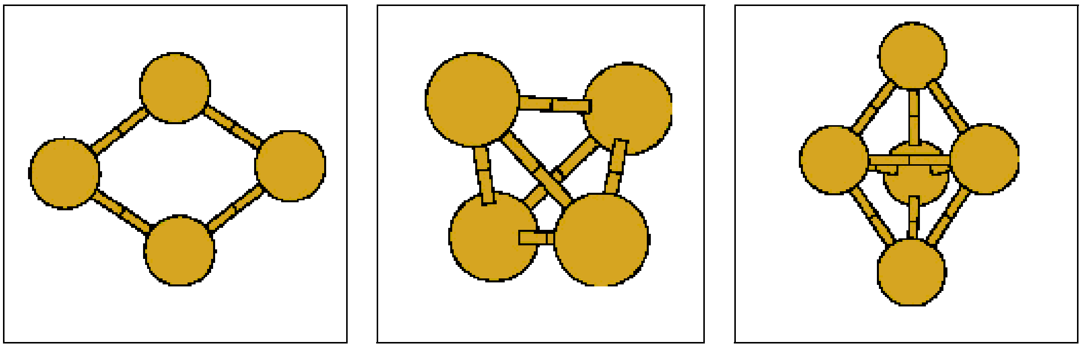

Si$_4$-1
with Set3
-14.88 eV
-14.67 eV

Si$_4$-2
with Set1 and Set2
-16.06 eV (Set1)
-11.74 eV

Si$_5$
with Set1 and Set2
-22.73 eV (Set1)
-18.09 eV

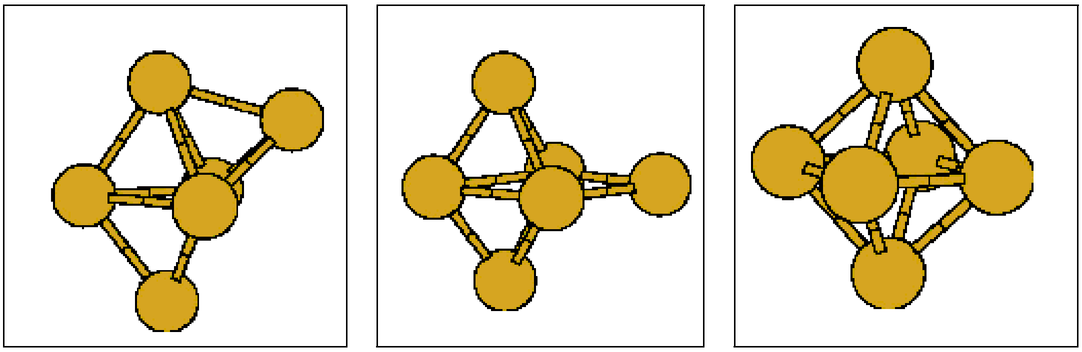

Si$_6$-1
with Set2
-26.77 eV
-24.72 eV

Si$_6$-2
with Set1
-26.68 eV
-23.81 eV

Si$_6$-3
With Set1
-29.86 eV
-22.46 eV

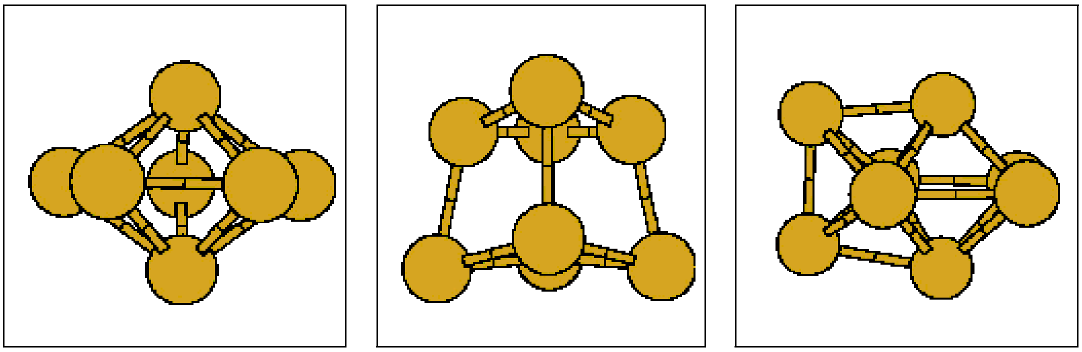

Si$_7$
with Set1 and Set2
-35.81 eV (Set1)
-27.97 eV

Si$_8$-1
with Set2, Set3, Set4
-38.89 eV (Set2)
-31.56 eV

Si$_8$-2
With Set1
-41.98 eV
-29.61 eV

Figure 8.1: Geometries found for Si$_n$, $4 \leq n \leq 8$. First energies are at the model potential level, and second energies are at the DFT level.

In the literature, the equatorially-capped trigonal bipyramid (Si_6-2) was found by Hartke [122] and Ramakrishna et al. [126] and the edge-capped trigonal bipyramid (Si_6-2) was found by Sieck et al. [63], Gong [131], Raghavachari et al. [55,56,175], Li et al. [150], and Wales et al. [174]. The octahedron (Si_6-3) was obtained by Luo et al. [172], Lu et al. [171], Hodbay et al. [173], Bolding-Anderson [59] with their potential and the Tersoff potential, and Iwamatsu [123] with the Gong potential.

Recently, Zdetsis [176] has challenged most of the ab-initio and DFT results published so far. He focused on the octahedron, the equatorially-capped trigonal bipyramid and edge-capped trigonal prism structures and performed ab-initio calculations at several levels of theory including HF, MP2, MP3, MP4(SDTQ), CCSD, and CCSD(T). Using the 6-31G* basis set, he found that at the MP2 level the octahedron was lower in energy than the other structures. However, with MP3, MP4(SDTQ), CCSD, and CCSD(T) the equatorially-capped trigonal bipyramid became lower in energy. With the D95* basis set, the overall picture was unchanged. These results are not in agreement with the early MP2, MP3, MP4(SDQ), and MP4 calculations using the 6-31G* basis set performed by Raghavachari et al. [175]. This situation indicates that Møller-Plesset perturbation theory gives poor performance and employing a higher level of theory is inevitable. These results are also not in agreement with the B3LYP calculation using the 6-31G* basis set performed in this thesis. This also suggests that especially for small energy differences B3LYP results have to be considered with precaution.

As a result, different levels of theory give different energy orderings for the candidate structures of Si_6. The reason behind these differences could be that small silicon clusters (at least in the size region n=2-5) actually are complicated multi-reference cases that should properly be treated by MCSCF/MRCI-methods [160]. The usual, much less expensive single-reference ab-initio treatments and standard DFT approaches do not describe the wavefunction qualitatively correctly. It is still a computational challenge to perform properly converged calculations of this type for representative regions of configuration space for a system of the size of Si_6. Therefore, the Si_6 case still has not been ultimately resolved yet.

Si_7: In contrast to Si_6, Si_7 seems to be a simple case. With both Set1 and Set2, a pentagonal bipyramid was obtained. This structure can also be derived by adding a cap atom to the equator of either the octahedron or the edge-capped trigonal bipyramid of Si_6. The pentagonal bipyramid was also found in the experimental studies (see section 2.1).

The pentagonal bipyramid has also been found many times in the literature [55,56,59,63,122,123,172,157]. For example, Mistirotis et al. [58] have found the pentagonal bipyramid with the SA method. In a very recent study, Zeng et al. [66] carried out ab-initio calculations (geometry optimizations at the MP2 level with the 6-31G* basis set followed by single point calculations at the CCSD(T) level with the same basis set) for several candidate structures in the range $7 \leq n \leq 11$. For Si_7, they also found the pentagonal bipyramid as the lowest energy structure.

Apart from the pentagonal bipyramid, there are only few other structures proposed for Si_7: Wales et al. [174] found one additional cap to the face-capped trigonal bipyramid. Surprisingly, Raghavachari et al. [56] found a tri-capped tetrahedron (it can also be understood as a capped octahedron) as the lowest energy structure. Li et al. [150] obtained a two-capped square pyramid. Bolding and Anderson [59] found a triangle capped rhombus with the SW potential and a two-capped trigonal bipyramid with the BH potential. Finally, Hodbay et al. [173] found a capped octahedron similar to the one found in the study of Raghavachari et al. [56].

Si_8: Three structures have been obtained for Si_8. These are Si_8-1 (stack of two rhombi) obtained with Set2, Set3, and Set4, Si_8-2 (two-capped octahedron) obtained with Set1, and Si_8-3 (distorted two-capped octahedron, capping positions are different from the ones in Si_8-2) obtained with Set1. At the model potential level with Set1, Si_8-2 is energetically more favorable. However, at the DFT level, Si_8-1 becomes the lowest energy isomer and is lower in energy than Si_8-2 and Si_8-3 by 1.95 eV and 2.19 eV, respectively. Up to Si_8, other global minimum structures might be derived from lower-size global minimum structures by capping. However, this situation is not valid for the case of Si_8.

The Si_8-1 structure is proposed for the first time in this current study. Si_8-2 and Si_8-3 have been reported before in the literature. More specifically, Si_8-2 was obtained by Luo et al. [172] and Mistriotis et al. [58]. Si_8-3 was reported by Ramakrishna et al. [126], Sieck et al. [63], Lu et al. [171], Gong [131], Raghavachari et al. [55], and Zeng et al. [66].

There are also other structures that have been proposed for Si_8 in the literature, different from those mentioned above: A cube was found in the study of Wales et al. [174], Iwamatsu [123] with the SW potential, Li et al. [150], and Bolding and Anderson [59] with the SW and BH potentials. Another structure proposed is a capped pentagonal bipyramid that was reported by Wang et al. [157] Iwamatsu [123] with the Gong potential, and Bolding and Anderson [59] with the Tersoff potential. A structure similar to the cube is the square antiprism that was also found by Bolding and Anderson [59] with their potential and by Hobday et al. [173].

Si_9: Two structures, namely Si_9-1 (two stacked rhombi with one cap) with Set1 and Set2 and Si_9-2 (tricapped trigonal prism) with Set1 have been obtained in this study. Si_9-1 is lower in energy both at the model and DFT levels. At the DFT level, Si_9-1 is lower in energy than Si_9-2 by only 0.43 eV.

Si_9-1 has been reported in the literature by Ramakrishna et al. [126], Sieck et al. [63], Lu et al. [171], and Zeng et al. [66]. Si_9-2 has been obtained by Luo et al. [172], Gong [131], Bolding and Anderson [59] with both their potential and Tersoff's potentials, as well as by Iwamatsu [123] with the Gong potential.

Apart from these structures, a capped cube was proposed by Wales et al. [174], Iwamatsu [123] with the SW potential, and Bolding and Anderson [59] with the SW potential. A tri-capped octahedron was reported by Mistriotis et al. [58] and Raghavachari et al. [55].

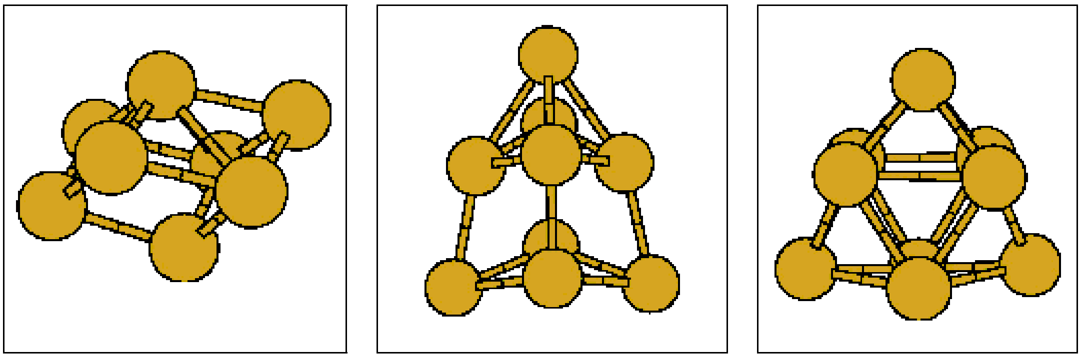

Si_8-3
with Set1
-41.70 eV
-29.37 eV

Si_9-1
with Set1 and Set2
-48.58 eV (Set1)
-34.75 eV

Si_9-2
with Set1
-48.51 eV
-34.32 eV

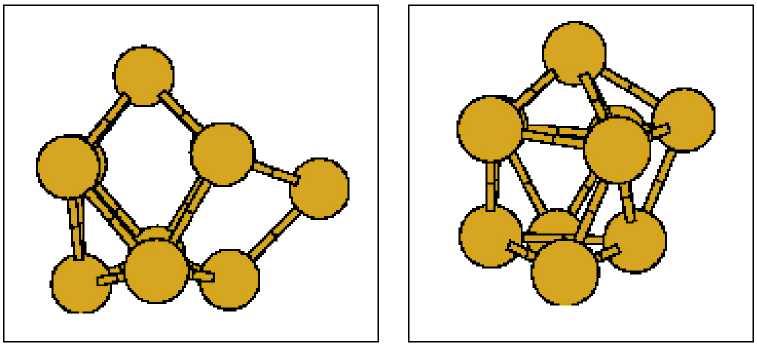

Si_{10}-1
with Set2
-49.01 eV
-42.81 eV

Si_{10}-2
with Set1
-54.79 eV
-39.55 eV

Figure 8.2: Geometries found for Si_n, $8 \leq n \leq 10$. First energies are at the model potential level, and second energies are at the DFT level.

Si_{10}: Two structures, Si_{10}-1 (tetra-capped trigonal prism (TTP)) with Set2 and Si_{10}-2 (slightly distorted two-capped square anti prism) with Set1, have been found in this study. Si_{10}-1 is much lower in energy than Si_{10}-2 by 3.26 eV. The TTP structure simply is the Si_9-2 structure (tri-capped trigonal prism) with an extra cap atom. A special interest has been given to these two structures, Si_{10}-1 and Si_9-2. This is due to the potential use of them as building blocks for medium-sized clusters as proposed in Ho et al. [7]. For this reason, a significant part of the present study was devoted to establishing a model potential that exhibits TTP as global minimum structure (or at least as very low-energy local minimum), as described in section 8.1.

The TTP structure was also found in the literature as the best structure for Si_{10} by Ramakrishna et al. [126], Luo et al. [172] (not exact TTP, a distorted version of

TTP), Lu et al. [171], Gong [131] (he also found a structure similar to Si_{10}-2, almost degenerate in energy with TTP), Iwamatsu [123] with the Gong potential, Zeng et al. [66], Bolding and Anderson [59] with both their and Tersoff's potentials, Wales et al. [174], and Hartke [122]. Raghavachari et al. [55,57], first proposed a tetra-capped octahedron (TCO) [56] but then he obtained TTP as lower in energy than TCO. Later, Raghavachari et al. [57] have put an end to the long debate about the best structure for Si_{10} by calculating single point energies of TCO and TTP at the QCISD(T) level (quadratic configuration interaction including the effects of triple excitations) with a polarized double-zeta (DZP) basis set using the effective core potential (ECP) approximation.

It is interesting that the Mistriotis potential [58] did not reproduce the exact TTP structure, instead a distorted tri-capped trigonal prism with an additional cap atom was found. Actually, this structure is similar to TTP, the only difference is the positioning of the additional cap atom. For this reason, modification of the Mistriotis potential was a very crucial step in order to get the TTP structure as the global minimum for Si_{10}.

As a summary, with parameter sets obtained from Mistriotis and modified Mistirotis model potentials have been extremely successful for finding the global minimum structures of small Si_n clusters with $n \leq 10$. In particular, a new global minimum structure could be found for Si_8, and a very hard case, Si_{10}, is resolved by finding the TTP structure, which may have importance as building block for larger clusters.

It is also apparent that none of the previous studies using empirical potentials could reproduce all the generally accepted global minimum structures up to Si_{10}. Typically, correct matches were obtained only for a few easy cases. This is in contrast to the performance of the modified Mistriotis potential established and tested in this study.

8.2.2 Structures of Si_n clusters for $11 \leq n \leq 14$

Global geometry optimizations at the model potential level have been continued beyond Si_{10}. It was hoped that the parameter sets fitted so successfully to Si_{10} (as described in the previous section) may continue to yield good structures also for medium-sized Si_n clusters. Structures obtained for the size range n=11-14 are shown in Fig. 8.3.

Si_{11}: A capped TTP (or pentacapped trigonal prism or bicapped Si_9-2), Si_{11}, was found as the best structure for Si_{11} with Set1, Set2, and Set4. Unfortunately, it seems to be only a low-energy local minimum for Si_{11} (see section 9.4). Similar structure to this one-capped TTP has also been found to be global minimum in the first-principles calculations of Zeng et al. [66]. The only difference in these structures is the positioning of the cap atoms.

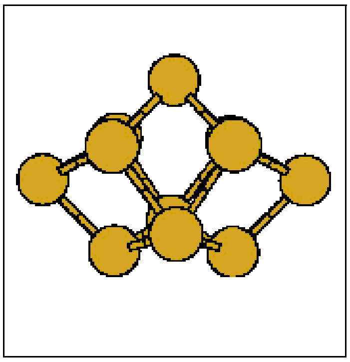

Si$_{11}$
with Set1, Set2, Set4
-61.57 eV (Set1)
-42.81 eV

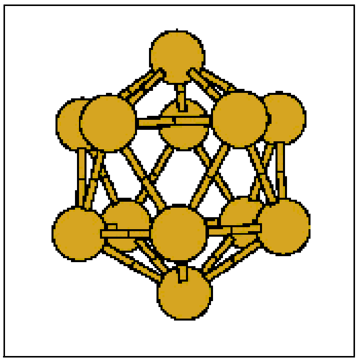

Si$_{12}$
with Set1, Set2, Set3
-60.31 eV (Set2)
-22.46 eV

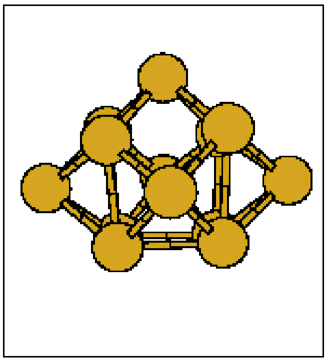

Si$_{13}$-1
with Set1
-74.51 eV
-48.97 eV

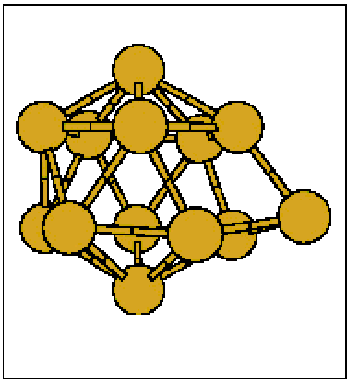

Si$_{13}$-2
with Set2
-65.58 eV
-27.97 eV

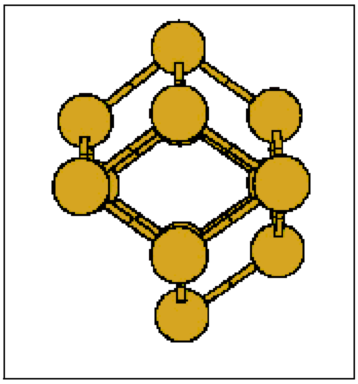

Si$_{13}$-3
with Set2
-65.66 eV
-23.81 eV

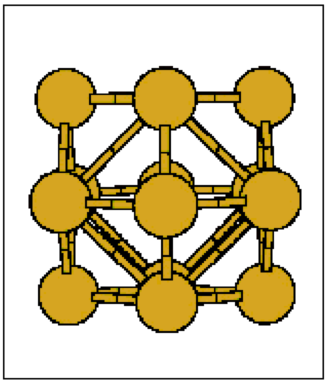

Si$_{14}$-1
with Set1
-82.06 eV
-53.67 eV

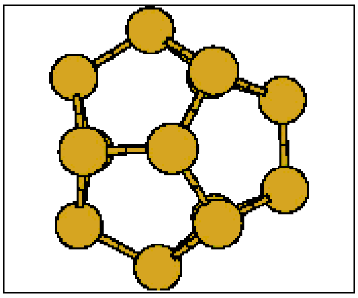

Si$_{14}$-2
with Set2 and Set3
-79.06 eV (Set3)
-29.61 eV

Figure 8.3: Geometries found for Si$_n$, $11 \le n \le 14$. First energies are at the model potential level, and second energies are at the DFT level.

Si_{12}: An icosahedron was found for Si_{12} with Set1, Set2, and Set3. This structure has a spherical and cage-like topology and it is not a continuation of the best Si_{11} structure found. Ramakrishna et al. [177] have also proposed the icosahedron structure for Si_{12} using TB-MD simulations. An icosahedron was also obtained in the study of Iwamatsu [123] with the Gong potential, by Gong et al. [93] using SA with his potential, by Lee et al. [178] using TB-MD simulations, and by Wang et al. [157] using a GA-TBMD methodology. As in the Si_{11} case, the best structure found for Si_{12}, an icosahedron, is a low-lying energy local minimum at the DFT level (see section .9.4)

Si_{13}: Three structures were found, Si_{13}-1 (a slightly distorted penta-capped cube) with Set1 and both Si_{13}-2 (singly capped icosahedron) and Si_{13}-3 (four stacked triangles with a cap on top) with Set2. At the DFT level, Si_{13}-1 is much lower in energy than both Si_{13}-2 and Si_{13}-3 by 21 eV and 25.16 eV, respectively. Si_{13}-1 and Si_{13}-2 were also proposed as the best structures for Si_{13} in the literature. In particular, Si_{13}-1 was first proposed by Grossman and Mitas [179] employing quantum Monte Carlo (QMC) simulations. Si_{13}-2 was obtained in the studies of Gong et al. [93], Lee, et al. [178], and Iwamatsu [123] with the Gong potential. All of the three structures found in this study are low-energy local minima just as in the cases of Si_{11} and Si_{12} at the DFT level (see section 9.4).

Si_{14}: Two structures were obtained as the best structures, Si_{14}-1 (hexa-capped cube) with Set1 and Si_{14}-2 (octa-capped trigonal prism) with Set2 and Set3. At the DFT level, Si_{14}-1 is lower in energy than Si_{14}-2 by 24.06 eV. The Si_{14}-2 structure was also found in the study of Sieck et al. [63] as a low-energy local minimum.

As a summary, for Si_n clusters with $11 \leq n \leq 14$, several structures were found. Most of them were already proposed as best structures in the literature. However, these structures are low-energy local minima (see section 9.4) at the DFT level. This behavior suggests that the performance of the parameter sets decreases beginning with Si_{11}.

8.2.3 Structures of Si_n clusters for $15 \leq n \leq 40$

Disagreement with the best literature results continues for still larger clusters. Generally, beginning with Si_{15}, the best clusters found in this study adopt structures in which there is at least one inner atom. The number of inner atoms increases up to 4 between Si_{30} and Si_{40}. To explain the general structural trend, some selected cluster sizes are shown in Fig.8.4

As indicated in the previous section, for Si_{13} and Si_{14} capped cube structures were found as the best structures with Set1. This trend also continues for Si_{15} for which a hexa-capped cube with an inner atom was found as the best structure. For larger clusters, this motif (hexa-capped with an additional inner atom) becomes dominant. As shown in Fig.8.4, for example, Si_{28} and Si_{32} contain lightly distorted versions of this building block at the bottom of the structures.

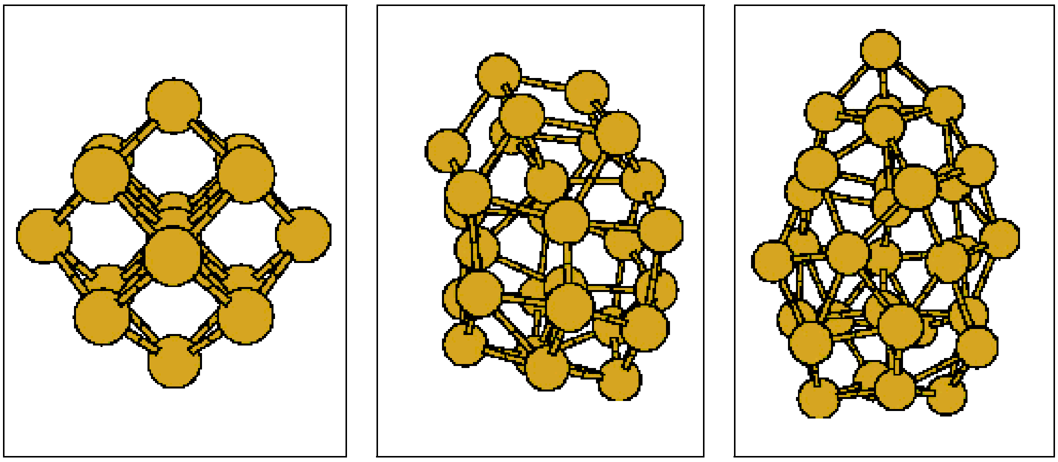

Si$_{15}$
with Set1

Si$_{28}$
with Set1

Si$_{32}$
with Set1

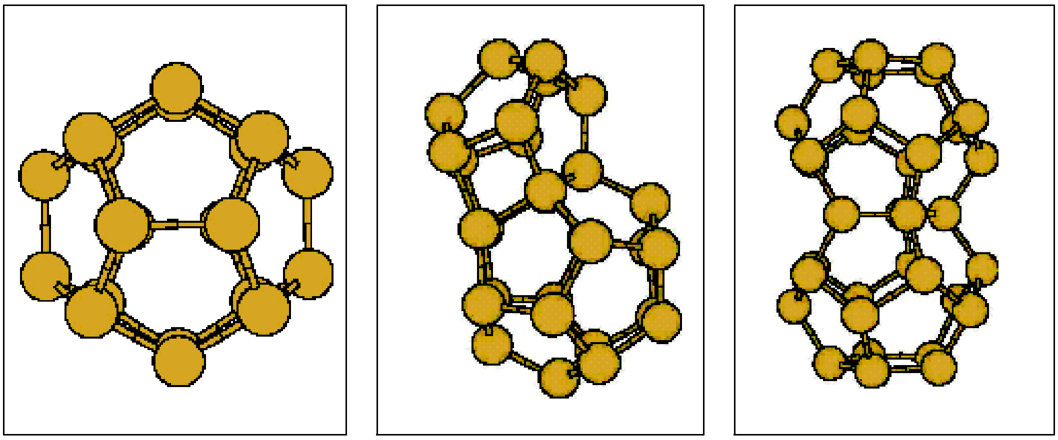

Si$_{20}$
with Set2 and Set3

Si$_{29}$
with Set3

Si$_{35}$
with Set2 and Set3

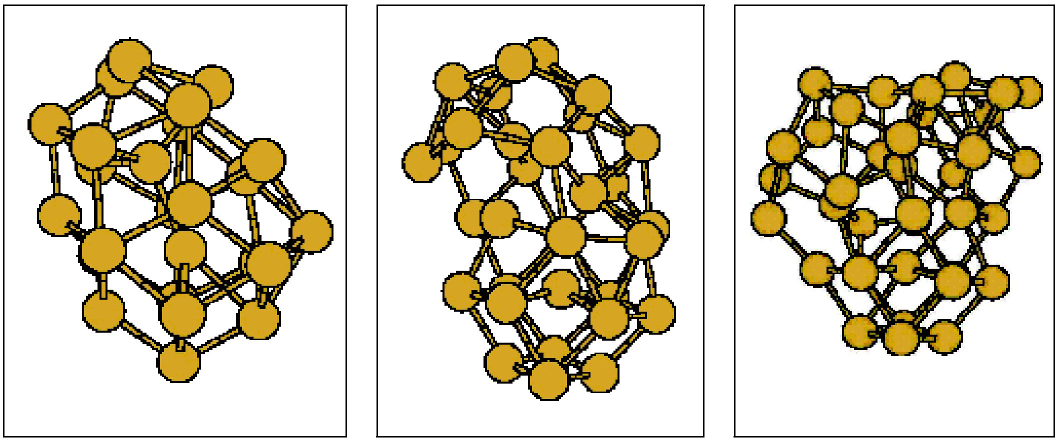

Si$_{25}$
with Set4

Si$_{32}$
with Set4

Si$_{38}$
with Set4

Figure 8.4: Geometries found for Si$_n$, $15 \leq n \leq 40$. Structures in the first row were obtained with Set1, in the second row with both Set2 and Set3, and in the last row with Set4.

With both Set2 and Set3, the structures found typically are cage structures. In particular, beginning with Si_{20}, a cage-like dodecahedron structure (containing five pentagons) becomes a building block. As shown in Fig. 8.4, a perfect dodecahedron, a cage consisting of 14 atoms attached to a dodecahedron, and a structure consisting of two fused dodecahedra with one atom missing have been found for Si_{20}, Si_{29}, and Si_{35}, respectively.

With Set4, another building block has appeared. As in the case of Set1, this building block contains a Si_{14} structure which can be defined as a sandwich of three layers, consisting of 4, 6, and 4 atoms, respectively. As examples, the best structures containing this building block for Si_{25}, Si_{32}, and Si_{38} are shown in Fig. 8.4. In all of these structures this building block is positioned at the bottom.

As a summary, structures obtained for the region $15 \leq n \leq 40$ are not similar to the global minimum structures proposed in the literature. Different growth patterns have been observed for the different parameter sets, although the performance of these parameter sets was not very different up to n=10. The structures from all the parameter sets are nearly prolate.

9 DFT relaxations and LMP2 energies for 10≤n≤19

During global parameter and geometry optimizations, a model potential has been used as a guiding function for DFT or ab-initio calculations. In this methodology, a good guiding function does not necessarily have to reproduce the correct energy ordering of the cluster structures, but it should reliably lead to low-energy minima on the DFT or ab-initio level. Therefore, structures obtained from global geometry optimizations using the Mistriotis and modified Mistriotis potentials were locally reoptimized at the DFT level. Global geometry optimization on the modified Mistriotis potential followed by relaxation at the DFT level has resulted in confirmation of some of the literature structures for $n \geq 10$ but also in several new structures with energies lower than those proposed in the literature so far. In addition to the local DFT optimizations, LMP2 single point calculations have been carried out for the relaxed structures obtained at the DFT level. In this Chapter, all the results obtained in this current study for Si_n clusters with $10 \leq n \leq 20$ are shown, in direct comparison to the structures proposed in the literature.

9.1 Structures and energies of Si_n clusters with 10≤n≤19

Lower energy Si_n clusters at the model potential and some selected Si_n clusters having different structural topologies have been further relaxed at the DFT level. For these geometry optimizations, the B3LYP hybrid functional with a 6-31G* basis set has been used up to $n \leq 15$. Additionally, single point energies of these DFT-relaxed structures have been calculated at the 2nd order local Møller-Plesset (LMP2) level of theory using the cc-pVTZ basis sets. All cluster energies given in the following tables are negative total atomization energies in eV. In all figures and tables, structures with a “Si” prefix are obtained in this study. Structures with “Jar” and “Jack” prefixes are taken from references [7] and [25], respectively.

In this section, results obtained in this study have been mostly compared to that of Ho et al. [7], Rata et al. [25], and Zeng at al. [66,67]. Ho et al. [7] examined the cluster sizes between 12-20 with a GA. Rata et al. [25] studied silicon clusters in the size range of 13-23 using a single parent GA. However, in their methodology, they have implemented a few new genetic operators that are directly able to produce prolate silicon clusters. Therefore, they did not perform an unbiased search for silicon clusters. Another weakness of their method is the use of only a single parent. This decreases the efficiency of the global search by reducing the diversity of children geometries. Overall, Rata et al. [25] aimed only for the production of prolate geometries since experimental studies (from IMM) have supported the existence of prolate structures for this size range. Zeng at al. [66,67] performed ab-initio calculations at MP2 and CCSD(T) levels for structures proposed in the literature, e.g. mostly for structures found by Ho et al. [7] and Rata et al. [25]. While employing high-level correlation treatments, they used only a small-size basis set (6-31G*). This suggests that the results obtained from Zeng et al. [66,67] must also be considered with some caution. In contrast to Zeng et al. [66,67], in this thesis the effect of electron correlation was examined at the better balanced LMP2/cc-pVTZ level. Hence, results obtained in this study offer more reliability.

Si_{10}: As discussed in the previous chapter, the accepted global minimum structure of Si_{10} is a TTP. There are also other low-energy minimum structures found in this study. Some of them are shown in Fig. 9.1 and their corresponding energies at both DFT and LMP2 levels are displayed in Table 9.1. Si_{10}-1 is a TTP, Si_{10}-2 is a distorted TTP (especially the trigonal prism unit is distorted and the positions of the cap atoms are different from that of Si_{10}-1), Si_{10}-3 is a different tetra-capped structure, namely a tetra-capped octahedron (TCO), Si_{10}-4 is a bicapped square antiprism, and Si_{10}-5 consists of a silicon dimer sandwiched by two rhombi.

At the DFT level, Si_{10}-1 (TTP) is the lowest-energy structure. It is lower in energy than the next local minimum structure, Si_{10}-2 (distorted TTP), by only 0.0035 eV. This is well below the accuracy of this level of theory, compared to experiment. Therefore, for DFT, these two structures are effectively degenerate in energy. This small energy difference increases to 0.018 eV for the case of the Si_{10}-3 structure. The TTP structure is also proposed as the lowest-energy structure in the literature [55,57,66,122,123,126,131,172], with a few exceptions: Raghavachari et al. [56] found Si_{10}-3 as the best structure, while Bolding and Anderson [59] and Wales et al. [174] found Si_{10}-4 as the lowest-energy structure with their and Tersoff's potentials.

However, LMP2 single point energy calculations for these structures are not completely in agreement with the results obtained from DFT calculations. The most striking difference is the change of the lowest-energy structure for Si_{10}. In particular, energy orderings of Si_{10}-1 and Si_{10}-2 at the DFT level are reversed at the LMP2 level: Si_{10}-2 becomes lower in energy than Si_{10}-1 by 0.0304 eV. This difference is comparable to the expected accuracy of MP2/cc-pVTZ, and therefore it is presumably real.

Si_{11}: Several different structures were found for Si_{11}. These and their corresponding energies both at the DFT and LMP2 levels are shown in Fig. 9.1 and Table 9.1, respectively. Si_{11}-1 contains two rhombi and three atoms inside these rhombi, Si_{11}-2 is a capped TTP structure, Si_{11}-3 is a tri-capped trigonal prism with two additional caps, and Si_{11}-4 is a penta-capped distorted trigonal prism. Si_{11}-1 was found by Zeng [180] a short time before we found it in this study. Si_{11}-2 was also proposed by Zeng et al. [66]. He obtained Si_{11}-2 by further relaxing a singly-capped Si_{10}-4 (bicapped square antiprism) at the MP2 level with a 6-311G(2d) basis set. Si_{11}-3 was predicted by Rohlfing and Raghavachari [57] based on HF/6-31G* and MP4SDQ/6-31G* calculations. Si_{11}-4 was proposed by Lee et al. [178] and Sieck et al. [63]. In the recent study of Zeng et al. [66], Si_{11}-2, Si_{11}-3, and Si_{11}-4 were considered at the MP2 level, with 6-31G* and 6-311G(2d) basis sets calculations. Then, he refined the energies of these structures by single point calculations at the CCSD(T) level, with the same basis sets. At the MP2/6-31G* and CCSD(T)/6-31G* levels, Si_{11}-4 was found as the lowest-energy structure. However, at the MP2/6-311G(2d) level, Si_{11}-2 and Si_{11}-4 were obtained as isoenergetic. Additionally, at the CCSD(T)/6-311G(2d) level, Si_{11}-3 became the lowest-energy structure. At the same level of theory, Si_{11}-2 was lower in energy than Si_{11}-4.

In the present study, energy orderings obtained from Zeng et al. [66] are changed at both DFT/B3LYP/6-31G* and LMP2/cc-pVTZ levels. At the DFT level, Si_{11}-1 (this structure can be derived easily by adding an extra atom to the two-atom group inside of these two rhombi of Si_{10}-5) is found as the lowest-energy structure. Si_{11}-1 is lower in energy than the next stable structure, Si_{11}-2, by 0.0707 eV. Si_{11}-2 is followed by Si_{11}-3 and Si_{11}-4 is found as the energetically least favorable isomer. However, at the LMP2 level, the picture is totally changed. Si_{11}-2 became the lowest-energy structure. Surprisingly, Si_{11}-1 is found as the least favorable isomer. Si_{11}-2 is lower in energy than the next stable isomer, Si_{11}-4, by only 0.1001 eV. Interestingly, for Si_{10}, Si_{10}-5 is found as the least stable isomer, and for Si_{11}, a derivative of Si_{10}-5, Si_{11}-1, is also found as the least stable structure at the LMP2 level.

Table 9.1: Energies and energy orderings of Si_{10}, Si_{11}, and Si_{12} at the DFT and LMP2 levels.

Structure	DFT (eV)	Order (DFT)	LMP2 (eV)	Order (LMP2)
Si_{10}-1	**-43.5904**	1	-50.7805	2
Si_{10}-2	-43.4579	2	**-50.8109**	1
Si_{10}-3	-43.2202	3	-49.9144	4
Si_{10}-4	-42.7341	4	-50.2757	3
Si_{10}-5	-42.5160	5	-48.5132	5
Si_{11}-1	**-47.4230**	1	-54.2363	4
Si_{11}-2	-47.3523	2	**-54.9661**	1
Si_{11}-3	-47.3382	3	-54.8237	3
Si_{11}-4	-47.1257	4	-54.8660	2
Si_{12}-1	**-51.9813**	1	**-59.8530**	1
Si_{12}-2	-51.4603	2	-59.1649	3
Si_{12}-3	-51.3234	3	-59.1709	2

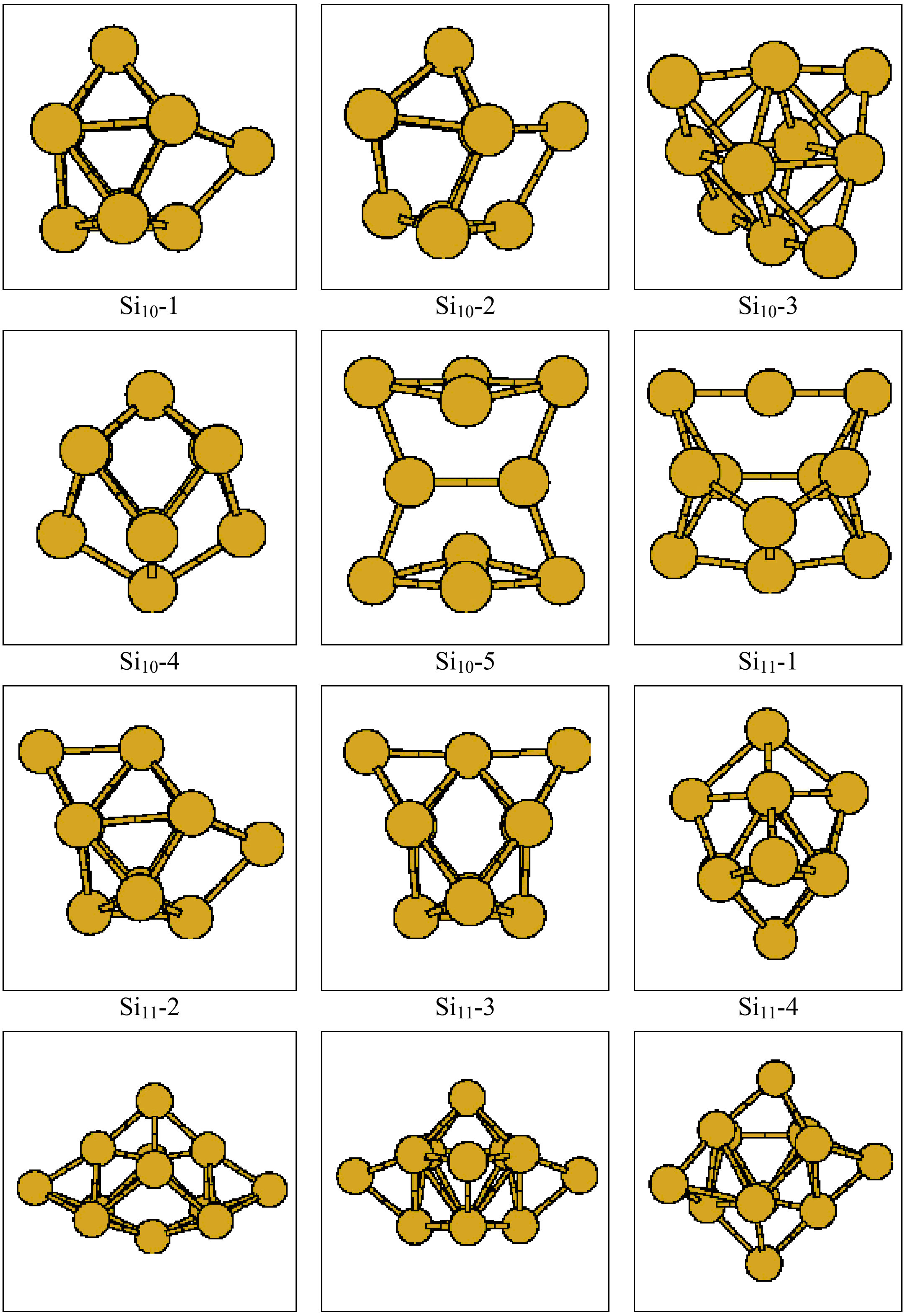

Si$_{10}$-1 Si$_{10}$-2 Si$_{10}$-3

Si$_{10}$-4 Si$_{10}$-5 Si$_{11}$-1

Si$_{11}$-2 Si$_{11}$-3 Si$_{11}$-4

Si$_{12}$-1 Si$_{12}$-2 Si$_{12}$-3

Figure 9.1: Structures found for Si$_{10}$, Si$_{11}$ and Si$_{12}$ at the DFT/B3LYP level.

For Si_{11}, it is apparent that the Si_{11}-2 isomer is the global minimum structure. This is very reasonable since it contains a very stable TTP unit.

Si_{12}: Three structures were identified for Si_{12}. Si_{12}-1 is a hexa-capped trigonal prism, which was also proposed by Ramakrishna et al. [126], Ho et al. [7], and Lu et al. [171]. Another isomer, Si_{12}-2, is also a hexa-capped trigonal prism, but the trigonal prism is slightly distorted. It can also be defined as bicapped TTP. This structure was also proposed by Sieck et al. [63]. Si_{12}-3 is a continuation of Si_{10}-4 and Si_{11}-4, by simple cappings. In the recent study of Zeng et al. [67] (a continuation study to [66]), the Si_{12}-1 structure was located in geometry optimizations at the MP2/6-31G* level. He also calculated the single point energies of his MP2 structures at several levels of theory such as MP3/6-31G*, MP4(SDQ)/ 6-31G*, CCSD/6-31G*, and CCSD(T)/ 6-31G*, finding Si_{12}-1 as the lowest-energy structure at all of these levels.

In this current study, Si_{12}-1 is found as the lowest-energy structure at the DFT/B3-LYP level. Si_{12}-1 is lower in energy than Si_{12}-2 and Si_{12}-3 by 0.521 eV and 0.6579 eV, respectively. For Si_{12}, LMP2 energy orderings agree with those of DFT. At the LMP2 level, Si_{12}-1 is the lowest-energy structure lower in energy than Si_{12}-2 and Si_{12}-3 by 0.6881 eV and 0.6821 eV, respectively.

Results obtained from this study and Zeng et al. [67] are completely in agreement for the global minimum structure of Si_{12}, as Si_{12}-1.

Si_{13}: Several structures were found for Si_{13} and some of them are shown in Fig. 9.2. Their corresponding energies at both the DFT and LMP2 levels are shown in Table 9.2. Si_{13}-1 is a hepta-capped trigonal prism which is proposed in this study for the first time. Actually, a similar structure was proposed by Rata et al. [25] for the Si_{13} cation. Si_{13}-2 is a singly capped Si_{12}-1 structure and it is also found for the first time here. Si_{12}-5 can be described as a distorted tri-capped trigonal prism with an additional rhombus attached to the bottom of the trigonal prism unit. Si_{12}-5 was already proposed in the literature by Sieck et al. [63] and Lu et al. [171]. It seems that in the literature Si_{12}-5 was the most frequently found structure. This structure was also considered in the MP2/6-31G* geometry optimization study of Zeng et al. [67]. There, Si_{12}-5 was not found as the lowest-energy structure at the MP2 and MP3 levels, however, it appeared energetically favorable at the MP4(SDQ), CCSD, and CCSD(T) levels of theory.

In this current study, at the DFT level, results were obtained that differ from Zeng's [67] ab-initio ones. More specifically, the most frequently found structure in the literature, Si_{13}-5, is found here as the least stable isomer. The lowest-energy structure is Si_{13}-1, followed by Si_{13}-2. Si_{13}-1 is lower in energy than Si_{13}-2 and Si_{13}-5 by 0.0616 eV and 0.3445 eV, respectively. In contrast, at the LMP2 level, the Si_{13}-5 structure is obtained as the lowest-energy structure as in the Zeng et al. [67] study.

Si_{13}-2 is the second most stable isomer. Si_{13}-3 is lower in energy than Si_{13}-2 and Si_{13}-1 by 0.0925 eV and 0.1791 eV, respectively.

Similar to Si_{12} case, for Si_{13} there is a consensus in the results obtained in this study and in the literature for the candidate global minimum structure, Si_{13}-5.

Si_{14}: There are fewer papers in the literature on *n*>=14. Most of the structures found in this study are shown in Fig. 9.2 and their corresponding energies are listed in the Table 9.2. Si_{14}-1 is a new structure and has been found for the first time in this study. It consists of two fused, bent pentagons at the bottom and a 6-atom ring in boat form on top. Si_{14}-2, is very similar to Si_{14}-1, the only difference being that both the 6-ring and the two fused 5-rings are in a chair-like conformation in Si_{14}-2. Si_{14}-3 can be described as two rhombi with a strongly puckered sixfold ring in-between. All of these three structures have been found for the first time in this study. Si_{14}-4 is a stack of two distorted rhombi, one fivefold ring, and an atom on top. It can also be described as a rhombus attached to Si_{10}-4. Si_{14}-4 was presented most frequently as the lowest-energy isomer for Si_{14} in the literature. It was first proposed by Sieck et al. [63] and then confirmed by Liu et al. [41]. Both Si_{14}-5 and Si_{14}-6 contain a distorted trigonal prism unit and also these structures were found for the first time in this study. Si_{14}-5 can be seen as a rhombus attached to a distorted TTP. Si_{14}-6 is very similar to Si_{14}-5, differing only by the placement of one of the cap atoms of the TTP unit and of the rhombus unit. There is only one structure in the literature resembling Si_{14}-5 and Si_{14}-6, it was, however, proposed for the Si_{14} cation by Rata et al. [25]. Zeng et al. [67] also considered Si_{14}-4 in his ab-initio calculations, finding Si_{14}-4 as

Table 9.2: Energies and energy orderings of Si_{13}, Si_{14}, and Si_{15} at the DFT and LMP2 levels.

Structure	DFT (eV)	Order (DFT)	LMP2 (eV)	Order (LMP2)
Si_{13}-1	**-56.4186**	1	-64.6071	3
Si_{13}-2	-56.3570	2	-64.6937	2
Si_{13}-3	-56.1479	3	-64.6071	3
Si_{13}-4	-56.1059	4	-64.3061	4
Si_{13}-5	-56.0741	5	**-64.7862**	1
Si_{14}-1	**-61.6597**	1	-69.4694	4
Si_{14}-2	-61.3652	2	-68.7155	6
Si_{14}-3	-61.1337	3	-68.7861	5
Si_{14}-4	-60.9757	4	-70.4508	2
Si_{14}-5	-60.8594	5	**-70.5150**	1
Si_{14}-6	-60.8530	6	-70.3234	3
Jar-Si_{15}	**-65.6001**	1	**-75.6097**	1
Si_{15}-1	-65.5377	2	-75.0220	2
Si_{15}-2	-65.0808	3	-74.9471	3

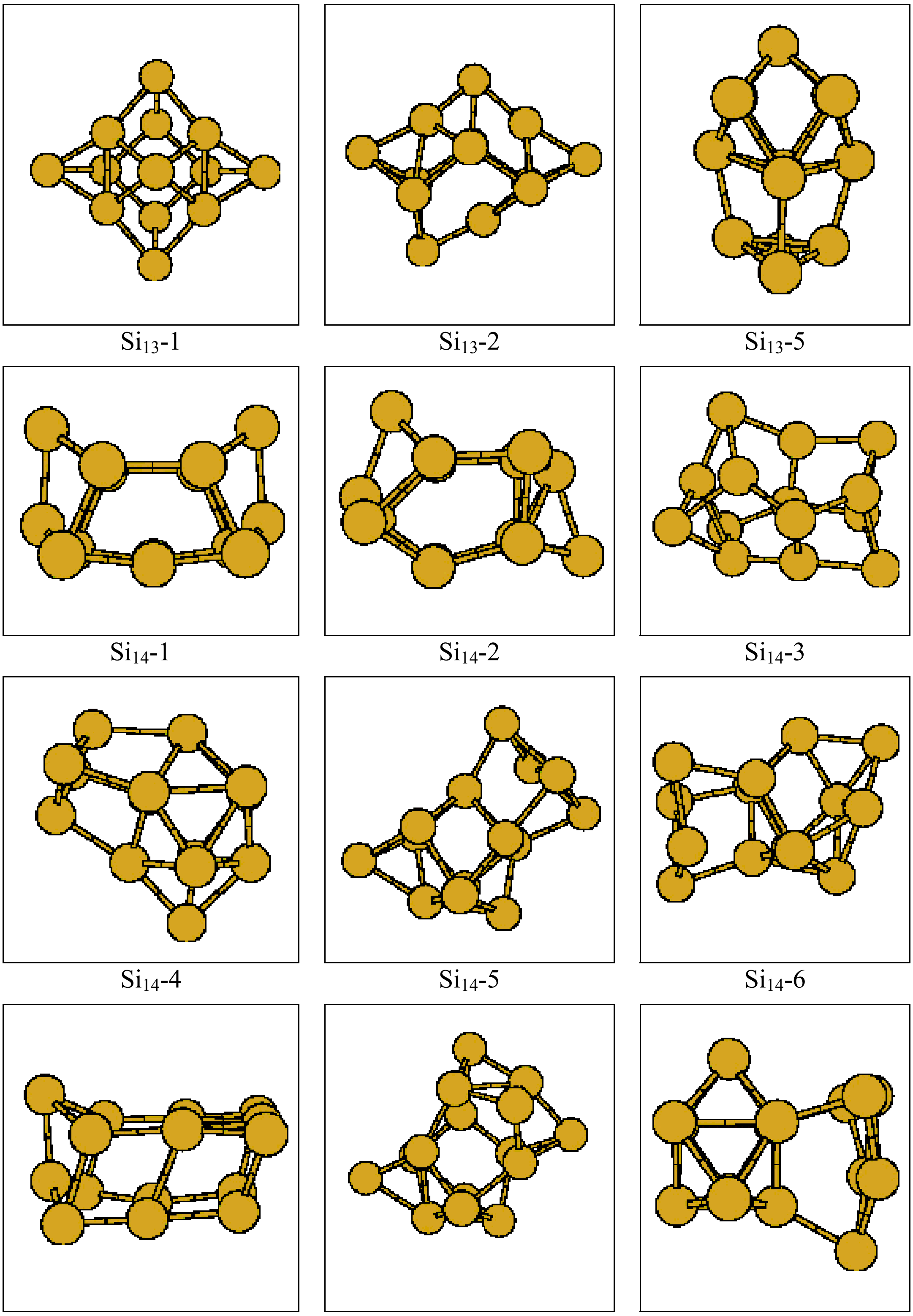

Si$_{13}$-1 Si$_{13}$-2 Si$_{13}$-5

Si$_{14}$-1 Si$_{14}$-2 Si$_{14}$-3

Si$_{14}$-4 Si$_{14}$-5 Si$_{14}$-6

Si$_{15}$-1 Si$_{15}$-2 Jar-Si$_{15}$

Figure 9.2: Sructures found here and in the literature for Si$_{13}$, Si$_{14}$, and Si$_{15}$ at the DFT/B3LYP level.

the lowest-energy structure at every level of theory applied. Unfortunately, in his calculations, the other structures shown in Fig. 9.2 were not included. Nevertheless, it may be concluded from the literature that the Si_{14}-4 isomer is very low in energy.

In this study, at the DFT level, Si_{14}-1 was found as the lowest-energy isomer, followed by the Si_{14}-2 isomer. In contrast, the rhombus capped TTP structures Si_{14}-5 and Si_{14}-6 were obtained as the energetically least favorable structures. Si_{14}-1 is lower in energy than Si_{14}-2, Si_{14}-5, and Si_{14}-6 by 0.2945 eV, 0.8003 eV, and 0.8067 eV, respectively. It is clear that DFT prefers the puckered pentagons structures over the rhombus capped TTP structures. However, this quantitative and qualitative preference is totally changed at the LMP2 level where Si_{14}-5 is the lowest-energy structure. The second most stable structure was found as Si_{14}-4 which was also found as the lowest-energy structure by Zeng et al. [67] as mentioned above. Si_{14}-5 is lower in energy than Si_{14}-4 by only 0.0642 eV. However, this energy difference increases to 1.0456 eV in the case of Si_{14}-1.

Similar to previous cluster sizes, for Si_{14} at the LMP2 level, a structure containing a trigonal prism unit, Si_{14}-5, became the lowest-energy isomer.

Si_{15}: With Si_{15}, the number of studies performed to search for global minimum structures decreases further, obviously due to the steeply increasing computational cost. Actually, only the studies of Ho et al. [7] and Rata et al. [25] cover this size of Si_n clusters in the literature.

Some of the selected Si_{15} cluster structures and their corresponding energies are displayed in Fig. 9.2 and Table 9.2. The structures shown are generally prolate isomers. Spherical clusters have also been obtained, however, their DFT and LMP2 energies are higher than those of the isomers shown in Fig. 9.2. Si_{15}-1 contains puckered pentagon units very similar to Si_{14}-1 and Si_{14}-2. It can be described as a stack of two puckered pentagons fused with two adjacent tetrahedrons. Si_{15}-1 can also be seen as a continuation of Si_{14}-5, however, this time the distortion of the trigonal prism and positioning of the capped atom are slightly different, placement of the capped rhombus is also changed, and an additional atom is capped to the rhombus. Briefly, Si_{15}-2 can be described as a rhombus attached to a distorted TTP, with an additional cap atom on the rhombus. Jar-Si_{15} is taken from the study of Ho et al. [7]. It consists of a connection of a tri-capped trigonal prism unit and an almost planar 6-atom group.

In the recent ab-initio study of Zeng et al. [67], Jar-Si_{15} was also considered. Additionally, he also included a fused tri-capped trigonal prism structure that was proposed for the Si_{15} anion by Rata et al. [25] into his calculations. In Zeng's study, at the MP2 and MP4(SDQ) levels, Rata's structure became energetically favorable, however, at the MP3, CCSD, and CCSD(T) levels Jar-Si_{15} was found as the lowest-energy structure.

Similarly, in this current work, Jar-Si_{15} is obtained as the lowest-energy structure at the DFT level. This structure is lower in energy than Si_{15}-1 and Si_{15}-2 by 0.0624 eV and 0.5193 eV respectively. At the LMP2 level, the overall picture is preserved, with increased energy differences. More specifically, Jar-Si_{15} is obtained as the lowest-energy structure, lower in energy than Si_{15}-1 and Si_{15}-2 by 0.5877 eV and 0.6626 eV, respectively.

For Si_{15}, there is an agreement between the results obtained from this study (both DFT and LMP2 levels) and in the literature [67]. All results indicate that the Jar-Si_{15} isomer is the candidate global minimum structure for Si_{15}. The Si_{14}-5 isomer is the candidate global minimum structure for Si_{14}. Si_{15}-2 is only a further capped Si_{14}-5. But, for Si_{15}, the Si_{15}-2 isomer was not obtained as the lowest-energy isomer. This is probably due to the fact that capping the Si_{14}-5 isomer distorted the very stable TTP unit in the Si_{15}-2 isomer. For this reason, the Si_{15}-2 isomer is not favored at LMP2 level.

Si_{16}: Several different structures have been found for Si_{16} such as spherical structures, structures containing puckered pentagons like Si_{14}-1 and Si_{15}-1, and structures containing trigonal prisms. Some of those structures and their corresponding energies are shown in Fig. 9.3 and Table 9.3. Si_{16}-1 is a combination of puckered pentagon and trigonal prism structures. It consists of a sandwich of two pentagons at one end which is fused with a TTP. The TTP structure differs from Si_{10}-1 only by the position of one cap atom. Si_{16}-2 consists of a slightly distorted bicapped square antiprism (Si_{10}-4) with an additional group on top, consisting of two fused rhombi. Si_{16}-3 is very similar to Si_{16}-1; it consists of a tetra-capped trigonal prism fused with two layers of puckered pentagons.

In the literature, Ho et al. [7] proposed two different structures shown in Fig. 9.3, namely Jar-Si_{16}-1 and Jar-Si_{16}-2. Jar-Si_{16}-1 is based on the distorted trigonal prism unit, while Jar-Si_{16}-2 contains puckered pentagons similar to Si_{14}-1. Of these two structures, they have predicted Jar-Si_{16}-2 as the lowest-energy isomer. This isomer differs from the other isomers proposed in this study for smaller cluster sizes by not having a trigonal prism unit. Zeng et al. [67] also considered these two structures in his ab-initio calculations. In those calculations, Jar-Si_{16}-1 was obtained as the lowest-energy structure at the MP2 and MP4(SDQ) levels, whereas at the MP3, CCSD, and CCSD(T) levels, Jar-Si_{16}-2 became the lowest-energy isomer.

In the DFT results of this current study, Jar-Si_{16}-2 is found as the lowest-energy isomer. This is followed by the Si_{16}-1 isomer. The energy difference between these structures is only 0.1925 eV. Jar-Si_{16}-1 is found as the least stable isomer. However, at the LMP2 level, energy orderings are changed drastically. The best structure at the DFT level moves to the end of the list at the LMP2 level. Simultaneously, the Jar-Si_{16}-1 isomer, which was at the end of the DFT list, becomes the lowest-energy structure at the LMP2 level. However, Jar-Si_{16}-1 is lower in energy than Si_{16}-1 by only 0.0394 eV.

For Si_{16}, Zeng et al. [67] found Jar-Si_{16}-2 as the lowest-energy isomer at the CCSD(T) level. In contrast, LMP2 results of this study suggest Jar-Si_{16}-1 as the lowest-energy isomer. As explained at the beginning of this section, Zeng's ab-initio results must be evaluated with caution. Therefore, Jar-Si_{16}-1 is the candidate global minimum structure for Si_{16}.

Table 9.3: Energies and energy orderings of Si_{16}, Si_{17}, and Si_{18} at the DFT and LMP2 levels.

Structure	DFT (eV)	Order (DFT)	LMP2 (eV)	Order (LMP2)
Jar-Si_{16}-2	**-69.1742**	1	-79.7475	5
Si_{16}-1	-68.9817	2	-80.0146	2
Si_{16}-2	-68.6881	3	-79.9304	3
Si_{16}-3	-68.5381	4	-79.7778	4
Jar-Si_{16}-1	-68.4245	5	**-80.0540**	1
Jar-Si_{17}	**-73.6198**	1	-85.3676	4
Si_{17}-1	-73.5806	2	-85.4325	3
Si_{17}-2	-73.5385	3	-85.6061	2
Si_{17}-3	-73.1400	4	**-85.6370**	1
Jack-Si_{18}	**-78.1298**	1	-90.9715	3
Jar-Si_{18}	-78.0719	2	-91.1921	2
Si_{18}-1	-77.8205	3	-88.2656	6
Si_{18}-2	-77.7254	4	**-91.5439**	1
Si_{18}-3	-77.5880	5	-89.8334	5
Si_{18}-4	-77.5805	6	-90.9911	4

Si_{17}: Just as in the case of Si_{16}, for Si_{17}, spherical structures, structures containing puckered pentagons, and trigonal prism based structures were found. Some of them are shown in Fig. 9.3 and their corresponding energies are listed in Table 9.3. Actually, only trigonal prism based structures are shown in Fig. 9.3 since other structural patterns are higher in energy at both the DFT and LMP2 levels. Si_{17}-1 can be described as a bicapped square antiprism (Si_{10}-4) attached to a puckered Si_7 unit. Si_{17}-2 consists of a tri-capped trigonal prism and a Si_6 unit composed of fused rhombi, with an additional single bridging atom between these two groups. A structure similar to Si_{17}-2 was proposed by Rata et al. [25]. However, the main difference between them is the positioning of the Si_6 unit composed of fused rhombi. Si_{17}-3 consists of a slightly distorted tetra-capped trigonal prism with an additional group attached to it that consists of two fused rhombi.

After finding a non-trigonal prism structure for Si_{16}, Ho et al. [7] located Jar-Si_{17} as the best Si_{17} isomer. This structure contains a TTP with a Si_6 unit composed of fused rhombi and an additional bridge atom attached to it, similar to the Si_{17}-2 isomer. In the ab-initio calculations by Zeng et al. [67], the Jar-Si_{17} isomer was also evaluated and this structure was obtained as the lowest-energy isomer at all levels of theory considered.

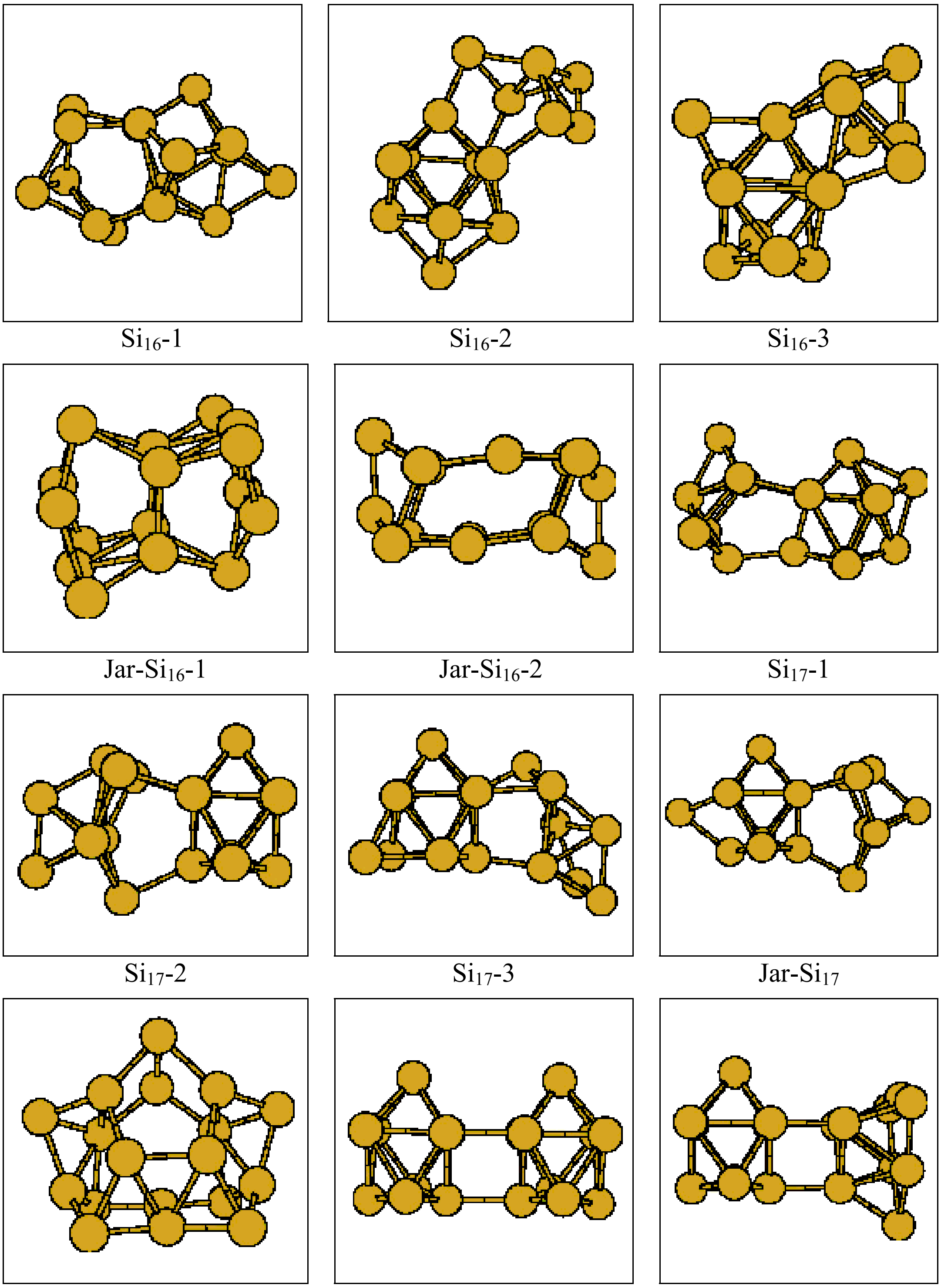

Si$_{16}$-1 Si$_{16}$-2 Si$_{16}$-3

Jar-Si$_{16}$-1 Jar-Si$_{16}$-2 Si$_{17}$-1

Si$_{17}$-2 Si$_{17}$-3 Jar-Si$_{17}$

Si$_{18}$-1 Si$_{18}$-2 Jar-Si$_{18}$

Figure 9.3: Sructures found here and in the literature for Si$_{16}$, Si$_{17}$, and Si$_{18}$ at the DFT/B3LYP level.

The DFT/B3LYP calculations performed in this study favored Jar-Si_{17} as the lowest-energy isomer, as in the study of Zeng et al. [67]. Si_{17}-1 was obtained as second most stable isomer. The energy difference between them is only 0.0392 eV. However, at the LMP2 level, the picture obtained from DFT calculations is totally overturned. In particular, Si_{17}-3, the worst structure at the DFT level, became the lowest-energy isomer at the LMP2 level. And, surprisingly, the DFT-champion Jar-Si_{17} was placed at the end of the energy list. Finally, in contrast to Si_{16}, even the intermediate minima change their ordering: Si_{17}-3 and Si_{17}-2 have switched places. The energy difference between these two structures, however, is only 0.0309 eV.

For Si_{17}, a new structure found in this study, Si_{17}-3, is the lowest-energy isomer at LMP2 level. This structure is a combination of the lowest-energy isomer of Si_6, the equatorially-capped trigonal bipyramid, and a TTP (slightly distorted). This combination makes the structure more stable. As a result, Si_{17}-3 is the global minimum structure for Si_{17}.

Si_{18}: The same trends that appeared in Si_{16} and Si_{17} continue for the case of Si_{18}. In particular, structures having significantly different topologies have been obtained after the relaxation at the DFT level. Some of the structures and their corresponding energies are displayed in Fig. 9.3 and Table 9.3. Si_{18}-1 is a spherical structure, again containing puckered pentagons and a Si_6 group composed of fused rhombi with an addition of rhombi. Si_{18}-2 can be defined as a combination of two tri-capped trigonal prism units.

In the literature, Ho et al. [7] proposed the Jar-Si_{18} isomer which consists of an attachment of a unit composed of a triangle and a puckered Si_6 to a tri-capped trigonal prism unit. Rata et al. [25] has also proposed a cation structure Si_{18} shown in Fig. 9.4, Jack-Si_{18}, which can be defined as a connection of a tri-capped trigonal prism with an octahedron by a three-atom bridge. In the ab-initio calculations of Zeng et al. [67], Jar-Si_{18}, Si_{18}-2, and Jack-Si_{18} were considered. In these calculations, at the MP2 level, Si_{18}-2 was found as the lowest energy isomer. However, at the MP3, MP4(SDQ), CCSD, and CCSD(T) levels, Jack-Si_{18} was located as the best energy structure.

In the DFT results of this current study, the Jack-Si_{18} isomer was obtained as the lowest-energy structure. Another literature result, Jar-Si_{18}, became the second most favorable structure. Jack-Si_{18} is lower in energy than Jar-Si_{18} by 0.0579 eV. After these two prolate structures, a spherical isomer Si_{18}-1 was found as the third lowest-energy isomer for Si_{18}. Surprisingly, another prolate structure Si_{18}-2 followed the spherical Si_{18}-1 isomer. This structure is one of the least stable isomers at the DFT level. However, at the LMP2 level, results appeared contradictory to the DFT ones. The spherical Si_{18}-1 isomer is placed at the end of the energy list. Si_{18}-2 was found as the lowest-energy isomer for Si_{18}, followed by Jar-Si_{18}. The energy difference between these two structures is 0.3518 eV.

For Si_{18}, in the study of Zeng et al. [67] the most important structures have been considered. They found Si_{18}-2 as the lowest-energy isomer at MP2 level. However, at CCSD(T) level Jack-Si_{18} was found as the lowest-energy isomer. Similar to their MP2 results, LMP2 results of this thesis supports Si_{18}-2 isomer against Jack-Si_{18}. As explained at the beginning of this section, their CCSD(T) results are not completely convincing because of the use of a small basis set. As a result, Si_{18}-2 may be a slightly better candidate for the global minimum structure for Si_{18}.

Si_{19}: For Si_{19}, the structures obtained are generally spherical. Some of them are depicted in Fig. 9.4 and their corresponding DFT and LMP2 level energies are listed in Table 9.4. Si_{19}-1 is based on the tri-capped trigonal prism unit with additional pentagons and rhombi. Si_{19}-2 has a spherical nature and it can be derived by capping Si_{18}-1.

In the literature, Ho et al. [7] proposed the spherical Jar-Si_{19}-1 isomer and the prolate Jar-Si_{19}-2 and Jar-Si_{19}-3 isomers. Jar-Si_{18}-1 consists of a cage including several pentagons and planar rhombi with an additional inner atom inside this cage. Jar-Si_{19}-2 is a combination of a slightly different TTP (Si_{10}-1) and a tri-capped trigonal prism unit. Jar-Si_{19}-3 is a combination of a tri-capped trigonal prism unit and a bicapped square antiprism (Si_{10}-4) unit. Additionally, Rata et al. [25] proposed a Si_{19} isomer, Jack-Si_{19}, which is a connection of a distorted Si_{10}-4 with an octahedron by a three-atom bridge. This structure contains the same octahedron and three-atom bridge units as the Jack-Si_{18} isomer.

Zeng et al. [67] considered the Jar-Si_{19}-1, Jar-Si_{19}-3, and Jack-Si_{19} isomers in his ab-initio calculations. Surprisingly, though, he did not include the Jar-Si_{19}-2 isomer. In his results, Jack-Si_{19} became the energetically favorable isomer only at the MP3 level. However, at the other levels of theory considered, the spherical Jar-Si_{19}-1 isomer was obtained as the lowest-energy isomer.

Table 9.4: Energies and energy orderings of Si_{19} at the DFT and LMP2 levels.

Structure	DFT (eV)	Order (DFT)	LMP2 (eV)	Order (LMP2)
Jack-Si_{19}	**-82.8240**	1	-96.5117	2
Jar-Si_{19}-2	-82.2977	2	**-96.6290**	1
Jar-Si_{19}-3	-82.2290	3	-96.2257	3
Jar-Si_{19}-1	-82.1972	4	-94.4282	5
Si_{19}-3	-81.8483	5	-94.2751	6
Si_{19}-1	-81.6600	6	-94.7954	4
Si_{19}-2	-81.6157	7	-92.6921	7

In the DFT results of this current study, Jack-Si_{19} was found as the lowest-energy isomer. This was followed by Jar-Si_{19}-2, Jar-Si_{19}-3, and Jar-Si_{19}-1. Jack-Si_{19} is lower in energy than the next stable isomer, Jar-Si_{19}-2, by 0.5263 eV. Overall, our and literatureDFT results suggest that spherical clusters are not favorable in contrast to the results by Zeng et al. [67]. At the LMP2 level, the energy ordering from the DFT level is not preserved. This time, another prolate isomer, Jar-Si_{19}-2, was obtained as the lowest-energy structure. This is followed by the Jack-Si_{19} isomer. The energy difference between them is only 0.1173 eV. In spite of the differences in the energy orderings, the qualitative structural results are the same for DFT and LMP2: Some prolate structures are energetically more favorable than the best spherical ones. This is in agreement with the experimental results for this cluster size.

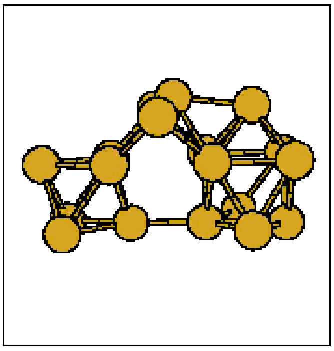
Jack-Si_{18}

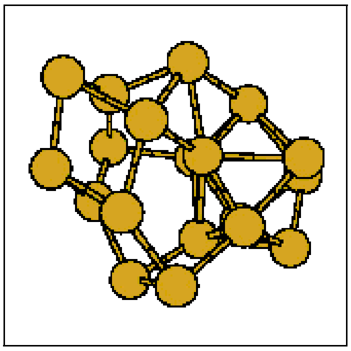
Si_{19}-1

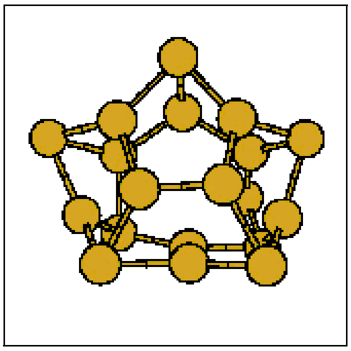
Si_{19}-2

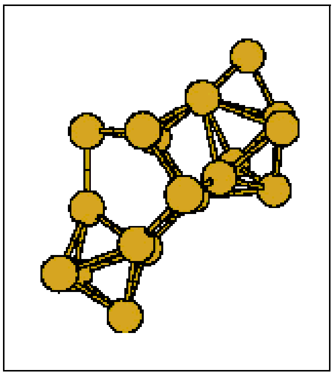
Jack-Si_{19}

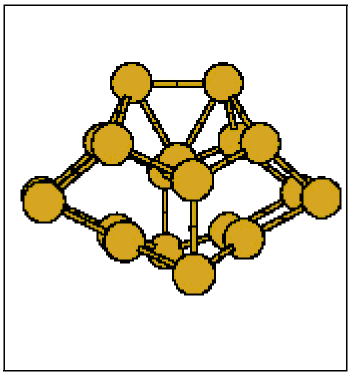
Jar-Si_{19}-1

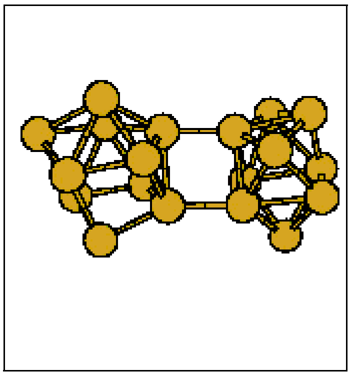
Jar-Si_{19}-2

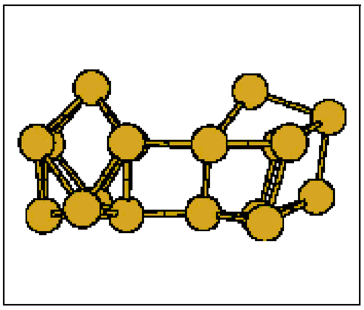
Jar-Si_{19}-3

Figure 9.4: Structures found here and in the literature for Si_{18} and Si_{19} at the DFT/B3LYP level.

In the study of Zeng et al. [67], for Si_{19} a spherical isomer, Jar-Si_{19}-1, was obtained as the lowest-energy isomer. This is very surprising since structural transition from prolate to spherical is expected to occur approximately with Si_{25}. In contrast, in this current study, the same spherical isomer, Jar-Si_{19}-1, and the other spherical isomers were found less stable than the prolate isomers at LMP2 level. Jar-Si_{19}-2 was obtained as the lowest-energy isomer for Si_{19} at LMP2 level. As explained at the beginning of this section, results obtained in this thesis are presumably more reliable and Jar-Si_{19}-2 is the best structure proposed for Si_{19}.

As a summary, for Si_n clusters with $10 \leq n \leq 19$, the best structures obtained from global optimization employing the Mistriotis and modified Mistriotis potentials have been further relaxed at the DFT/B3LYP level with a 6-31G* basis and with an ECP combined with a (3s3p1d) basis, respectively, followed by single point energy calculations at the LMP2 level with the cc-pVTZ basis set. The best structures found from these calculations are summarized in Table 9.4. Some of these structures were found for the first time in this study and were recently published [134].

In particular, at the DFT level, structures proposed in the literature were reproduced for Si_{10}, Si_{11}, and Si_{12}. For Si_{13} and Si_{14}, several new isomers have been located. Note that structural preferences at the DFT level indicate an oscillatory behavior. For example, for Si_{10}, a trigonal prism based structure is favored. This immediately changes to a sequence of rhombi for the next size Si_{11}. However, for Si_{12}, again a trigonal prism based structure has been obtained as for the case of Si_{13}. But, for Si_{14}, a structure based on puckered pentagons is favored. For Si_{15}, again a return to a trigonal prism based structure was observed. However, for Si_{16}, the structural pattern is changed one more time by again favoring a puckered pentagon based structure. And finally, for Si_{17}, Si_{18}, and Si_{19}, trigonal prism based structures appeared again. Thus, while many global minima have trigonal prism based structures, also other structural patterns occur.

Table 9.5: Lowest energy isomers predicted at the DFT and LMP2 levels.

Cluster	DFT	LMP2
Si_{10}	Si_{10}-1	Si_{10}-2
Si_{11}	Si_{11}-1	Si_{11}-2
Si_{12}	Si_{12}-1	Si_{12}-1
Si_{13}	Si_{13}-1	Si_{13}-5
Si_{14}	Si_{14}-1	Si_{14}-5
Si_{15}	Jar-Si_{15}	Jar-Si_{15}
Si_{16}	Jar-Si_{16}-2	Jar-Si_{16}-1
Si_{17}	Jar-Si_{17}	Si_{17}-3
Si_{18}	Jack-Si_{18}	Si_{18}-2
Si_{19}	Jack-Si_{19}	Jar-Si_{19}-2

This picture is totally changed at the LMP2 level of theory by eliminating the structures different from the trigonal prism based ones. That is, all the lowest-energy clusters contain a trigonal prism subunit at the LMP2 level. More specifically, tri-capped and tetra-capped trigonal prisms become subunits for these cluster sizes.

Based on their mobility experiments, Jarrold et al. [2,3,4,5,6] predicted that medium-sized Si_n clusters should have prolate structures, in particular, containing tri-capped or a tetra-capped trigonal prism subunits. The results obtained at both DFT and LMP2 levels are in good agreement with these predictions. Interestingly, the agreement is better for LMP2 than for DFT.

In order to check the stability of the Si_n clusters, the cohesive energies (total energy of a cluster divided by the number of atoms) and the second energy differences [93], (Δ_2), of Si_n clusters with $10 \leq n \leq 19$ are plotted in Fig. 9.5, 9.6 and Fig 9.7, respectively. The second energy differences are defined as $\Delta_2(n) = E(n+1) + E(n-1) - 2E(n)$.

At the DFT level, the values of cohesive energies are found between -4.3 eV/atom and -4.4 eV/atom (cf. Fig. 9.5), not far away from but also not identical to the bulk cohesive energy (≈ -4.64 eV/atom). Additionally, minimum points of the cohesive energy curve can be regarded as particularly stable cluster sizes. Using this criterion, Si_{10}, Si_{14} and Si_{19} are stable cluster sizes at the DFT level. At the LMP2 level, cohesive energies calculated have different values, between -5.0 eV/atom and -5.1 eV/atom, however, stable cluster sizes are in agreement with DFT. In particular, Si_{10}, Si_{14}, Si_{15}, Si_{18}, and Si_{19} were found as stable clusters at the LMP2 level.

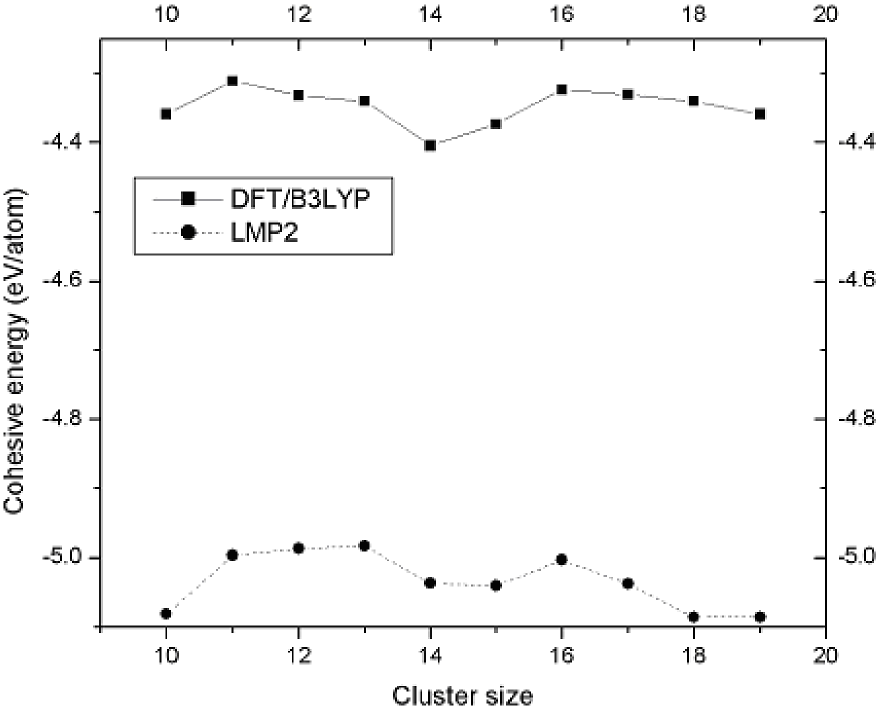

Figure 9.5: Cohesive energies in eV/atom for Si_n clusters listed in Table 9.5 as a function of cluster size as calculated with DFT/B3-LYP and LMP2.

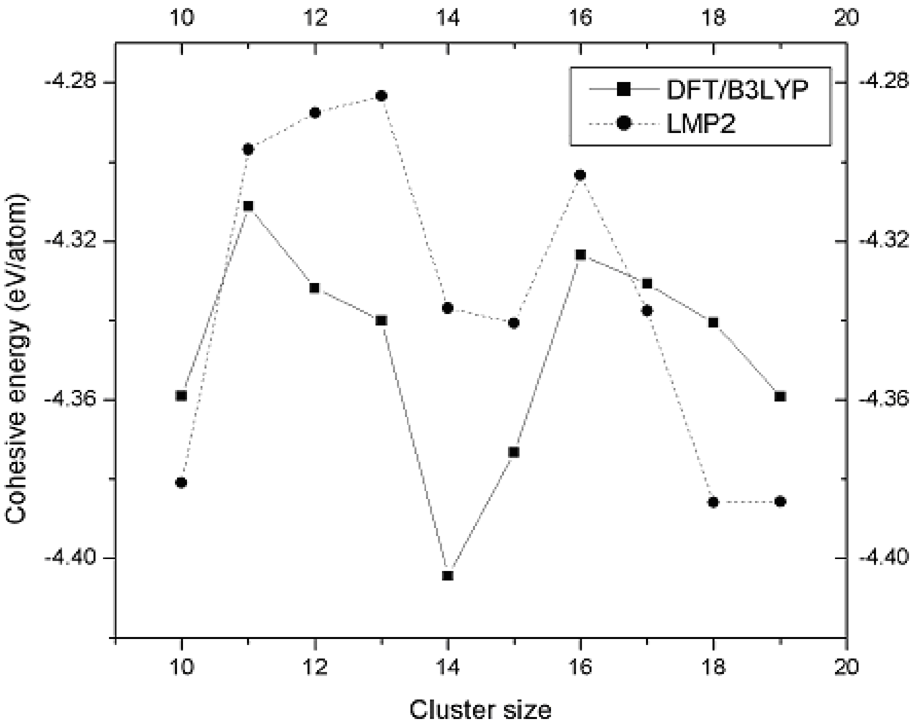

Figure 9.6: Cohesive energies in eV/atom for Si_n clusters listed in Table 9.5 as a function of cluster size as calculated with DFT/B3-LYP and LMP2 (LMP2 energies are shifted by 0.7 eV).

In order to remove the bulk limit discrepancy found at the LMP2 level, the LMP2 cohesive energies are arbitrarily shifted by 0.7 eV/atom, so that the resultant corrected LMP2 cohesive energies are in good agreement with the DFT results, as shown in Fig. 9.6.

Discrepancies to the bulk value are probably due to the fact that cluster sizes considered are far away from the bulk. This situation will probably change after the experimentally observed structural transition region. The difference in cohesive energies calculated at DFT and LMP2 levels might possibly be due to basis set superposition error (BSSE). For more reliable results, one needs at least CCSD(T) with a huge basis, or even CASSCF/MRCI.

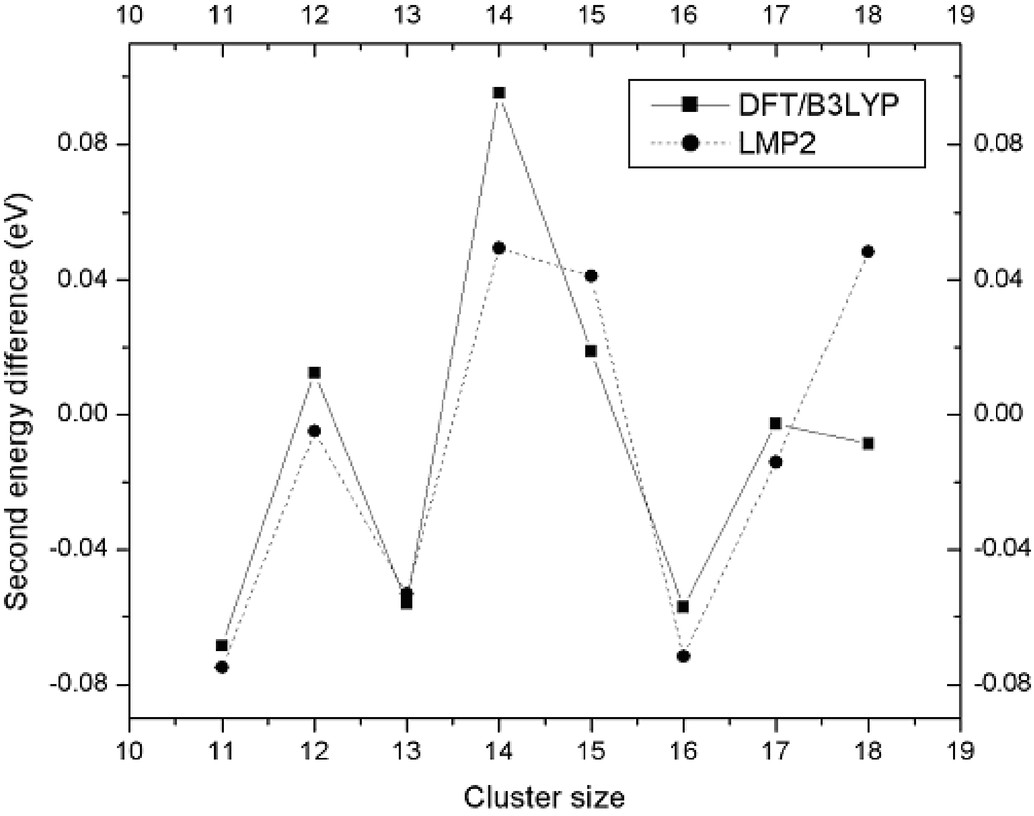

Figure 9.7: The second energy difference (Δ_2) for Si_n clusters listed in Table 9.5 as a function of cluster size as calculated with DFT/B3-LYP and LMP2.

In Fig. 9.7, the second energy differences are plotted against the cluster size. It can easily be seen that at *n*=12, 14, and 17 and *n*=12, 14, and 18 there are peaks in Δ_2 at the DFT and LMP2 levels, respectively. This implies that at these cluster sizes the Si_n clusters should have relatively higher stability than their neighbors.

Viewing the 2nd energy differences and the cohesive energies together, it can be concluded that Si_{10}, Si_{12}, Si_{14}, Si_{18}, and Si_{19} seem to be more stable than Si_{11}, Si_{13}, and Si_{16}. All these structures have been carefully examined for possible explanations of this finding. Unfortunately, no satisfactory explanation could be found, based on the structures alone. Of course, also electronic effects or a combination of structural and electronic effects may be responsible. However, it should also be noted that the energy differences between more stable and less stable cluster sizes are not very large and may easily change or disappear at a higher-level treatment. Therefore, no further analysis of these findings was done here.

We have slowly approached the prolate-to-spherical shape transition region proposed by Jarrold's [2,3,4,5] ion mobility measurements, Schäfer's [8] binding energy measurements and Fuke's [9] ionization potential measurements. In the next chapter, this transition region will be examined in detail.

9.2 Charged Si_n clusters with 10≤n≤19

Optimized structures found for Si_n clusters with 10≤n≤19 in this current study were also relaxed as cation and anion at the DFT/B3LYP level in order to check for possible effects of these charges on the structures. Clearly, substantial changes of the structures would render most of the results in this study useless, since all experiments are done on cations and anions, not on neutrals. Generally, for Si_n anions, relaxed structures were found to be slightly distorted compared to the starting neutral optimized structure. The same situation was also observed for Si_n cations with a few exceptions: for Si_{10}, Si_{10}-2 was relaxed to Si_{10}-1; and for Si_{11}, Si_{11}-4 was relaxed to a capped distorted TTP. Because of this almost complete absence of significant structural influences of the charge state, comparisons of theoretical results for neutral clusters with experimental results for charged ones, as done here and in much of the literature, are well justified.

9.3 Ion mobility simulations for Si_n clusters with 10≤n≤19

As explained in section 2.8, structural assignments for unknown species observed in mobility measurements become possible by comparison of the measured mobilities with mobilities computed for reasonable candidate geometries. Therefore, for all structures considered in this chapter, PA, EHSS, and Trajectory mobilities were calculated. In these three different mobilities, the Trajectory mobility calculation method should give the most reliable estimate. For these calculations, a software called MOBCAL [181] has been used. Experience shows that the mobilities computed for correct structures agree with experiment within ~1.5% and often better. (This error margin reflects the experimental error and estimated uncertainties in both the mobility calculations and the bond parameters of cluster geometries). In order to make a comparison with experimental measurements, mobilities measured for cations have been used. In Fig. 9.8, Trajectory mobilities were plotted. In this plot, “Jarrold” and “Jackson” represent the mobilities calculated for structures found by Ho et al. [7] and Rata et al. [25]. “Lowest Si” and “Closest Si” represent the lowest-energy isomer found in this current study at the DFT level and the isomer for which the calculated mobility comes closest to the experimental mobility amongst all isomers found in this current study at the DFT level, respectively.

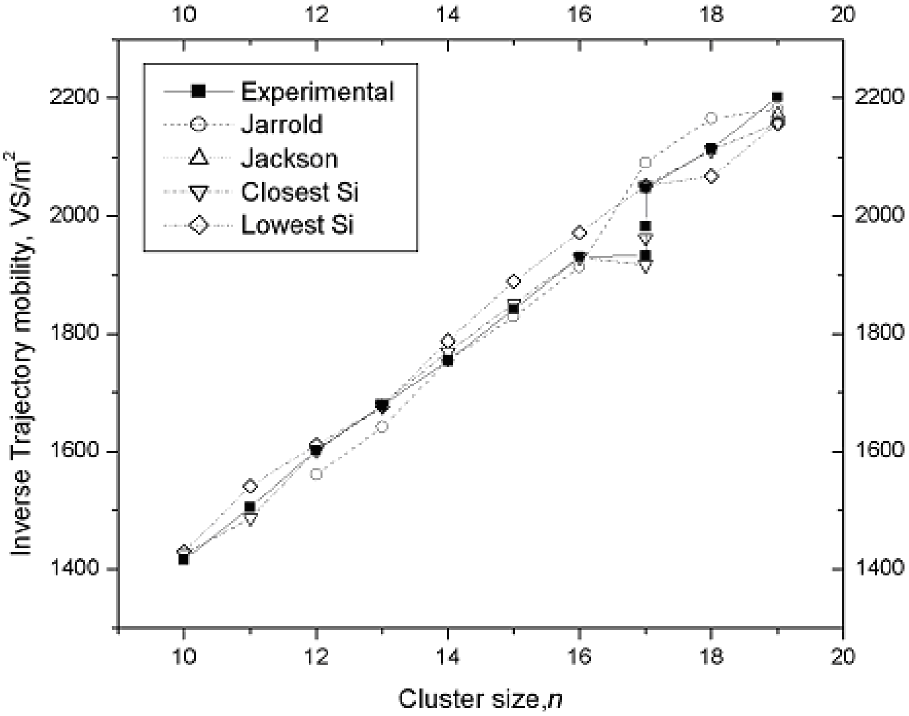

Figure 9.8: The Trajectory mobilities for Si_n clusters with $10 \leq n \leq 19$.

In Fig. 9.8, Trajectory mobilities calculated for Si_n clusters with $10 \leq n \leq 19$ are in agreement with experimental data, especially for n=10,12,13,17,19. "Jarrold" structures also have mobilities similar to the experimental ones. (In Fig. 9.8, for the "Jackson" data, only Si_{19} case is plotted). It should also be noted, however, that in many cases several different structural isomers fall within the error bars of the experimental data. This indicates that the mobility data alone are not sufficient to discern between several conflicting prososals for the inner structures of these clusters.

10 Structural transition region and beyond

Raman and infrared experiments on Si_n clusters have not yet been able to provide ground-state vibrational frequencies for clusters with more than seven atoms. This is due to the difficulty of producing sufficient numbers of larger clusters, which are necessary to obtain an observable signal. In contrast, ion mobility measurements have provided useful information about the structures of Si_n clusters containing over a dozen atoms. However, ion mobility gives only information about the outer shape of the clusters. For this reason, it can only exclude proposed structures with significantly wrong outer shape, but it cannot differentiate between different structures with very similar outer shape. The mobility experiments can only be conducted for anions and cations. However, it was generally found and accepted that structures of cationic and neutral clusters are very similar. These ion mobility measurements [2,3,4,5] indicate a shape transition from prolate to spherical clusters beginning with Si_{24}^+ and Si_{26}^- for the Si_n cation and anions. This shape transition is also supported by Schäfer's [8] binding energy measurements and Fuke's [9] ionization potential measurements. This chapter gives a detailed description of the calculated energies and structures obtained from DFT relaxation of the best geometries found at the model potential level, followed by MP2 single-point calculations. Additionally, structures proposed from recent studies in the literature will also be included and compared to those found in this study to gain a better understanding of structures adopted in this transition region.

10.1 Computational strategy

Up to here, structures obtained from global geometry optimization at the model potential level have been relaxed at the DFT/B3LYP level. However, the system size considered in the transition region makes the use of DFT/B3LYP too expensive, so that instead the structures are first optimized using RI-DFT/BP86 with the TZVP basis set and the MARI-J approximation. The structures resulting from this step are then further relaxed at the DFT/B3LYP level. Finally, similarly to the previous Chapter, LMP2 single point energies are calculated for the structures relaxed at the DFT/B3LYP level.

10.2 Structures and energies of Si_n clusters with $20 \leq n \leq 28$

Only very few searches for the lowest-energy structures of silicon clusters in this interesting size range have been made. This is due to the exponential increase in the number of possible candidate structures with increasing cluster size. Moreover, larger Si_n clusters need much more computer resources. In spite of these drawbacks, a very small set of people worldwide actually has started attempts to find the global minimum structures of silicon clusters in the transition region, in parallel to our own attempts: Thomas Frauenheim (Paderborn, Germany), Koblar Jackson (Michigan University) and Alexandre Shvartsburg (York University, Canada), working together in various different settings and producing most of the subsequently cited papers, and, independently and only fairly recently, the group of Zeng (University of Nebraska-Lincoln, USA). An early attempt is the study of Ho et al. [7]. They have searched for global minima structures in the $12 \leq n \leq 20$ region using a tight-binding approach and a genetic algorithm. They compared the calculated mobilities of their low-energy structures with the measured values and found good agreement with the experiments up to Si_{18}. Their lowest-energy structures are generally prolate isomers based on the trigonal prism unit, however, they found spherical structures for Si_{19} and Si_{20}. These calculations predict the transition from prolate to spherical clusters to occur for smaller cluster sizes than found experimentally. They suggest that this could be due to an entropic effect similar to that found for carbon clusters. For carbon, the fullerene is predicted to be the most stable geometry for a cluster as small as C_{20}^+, but C_{30}^+ is the smallest fullerene observed experimentally. This occurs since at the high temperature required to induce isomerization, the fullerene is not a low-energy structure for the smaller clusters. It only becomes competitive around C_{28} [182,183].

A recent study supporting the structural transition was conducted by Sieck at al. [64] using a SA-MD method with DFTB and DFT-GGA (Generalized gradient approximation) using the Perdew-Burke-Ernzerhof (PBE) exchange correlation functional. They only searched the Si_{25}, Si_{29}, and Si_{35} cases, finding a prolate structure for Si_{25} and spherical structures for Si_{29} and Si_{30}.

Another recent study for the transition region, only for Si_{21} and Si_{25}, has been carried out by Zeng et al. [65]. In this study [65], the basin-hopping global optimization method was employed with the SW, modified SW, and Gong potentials. The resulting low-energy structures were then further relaxed at the DFT/B3LYP level with the 6-31G* basis set. Finally, single point energies of these clusters were calculated at the CCSD level with the 6-31G* basis set. With this methodology, they proposed two new structures for Si_{21} and Si_{25}, with lowest energy in both their DFT and CCSD calculations, but different from the literature ones. These structures have a common property in that they consist of a spherical cage containing an endohedral atom. Based on their spherical structure for Si_{21}, Zeng et al. [65] suggested that the prolate to near-spherical structural transition is likely to occur in the range of $21 \leq n \leq 25$. This early shape transition was also supported by the ionization potential measurements of Fuke et al. [9]. They estimated the transition to occur between n=20 and n=22.

Rata et al. [25] searched Si_n cluster ions and neutrals up to n=23. They only proposed neutral structures containing trigonal prism units for Si_{21}, Si_{22}, and Si_{23}. Only a few months before completion of the present thesis, this study was considerably extended by Jackson et al. [68] by searching Si_n and Si_n^+ clusters with n=20-27 using a brute-force random multistart approach, with a few added tricks. The essence of their approach is to create random configurations of n atoms in a highly compressed space. These super-compressed structures are allowed to explode, relaxing to local minima via a standard gradient-based algorithm. Due to this "explosion" trick, a larger part of configuration space is explored, compared to that reached from relaxing more reasonable starting geometries. Millions of such minima are generated for each n by starting from different random geometries. Actually, it turned out that they had to specifically introduce elongated starting geometries in order to arrive at a sufficient sample of prolate final geometries. Performing millions of gradient minimizations requires fast evaluation of energies and atomic forces, so that a density-functional tight-binding (DFTB) method is employed for this purpose. Then, for each size, 200-400 of the best DFTB local minima are selected for further relaxation by DFT using the Perdew-Burke-Ernzerhof (PBE) functional with a (3s5p3d) basis set. In addition to neutral Si_n clusters, candidate global minima of Si_n^+ clusters were generated by removing an electron from all Si_n clusters followed by DFT relaxation. In their results, there is a consistency with the ion mobility measurements. Specifically, for Si_n^+ clusters, at n=24 spherical clusters become competitive with prolate ones. For Si_{25}^+, they found a spherical and a prolate structure whose cohesive energies are the same. Finally, beginning with n=26, spherical clusters are favored over prolate ones. A similar picture was obtained for Si_n neutrals by favoring a spherical cluster starting with n=26. Generally, structures found as a prolate isomer have a combination of a trigonal prism based unit and an octahedron unit bridged by a six-fold ring (resembling that of an adamantane unit in bulk Si). Jackson et al. [68] involved up to n=27 in their study. However, there is a discrepancy for the shape transition in the results beyond n=27. In particular, the lowest-energy structure found for Si_{28}, which we obtained by private communication with Prof. Jackson, is not a totally spherical cluster like Si_{26} and Si_{27}. Instead, it contains a tetra-capped trigonal prism unit at one end of the cluster, giving it an oblate shape. Probably because of this discrepancy, Jackson et al. [68] did not include the results for n=28 in their study.

As a summary, these first investigations give some support to the structural transition from prolate to spherical observed in the ion mobility measurements and other experiments. Note, however, that none of these studies is fully conclusive and without problems: Ho et al. did not even perform a global search for the transition region itself. Sieck et al. only looked at isolated cluster sizes, and it may be doubted that their MD-SA is sufficiently reliable at the DFTB level. The work of Jackson et al., albeit of a brute-force nature, probably is the most complete attempt so far, but they did not go beyond the DFT level, which has proven to be insufficient for smaller clusters. In the study of Zeng et al., their low-level CCSD(T) calculations probably do not add any reliability beyond what the DFT level already provides; also, their results place the transition at significantly smaller sizes. Therefore, in the following, the structural transition region will be considered again in detail. Similar to the previous chapter, the structures obtained from this current study are found by relaxation of the most promising structures obtained from global optimization at the model potential level. For the relaxation, first RI-DFT/BP86 with the TZVP basis set is used. Resulting structures are then further relaxed using DFT/B3LYP with a (3s3p1d) basis set and an ECP. For the resulting structures, single point energy calculations were performed at the LMP2 level with the cc-pVTZ basis set. Additionally, all the literature structures shown in the figures were also relaxed at the same level of theory.

Si_{20}: For Si_{20}, both prolate and spherical structures were found, as shown in Fig. 10.1. Additionally, some of the important structures proposed in the literature have also been displayed. Corresponding energies of these structures at both DFT and LMP2 levels are listed in Table 10.1.

For Si_{20}, in addition to the structures considered here, there are also different structures proposed in the literature. For example, Miller [184] presented a pentagonal growth pattern sequence for Si_{20} in which it is composed of layers containing 1-5-1-5-1-5-2 atoms. Kaxiras and Jackson [60] proposed a structure consisting of three stacked rings based on six-rings units, capped by one atom on the bottom and the top. Grossman and Mitas [61] discovered a family of stable elongated Si_n clusters built from stacked triangles. In this family, Si_{20} can be considered to be composed of six layers of triangles capped by two atoms on the long axis. Using a generalized simulated annealing (GSA) method, Lemes et al. [185] proposed a structure that is formed by three puckered planes with five, six, and five Si atoms, respectively, capped by two atoms on the bottom and one on the top. Furthermore, it contains an inner atom close to the six-atom plane. In a recent study, Li and Cao [186] considered 15 stable structures proposed in the literature for Si_{20} including all of the above ones, using full-potential linear-muffin-tin-orbital molecular-dynamics (FP-LMTO-MD). They obtained a structure similar to Jar-Si_{20}-4 as the lowest-energy isomer. Actually, they also considered the Jar-Si_{20}-4 isomer in their calculations but the final structure obtained differs from Jar-Si_{20}-4 only by the positioning of two TTP substructures.

Mitas et al. [187] considered several Si_{20} isomers, including the spherical Jar-Si_{20}-1 and Jar-Si_{20}-4 isomers, another spherical Si_{20} isomer proposed by Song et al. [188], and their constructed elongated structure containing two TTP subunits like Jar-Si_{20}-4. In their ab-initio study, HF, LDA, BPW91, B3PW91, BLYP, B3LYP calculations were performed, with the 6-311G* basis set. In their calculations at the HF level, the structure from Song et al. [188] was found as the lowest-energy structure. At the LDA, BPW91, and B3PW91 levels, the spherical Jar-Si_{20}-1 isomer was located as the best structure. In contrast to the other levels of theory, the BLYP, B3LYP and quantum Monte Carlo calculations suggested the constructed elongated Si_{20} isomer as the lowest-energy isomer. This study emphasizes the necessity of employing a hybrid functional instead of LDA. Moreover, the selection of the hybrid functional is also very important to obtain more reliable results. For example, the hybrid functionals BPW91 and B3PW91 have given the same spherical structure as the lowest-energy isomer. However, when a better functional like BLYP or B3LYP was employed, the structural preferences were changed from spherical to prolate.

In the recent ab-initio calculations of Zeng et al. [67] three isomers of Si_{20} were considered: Jack-Si_{20}, Jar-Si_{20}-1 and a third structure (which is composed of two bicapped square antiprisms (Si_{10}-4) predicted by Mitas et al. [187] using quantum Monte Carlo calculation). At the MP2 level, the calculations by Zeng et al. [67] favored the structure proposed by Mitas, however, at the MP4(SDQ) level, Jar-Si_{20}-1 was found as the lowest-energy structure, whereas at the MP3, CCSD, and CCSD(T) levels, the Jack-Si_{20} isomer became the energetically favorable structure.

Among these ab-initio studies, the most reliable results for Si_{20} were obtained from Zeng et al. [67] at the CCSD(T) level, favoring Jack-Si_{20} as the lowest-energy isomer.

Table 10.1: Energies and energy orderings of Si_{20} and Si_{21} at the DFT and LMP2 levels.

Structure	DFT (eV)	Order (DFT)	LMP2 (eV)	Order (LMP2)
Jack-Si_{20}	**-87.6361**	1	-102.6785	3
Si_{20}-1	-87.0370	2	-100.6886	7
Si_{20}-2	-86.7165	3	-99.5772	8
Si_{20}-3	-86.7077	4	-101.6949	6
Si_{20}-4	-86.7026	5	-99.1441	9
Jar-Si_{20}-2	-86.6906	6	-103.7855	2
Jar-Si_{20}-4	-86.6260	7	**-104.8573**	1
Jar-Si_{20}-3	-86.6258	8	-102.2616	4
Jar-Si_{20}-1	-86.4646	9	-101.9032	5
Jack-new-Si_{21}	**-92.5138**	1	-108.0509	3
Si_{21}-1	-91.4062	2	-106.1978	6
Jack-old-Si_{21}	-91.3790	3	-108.4274	2
Zeng-Si_{21}	-91.3137	4	-107.4233	4
Si_{21}-2	-91.3028	5	-106.2885	5
Si_{21}-4	-90.8502	6	-104.2739	7
Jar-Si_{21}	-90.6144	7	**-108.7730**	1

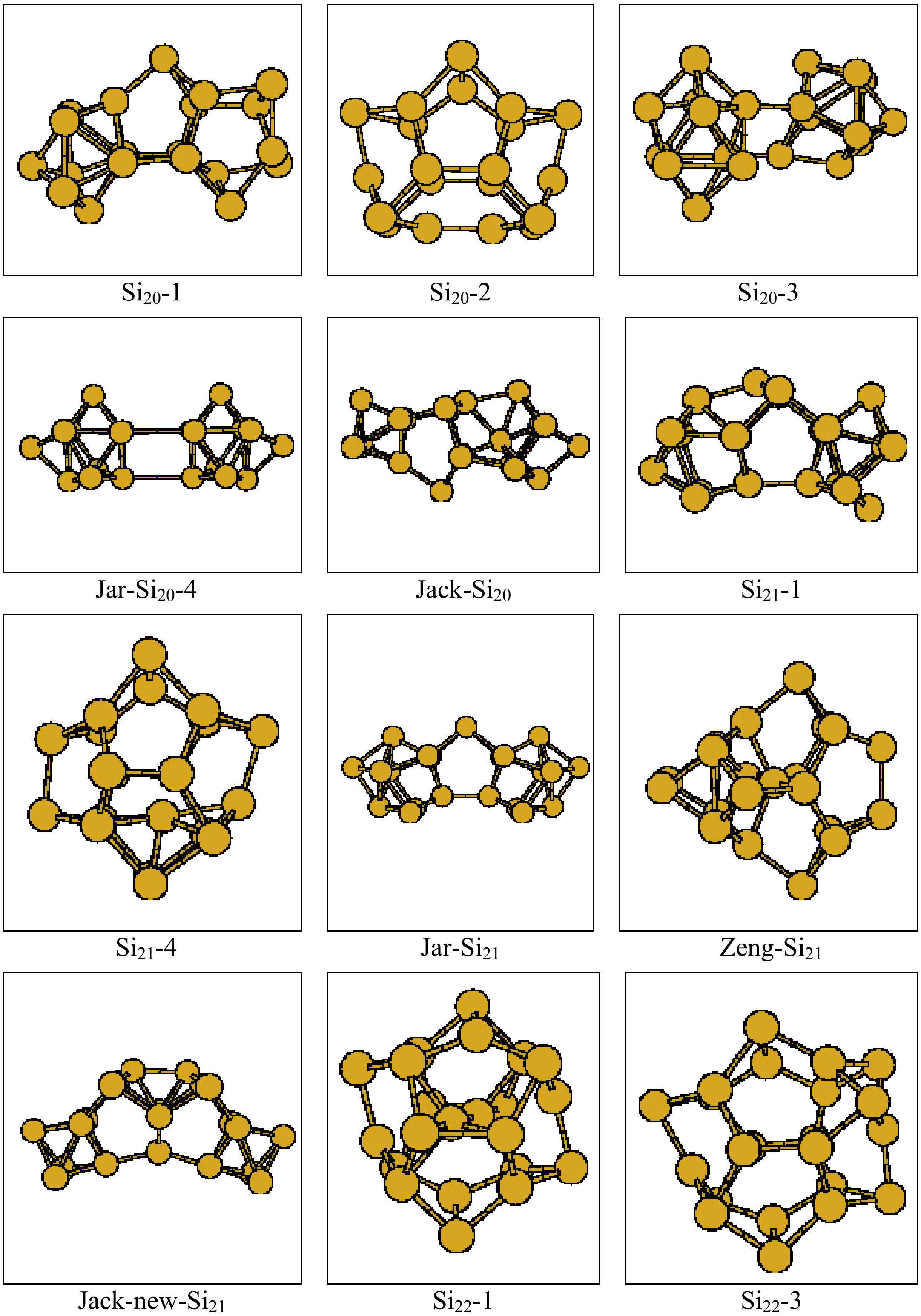

Si_{20}-1 Si_{20}-2 Si_{20}-3

Jar-Si_{20}-4 Jack-Si_{20} Si_{21}-1

Si_{21}-4 Jar-Si_{21} Zeng-Si_{21}

Jack-new-Si_{21} Si_{22}-1 Si_{22}-3

Figure 10.1: Structures found here and in the literature for Si_{20}, Si_{21}, and Si_{22} at the DFT/B3LYP level.

Among the structures shown in Fig. 10.1, Si_{20}-1 is composed of a tri-capped trigonal prism unit and a Si_{10} unit consisting of two puckered pentagons, with a single-atom bridge between these two units. Si_{20}-2 is a spherical structure containing pentagons and rhombi. Si_{20}-3 is a combination of a bicapped square antiprism (Si_{10}-4) and a TTP (Si_{10}-1) unit. Ho et al. [7] proposed 4 different candidate structures for Si_{20} and among these structures only Jar-Si_{20}-4 is composed of two TTP (Si_{10}-1) units. Among the other structures proposed by Ho et al. [7], Jar-Si_{20}-1 is a spherical structure with an additional inner atom. Jar-Si_{20}-2 is also a combination of two TTP subunits, but their positioning is not in the same plane as in Jar-Si_{20}-4. Jar-Si_{20}-3 is very similar to Jar-Si_{20}-4, it only differs in some of the bond lengths. Finally, Rata et al. [25] and Jackson et al. [68] proposed the Jack-Si_{20} isomer which is composed of three units: an octahedron, a Si_6 unit in the middle, and a Si_8 unit.

In this current study, at the DFT/B3LYP level, the Jack-Si_{20} isomer is found as the lowest-energy isomer for Si_{20}. This is followed by the structures obtained in this study, and by the other structures from Ho et al. [7]. The energy difference between Jack-Si_{20} and Si_{20}-1 is 0.5991 eV. At the third place in the DFT energy list a spherical isomer Si_{20}-2 appears for the first time. However, the other spherical structure Jar-Si_{19}-1 is placed at the end of the energy list. The energy difference between these two isomers is obtained as 0.2519 eV.

However, at the LMP2 level, the energy ordering is totally changed: Jar-Si_{19}-4 isomer is favored as the lowest-energy isomer. This is followed by Jar-Si_{20}-2 and then Jack-Si_{20}. The LMP2 energy of Jar-Si_{19}-4 is lower than Jar-Si_{20}-2 and Jack-Si_{20} by 1.0718 eV and 2.1788 eV, respectively. As a summary, at both levels of theory prolate isomers are favored over spherical ones.

As explained in the previous chapter, in the ab-initio study of Zeng et al. [67], in spite of employing a reasonable theoretical level, CCSD(T), the basis set used is too small. This reduces the reliability of this study. As mentioned above, they obtained Jack-Si_{20} as the lowest-energy isomer, however, this structure was not favored in the LMP2 calculations of this thesis. Instead, Jar-Si_{20}-4 was obtained as the lowest-energy isomer. Therefore, this isomer probably is the better candidate for the true global minimum structure.

Si_{21}: Similar to Si_{20}, both prolate and spherical structures have been found for Si_{21}. Some of these structures and important structures presented in the literature are shown in Fig. 10.1. Their energies are listed in Table 10.1. Si_{21}-1 can be defined as a connection of two tricapped trigonal prism units by a 3-atom bridge. Si_{21}-2 is not shown in Fig. 10.1 since it is very similar to Si_{21}-1. It only differs from Si_{21}-1 by having a slightly rotated tri-capped trigonal prism unit at one end. Si_{21}-4 is a spherical structure with an additional inner atom. The same structure was also obtained by Pederson et al. [62] by performing geometry optimizations within the local density approximation (LDA). Ho et al. [7] proposed Jar-Si_{21}, in which two bicapped square antiprism (Si_{10}-4) units are bridged by an atom. Zeng et al. [65] presented Zeng-Si_{21} which is a spherical structure having an additional inner atom.

Rata et al. [25] proposed the Jack-old-Si_{21} structure which is very similar to Si_{21}-1 and Si_{21}-2, differing by different positioning of one of the tri-capped trigonal prisms. Finally, in the recent work of Jackson et al. [68], Jack-new-Si_{21} was found as the lowest-energy isomer for Si_{21}. This structure differs from the other prolate structures by not having a unit based on either a trigonal prism or a square antiprism. Instead, it is composed of two octahedrons at either ends connected by a 9-atom unit.

Zeng et al. [65] considered their structure Zeng-Si_{21}, Jar-Si_{21}, Jack-old-Si_{21}, and Si_{21}-4 in their ab-initio calculation. Zeng-Si_{21} was obtained as the lowest energy isomer with DFT/B3LYP/6-31G*. Jack-old-Si_{21}, Jar-Si_{21}, and Si_{21}-4 were ranked after it in the energy list. They obtained Zeng-Si_{21} lower in energy than the second most stable isomer, Jack-old-Si_{21}, by 0.411 eV. The same energy ordering was also preserved at the CCSD/6-31G* level, but with increased energy differences. For example, the difference between Zeng-Si_{21} and Jack-old-Si_{21} was obtained as 0.586 eV.

In this current study, at the DFT level, contrary to the results obtained from Zeng et al. [65], Zeng-Si_{21} is placed after the Jack-old-Si_{21} and before the Jar-Si_{21} isomers in the energy list. Zeng-Si_{21} is lower in energy than Jar-Si_{21} by 0.6993 eV and it is higher in energy than Jack-old-Si_{21} by 0.0653 eV. The reason for this discrepancy might be due to the use of different basis sets. For this reason, the use of a larger basis set is necessary to obtain more reasonable and converged results. The basis set used in this current study is slightly larger than that of Zeng's. Neither of the structures considered in this paragraph is the lowest-energy isomer. Instead, a more recent structure, Jack-new-Si_{21}, is located as the lowest-energy isomer at the DFT level. Then, Si_{21}-1 is placed in the energy list. The energy difference between these two structures is found as 1.1076 eV. Surprisingly, the spherical structures Zeng-Si_{21} and Si_{21}-4 are found above the prolate Jar-Si_{21} isomer which is actually obtained as the least stable isomer.

However, at the LMP2 level, the energy ordering is totally changed compared to that of DFT. The least stable isomer at the DFT level, Jar-Si_{21}, became the lowest-energy isomer at the LMP2 level. This structure is followed by Jack-old-Si_{21} which is higher in energy than Jar-Si_{21} by 0.3456 eV. The spherical structures Zeng-Si_{21} and Si_{21}-4 are not favored energetically just as at the DFT level. In particular, the spherical Si_{21}-4 isomer is found as the least stable isomer.

The only ab-initio results available in the literature are those from Zeng et al. [65] at the CCSD level, proposing that Zeng-Si_{21} is the lowest-energy isomer for Si_{21}. Similar to the Si_{20} case, in Zeng's study a reasonable level of theory has been used but with a small basis set only. Therefore, results obtained in this current study are likely to offer more reliability. As a result, the lowest-energy isomer, Jar-Si_{21}, obtained here at the LMP2 level becomes the most likely candidate for the global minimum structure for Si_{21}.

Si_{22}: Some of the Si_{22} structures found here and proposed in the literature and their DFT and LMP2 energies are shown in Fig. 10.1 and 10.2 and Table 10.2, respectively. Si_{22}-1 is very similar to the spherical structure Si_{21}-1, differing only by having an extra inner atom so that the total number of inner atoms is increased to two. Si_{22}-3 is also a spherical isomer containing no-inner atoms. Si_{22}-6 can be defined as a combination of a tri-capped trigonal prism unit and a bicapped square antiprism (Si_{10}-4) combined by a three-atom bridge. Ho et al. [7] proposed the prolate Jar-Si_{22}-1 and Jar-Si_{22}-2 isomers. Only the Jar-Si_{22}-2 isomer is shown in Fig. 10.2. It is composed of two bicapped square antiprism (Si_{10}-4) units bridged by a two-atom group. Jar-Si_{22}-1 is actually almost the same structure as Jar-Si_{22}-2, only the positioning of the two-atom bridge in Jar-Si_{22}-1 is different from that of Jar-Si_{22}-2. Rata et al. [25] presented the Jack-new-Si_{22} isomer that contains a slightly distorted TTP (Si_{10}-1) unit and a tri-capped trigonal prism unit bridged by a three-atom group. When this structure is optimized at the DFT/B3LYP level, the TTP unit is transformed to a bicapped square antiprism (Si_{10}-4) unit. The resulting structure is very similar to the structure Jack-new-Si_{22}, proposed by Jackson et al. [68].

At the DFT/B3LYP level, the Jack-new-Si_{22} isomer is obtained as the lowest-energy isomer in this current study. This structure is followed by the Jack-old-Si_{22} and Jar-Si_{22}-2 isomers, with B3LYP energy differences of 0.128 eV and 0.3792 eV, respectively. Similar to the Si_{21} case, there are spherical isomers such as Si_{22}-1 and Si_{22}-3 which are lower in energy than prolate isomers like Si_{22}-6 and Jar-Si_{22}-1 (the least stable isomer at the B3LYP level). However, this picture is not preserved at the LMP2 level. Results similar to the previous clusters sizes are obtained. For example, the spherical isomers Si_{22}-1 and Si_{22}-3 are placed at the end of the LMP2 energy list. Furthermore, a prolate isomer, Jar-Si_{22}-2, is found as the lowest-energy isomer. This structure is followed by the Jack-old-Si_{22} and Jar-Si_{22}-1 isomers, respectively, with energy differences of 0.2667 eV and 1.1161 eV, respectively. As a result, Jar-Si_{22}-2 is the best candidate structure for global minimum of Si_{22}.

Table 10.2: Energies and energy orderings of Si_{22} and Si_{23} at the DFT and LMP2 levels.

Structure	DFT (eV)	Order (DFT)	LMP2 (eV)	Order (LMP2)
Jack-new-Si_{22}	**-96.3087**	1	-112.6562	4
Jack-old-Si_{22}	-96.1789	2	-114.2391	2
Jar-Si_{22}-2	-95.9295	3	**-114.5058**	1
Si_{22}-1	-95.7734	4	-110.9814	6
Si_{22}-3	-95.0653	5	-107.9474	7
Si_{22}-6	-94.8878	6	-111.0189	5
Jar-Si_{22}-1	-94.1311	7	-113.3897	3
Jack-Si_{23}	**-100.8140**	1	**-118.6788**	1
Si_{23}-1	-99.9949	2	-116.9087	3
Jar-Si_{23}	-99.5974	3	-118.5849	2
Si_{23}-2	-99.4417	4	-114.5046	5
Si_{23}-3	-99.3861	5	-115.9060	4

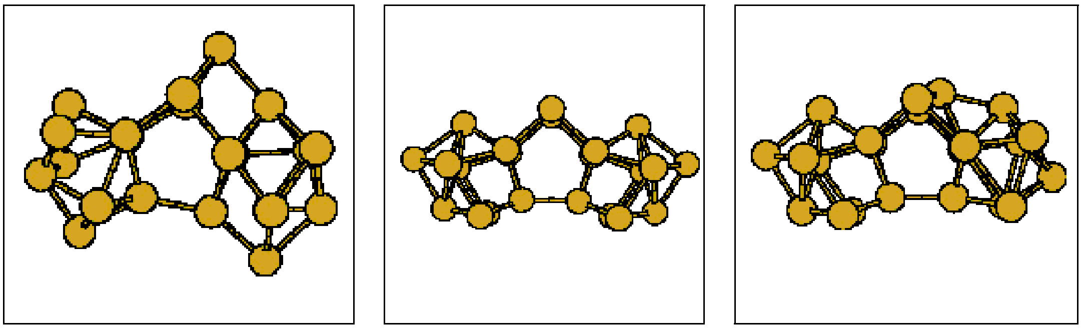

Si$_{22}$-6 Jar-Si$_{22}$-2 Jack-new-Si$_{22}$

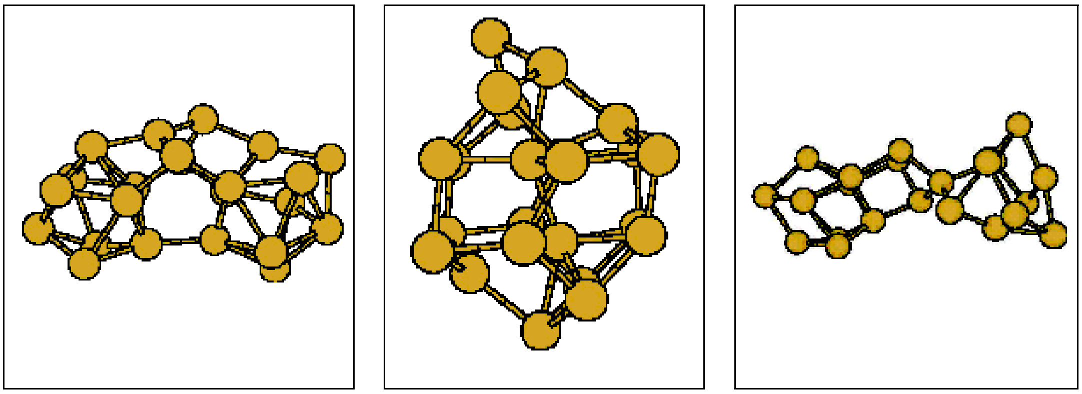

Si$_{23}$-1 Si$_{23}$-2 Si$_{23}$-3

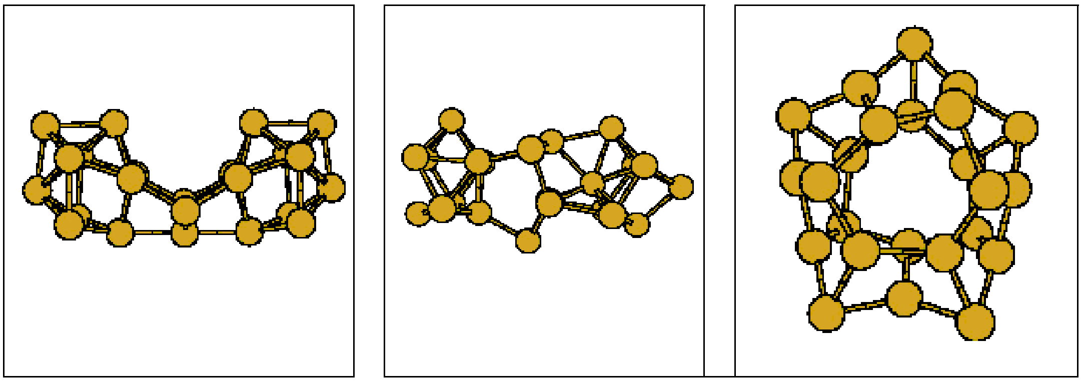

Jar-Si$_{23}$ Jack-Si$_{23}$ Si$_{24}$-1

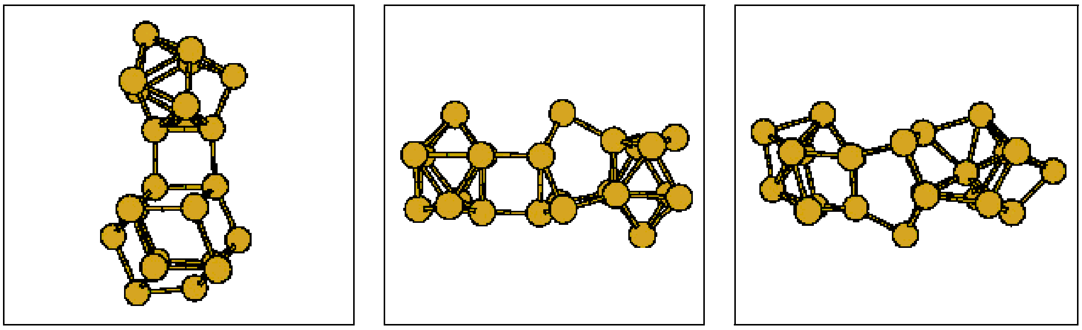

Si$_{24}$-3 Jar-Si$_{24}$ Jack-Si$_{24}$

Figure 10.2: Structures found here and in the literature for Si$_{20}$, Si$_{21}$, and Si$_{22}$ at the DFT/B3LYP level.

Si_{23}: Both prolate and spherical isomers are located for Si_{23} as shown in Fig. 10.2. Their DFT and LMP2 energies are listed in Table 10.2. Si_{23}-1 can simply be derived from the Jack-new-Si_{22} isomer by adding an extra atom to the three-atom bridge connecting the square prism and tri-capped trigonal prism units. Si_{23}-2 is a spherical structure that can be obtained by capping the Si_{22}-1 isomer. Si_{23}-3 is another prolate structure having a bicapped square antiprism (Si_{10}-4) unit. Ho et al. [7] proposed the Jar-Si_{23} isomer that can be derived from Jar-Si_{22}-1 by adding an extra cap atom to the two-atom bridge. Rata et al. [25] and Jackson et al. [68] found the same Jack-Si_{23} isomer as the lowest-energy isomer. It can be obtained from Jack-Si_{20} by exchanging the octahedron unit by a tri-capped trigonal prism unit.

Geometry optimizations at the DFT level performed in this study favored the Jack-Si_{23} isomer energetically. It is followed by the Si_{23}-1 and Jar-Si_{23} isomers, which are higher in energy than Jack-Si_{23} by 0.8191 eV and 1.2166 eV, respectively. Spherical isomers are placed almost at the end of the energy list. Contrary to previous cluster sizes, LMP2 changes the energy order only slightly. Jack-Si_{23} is also found as the lowest-energy isomer. This isomer is again followed by the Jar-Si_{23} and Si_{23}-1 isomers, with energies higher than Jack-Si_{23} by 0.0939 eV and 1.7701 eV, respectively. As the least stable isomer the spherical structure Si_{23}-2 is found. As a result, DFT and LMP2 agreed to locate the same isomer, Jack-Si_{23}, as the lowest-energy isomer. Therefore, this structure is the best candidate for the global minimum of Si_{23}.

Si_{24}: A spherical isomer Si_{24}-1 containing 12 puckered pentagons and 2 hexagons is found as the lowest-energy structure in this study. A prolate isomer is also located, Si_{24}-3, which is composed of a TTP (Si_{10}-1) unit and a hexacapped cube unit. In the literature, Ho et al. [7] proposed the Jar-Si_{24} isomer which is composed of two tri-capped trigonal prism units at either ends bridged by a six-atom group. Recently, Jackson et al. [68] reported Jack-Si_{24} which is composed of a bicapped square antiprism (Si_{10}-4) unit, a Si_6 unit, and eight-atom units that appeared similarly in the case of the Jack-Si_{23} isomer. All of these structures and their corresponding energies are shown in Fig. 10.2 and Table 10.3, respectively.

When considering the energies obtained from DFT/B3LYP calculations, Jack-Si_{24} is the lowest-energy isomer. This is followed by another literature structure, Jar-Si_{24}, which is higher in energy than Jack-Si_{24} by 1.1993 eV. After the prolate Jar-Si_{24} isomer, the spherical Si_{24}-1 is located as a low-energy isomer. As the least favorable structure, Si_{24}-3 is found, which contains a TTP subunit. At the LMP2 level, similar to the DFT level, Jack-Si_{24} is obtained as the lowest-energy isomer. This isomer is followed by the Si_{24}-3 and Jar-Si_{24} isomers, with energies higher than Jack-Si_{24} by 0.9976 eV and 1.5987 eV, respectively. Similar to the Si_{23} case, DFT and LMP2 are in agreement for the best candidate global minimum structure of Si24 as Jack-Si_{24}.

Si_{25}: Because of being an important cluster size in the structural transition region, Si_{25} is extensively investigated in the literature. Some of the structures found in this current study and of the structures proposed in the literature and their corresponding

DFT/B3LYP and LMP2 energies are displayed in Fig. 10.3 and Table 10.3, respectively. Similar to the Si_{24} cluster, the best structure found in this study is spherical (Si_{25}-1), containing almost the same outer cage as Si_{24} with an additional inner atom. Another similarity to the Si_{24} cluster is that the prolate structures found for Si_{25} contain a combination of a TTP (Si_{10}-1) unit and a hexacapped cube unit just like Si_{24}-3. However, these structures are not favored at the DFT level. In the literature, Ho et al. [7] proposed the Jar-Si_{25} isomer which is a combination of a TTP unit and a Jar-Si_{15} structure. Jackson et al. [68] reported the Jack-Si_{25} isomer which is very similar to Jack-new-Si_{21}, only an octahedron unit in Jack-new-Si_{21} is replaced with a bicapped square antiprism (Si_{10}-4) unit. Zeng et al. [65] found a spherical structure, Zeng-Si_{25}, which is very similar to the Si_{25}-1 isomer. Finally, Sieck et al. [64,189] found several isomers both prolate and spherical. Among them, Frauen-Si_{25}-4 is a prolate isomer composed of three units: a Si_{10}-4 unit, a Si_6 unit, and a nine-atom group. Frauen-Si_{25}-5 is very similar to Frauen-Si_{25}-4, differing only by the exchange of the nine-atom group with a tri-capped trigonal prism unit.

In addition to these studies, Grossman and Mitas et al. [187] proposed a prolate and a spherical isomer for Si_{25} obtained from quantum Monte Carlo simulations. Their prolate structure is similar to Frauen-Si_{25}-5. The only differences are the attachment positions of the Si_{10}-4 and hexagonal-chair units to the tri-capped trigonal prism unit. The spherical isomer proposed by them resembles the Si_{25}-1 and Zeng-Si_{25} isomers. Grossman and Mitas et al. [187] found that the spherical isomer is slightly lower in energy than the prolate one. The stability of structures featuring internal atoms which are encapsulated in the distorted cage-like configurations was earlier suggested by Röthlisberger et al. [190] for Si_{33} and Si_{45}. They have characterized the important role of internal atoms such that i) they saturate the dangling bonds of the

Table 10.3: Energies and energy orderings of Si_{24} and Si_{25} at the DFT and LMP2 levels.

Structure	DFT (eV)	Order (DFT)	LMP2 (eV)	Order (LMP2)
Jack-Si_{24}	**-105.5818**	1	**-122.7836**	1
Jar-Si_{24}	-104.3825	2	-121.1849	3
Si_{24}-1	-104.1998	3	-118.0942	4
Si_{24}-3	-103.6243	4	-121.7860	2
Jack-Si_{25}	**-110.4948**	1	-128.3857	2
Frauen-Si_{25}-5	-109.7304	2	-109.6323	10
Frauen-Si_{25}-4	-109.5323	3	-123.1601	9
Frauen-Si_{25}-2	-109.4481	4	-127.2325	5
Zeng-Si_{25}	-109.2519	5	-127.2442	4
Si_{25}-1	-109.1513	6	-127.3449	3
Si_{24}-2	-108.9007	7	-124.8768	8
Frauen-Si_{25}-1	-108.8088	8	-126.1234	7
Frauen-Si_{25}-3	-108.5595	9	-126.2548	6
Jar-Si_{25}	-108.2835	10	**-128.3952**	1

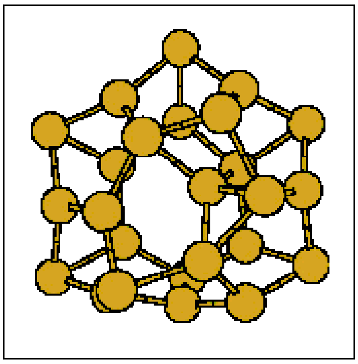

Si_{25}-1

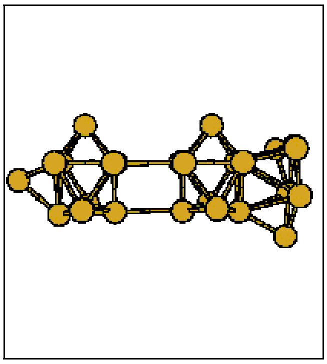

Jar-Si_{25}

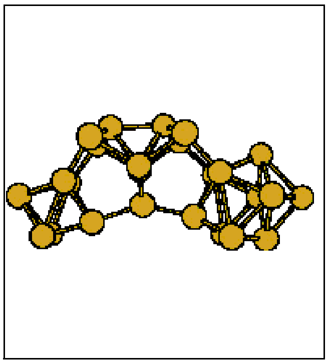

Jack-Si_{25}

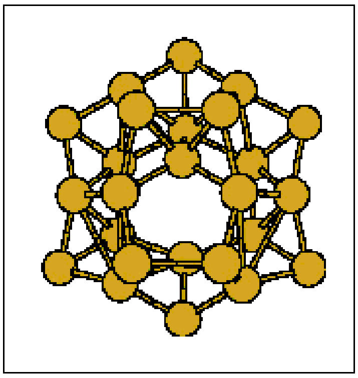

Zeng-Si_{25}

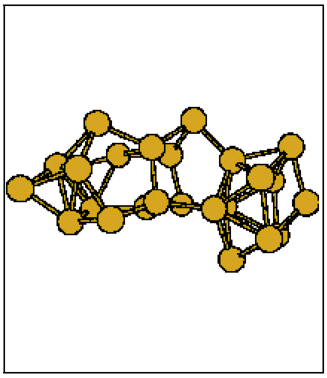

Frauen-Si_{25}-4

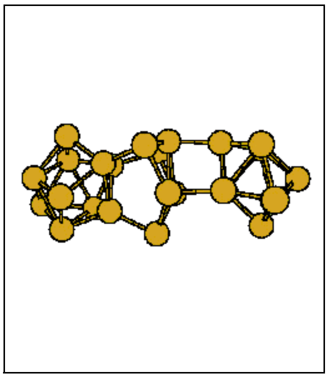

Frauen-Si_{25}-5

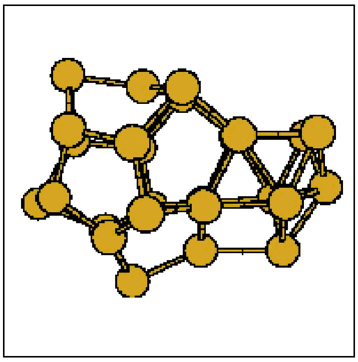

Si_{26}-1

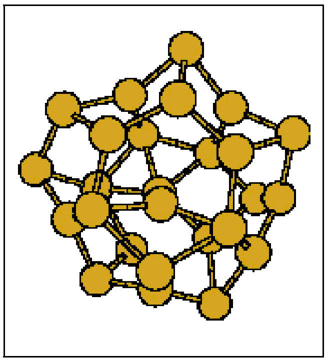

Si_{26}-3

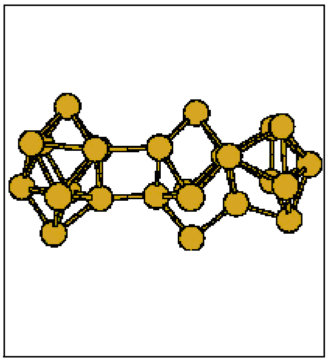

Jar-Si_{26}

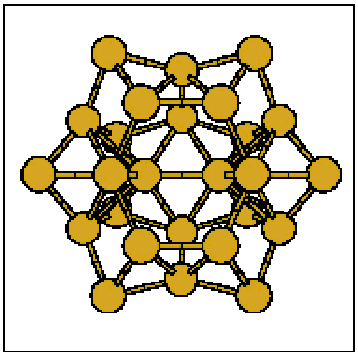

Jack-Si_{26}

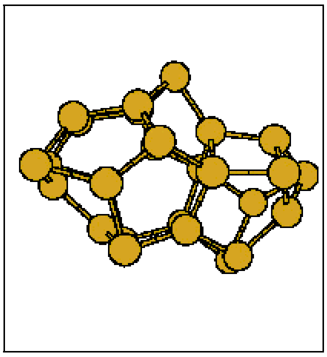

Si_{27}-1

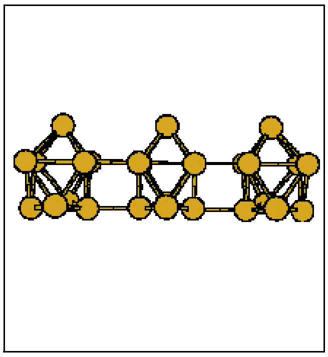

Jar-Si_{27}

Figure 10.3: Structures found here and in the literature for Si_{25}, Si_{26}, and Si_{27} at the DFT/B3LYP level.

surface atoms which would otherwise be mostly threefold coordinated, ii) they act as catalytic centers for transforming one cluster isomer into another one: their high coordination and multiple weak bonds enable structures to relax through a sequence of rebonding and restructuring steps. This also suggests a mechanism for the system to overcome the large energy barriers in the formation process of larger compact structures. Almost with the same reasoning Grossman and Mitas et al. [187] concluded that the structural transition from prolate to spherical structures is related to the onset of formation of structures composed of irregular cages with a small number of encapsulated atoms which have both structural and dynamical roles in the formation process.

In the recent ab-initio calculations of Zeng et al. [65] only the two prolate and spherical structures by Grossman and Mitas et al. [187] and the Zeng-Si_{25} structure were considered. At both the DFT/B3LYP and CCSD levels (both with the 6-31G* basis set), they found the Zeng-Si_{25} isomer as the lowest-energy structure. After this spherical structure, Grossman and Mitas's prolate isomer was obtained at both levels of theory.

In the results of this current study, at the DFT/B3LYP level a prolate isomer, Jack-Si_{25} is found as the lowest-energy isomer. This structure is followed by Frauenheim's prolate isomers. In particular, Frauen-Si_{25}-5 is found as the second stable isomer for Si_{25}, which is higher in energy than Jack-Si_{25} by 0.7644 eV. Contrary to the studies of Zeng et al. [65] and Grossman and Mitas et al. [187], spherical isomers are found less stable than the prolate ones. Surprisingly, a prolate isomer, Jar-Si_{25}, is obtained at the end of the DFT energy list. At the LMP2 level, Jar-Si_{25} is obtained as the lowest-energy isomer. This isomer is followed by the Jack-Si_{25} and Si_{25}-1 isomers, with energies higher than Jar-Si_{25} by 0.0095 eV and 1.0503 eV, respectively. The energy difference between Jar-Si_{25} and Jack-Si_{25} is too small to be real and hence these structures are isoenergetic. Zeng-Si_{25} is placed in the LMP2 energy list after the similar Si_{25}-1 isomer.

In this current study, the spherical Zeng-Si_{25} structure is not favored at both DFT and LMP2 levels. As explained in several places, the reliability of Zeng's results probably is insufficient. Since the current LMP2 results suggest that the Jar-Si_{25} and Jack-Si_{25} have almost the same energies, either Jar-Si_{25} or Jack-Si_{25} is the best candidate global minimum structure for Si_{25}.

Si_{26}: From the ion mobility experiments, for Si_n cations the structural transition from prolate to spherical clusters was suggested to occur between $24 \leq n \leq 26$. For this reason, the *n*=26 case can be considered as the last possible cluster size for the transition. Nevertheless, not so much effort has been invested so far for Si_{26} compared to the Si_{25} case. The results obtained for Si_{26} in this current study resemble those for previous sizes. Some of the structures obtained in this study and in the literature and their corresponding energies are shown in Fig. 10.3 and Table 10.4, respectively. As the best structure, a spherical isomer, Si_{26}-1, is located. However, this spherical structure differs from Si_{25}-1 by having no inner atoms. It can be described as a fused cage containing a distorted Si_{20} cage and another cage containing 11 atoms. Another spherical structure is the Si_{26}-3 isomer which can be seen as a continuation of Si_{25}-1. Besides these spherical structures, prolate structures containing TTP and tri-capped trigonal prism subunits are also obtained. However, their DFT/B3LYP energies are found to be higher than those of the spherical ones. In the literature, Ho et al. [7] proposed a prolate Jar-Si_{26} isomer which is composed of two units: a bicapped square antiprism (Si_{10}-4) and a Si_{10}-4 group fused with a distorted tri-capped trigonal prism. In addition to this structure, in their recent study, Jackson et al. [68] proposed the Jack-Si_{26} isomer. This structure is a spherical isomer containing the same cage structures that already appeared in the Si_{25}-1 and Zeng-Si_{25} isomers. However, this time the cage structure encapsulates two internal atoms. Actually, a structure closely resembling the Jack-Si_{26} isomer is found in this current study, however, the orientations of the internal atoms are different: A 180° rotation of the internal atoms leads to the structure found in this study. This small orientation difference, however, causes an energy gain of 1.8234 eV in Jack-Si_{26} over the structure found in this study. Upon finding a spherical structure as the lowest energy for Si_{26}, Jackson et al. [68] concluded that they had located the structural transition in their study.

In this current study, at the DFT/B3LYP level, the Jack-Si_{26} isomer is found as the lowest-energy structure. This structure is followed by other spherical isomers such as Si_{26}-1 and Si_{26}-3, higher in energy than the Jack-Si_{26} isomer by 0.8115 eV and 1.0385 eV, respectively. A prolate isomer Jar-Si_{26} is found as the least stable isomer at the DFT level. DFT results for Si_{26} are also in agreement with the experimentally proposed structural transition by favoring the spherical Jack-Si_{26} isomer as the lowest-energy structure. On the other hand, at the LMP2 level, the picture obtained with DFT is not supported. In particular, the prolate Jar-Si_{26} isomer is found as the lowest-energy structure for Si_{26}, contrary to the theoretical results of Jackson et al. [68] and to deductions from experiment. This structure is followed by Jack-Si_{26} and Si_{26}-1 higher in energy than Jar-Si_{26} by 2.7216 eV and 4.4487 eV, respectively.

Actually, for the previous cluster sizes LMP2 never preferred spherical isomers over prolate ones, and this situation did not change after the transition region. Additionally, a similar behavior was encountered in the MP2 level calculations of Zeng et al. [67] except for the Si_{19} case. However, they considered only clusters up to the Si_{20} case. This discrepancy to the experiment is for the first time noticed in this current theoretical study, using LMP2 with a reasonably large cc-pVTZ basis set.

All structures found by Jackson et al. [68] supported the shape transition, however results obtained in this current study are in disagreement with the proposal of Jackson, by finding prolate structures as the most stable isomers. This picture suggests that Jackson's proposal about the shape transition either is only accidentally correct or incomplete. Then, of course, there is one remaining question: why experiments supported the shape transition. In IMM experiments, clusters formed at

Table 10.4: Energies and energy orderings of Si$_{26}$ and Si$_{27}$ at the DFT and LMP2 levels.

Structure	DFT (eV)	Order (DFT)	LMP2 (eV)	Order (LMP2)
Jack-Si$_{26}$	**-113.8666**	1	-131.0671	2
Si$_{26}$-1	-113.0551	2	-129.3400	4
Si$_{26}$-3	-112.8281	3	-130.0785	3
Jar-Si$_{26}$	-112.4145	4	**-133.7887**	1
Jack-Si$_{27}$	**-118.0959**	1	-136.5401	2
Si$_{27}$-1	-118.0315	2	-133.6337	3
Jar-Si$_{27}$	-116.0256	3	**-141.4376**	1
Jack-Si$_{28}$	**-123.0766**	1	-142.6874	2
Si$_{28}$-1	-122.2899	2	-139.2082	4
Si$_{28}$-3	-121.7973	3	-139.5804	3
Jar-Si$_{28}$	-121.1199	4	**-143.0339**	1
Si$_{29}$-1	**-126.3207**	1	-142.9788	1
Si$_{29}$-2	-125.9461	2	-142.8842	2
Jar-Si$_{29}$	-125.9250	3	**-**	-

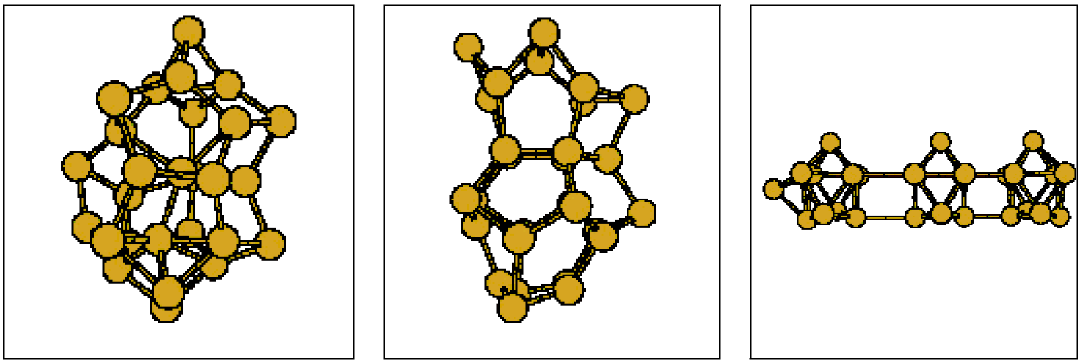

Jack-Si$_{27}$ Si$_{28}$-1 Jar-Si$_{28}$

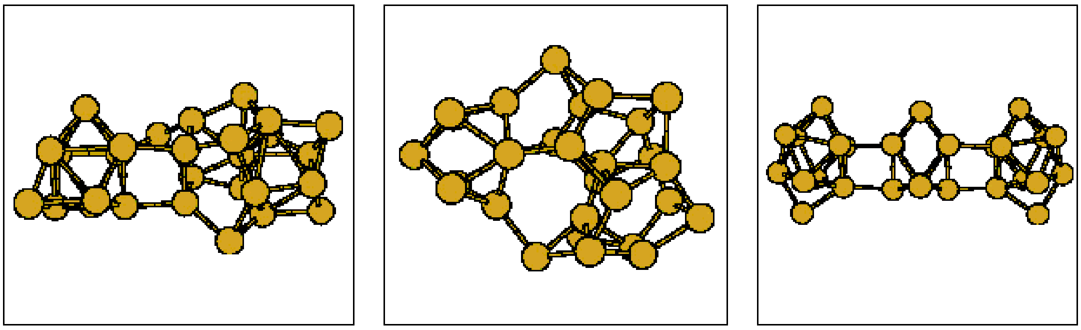

Jack-Si$_{28}$ Si$_{29}$-1 Jar-Si$_{29}$

Figure 10.4: Structures found here and in the literature for Si$_{27}$, Si$_{28}$, and Si$_{29}$ at the DFT/B3LYP level.

various sizes might not be global minimum structures. As a result, mobilities might be measured for structures different from the global minima.

Si_{27}: Beginning with this cluster size, structures should be spherical according to the ion mobility experiments. Some of the structures found in this current study and proposed in the literature and their corresponding energies at both DFT and LMP2 levels can be seen in Fig. 10.3 and 10.4 and Table 10.4, respectively. Si_{27}-1 has been found in this current study. It is a spherical isomer which has the same characteristics found for Si_{26}-1. In particular, it is composed of a distorted Si_{20} cage fused to another cage containing 12 atoms. Cage structures similar to Si_{25}-1 are also found, but are higher in energy at the DFT level. In addition to spherical structures, prolate structures containing tri-capped trigonal prism and bicapped square antiprism units (Si_{10}-4) have been located, but they are higher in energy than the spherical ones at the DFT level. In the literature, as a continuation to the study of Ho et al. [7], the prolate Jar-Si_{27} [191] isomer was proposed which simply is a sequence of three tri-capped trigonal prism units. In stark contrast to this, Jackson et al. [68] reported a spherical isomer, Jack-Si_{27}, containing two internal atoms. This structure differs from the Jack-Si_{26} isomer in shape.

In this current study, at the DFT level, a trend similar to that which appeared for Si_{26} is observed, by spherical isomers being favored energytically over the prolate ones. More specifically, the spherical Jack-Si_{27} isomer is found as the lowest-energy structure. It is lower in energy than next spherical isomers Si_{27}-1 by 0.0644 eV. Additionally, the prolate isomer Jar-Si_{27} is found as the least stable isomer, higher in energy than the Jack-Si_{27} isomer by 2.0703 eV. But, at the LMP2 level, the DFT picture is completely changed: prolate Jar-Si_{27} is obtained the lowest-energy isomer. It is lower in energy than Jack-Si_{27} and Si_{27}-1 by 4.8975 eV and 7.8039 eV, respectively.

Disagreement to DFT calculations and experimental observations continued for Si_{27} by favoring a prolate structure as the lowest-energy isomer at the LMP2 level.

Si_{28}: Both prolate and spherical isomers are found in this current study as candidates for the lowest-energy structure of Si_{28}. Similar to previous sizes, the prolate structures found contain tri-capped trigonal prism and bicapped square antiprism (Si_{10}-4) units and are not favored at the DFT level. On the other hand, spherical clusters are found lower in energy than the prolate ones. Only one of the structures found and two structures proposed in the literature are displayed in Fig. 10.4. Their corresponding energies are listed in Table 10.4. Si_{28}-1 has the same characteristics encountered for the cases of Si_{26}-1 and Si_{27}-1. In particular, it contains a distorted Si_{20} cage fused with another cage containing 13 atoms. In the literature, Jarrold [191] proposed a prolate structure which is composed of a sequence of a TTP (Si_{10}-1) and two tri-capped trigonal prism units. Another structure reported for Si_{28} is Jack-Si_{28}, taken from Jackson [192].Surprisingly this structure is not published in their latest study [68]. A fairly obvious reason could be that this structure is composed of a tetra-capped trigonal prism unit and a small cage-like unit. Very simply, this structure is not spherical like the structures proposed for previous Si_{26} and Si_{27} cluster sizes. Therefore, it leads to a contradiction to the experimentally observed structural transition from prolate to spherical. In all fairness, it should be remarked that Jackson qualified his structure Jack-Si_{28} as a preliminary result. Nevertheless, this documents at least the great difficulties of these studies and also implies that other studies performed in the literature do not totally agree with the experimental observations.

In this current study, at the DFT level, Jack-Si_{28} is obtained as the lowest-energy structure. This structure is followed by the spherical structures found in this study, Si_{28}-1 and Si_{28}-2, which are higher in energy than Jack-Si_{28} by 0.7867 eV and 1.2793 eV, respectively. Finally, at the end of the DFT list, the Jar-Si_{28} isomer is placed. At the LMP2 level, structural preferences that appeared in the DFT level are reversed: the prolate Jar-Si_{28} isomer is the lowest-energy structure. This structure is followed by the prolate Jack-Si_{28} isomer, which is higher in energy than Jar-Si_{28} by 0.3465 eV. The spherical isomers are found as the least stable isomers at the LMP2 level.

Si_{29}: Beginning with Si_{29}, systematic investigations carried out to find the lowest-energy structures becomes rare in the literature. Jarrold [191] continued to construct a prolate structure for Si_{29}, Jar-Si_{29}, as shown in Fig. 10.4. This structure is composed of a sequence of three units: at either ends of the structure there is a bicapped square antiprism (Si_{10}-4) unit, joined in the middle by a tri-capped trigonal prism unit. Sieck et al. [64] have also considered the Si_{29} case in their SA-MD study with the DFTB formalism. They proposed some spherical structures containing two internal atoms, and a non-totally spherical structure resembling the Si_{29}-1 isomer shown in Fig. 10.4. Within the DFTB scheme, they found these structures to be almost isoenergetic. The corresponding energies of the structures shown in Fig. 10.4 are listed in Table 10.4.

In this current study, at the DFT level, the Si_{29}-1 isomer is found as the lowest-energy isomer. It can be described as a connection of a spherical cage unit containing one inner atom and a tri-capped trigonal prism unit. In additional to the Si_{29}-1 isomer, other spherical isomers containing a distorted Si_{20} unit or a cage as encountered in Si_{25}-1 and some prolate isomers have also been found. However, they were higher in energy at the DFT level. As the least stable isomer, the prolate Jar-Si_{29} is obtained with an energy higher than Si_{29}-1 by 0.3957 eV. The results obtained from DFT calculations are consistent with previous cluster sizes by favoring a spherical isomer instead of a prolate one after the experimentally observed transition region. Unfortunately, at the LMP2 level, single point energy of prolate Jar-Si_{29} could not be calculated because of the problem encountered during the formation of orbital domains. For this reason, at the LMP2 level, structural preferences remain unclear.

10.3 Beyond the structural transition

It is important to know the lowest-energy structures after the shape transition to judge the validity of the dominance of the spherical growth pattern encountered in ion mobility experiments. Furthermore, experimental findings indicate the simultaneous presence of several different structural classes; this is visible in the diagram by Schäfer et al. that was presented already in the introduction of this thesis. And last but not least, the shape transition at about n=25 is only the first size region of interest. Obviously, none of the cluster isomers shown above contain structural patterns similar to that of bulk silicon phases. Therefore, with further increasing cluster size, at some point another transition to bulk-like atom arrangements has to happen (at least in the cluster cores). This is clearly an extremely important size region, in particular also for nanotechnology applications. However, after the shape transition region, systematic searches for finding the lowest-energy structures for Si_n clusters become dramatically less frequent in the literature, mainly because of the high demands of computer resources and the exponential increase in the number of local minima with increasing cluster size. For all these reasons, in this current study systematic investigations for finding the lowest-energy structures have been continued up to Si_{35} using a reasonable level of theory. In particular, the functional and basis set employed for the previous cluster sizes are preserved for the calculations for $30 \leq n \leq 35$ region.

Chemical reaction experiments performed by Smalley et al. [42,43] demonstrated that Si_{33}, Si_{39}, and Si_{45} were less reactive toward ammonia and ethylene than neighboring cluster sizes. In order to understand why these cluster sizes have lower reactivity, some theoretical works have been focused on these sizes. The first attempt was done by Kaxiras and Jackson [60]. However, they could not perform an unbiased study, instead they constructed spherical and prolate clusters using two approaches. Mainly, they were motivated by analogy to bonding in bulk Si and on Si surfaces. Their first construction approach produces prolate clusters consisting of puckered six-fold rings, stacked along a central axis of three-fold rotational symmetry and capped by single atoms at either ends. The second approach produces spherical clusters containing as many internal atoms and a shape as nearly spherical as possible. In particular, both approaches for prolate and spherical clusters were borrowed directly from the diamond lattice and Si surface reconstructions, respectively. The constructed clusters were then optimized by conjugate gradient minimization and the binding energies of these clusters calculated at the DFT-LDA level. Additionally, they included the generalized gradient approximation (GGA) for the exchange and correlation energy functional to get improved energies. In their calculations, binding energies for prolate clusters have an almost constant value, whereas for the spherical clusters it smoothly approaches to the bulk limit. Additionally, there was an intersection in the binding energies of prolate and spherical clusters approximately at n=23. This suggests that there is a transition in the shape of the most stable clusters as their size increases (This is an early prediction/confirmation of the shape transition near n=25). Furthermore, they also observed that the spherical clusters become even more stable with the existence of the interior atoms in the cluster structure.

Shortly afterwards, Rötlisberger et al. [190] applied an LDA based Car-Parrinello method to several clusters, including Si_{45}. The lowest-energy structures found from these relaxations feature two shells: an inner shell containing a few core atoms and an outer shell formed by a fullerene-like cage of 38 atoms. Unlike carbon fullerenes, however, these cages were puckered as a consequence of the much higher tendency of Si to form distorted sp^3 hybrids. They also explained the function of the internal atoms inside the fullerene cage as stabilizing the outer cage by reducing the number of dangling bonds.

Another study was performed by Pan and Ramakrishna [193] to clarify the predictions by Smalley et al. [42,43] about the unreactivity of certain cluster sizes such as Si_{33}, Si_{39}, and Si_{45}. They argued that the structures of the unreactive clusters should not have any dangling bonds. Therefore, they constructed model structures featuring a bulklike core of a five atoms surrounded by a fullerene-like surface similar to the structures found by Rötlisberger et al. [190]. In their model, the five-atom core has the exact structure of bulk silicon with one atom in the center bonded to four atoms arranged in a perfect tetrahedral symmetry. In particular, they generated the Si_{33} and Si_{45} structures by inserting the five-atom core inside the 28- and 40-atom fullerene, respectively. Gong [194] has also dealt with a Si_{33} cluster which was obtained by doping the fullerene cage of Si_{28} with $Si_{5.}$ The resulting Si_{33} structure is very similar to that of Kaxiras and Jackson [60].

In addition to these studies, recently Li et al. [195,196,197,198] performed a full-potential linear-muffin-tin-orbital molecular dynamics (FP-LMTO-MD) study for the investigation of the larger clusters. They found a puckered ball structure for Si_{60} [195,196] and stable distorted fullerene cage structures for Si_n clusters with n=24, 26, 28, 30, and 32 [197]. They also considered a fullerene structure for Si_{20} [197], however, it was found to be less stable than a stack of TTP units. They also investigated [198] a Si_{36} fullerene cage and a Si_{36} prolate isomer constructed by stacking of four tri-capped trigonal prism units. Similar to the other perfect initial fullerene cages, the Si_{36} cage relaxed to a distorted cage. Interestingly, they found that the stacked TTP structure by is slightly more stable than the distorted cage-like structure. This study has also produced results in contradiction to the experimentally observed shape transition by favoring a prolate structure for Si_{36}. However, in a more recent study Sun et al. [199] found a trend opposite to the one that appeared in Li et al. [198]: prolate isomers containing stacked tri-capped trigonal prism units not being favored over cage-like structures at the DFT-GGA level.

In all of these studies, no unbiased search is conducted, instead a few prototypes of prolate and spherical isomers were constructed in an ad-hoc fashion and then their energies were calculated within the desired level of theory. In contrast, in this current study, we continue searching in an unbiased, global manner for the lowest-energy cluster structures, for the first time in the $30 \leq n \leq 35$ region. The structures

Table 10.5: Energies and energy orderings of Si_n clusters with $30 \le n \le 35$ at the DFT levels.

Structure	DFT (eV)	Structure	DFT (eV)
Si_{30}-1	**-131.1631**	Si_{31}-1	**-136.2335**
Si_{30}-2	-131.0586	Si_{31}-2	-135.5849
Si_{30}-3	-131.0197	Si_{31}-3	-135.4304
Si_{30}-4	-130.9498	Si_{31}-4	-134.9700
Si_{32}-1	**-140.5719**	Si_{33}-1	**-145.8169**
Si_{32}-2	-139.9621	Si_{33}-2	-145.1675
Si_{32}-3	-139.9306	Si_{33}-3	-144.7009
Si_{32}-4	-139.6318	Si_{33}-4	-144.4754
Si_{34}-1	**-149.1315**	Si_{35}-1	**-153.7800**
Si_{34}-2	-148.9639	Si_{35}-2	-153.7607
Si_{34}-3	-148.8579	Si_{35}-3	-153.3664
Si_{34}-4	-148.6453	Si_{35}-4	-152.8755

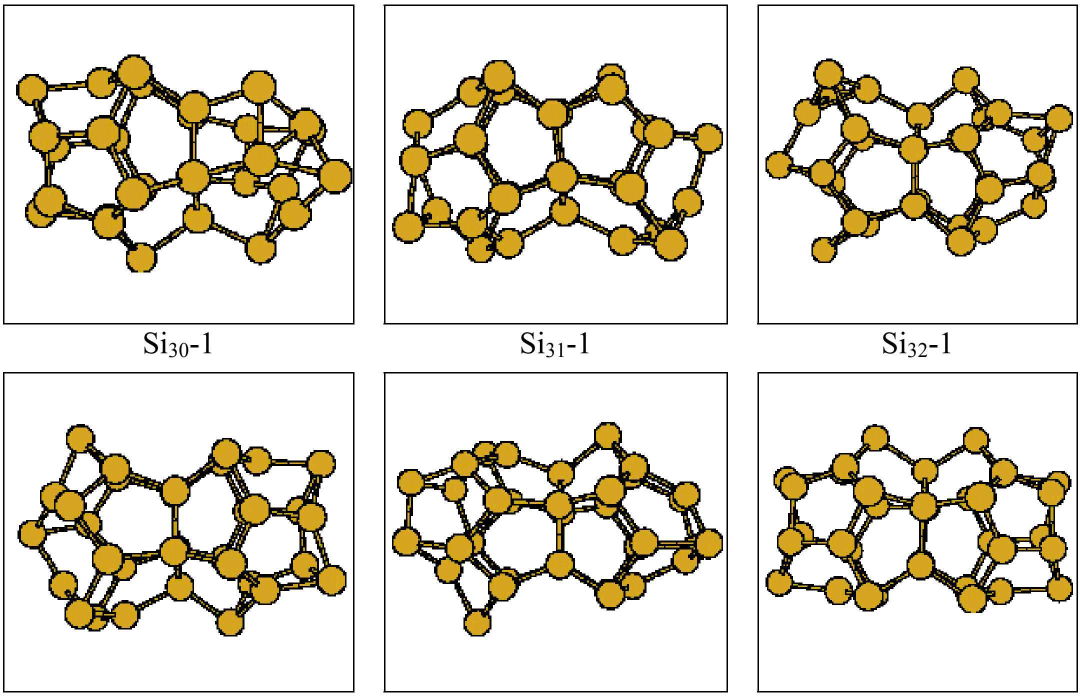

Si_{30}-1 Si_{31}-1 Si_{32}-1

Si_{33}-1 Si_{34}-1 Si_{35}-1

Figure 10.5: Structures found here and in the literature for Si_n clusters with $30 \le n \le 35$ at the DFT/B3LYP level.

found and their energies at the DFT/B3LYP level are displayed in Fig. 10.5 and Table 10.5, respectively. All the structures found as the lowest-energy structure contain a distorted Si_{20} cage fused to another cage just as encountered for Si_{26}-1, Si_{27}-1, and Si_{28}-1. Note that the other cage attached to the distorted Si_{20} cage reaches a size of 20 atoms for Si_{35}, resulting in two fused distorted Si_{20} cages. Except for these spherical building blocks, totally spherical structures containing puckered pentagons such as those that appeared in Si_{24}-1 and Si_{25}-1 are also found, but higher in energy. Additionally, contrary to the previous cluster sizes, prolate isomers are rarely located .

10.4 Summary

As a summary, relaxation of the structures found from Mistriotis and modified Mistriotis potentials are carefully continued for the structural transition region and beyond. The best structures obtained at the DFT/B3LYP level and LMP2 level are summarized in Table 10.6.

Table 10.6: Lowest energy isomers predicted at the DFT and LMP2 levels.

Cluster	DFT	LMP2
Si_{20}	Jack-Si_{20}	Jar-Si_{20}-4
Si_{21}	Jack-new-Si_{21}	Jar-Si_{21}
Si_{22}	Jack-new-Si_{22}	Jar-Si_{22}-2
Si_{23}	Jack-Si_{23}	Jack-Si_{23}
Si_{24}	Jack-Si_{24}	Jack-Si_{24}
Si_{25}	Jack-Si_{25}	Jar-Si_{25}
Si_{26}	Jack-Si_{26}	Jar-Si_{26}
Si_{27}	Jack-Si_{27}	Jar-Si_{27}
Si_{28}	Jack-Si_{28}	Jar-Si_{28}
Si_{29}	Si_{29}-1	

Cluster	DFT
Si_{30}	Si_{30}-1
Si_{31}	Si_{31}-1
Si_{32}	Si_{32}-1
Si_{33}	Si_{33}-1
Si_{34}	Si_{34}-1
Si_{35}	Si_{35}-1

Results obtained at the DFT level strongly support the structural transition from prolate to spherical beginning with Si_{26}. Among the prolate structures, for Si_{20} and Si_{21}, structural patterns containing octahedron subunits dominate, whereas for Si_{22}, Si_{23}, and Si_{24}, tri-capped trigonal prism and bicapped square antiprism units become more prevalent. A mixture of these subunits (an octahedron and a bicapped square antiprism) turns out to be the best structure for Si_{25}. For $n \geq 25$, spherical isomers begin to dominate with different characteristics in shape. In particular, Si_{26} and Si_{27} have the same structural features: They consist of two internal atoms surrounded by a distorted cage, however, the outer cages differ from each other. Si_{28} and Si_{29} have also common structural properties: a cage containing an internal atom attached to a trigonal prism based unit. Then, another spherical structural pattern begins to appear for the $30 \leq n \leq 35$ region: a distorted Si_{20} cage fused to another distorted cage.

In contrast, at the LMP2 level, a dominance of spherical structures after the transition region could not be observed, instead, prolate isomers are obtained as the lowest-energy structures for $n \leq 29$. Due to excessive demands on computer time, these single point energy calculations could not be carried out for the $30 \leq n \leq 35$ region, however, based on the previous results it appears likely that LMP2 may continue to prefer prolate structures instead of spherical ones for this region.

The cohesive energies and the second energy differences, (Δ_2), of Si_n clusters with $10 \leq n \leq 35$ are plotted in Fig. 10.6 and Fig 10.7., respectively. As mentioned in the previous chapter, there is an agreement between DFT and LMP2 cohesive energy and Δ_2 approximately up to Si_{17}. In contrast, this agreement is not preserved for larger cluster sizes. Unfortunately, the reason behind this is unclear.

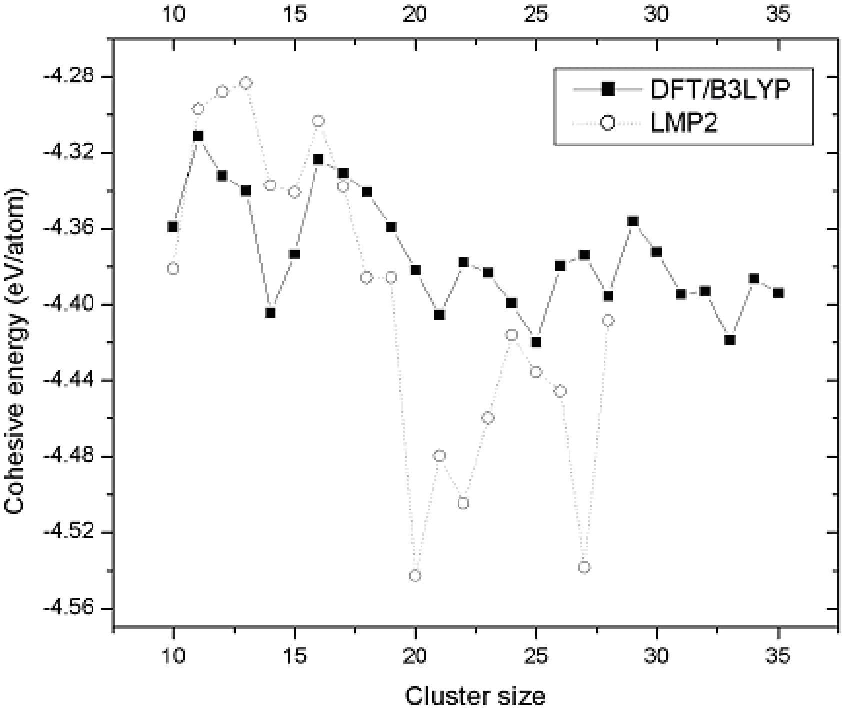

Figure 10.6: Cohesive energies in eV/atom for Si_n clusters listed in Table 10.6 as a function of cluster size as calculated with DFT/B3-LYP and LMP2 (LMP2 energies are shifted by 0.7 eV).

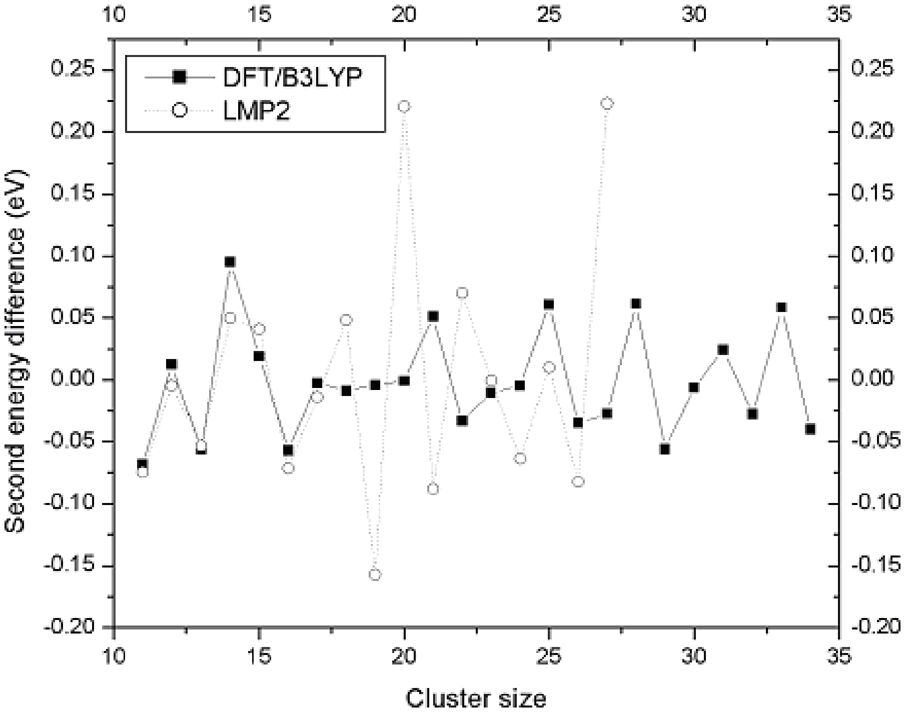

Figure 10.7: The second energy difference (Δ_2) for Si_n clusters listed in Table 9.5 as a function of cluster size as calculated with DFT/B3-LYP and LMP2.

All these contradictory results in the experimentally observed structural transition region leave two important questions to be answered: (1) Experimentally, clusters are produced by pulsed laser vaporization of a silicon rod, followed by supersonic expansion into a molecular beam apparatus, together with buffer gas. Are the clusters formed under these conditions likely to be well represented by global minimum energy structures, or is there are bias towards certain other low-energy structures, with possible dependence on the actual experimental conditions? (2) Is the level of theory used for the current theoretical studies high enough to get reliable results? Both questions are very difficult to answer. Since silicon clusters in this size region are very large systems for ab-initio and DFT calculations, desirable levels of theory with a reasonably large basis set become impractical. For this reason, one has to use a moderate level of theory with a moderate basis set to obtain at least moderately reliable predictions for theoretical support of the experimental observations. Unfortunately, at present, this yields many inconsistencies in the predictions obtained which has been documented throughout this current study. Just to repeat one particular example, Zeng et al. [65] predicted the structural transition at an earlier cluster size, Si_{21}, than the experimentally observed size, at both the DFT/B3LYP and CCSD levels, with a 6-31G* basis set. However, the lowest-energy spherical structure found by Zeng et al. [65] became only a local minimum in this current study both with DFT/B3LYP using a (3s3p1d) basis set and an ECP and with LMP2 using the cc-pVTZ basis set. Even though the same level of theory, DFT/B3LYP, has been employed by Zeng at al. [65] and in this current study, the basis sets used were different. This resulted in a marked difference in the energy orderings of the candidate structures. The observation that a slight change in basis set can cause a marked change in the results is a clear indication for the level of theory being too low. This lends further support to our conclusion that higher-level results than currently affordable are needed to resolve the present contradictory puzzle around the silicon cluster shape transition.

10.5 Charged Si_n clusters with $20 \leq n \leq 35$

Optimized structures for Si_n clusters with $20 \leq n \leq 35$ found in this current study were also relaxed as cation and anion at the DFT/B3LYP level in order to check the effect of charge.

As already observed for smaller cluster sizes in section 9.2, for Si_n anions and cations, the relaxed ionic structures were found to be only slightly distorted compared to their neutral counterparts.

10.6 Ion mobility simulations for Si_n clusters with $20 \leq n \leq 35$

As described in section 9.3 mobilities of any structure can be calculated with three different methods. This was done for Si_n clusters with $10 \leq n \leq 19$ in section 9.3. Here, these calculations are performed for the $20 \leq n \leq 35$ size region. Since trajectory mobilities are more reliable, in Fig. 10.8, trajectory mobilities were plotted for the $20 \leq n \leq 35$ size range. In this figure, filled black circles represent the measured mobilities. Beginning with $n=24$, there are multiple structures observed in measurements. “Zeng” and “Paderborn” represent the mobilities calculated for structures found by Zeng et al. [65] and Frauenheim [189], respectively. The remaining designations are as in section 9.3.

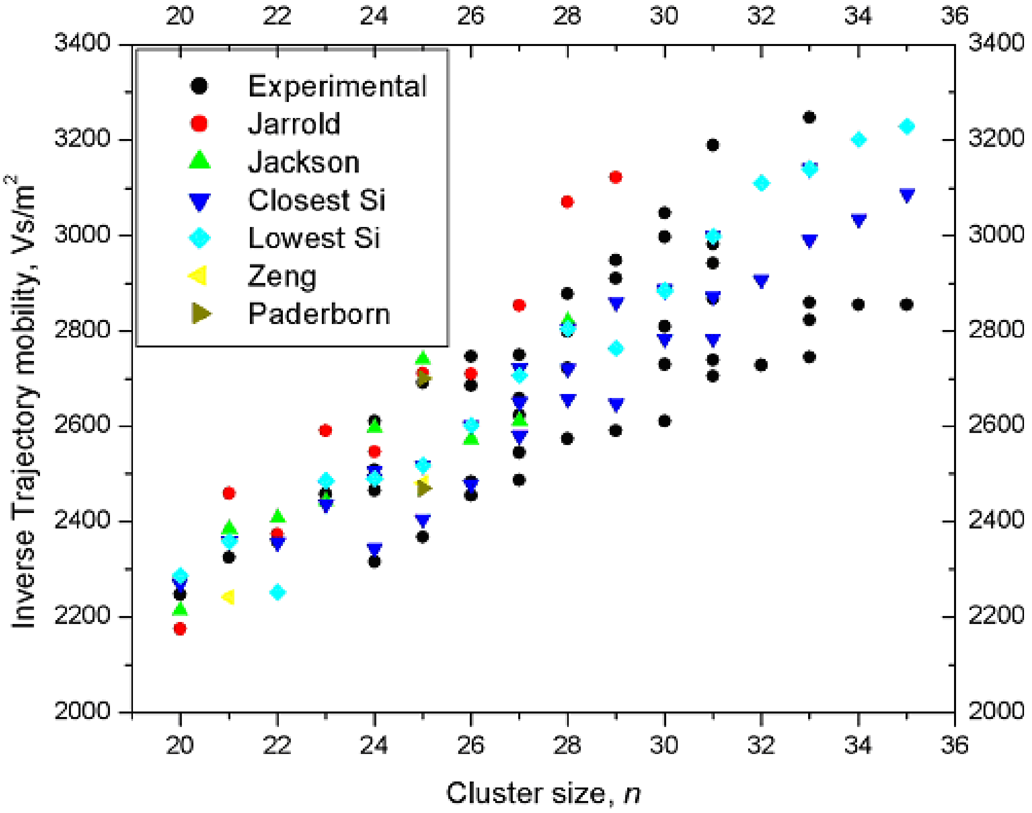

Figure 10.8: The Trajectory mobilities for Si_n clusters with $20 \le n \le 35$.

In Fig. 10.8, calculated mobilities for structures found in this current study match experimental data for many cluster sizes, especially for *n*=20,21,23,24,28,30,31. In particular, in the transition region, typically more than just one experimental data point can be matched rather closely. "Jarrold" structures, except for cluster sizes *n*=22,25,26, generally have mobilities higher than the experimental ones. "Jackson" structures also seem in agreement with experimental data, especially for the sizes *n*=21,23,27,28 As already observed for smaller clusters in section 9.3, a closer inspection of the data in Fig. 10.8 reveals that in many cases qualitatively different structures have calculated mobilities close to measured ones. Therefore, unfortunately, the mobility data alone turn out to be insufficient to decide between competing proposals for the inner structures of the clusters, also in this critical size region.

11 Conclusion

11.1 Summary

In this thesis, Si_n clusters in the size range n=4-35 have been investigated, ultimately aiming at providing some more comprehensive explanations for the structural transition observed mainly in ion mobility experiments. For this purpose, an evolutionary algorithm containing two major ingredients, namely GAGA and PHENIX, has been used. GAGA is a simple but effective scheme to allow for global geometry optimizations at expensive ab-initio levels. It combines global geometry optimizations on a model potential with global parameter optimizations of this model potential, using ab-initio single-point data. GAGA requires an empirical potential as guiding function. PHENIX, which is based on a Deaven-Ho-style genetic algorithm (GA), is responsible for the actual global geometry optimizations of the silicon clusters.

In order to perform global geometry optimizations on the model potential, one needs globally optimized parameter sets of these model potentials. In order to test the reliability of the global parameter optimization, an important cluster size Si_{10} (a candidate for a growth pattern for medium-sized silicon clusters) was used as a benchmark system. In this manner, first standard potentials from the literature, namely the SWG and Mistriotis potentials, have been extensively tried. However, when globally optimized parameter sets for these potentials were used for global geometry optimizations of Si_{10} with the help of PHENIX, the accepted global minimum structure of Si_{10}, the tetra-capped trigonal prism (TTP), could not be located. At best, the TTP structure was obtained only as low-energy minimum. After this failure, the Mistirotis potential was modified, following Gong's modification of the Stillinger and Weber potential. This modified Mistriotis potential was then subjected to the GAGA scheme to generate globally optimized parameter sets for it. Fortunately, this time one parameter set could be found for which the TTP structure was obtained as the global minimum structure for Si_{10}. Additionally, other parameter sets for the modified Mistirotis potential that result in the TTP structure as a low-energy minimum were also obtained.

The four most promising globally optimized parameter sets were then used for the global geometry optimization of Si_n clusters with $4 \leq n \leq 40$, to test their reliability in reproducing the known global minimum structures. For $n \leq 10$, all the global minimum structures proposed in the literature could be reproduced successfully. For Si_8, two structures proposed in the literature were reproduced. Surprisingly, in additional, a new structure was found as as global minimum at the DFT level.

Contining these global geometry optimizations on the model potentials to larger clusters, some low-energy isomers could be reproduced for $11 \leq n \leq 14$. Unfortunately, for $n>15$, the structures obtained in this way generally had a spherical shape and were different from the proposed structures in the literature.

A good guiding function does not necessarily have to reproduce the correct energy ordering of the cluster structures, but it should reliably lead to low-energy minima upon further relaxation on the DFT or ab-initio level. Therefore, structures obtained from global geometry optimizations using the Mistriotis and modified Mistriotis potentials were locally reoptimized at the DFT/B3LYP level. These DFT relaxations were followed by single point energy calculations at the LMP2 level in order to get more reliable results. These DFT relaxations and LMP2 single-point calculations were also carried out for the best structures proposed in the literature.

In the DFT relaxations, for Si_{11} and Si_{12}, the best literature results were reproduced. For Si_{13} and Si_{14}, several new isomers could be located that are better than the best ones from the literature. Except Si_{11} and Si_{14}, the dominance of structures containing the trigonal prism is continued. For $15 \leq n \leq 19$, the best literature results could not be improved further. Surprisingly, at the LMP2 level, marked discrepancies to the DFT results were observed. For many clusters sizes, the relative energy ordering of the most important minima at the DFT level was changed partly or even completely upon switching to LMP2.

The cluster size region $20 \leq n \leq 30$ has a special significance because of the structural transition from prolate to spherical outer cluster shapes, as observed mainly in ion mobility measurements. There, the structural transition appeared at $n=24$ and $n=26$ for silicon cations and anions, respectively. The same transition was also supported by other experiments such as binding energy and ionization potential measurements. However, the latter experiment suggested the transition to occur between $n=20$ and 22. In order to comprehend this transition and to complement the experimental information on outer shapes with inner structures, recent works from the literature and this work have focused their attention on this size range.

Results obtained at the DFT level strongly support the shape transition form prolate to spherical structures beginning with Si_{26}. Up to $n=25$, the best structures have prolate outer shapes. In their inner structures, a small set of characteristic building blocks is found repeatedly. For $n \geq 25$, spherical isomers begin to dominate. They exhibit different characteristics in shape, but all contain cages with inner atoms.

In stark contrast, at the LMP2 level, the dominance of spherical structures after the transition region could not be confirmed. Instead, just as before the transition region, prolate isomers are obtained as the lowest-energy structures for $n \leq 29$. This discrepancy to the DFT results and to the mobility experiments raises the suspicion that the apparent agreement between DFT results and experiment probably is fortuitous. It could be based either on insufficient levels of theoretical description, concerning both the structural search and the electronic structure calculations, or on cluster preparation not being thermodynamically controlled in the experiment, or on both.

In this current study, a systematic global structure optimization followed by DFT relaxation was extended beyond of the transition region for the first time, including also the size region $30 \leq n \leq 35$. For this region, all the lowest-energy structures found contain a distorted Si_{20} cage fused to another cage.

11.2 Outlook

Very recently, some authors [68] have claimed to have solved the mystery of the shape transition of silicon clusters, based upon DFT calculations. While this study could confirm that there is some agreement between experimental data and DFT results, it has also revealed that MP2 results (which are in many cases considered to be more reliable than DFT) are not in agreement with the DFT findings and that the central experimental mobility data are not sufficient to decide between various structural alternatives.

To resolve this issue from the theoretical side, higher-level calculations are required. It can reasonably be expected that e.g. CCSD(T)/cc-pVQZ calculations should come close to the “final answer” – provided that all clusters considered here are single-reference cases (otherwise, still more expensive CASSCF/MRCI calculations would become necessary). In the near future, with somewhat faster computers and with further algorithmic advances (linear scaling for CC-methods also for 3D extended systems, lower scaling of these methods with basis set size), it will become possible to do single-point calculations at this level of theory for a representative collection of cluster isomers in the shape transition region, maybe even a few representative local structure relaxations. Such a study will have a chance of settling the theoretical discrepancies uncovered in the present work.

Given the observed discrepancies between DFT and MP2 results, however, it may also be possible that the current tactics of performing local geometry optimizations at the DFT level and supplementing this by higher-level single-point calculations is not good enough and that local geometry optimizations at a correlated ab-initio level are necessary. This would increase computational demands further.

Unfortunately, global structure optimization directly at a correlated level of ab-initio theory will remain a dream for a much longer time. Therefore, another necessary step will be to develop better empirical Silicon potentials as guiding functions for global search, after the presently known potentials have been found to be not sufficient in the present study, even if improvements are added to them. One possible line of attack would be to exploit the full GAGA algorithm and to reoptimize potential parameters in a cluster-size-specific manner even in the shape transition region (which was avoided in the present work, due to computational costs). As an extension of this, one may also aim at a size-specific reparametrization of semiempirical methods, e.g. MNDO/d. This, however, would increase the computational cost of the global cluster optimization by a few orders of magnitude and hence compromise its reliability.

Since the mobility data have been found insufficient to discern between various structures here, future studies should also include systematic calculations of other experimental observables for all cluster isomers, e.g. ionization potentials and polarizabilities. Again, quantitatively reliable results for these properties require faster computers and better algorithms than those available at present.

Ultimatively, it would be desirable to complement the picture of static cluster structures by simulations of cluster dynamics, including their assembly and fragmentation. Obviously, present-day empirical potentials are not of sufficient accuracy for this purpose. Likewise, Car-Parrinello molecular dynamics with GGA DFT functionals will face the same problems as the static DFT results in this work. Any higher level of theory will probably be impossible for these systems and for such an approach for a very long time. However, direct dynamics using a system-specifically reparametrised semiempirical approach may again be a viable alternative. Only then it will be possible to theoretically address the remaining question of whether the cluster structures observed in the experiments so far can indeed be modeled by seeking global minima or are perhaps biased towards certain types of low-energy local minima by kinetic effects arising during experimental cluster preparation.

12 References

---

[1] A. A. Shvartsburg, R. R. Hudgins, P. Dugourd, and M. F. Jarrold, *Chem. Soc. Rev*. 30 (2001), 26.

[2] M. F. Jarrold and J. E. Bower, *J. Chem. Phys*. 96 (1992), 9180.

[3] R. B. Hudgins, M. Imai, M. F. Jarrold, and P. Dugourd, *J. Chem. Phys*. 111 (1999), 7865.

[4] A. A. Shvartsburg, B. Liu, M. F. Jarrold, and K. M. Ho, *J. Chem. Phys*. 112 (2000), 4517.

[5] M. F. Jarrold and V. A. Constant, *Phys. Rev. Lett*. 67 (1991), 2994.

[6] A. A. Shvartsburg, M. F. Jarrold, B. Liu, Z. Y. Lu, C. Z. Wang, and K. M. Ho, *Phys. Rev. Lett*. 81(1998), 4616.

[7] K. Ho, A. A. Shvartsburg, B. Pan, Z. Yilu, C. Wang, J. G. Wacker, J. L. Fye, and M. F. Jarrold, *Nature* 392, (1998), 582.

[8] T. Bachels and R. Schäfer, *Chem. Phys. Lett*. 324 (2000), 365.

[9] K. Fuke, K. Tsukamoto, F. Misaizu, and M. Sanekata, *J. Chem. Phys*. 99 (1993), 7807.

[10] M.F. Jarrold and E.C. Honea, *J. Phys. Chem*. 95 (1991), 9181.

[11] R. W. Schmude, Q. Ran, K. A. Gingerich, and J. E. Kingcade, *J. Chem. Phys*. 102 (1995), 2574.

[12] W. Schmude, Q. Ran, and K. A. Gingerich, *J. Chem. Phys*. 99 (1993), 7998.

[13] Q. Ran, R. W. Schmude, M. Miller, and K. A. Gingerich, *Chem. Phys. Lett*. 230 (1994), 337.

[14] D. M. Deaven and K. M. Ho, *Phys. Rev. Lett*. 75, (1995), 288.

[15] C. C. Arnold and D. M. Neumark, *J. Chem. Phys*. 99, (1993), 3353.

[16] E. C. Honea, A. Ogura, C. A. Murray, K. Raghavachari, W. O. Sprenger, M F. Jarrold, and W. L. Brown, *Nature* 366, (1993), 42.

[17] S. Li, R. J. Van Zee, W. Weltner, Jr. and Krishnan Raghavachari, *Chem. Phys. Lett*. 243 (1995), 275.

[18] J. Muller, B. Liu, A. A. Shvartsburg, S. Ogut, J. R. Chelikowsky, K. W. M. Siu, K. M. Ho, and G. Gantefor, *Phys. Rev. Lett*. 85 (2000), 1666.

[19] O. Cheshnovsky, S. H. Yang, C. L. Pettiette, M. J. Craycraft, Y. Liu, and R. E. Smalley, *Chem. Phys. Lett*. 138 (1987), 119.

[20] H. Kawamata, Y. Negishi, R. Kishi, S. Iwata, A. Nakajima, and K. Kaya, *J. Chem. Phys*. 105 (1996), 5369.

[21] N. Binggeli and J. R. Chelikowsky, *Phys. Rev. Lett*. 75 (1995), 493.

[22] J. R. Chelikowsky and N. Binggeli, *Mater. Sci.Forum* 232 (1996), 87.

[23] S. Ogut and R. J. Chelikowsky, *Phys. Rev. B* 55 (1997), 4914.

[24] A. A. Shvartsburg, B. Liu, M. F. Jarrold, and K. M. Ho, *J. Chem. Phys*. 112 (2000), 4517.

[25] I. Rata, A.A. Shvartsburg, M. Horoi, T. Frauenheim, K. W. M. Siu, and K. A. Jackson, *Phys. Rev. Lett* 85, (2000), 546.

[26] K. Jackson, A. R. Pederson, D. Porezag, Z. Hajnal, and T. Frauenheim, *Phys. Rev. B* 55 (1997), 2549.

[27] R. Fournier, S. B. Sinnot, and A. E. DePristo, *J. Chem. Phys*. 97 (1992), 4149.

[28] A. Bloomfield, R. R. Freeman, and W. L. Brown, *Phys. Rev. Lett*. 54, (1985), 2246.

[29] T. P. Martin and H. Schaber, *J. Chem. Phys*. 83 (1985), 855.

[30] Y. Liu, Q. L. Zhang, F. K. Tittel, R. F. Curl, R. E. Smalley, *J. Chem. Phys*. 85 (1986), 7434.

[31] Q. L. Zhang, Y. Liu, R. F. Curl, F. K. Tittel, and R. E. Smalley, *J. Chem. Phys*. 88 (1988), 1670.

[32] M. F. Jarrold and J. E. Bower, *J. Phys. Chem*. 92 (1988), 5702.

[33] E. H. Copland and N. S. Jacobson, *The electrochemical society interface* (Summer 2001), 28.

[34] R. Schäfer, S. Schlecht, J. Woenckhaus, and J. A. Becker, *Phys. Rev. Lett*. 76 (1996), 471.

[35] I. Vasiliev, S. Ögüt, and J. R. Chelikowsky, *Phys. Rev. Lett*. 78 (1997), 4805.

[36] V. E. Bazterra, M. C. Caputo, M. B. Ferrara, and P. Fuentealba, *J. Chem. Phys*. 117 (2002), 11158.

[37] J. R. Heath, Y. Liu, S. C. O'Brien, Q. L. Zhang, R. F. Curl, F. K. Tittel, and . E. Smalley, *J. Chem. Phys*. 83 (1985), 5520.

[38] D. J. Trevor, D. M. Cox, K. C. Reichmann, R.O. Brickman, and A. Kaldor, *J. Phys. Chem*. 91 (1987), 2598.F. Misaizu, and M. Sanekata, *J. Chem. Phys*. 99 (1993), 7807.

[40] C. B. Winstead, S. J. Paukstis, and J. L. Gole, *Chem. Phys. Lett*. 237 (1995), 81.

[41] B. Liu, Z. Lu, B. Pan, C. Wang, K. Ho, A. A. Shvarstburg, and M. F. Jarrold, *J. Chem. Phys*. 109 (1998), 9401.

[42] L .R. Anderson, S. Maruyama, and R. E. Smalley, *Chem. Phys. Lett*. 176 (1991), 348.

[43] S. Maruyama, L. R. Anderson, and R. E. Smalley, *J. Chem. Phys*. 93 (1990), 5349.

[44] S. Maruyama, L. R. Anderson, and R. E. Smalley, *Mat. Res. Soc. Symp. Proc*. 206 (1991), 63.

[45] M. F. Jarrold, J. E. Bower, and K. Creegan, *J. Chem. Phys*. 90 (1989), 3615.

[46] K. M. Creegan and M. F. Jarrold, *J. Am. Chem. Soc*. 112 (1990), 3768.

[47] M. F. Jarrold, U. Ray, K. M. Creegan, *J. Chem. Phys*. 93 (1990), 224.

[48] U. Ray and M. F. Jarrold, *J. Chem. Phys*. 94 (1991), 2631.

[49] U. Ray and M. F. Jarrold, *J. Chem. Phys*. 93 (1990), 5709.

[50] M. F. Jarrold , Y. Ijira, and U. Ray, *J. Chem. Phys*. 94 (1991), 3607.

[51] A. Maruyama, M. Kohno, and S. Inoue, *Ther. Sci. Eng*. 7 (1999), 1.

[52] Ph. Dugourd, R. R. Hudgins, D. E. Clemmer, and M. F. Jarrold, *Rev. Sci. Instrum*. 68 (1997), 1122.

[53] M. F. Mesleh, J. M. Hunter, A. A. Shvartsburg, G. C. Schatz, and M. F. Jarrold, *J. Phys. Chem*. 100 (1996), 16082.

[54] A. A. Shvartsburg and M. F. Jarrold, *Chem. Phys. Lett*. 317 (2000), 615.

[55] K. Raghavachari and C. M. Rohlfing, *J. Chem. Phys*. 89 (1988), 2219.

[56] K. Raghavachari and V. Logovinsky, *Phys. Rev. Lett*. 55 (1985), 2853.

[57] K. Raghavachari and C. M. Rohlfing, *Chem. Phys. Lett*. 198 (1992), 521.

[58] A. D. Mistriotis, N. Flytzanis, and S. C. Farantos, *Phys. Rev. B* 39 (1989), 1212.

[59] B. C. Bolding and A. C. Andersen, *Phys. Rev. B* 41 (1990), 10568.

[60] E. Kaxiras and K. Jackson, *Phys. Rev. Lett*. 71 (1993), 727.

[61] J. C. Grossman and L. Mitas, *Phys. Rev. B* 52 (1995), 16735.

[62] M. R. Pederson, K. Jackson, D. V. Porezag, Z. Hajnal, and Th. Frauenheim, *Phys. Rev. B* 54 (1996), 2863.

[63] A. Sieck, D. Porezag, T. Frauenheim, M. R. Pederson, and K. Jackson, *Phys. Rev. A* 56 (1997), 4890.

[64] A. Sieck, T. Frauenheim, and K. A. Jackson, *Phys. Stat. Sol. (b)* 240 (2003), 537.

[65] S. Yoo, X. C. Zeng, X. Zhu, and J. Bai, *J. Am. Chem. Soc*. 125 (2003), 13318.

[66] X. Zhu and X. C. Zeng, *J. Chem. Phys*. 118 (2003), 3558.

[67] X. L. Zhu, X. C. Zeng, Y. A. Lei, and B. Pan *J. Chem. Phys*. 120 (2004), 8985.

[68] K. A. Jackson, M. Horoi, I. Chaudhuri, T. Frauenheim, and A. A. Shvartsburg, *Phys. Rev. Lett.* 93 (2004), 013401.

[69] Chapter 10: "Minimization or maximization of functions", *Numerical recipes in fortran 77*: The art of scientific computing, Cambrigde University Press, page:387.

[70] J. C. Culberson, *Technical Report TR 96-18* (1996), University of Alberta, Canada.

[71] R. H. Byrd, P. Lu, J. Nocedal, and C. Zhu, *Technical report NAM-08* (1994), "A limited memory algorithm for bound constrained optimization", Nortwestern University, Department of electrical engineering and computer science.

[72] C Bliek, P. Spellucci, L. N. Vicente, A. Neumaier, L. Granvilliers, E. Monfroy, F. Benhamou, E. Huens, P. Van Hentenryck, D. Sam-Haroud, and B. Faltings, *The Coconut project*, "Algorithms for solving nonlinear constrained and optimization problems: the state of the art. (2001)".

[73] P. M. Pardalos and H. E. Romeijn, *Handbook of Global Optimization (Volume 2)*, Chapter 15: Global Optimization: Software, Test Problems, and Applications, Kluwer academic publishers, 2002.

[74] http://www.cs.sandia.gov/opt/survey/main.html.

[75] A. V. Levy, A. Montalvo, *Journal on Scientific and Statistical Computing* 6 (1985) 15.

[76] S. Gomez, N. del Castillo, L. Castellanos, and J. Solano, *Parallel Computing* 29 (2003) 523.

[77] F. Lim, G. Beliakov, and L. M. Batten, *Phys. Chem. Chem. Phys.* 5 (2003), 3884.

[78] G. Beliakov, *Optimization Methods & Software* 19 (2004), 137.

[79] S. Kirkpatrick, C. D. Gelatt, and M. P. Vecchi, *Science* 220 (1983), 671.

[80] S. Geman and D. Geman, *IEEE Transactions on Pattern Analysis and Machine Intelligence* 6 (1984), 721.

[81] Z. Li and H. A. Scheraga, *Proc. Natl. Acad. Sci.* 84 (1987), 6611.

[82] J. Lee, In-Ho Lee, and J. Lee, *Phys. Rev. Lett.* 91 (2003), 80201.

[83] A. Cheung, C. S. Adjiman, P. Kolar, T. Ishikawa, *Fluid Phase Equilibria* 194–197 (2002) 169.

[84] C. A. Floudas, *Deterministic Global Optimization: Theory, Methods, and Applications*, Kluwer Academic Publishers, Dordrecht, London, 2000, *Nonconvex optimization and its applications*, vol. 37.

[85] D. Maranas and C. A. Floudas, *J. Chem. Phys*. 97 (1992), 7667.

[86] A. Floudas and V. Visweswaren, *Comput. Chem. Eng*. 14 (1990), 1397.

[87] D. J. Wales and J. P. K. Doye, *J. Phys. Chem A* 101 (1997), 5111.

[88] B. Hartke, *J. Comp. Chem* 20, (1999), 1752.

[89] M. Locatelli and F. Schoen, *Computational Optimization and Applications* 21 (2002) 55.

[90] M. Locatelli and F. Schoen, *Computational Optimization and Applications* 26 (2003), 173.

[91] C. S. Shao, R. Byrd, E. Eskow, and R. B. Schnabel, *Journal of Global Optimization* 16 (2000), 167.

[92] G. Bilalbegovic, *Phys. Lett. A* 308 (2003), 61.

[93] X. G. Gong, Q. Q. Zheng, and Y. Z. He, J. *Phys. Condens. Matter* 7 (1995), 577.

[94] M. R. Lemes, C. R. Zacharias, and A. Dal Pino, *Phys. Rev. B*. 56 (1997), 9279.

[95] A. D. Mistriotis, N. Flytzanis, and S. C. Farantos, *Phys. Rev. B* 39(2) 1212 (1989).

[96] S. Yoo and X. C. Zeng, *J. Chem. Phys*. 119 (2003), 1442.

[97] J. Holland, *Adaptation in natural and artificial systems*, The University of Michigan Press, 1975.

[98] H. M. Cartwright, *An introduction to evolutionary computation and evolutionary algorithms, Structure and Bonding*, Vol.110 (2004), Springer-Verlag Berlin Heidelberg.

[99] D.E. Goldberg, *Genetic algorithms in search, optimization, and machine learning*, (1989) Addison-Wesley Publishing.

[100] L. Davis, *Genetic algorithms and simulated annealing*, (1987), Pitman Publishing, London.

[101] B. Hartke, *Application of EAs to global cluster geometry optimization, Structure and Bonding*, Vol.110 (2004), Springer-Verlag Berlin Heidelberg.

[102] B. Hartke, *Chem. Phys. Lett*. 258 (1996), 144.

[103] L. J. Munro, A. Tharrington, and K. D. Jordan, *Comput. Phys. Commun*. 145 (2002), 1.

[104] J. P. Neirotti, F. Calvo, D. L. Freeman, and J. D. Doll, *J. Chem. Phys*. 112 (2000), 10340.

[105] F. Calvo, J. P. K. Doye, *Phys. Rev. E* 63 (2000), 010902.

[106] J-B. Maillet, A. Boutin, S. Buttefey, F. Calvo, and A. H. Fuchs, *J. Chem. Phys*. 109 (1998), 329.

[107] J. Akola, K. Rytkönen, and M. Manninen, *Eur. Phys. J. D* 16 (2001), 21.

[108] F. Ruette and C. Gonzälez, *Chem. Phys. Lett*. 359 (2002), 428.

[109] Y. Xiang, D. Y. Sun, and X. G. Gong, *J. Phys. Chem. A* 104 (2000), 2746.

[110] B. Hartke, *J. Phys. Chem* 97 (1993), 9973.

[111] Y. Xiao and D. E. Williams, *Chem. Phys. Lett* 215 (1993), 17.

[112] Y. Zeiri, *Phys. Rev. E* 51 (1995), 2769.

[113] S. K. Gregurick, M. H. Alexander, and B. Hartke, *J. Chem. Phys* 104, (1996), 2684.

[114] J. A. Niesse and H. R. Mayne, *J. Chem. Phys* 105, (1996), 4700.

[115] J. A. Niesse and H. R. Mayne, *Chem. Phys. Lett* 261, (1996), 576.

[116] A. Tomasulo and M. V. Ramakrishna, *J. Chem. Phys* 105, (1996), 10449.

[117] R. Judson, *Rev. Comput. Chem* 10, (1997), 1.

[118] K. Michaelian, *Chem. Phys. Lett.* 293, (1998), 202.

[119] C. R. Zacharias, M. R. Lemes, and A. Dal Pino, *Theochem* 430, (1998), 29.

[120] R. P. White, J. A. Niesse and H. R. Mayne, *J. Chem. Phys* 108, (1998), 2208.

[121] B. Hartke, *Chem. Phys. Lett* 240, (1995), 560.

[122] B. Hartke, *Theo. Chem. Acc* 99, (1998), 241.

[123] M. Iwamatsu, *J. Chem. Phys.* 112, (2000), 10976.

[124] S. Hobday, R. Smith, and J. BelBruno, *Nuc. Inst. And Mater. in Phys. Res. B* 153 (1999), 247.

[125] A. Sieck, Th. Frauenheim, and K. A. Jackson, *Phys. Stat. Sol. (b)* 240 (2003), 537.

[126] M. V. Ramakrishna and A. Bahel, *J. Chem. Phys*. 104 (1996), 9833.

[127] S. Li, R. L. Johnston and J. N. Murrell, *J. Chem. Soc. Faraday Trans*. 88(9), 1229 (1992).

[128] Z. Y. Lu, C. Z. Wang, and K. M. Ho, *Phys. Rev. B*. 61 (2000), 2329.

[129] B. Hartke, H. J. Flad, and M. Dolg, *Phys.Chem.Chem.Phys*. 3 (2001), 5121.

[130] F. H. Stillinger and T. A. Weber, *Phys. Rev. B* 31 (1985), 5262.

[131] X. G. Gong, *Phys. Rev. B* 47 (1993), 2329.

[132] A. D. Mistriotis, G. E. Froudakis, P. Vendras, and N. Flytzanis, *Phys. Rev. B* 47 (1993), 10648.

[133] P. N. Keating, *Phys. Rev*. 145 (1966), 637.

[134] A. Tekin and B. Hartke, *Phys. Chem. Chem. Phys* 6 (2004), 503.

[135] J. Tersoff, *Phys. Rev. Lett*. 56 (1986), 632.

[136] J. Tersoff, *Phys. Rev. B* 38 (1988), 9902.

[137] J. Tersoff, *Phys. Rev. B* 37 (1988), 6991.

[138] M. S. Dow and M. I. Baskes, *Phys.Rev.Lett*. 50 (1983), 1285.

[139] M. S. Dow and M. I. Baskes, *Phys.Rev. B* 29 (1984), 6443.

[140] J. Cai, Phys. *Stat. Sol. (b)* 212 (1999), 9.

[141] D. Conrad and K. Scheerschmidt, *Phys. Rev. B* 58 (1998), 4538.

[142] D. W. Brenner, *Phys. stat. sol. (b)* 217, (2000), 23.

[143] G.C. Abell, *Phys. Rev. B* 31 (1985), 6184.

[144] M. I. Baskes, *Phys. Rev. Lett*. 59 (1987), 2666.

[145] R. Biswas and D. R. Hamann, *Phys. Rev. Lett*. 55 (1985), 2001.

[146] R. Biswas and D. R. Hamann, *Phys. Rev. B* 36 (1987), 6434.

[147] M. Z. Bazant and E. Kaxiras, *Phys. Rev. Lett* 77 (1996), 4370.

[148] M. Rasammy, M. Valiev, and G. W. Fernando, *Phys. Rev. B* 58 (1998), 9700.

[149] E. Pearson, T. Takai, T. Halicioglu, and W. A. Tiller, *J. Cryst. Growth* 70 (1984), 33.

[150] S. Li, R. L. Johnston and J. N. Murrell, *J. Chem. Soc. Faraday Trans*. 88 (1992), 1229.

[151] K. E. Khor and S. Das Sarma, *Phys. Rev. B* 38 (1988), 3318.

[152] J. Chelikowsky, *Phys. Rev. Lett*. 60 (1988), 2669.

[153] J. Chelikowsky, J. C. Philips, M. Kamal, and M. Strauss, *Phys. Rev. Lett*. 62 (1989), 292.

[154] Th. Frauenheim, G. Seifert, M. Elstner, Z. Hajnal, G. Jungnickel, D. Porezag, S. Suhai, and R. Scholz, *Phys. Stat. Sol. (b)* 217 (2000), 41.

[155] T. L. Lenosky, J. D. Kress, I. Kwon, A. F. Voter, B. Edwards, D. F. Richards, S. Yang, and J. B. Adams, *Phys. Rev. B*. 55, (1997), 1528.

[156] B. Paizs and A. Suhai, *J. Comp. Chem*. 19 (1998), 575.

[157] J. Wang, G. Wang, F. Ding, H. Lee, W. Shen, and J. Zhao, *Chem. Phys. Lett*. 341 (2001), 529.

[158] W. Koch and M. C. Holthausen, *A chemist's guide to density functional theory*, Wiley-VCH, Weinheim, 2001.

[159] F. Jensen, *Introduction to computational chemistry* (1999), Wiley publications (England).

[160] M. Baumhauer, *Diploma Thesis*, Stuttgart, 1996.

[161] S. Saebø and P. Pulay, *J. Chem. Phys*. 115 (2001), 3975.

[162] M. Schütz, G. Hetzer, and H. J. Werner, *J. Chem. Phys*. 111 (1999), 5691.

[163] J. W. Boughton and P. Pulay, *J. Comput. Chem*. 14 (1993), 736.

[164] G. Hetzer, P. Pulay, and H. J. Werner, *Chem. Phys. Lett*. 290 (1998), 143.

[165] M. Sierka, A. Hogekamp, and R. Ahlrichs, *J. Chem. Phys*. 118 (2003), 9136.

[166] L. Füsti-Molnár and P. Pulay, *J. Chem. Phys*. 117 (2002), 7827.

[167] M. J. Frisch, G. W. Trucks, H. B. Schlegel, G. E. Scuseria, M. A. Robb, J. R. Cheeseman, V. G. Zakrzewski, J. A. Montgomery, Jr., R. E. Stratmann, J. C. Burant, S. Dapprich, J. M. Millam, A. D. Daniels, K. N. Kudin, M. C. Strain, O. Farkas, J. Tomasi, V. Barone, M. Cossi, R. Cammi, B. Mennucci, C. Pomelli, C. Adamo, S. Clifford, J. Ochterski, G. A. Petersson, P. Y. Ayala, Q. Cui, K. Morokuma, N. Rega, P. Salvador, J. J. Dannenberg, D. K. Malick, A. D. Rabuck, K. Raghavachari, J. B. Foresman, J. Cioslowski, J. V. Ortiz, A. G. Baboul, B. B. Stefanov, G. Liu, A. Liashenko, P. Piskorz, I. Komaromi, R. Gomperts, R. L. Martin, D. J. Fox, T. Keith, M. A. Al-Laham, C. Y. Peng, A. Nanayakkara, M. Challacombe, P. M. W. Gill, B. Johnson, W. Chen, M. W. Wong, J. L. Andres, C. Gonzalez, M. Head-Gordon, E. S. Replogle, and J. A. Pople,, *Gaussian 98*, Revision A.11.4, Gaussian Inc., Pittsburgh PA, 2002.

[168] M. J. Frisch, G. W. Trucks, H. B. Schlegel, G. E. Scuseria, M. A. Robb, J. R. Cheeseman, J. A. Montgomery, Jr., T. Vreven, K. N. Kudin, J. C. Burant, J. M. Millam, S. S. Iyengar, J. Tomasi, V. Barone, B. Mennucci, M. Cossi, G. Scalmani, N. Rega, G. A. Petersson, H. Nakatsuji, M. Hada, M. Ehara, K. Toyota, R. Fukuda, J. Hasegawa, M. Ishida, T. Nakajima, Y. Honda, O. Kitao, H. Nakai, M. Klene, X. Li, J. E. Knox, H. P. Hratchian, J. B. Cross, C. Adamo, J. Jaramillo, R. Gomperts, R. E. Stratmann, O. Yazyev, A. J. Austin,R. Cammi, C. Pomelli, J. W. Ochterski, P. Y. Ayala, K. Morokuma,G. A. Voth, P. Salvador, J. J. Dannenberg, V. G. Zakrzewski, S. Dapprich, A. D. Daniels, M. C. Strain, O. Farkas, D. K. Malick, A. D. Rabuck, K. Raghavachari, J. B. Foresman, J. V. Ortiz, Q. Cui, A. G. Baboul,

S. Clifford, J. Cioslowski, B. B. Stefanov, G. Liu, A. Liashenko, P. Piskorz, I. Komaromi, R. L. Martin, D. J. Fox, T. Keith, M. A. Al-Laham, C. Y. Peng, A. Nanayakkara, M. Challacombe, P. M. W. Gill, B. Johnson, W. Chen, M. W. Wong, C. Gonzalez, and J. A. Pople, Gaussian 03, Revision B.04, Gaussian Inc., Pittsburgh PA, 2003.

[169] O. Treutler and R. Ahlrichs, *J. Chem. Phys*. 102 (1995), 346; M. v.Arnim and R. Ahlrichs, *J. Comp. Chem*. 19(1998), 1746; K. Eichkorn, O. Treutler, H. Oehm, M. Haeser and R. Ahlrichs, *Chem. Phys. Lett*. 242 (1995), 652; K. Eichkorn, F. Weigend, O. Treutler and R. Ahlrichs, *Theo. Chem. Acc*. 97 (1997), 119.

[170] Program system *Molpro*, version 2002.8, University of Birmingham (1997).

[171] Z. Y. Lu, C. Z. Wang, and K. M. Ho, *Phys. Rev. B* 61 (2000), 2329.

[172] Y. Luo, J. Zhao, and G. Wang, *Phys. Rev. B* 60 (1999), 10703.

[173] S .Hobday, R. Smith, and J. BelBruno, *Nuc. Inst. Meth. Phys. Res. B* 153 (1999), 247.

[174] D. J. Wales and M. C. Waterworth, *J. Chem. Soc. Faraday Trans*. 88 (1992), 3409.

[175] R. C. Haddon, L. E. Brus and K. Raghavachari, *Chem. Phys. Lett*. 125, 459 (1986).

[176] A. D. Zdetsis, *Phys. Rev. A* 64 (2001), 023202.

[177] A. Bahel and M. V. Ramakrishna, *Phys. Rev. B* 51 (1995), 13849.

[178] I. Lee, K. J. Chang, and Y. H. Lee, *J. Phys.: Condens. Matter* 6 (1994), 741.

[179] J. C. Grossman and L. Mitas, *Phys. Rev. Lett*. 74 (1995), 1323.

[180] Private Communications with Prof. X. C. Zeng.

[181] http://nano.chem.indiana.edu/software.html

[182] E. J. Bylaska, P. R. Taylor, R. Kawai, and J. H. Weare, *J. Phys. Chem*. 100 (1996), 6966.

[183] J. M. L. Martin, *Chem. Phys. Lett*. 255 (1996), 1.

[184] C. Miller, *Science* 252 (1991), 1092.

---

[185] M. R, Lemes, C. R. Zacharias, and A. Dal Pino, *Jr. Phys. Rev. B* 56 (1997), 9279.

[186] B. X. Li and P. L. Cao, *Phys. Rev. A* 62 (2000), 023201.

[187] L. Mitas, J. C. Grossman, I. Stich, and J. Tobik, *Phys. Rev. Lett.* 84 (2000), 1479.

[188] J. Song, S. E. Ulloa, and D. A. Drabold, *Phys. Rev. B* 53 (1996), 8042.

[189] Structures obtained from Prof. Th. Frauenheim via private communication.

[190] U. Röthlisberger, W. Andreoni, and M. Parrinello, *Phys. Rev. Lett.* 72 (1994), 665.

[191] All the structures beginning with "Jar" prefix shown in figures are taken from Prof. M. F. Jarrold via private communication.

[192] Jack-Si_{28} is taken from Prof. K. Jackson via a private communication.

[193] J. Pan and M. V. Ramakrishna, *Phys. Rev. B* 50 (1994), 15431.

[194] X. G. Gong, *Phys. Rev. B* 52 (1995), 14677.

[195] B. X. Li, M. Jiang, P. L. Cao, *J. Phys.: Condens. Matter* 11 (1999), 8517.

[196] B. X. Li, P. L. Cao, and D. L. Que, *Phys. Rev. B* 61 (2000), 1685.

[197] B. X. Li and P. L. Cao, *J. Phys.: Condens. Matter* 13 (2001), 10865.

[198] B. X. Li, P. L. Cao, X. Y. Zhou, *Phys. Lett. A* 288 (2001), 41.

[199] Q. Sun, Q. Wang, P. Jena, S. Waterman, and Y. Kawazoe, *Phys. Rev. A* 67 (2003), 63201.